Durham E-Theses

The stability of liquid lubricated journal bearings

Horner, D.

How to cite:

Horner, D. (1984) *The stability of liquid lubricated journal bearings*, Durham theses, Durham University. Available at Durham E-Theses Online: http://etheses.dur.ac.uk/7470/

Use policy

The stability of Liquid Lubricated

Journal bearings

by

D.Horner

University of Durham

A dissertation submitted for the degree of

Doctor of Philosophy

1984

ABSTRACT

The dynamic characteristics of journal bearings have been predicted by solving Reynolds equation with a common cavitation model. A perturbation analysis has been used to express the equations governing the fluid film pressure and cavitation region state in terms of a dynamic journal displacement vector. The use of these equations has been demonstrated on the long and short bearing approximations. The stability performance has been predicted for both rigid and flexible bearing systems.

A perspex test bearing has been used to observe cavitation under steady and dynamic loads, and a high speed test apparatus was developed for the measurement of lubricating film performance at whirl onset conditions. Although the test results were consistent and repeatable, the stability performance of the bearings tested was substantially less than the predictions of the simple bearing theory and other workers results. It is thought that the poor performance was due to oil starvation.

Acknowledgement

I am indebted to the technical and academic staff of the Department of Engineering for their assistance during the course of the project. My thanks must also go to the members of other University departments who helped me with their specialist knowledge and skills.

Above all the encouragement and guidance given by Professor Marsh has been greatly appreciated.

CONTENTS

LIST OF TABLES

LIST OF FIGURES

Symbols

A..	non-dimensional film stiffness
$[A(\sigma)]$	non-dimensional film stiffness matrix
B..	non-dimensional film damping coefficient
C	bearing radial clearance
C..	constant of integration
C_M	mounting damping coefficient
D	streamer density function
F.	film force component
H	compressibility number $= 6\mu_a \omega_o R^2 / P_a C^2$
I	unit matrix
I_ℓ^{mn}	integral $\int \sin^m(\phi) \cos^n(\phi) / h_o^\ell \, d\phi$
L	bearing width
M.	mass of bearing element
P	film pressure
R	mean bearing radius
R_B	bearing displacement radial direction
Re_c	Reynolds number based on radial clearance $= \rho VR / C$
S_B	bearing displacement tangential direction
S_M	mounting stiffness
T	lubricant surface tension

U
V } bearing surface velocities
W

X
Y } lubricant body forces
Z

f..   non-dimensional film force coefficients
h   film thickness
i   unit imaginary number $= \sqrt{-1.0}$
n   normal to film boundary surface
p′   non-dimensional film pressure
r   radial cartesian coordinate
s   tangential cartesian coordinate
t   time
u
v } lubricant velocity components
w

x
y } cartesian clearance space coordinates
z

β film boundary surface angle

$\gamma.$ stability parameter $= \quad M.C\,\omega_o^2 / \ 4P_a\,RL$

ϵ eccentricity ratio

ζ non-dimensional axial coordinate

Θ attitude angle

λ complex time constant

μ lubricant viscosity

ρ lubricant density

σ complex non-dimensional time constant

ϕ angular coordinate

ϕ_r angular coordinate in the relative coordinate system

ω_o journal rotational angular velocity

ω_1 journal orbital natural frequency

Subscripts

a	ambient condition
B	general film boundary surface
B	bearing centrebody
RB	sum of bearing rotor and centrebody paramters
c	critical film parameter value
c	film cavitation boundary surface
f	film formation boundary surface
M	bearing flexible mounting
n	normal to film boundary surface
R	rotor
r	radial coordinate direction
s	tangential coordinate direction

Superscripts

′	non-dimensional parameter derived from dimensioned value

1 INTRODUCTION

Ever since Reynolds discovered the principles governing hydrodynamic lubrication, the development of a mathematical model for bearing behaviour has attracted the attention of mathematicians and engineers alike. Whilst the theory of liquid lubricated bearings has still not reached an entirely satisfactory state, a more complete theory has been developed for both the steady state and dynamic performance of gas bearings. This situation has arisen because gas bearings are simpler to analyse, even though the compressibility of a gaseous lubricant has to be taken into account.

The major difference between the two types of hydrodynamic bearing is that lubricants in the liquid phase are prevented from extending throughout the clearance space by the formation of substantial bodies of fluid in the gas phase, whereas a gas bearing's lubricant is present in the gas phase throughout the clearance space. In addition a gaseous lubricating film is largely isothermal, which contrasts with the large thermal gradients found in bearings running at typical duties for liquid lubricants. Most problems have been encountered with the liquid lubrication of journal bearings since not only is the load bearing film not isothermal but a region of cavitation is expected to form in part of the clearance space. The mechanism governing the action of the cavities is not fully understood, and
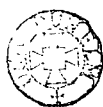
a universal model of cavitation behaviour has yet to be accepted.

A number of theories have been developed to describe the generation and behaviour of the cavities that form in a journal bearing. The relative merits of these theories are still being debated in the technical press and at conferences. Indeed the first Leeds-Lyon Symposium on Tribology(1) was devoted to cavitation in bearings. The conference report edited by Dowson Godet and Taylor provides a wealth of information and references. Although much attention has been focussed on the nature of the flow at the lubricating film's rupture surface, no wholly satisfactory description of the phenomena has emerged. So far only a few of these cavitation models have proved sufficiently amenable for general use in predicting bearing performance.

A number of flow models have also been postulated for the formation surface, where the lubricating film is initiated. The lubricating film in a typical journal bearing normally starts at an oil supply groove, hence this aspect of fluid film behaviour is of more concern to the lubrication of non-conformal surfaces. However when a journal bearing is running in a starved condition the mechanism of film formation becomes important since the boundary surface is free to find an equilibrium position which balances the flow of lubricant across the film formation boundary surface.

The first solutions to the lubrication equations represented infinitely wide bearings operating at steady state conditions. These were followed by similar solutions for finite width bearings using a variety of mathematical techniques to overcome the algebraic problems. Later DuBois and Ocvirk(2) brought into general use a technique for analysing short bearings. The short bearing equations neglect the pressure gradient term in the circumferential direction, creating a version of Reynolds equation which has a comparatively simple set of solutions. One of the features which makes this type of solution so manageable is that boundary values for fluid pressure at the sides of the bearing are sufficient to specify the pressure distribution throughout the load bearing film. Consequently there are no remaining arbitrary constants with which to consider the effects of cavitation.

The usual boundary condition used to define the extent of the lubricating film in the short bearing solution, is that the bounding surface is at a uniform pressure. The value of fluid pressure at the boundary is often taken to be atmospheric, in which case the lubricating film extends throughout the predicted region of above ambient pressure. Despite such a rudimentary treatment of cavitation phenomena, the resulting solutions give good steady state performance predictions for short bearings. The simplicity of the short bearing equations and the relative ease with which they can be solved, combined with their

reasonable performance predictions and immunity to the controversy over cavitation, has ensured the Ocvirk solutions a secure place in lubrication theory.

With the advent of calculating machines and electronic computers, more emphasis has been placed in recent years on the solutions for finite width bearings. The rapid calculating ability of these machines has enabled the effect of viscous losses on the fluid temperature, and hence viscosity, to be taken into account. But usually the simpler forms of boundary conditions have been retained.

For a long time journal bearings have been recognised as being susceptible to instability arising from the pressure distribution in the lubricating film. In 1919 Harrison(3) presented a dynamic solution for the full Sommerfeld form of Reynolds equation, and observation of half speed whirl was first reported by Newkirk(4) in 1925. It was during the first half of this century, as the general level of shaft speeds rose, that consideration of a bearing's dynamic characteristics became an important aspect in the design of most high speed machinery.

The first attempts to model the unstable behaviour of lubricating films considered only the film forces generated at steady operating conditions, neglecting the force components due to translational journal velocity. These simple models of oil

film induced whirl have been summarised by Cameron(5). Since these simple dynamic models do not exhibit a strong tendency to predict the half speed vibrational frequency which is normally observed, a more complete set of equations have to be used. Including the time dependent terms from Reynolds equation in the analysis has been shown by Morrison(6) and Holmes(7) to generate significantly different dynamic performance predictions. This demonstrates the importance of the translational journal velocity on the generation of pressure in the lubricating film.

Modern numerical solutions to the lubrication equations are often used to generate dynamic performance predictions by notionally perturbing the journal. Once the steady state performance has been calculated, the local film stiffness and damping are assessed. The local film stiffnesses are usually determined by recalculating the lubricating film pressure distribution, and hence the film forces, after displacing the journal centre a small distance in each of the coordinate directions. Similarly the forces generated by translational journal velocities can be calculated by introducing small journal velocities into the lubrication equations. The technique assumes that the dynamic film pressure distribution in a bearing can be predicted by summing the calculated steady state and perturbed pressure fields. Hence all such analyses must be considered as quasi-static.

Since the technique described uses small journal perturbations, the dynamic film characteristics are determined by finding the difference between pairs of similarly sized quantities. A more appropriate technique is to generate equations describing the difference between the steady and perturbed states, and then solve these new equations describing the difference. Thus the dangers associated with finding the difference between two quantities of the same order are avoided. In addition more attention can be devoted to finding the appropriate boundary equations for the dynamic system. The theoretical content of this thesis is devoted to deriving these equations and finding their solutions using typical simplifying assumptions and a simple cavity model.

After determining the dynamic fluid film behaviour, the stability of a rigid rotor supported by the film can be assessed. However very few rotating machines have such a simple analogue. Most machines possess flexibility in their shafts and often have flexibility built into their mountings, both of which have a significant affect on the stability of the system.

The dynamic modelling of systems comprising bearings and shafts is normally performed by including the calculated dynamic model of the lubricating film with the usual spring and damper models for the machine structure. The process of vibrational analysis is routinely performed by computers using the full set

of eight stiffness and damping coefficients describing the fluid film behaviour.

A much simpler but very powerful technique makes use of the dynamic stiffness parameter for the dynamic model of the lubricating film, instead of the complete set of stiffness and damping coefficients. The dynamic stiffness parameter is the value of the film stiffness at whirl onset conditions when the film exhibits no nett damping. Thus running speeds which lead to resonance in the simplified system model will indicate the operating conditions at which whirl onset will occur. Hence when this technique is used in the design of rotating machinery, the principal aim is to ensure that critical running speeds at which the film exhibits very little damping do not exist close to the normal running speed of the machine.

Ever since the emergence of hydrodynamic lubrication as a subject in its own right, there have always been very few reported experimental investigations concerning bearing dynamics, in comparison to the number of theoretical studies that have been published. This is largely due to the particular difficulty in measuring the dynamic performance of a lubricating film. Typical test arrangements have consisted of a test bearing loaded against a shaft which is supported by other slave bearings. The principal difficulty with this type of arrangement is evaluating the interaction between the test and support bearings. In

addition, test results are influenced by flexibility in the structure of the apparatus, and occasionally the dynamic behaviour exhibited has been dominated by shaft whip.

The principal aim of experimental work reported in this thesis has been to demonstrate with oil lubricated bearings an experimental technique already used to study the whirl onset performance of gas bearings. The technique uses a single bearing system so that there is no possibility of interaction between test and slave bearings. The rotor is also designed so that it is effectively rigid, hence the results can not be influenced by the phenomena of shaft whip. A feature of the technique is that each test bearing can be made to go unstable over a wide range of operating conditions by varying the stiffness of the structure supporting the bearing assembly. Thus an essentially simple apparatus capable of collecting data from a wide range of operating conditions has been used to generate experimental data, whilst avoiding some of the major problems associated with dynamic testing.

Although special bearing geometries such as lemon bore and offset-halves have been demonstrated in some circumstances to give better stability and damping characteristics than the plain journal bush, there is no consistent rule indicating when the alternative types are used to best advantage, or adequate guidelines to the degree of improvement to be expected. Thus an

experimental method capable of accurately measuring the dynamic
properties of various bearing geometries is of prime importance
to the designers of high speed machinery.

2   DEVELOPMENT OF FLUID FILM EQUATIONS

Reynolds lubrication equation in one form or another has been at the heart of most bearing performance analyses for slightly less than a century. The longevity of Reynolds work is confirmation that he isolated the primary mechanisms governing the generation of pressure within a continuous fluid film. But all the fluid in a bearing does not necessarily comply with Reynolds assumptions. For a self acting gas bearing the working fluid is present in a continuous film throughout the clearance space, and Reynolds equation is applicable to all the fluid in the lubricating film. However with a liquid lubricant, cavitation is normally expected to disturb the fluid film to create a region where Reynolds equation is not normally applied. Therefore a system of cavitation equations is required to describe the flow of lubricant and cavity fluid through the cavitation region, in the same manner that Reynolds equation is a description of lubricant flow within a continuous load bearing film.

Since these mathematical descriptions of fluid flow are differential equations, an additional set of boundary equations is required before a solution can be attempted. One of the major difficulties in solving the system of lubrication equations is that the locations of the boundaries between the full film and cavitation regions are not known in advance, consequently the

division of the clearance space between the two types of region is also a part of the solution.

The following sections develop a system of equations to be solved for the fluid film pressures acting on a journal, which will then be used in the subsequent assessment of stability. Isothermal and hence isoviscous solutions have been used in order to generate simple algebraic expressions capable of manipulation during the dynamic analysis. Just as Reynolds equation incorporates the primary mechanisms of fluid flow in a thin film, an isoviscous solution demonstrates the principal performance features of bearings at typical duty conditions.

2.1   REYNOLDS EQUATION

Modern derivations of Reynolds equation usually start from the Navier-Stokes equations which are a general statement of the laws of motion for a viscous fluid.   The technique used for the derivation is to apply continuity to an elemental volume in the region of continuous fluid.   The typical two dimensional form of Reynolds equation is found by integrating the fluid velocity components crossing the surfaces of an elemental volume spanning the clearance space.   The net mass flow into the element is then related to the rate at which the elemental volume is changing. The following equation (2.1) is a form of the Navier-Stokes

equations which has been derived from the text by Lamb(8).

$$\rho \frac{Du}{Dt} = X - \frac{\partial P}{\partial x} - \frac{2}{3} \frac{\partial}{\partial x}\left(\mu \left(\frac{\partial u}{\partial x} + \frac{\partial v}{\partial y} + \frac{\partial w}{\partial z} \right) \right) + 2 \frac{\partial}{\partial x}\left(\mu \frac{\partial u}{\partial x} \right)$$
$$+ \frac{\partial}{\partial y}\left(\mu \left(\frac{\partial u}{\partial y} + \frac{\partial v}{\partial x} \right) \right) + \frac{\partial}{\partial z}\left(\mu \left(\frac{\partial u}{\partial z} + \frac{\partial w}{\partial x} \right) \right) \qquad (2.1)$$

Similar equations can be derived for orthogonal directions 'y' and 'z' of a typical fluid film system shown on figure 2.1. As with most hydrodynamic problems the full Navier-Stokes equations are far too complicated for algebraic manipulation. Since the detail of the simplification of these equations can be found in most text books on hydrodynamics and lubrication, emphasis is given in the following paragraphs to the assumptions and techniques used rather than the detail of the algebra.

First of all it is assumed that the body forces 'X,Y,Z' from whatever source are small compared to the shear stresses and pressure forces acting on the fluid. Thus surface tension, gravity, electromagnetic and atomic forces are neglected, eliminating the body force term from equation (2.1). The lubricant flow is also assumed to be laminar, implying that the flow is dominated by viscosity rather than inertia. For journal bearings operating at a steady state condition Brand(9) has shown that inertia effects can be neglected provided that $Re_c < R/C$. Similarly Taylor(10) discovered that turbulence in the form of vortex rings would develop for high Reynolds number flow between concentric cylinders. Taylor's condition for laminar flow is

$Re_c < 41.1 \sqrt{R/C}$. Further work by Cole(11) has indicated that the critical value of Reynolds number for Taylor vortices rises with increasing eccentricity. Tests performed by Vohr(12) to repeat this work indicate that the rise may only be marginal for typical clearance ratio values. Thus for steady state operation that satisfies both the above conditions, the inertia associated terms in Reynolds equation can be omitted. Provided that the velocities and accelerations associated with a translational journal motion are small, the inertia terms can also be neglected for a dynamic operating condition. The orbital frequency of oil film whirl is normally expected to be about half the journal rotational frequency. Thus the fluid inertia terms can be neglected for the small amplitude motions of whirl onset, and hence for stability analyses.

Finally assumptions can be made based upon the geometry of typical journal bearings. The fluid velocity components 'u' and 'w' along directions 'x' and 'z' in the plane of a thin film normally change relatively little when compared to the substantial changes that take place in the very short distances across the film thickness, the 'y' direction. Thus some spatial derivatives of velocity can be discarded. Implied in the last assumption is that there are no significant currents of lubricant at right angles to the plane of the film, thus the velocity components 'v' are sufficiently small to be neglected. Implementing all these assumptions simplifies the Navier-Stokes

equations to the following reduced form.

$$\frac{\partial P}{\partial x} = \frac{\partial}{\partial y}\left(\mu \frac{\partial u}{\partial y} \right)$$

$$\frac{\partial P}{\partial y} = 0 \tag{2.2}$$

$$\frac{\partial P}{\partial z} = \frac{\partial}{\partial y}\left(\mu \frac{\partial w}{\partial y} \right)$$

This simple set of equations is easily integrated across the clearance space provided that a constant fluid viscosity is assumed. Integrating twice gives general expressions for the velocity profiles, but boundary conditions are required to specify the solution. Except for some gas lubricated systems there is no slip between the lubricant and the bearing surfaces, consequently the constants of integration can be evaluated for typical bearing arrangements using the bounding journal and bearing surface velocities. To obtain simple expressions from the integration, the y-axis is usually defined as normal to the plane of the film with the surface velocities along the x-axis. The resulting equations for the fluid velocity components are as follows:-

$$u = \frac{y(y-h)}{2\mu} \frac{\partial P}{\partial x} + \frac{(U_2 - U_1)y}{h} + U_1$$

$$v = 0 \tag{2.3}$$

$$w = \frac{y(y-h)}{2\mu} \frac{\partial P}{\partial z}$$

Reynolds equation is constructed by applying the continuity of mass condition to a small elemental volume bridging the clearance space. In cartesian coordinates Reynolds equation is:-

$$\frac{\partial}{\partial x}\left(\frac{\rho h^3}{12\mu}\frac{\partial P}{\partial x}\right) + \frac{\partial}{\partial z}\left(\frac{\rho h^3}{12\mu}\frac{\partial P}{\partial z}\right) = \frac{\partial}{\partial x}\left(\rho\frac{(U_1+U_2)h}{2}\right) + \frac{\partial}{\partial t}(\rho h) \quad (2.4)$$

Since journal bearings have a cylindrical form of clearance space and the inertia terms associated with circular motion have been shown by Brand to be small, Reynolds equation is easily transformed into the more convenient polar coordinate system shown on figure 2.2. At the same time non-dimensional quantities can be formed using the following definitions.

$$
\begin{array}{ll}
p' = P / P_a & \phi = x / R \\
\rho' = \rho / \rho_a & \zeta = z / L \\
\mu' = \mu / \mu_a & h' = h / C \\
H = 6\mu_a\omega_o R^2 / P_a C^2 & \omega_o = (U_1 + U_2)/ R
\end{array} \quad (2.5)
$$

Thus a non-dimensional form of Reynolds equation suitable for journal bearing work is:-

$$\frac{\partial}{\partial\phi}\left(\frac{\rho'h'^3}{\mu'}\frac{\partial p'}{\partial\phi}\right) + \left(\frac{R}{L}\right)^2 \frac{\partial}{\partial\zeta}\left(\frac{\rho'h'^3}{\mu'}\frac{\partial p'}{\partial\zeta}\right)$$
$$= H\left(\frac{\partial(\rho'h')}{\partial\phi} + \frac{2}{\omega_o}\frac{\partial(\rho'h')}{\partial t}\right) \quad (2.6)$$

At this stage it should be noted that Reynolds equation has been derived for a thin continuous laminar film of liquid or gaseous fluid that conforms to the assumptions described. This

derivation has been performed in a fixed coordinate system, so all variables should be expressed in terms of the fixed coordinates 'ϕ' and 'ς'. Consequently for the small clearance ratios 'C/R' normally found in journal bearings the film height is adequately approximated by the equation (2.7).

$$h = C (1 + \epsilon \cos(\phi - \Theta)) \qquad (2.7)$$

Reynolds equation has been derived from the equations of motion for a viscous fluid and describes the generation of pressure within a continuous film in order to satisfy continuity of mass. The equation presents a boundary value problem for which there are no general solutions. The boundary conditions necessary for the solution of the problem are normally a sophisticated set of expressions in themselves. The simplest set of boundary conditions are for the self-acting gas bearing with a plain bore. For this type of configuration the bearing is immersed in lubricant, hence the boundary conditions are that the fluid at the sides of the clearance space will be at ambient pressure, and Reynolds equation is applicable throughout the annular clearance space.

Liquid lubricated bearings are substantially different since cavitation is usually expected to take place in the divergent section of the clearance space. That is the continuous film of lubricant ruptures forming cavities in the film. For such cases Reynolds equation is directly applicable to the full film region

of liquid found in the loaded part of a bearing, but not the cavitation region. The boundary conditions for this type of liquid lubrication are again ambient pressure where the film reaches the sides of the bearing, but have yet to be determined for the interior boundaries where the film ruptures and reforms. For the case of ventilated cavities one boundary condition is that of ambient pressure at the internal boundary surfaces. The cavitation region, being a volume containing two fluids of different phases, requires special consideration to determine an appropriate set of equations which describe the flow in and around the cavities.

Reynolds equation as derived has been found satisfactory for predicting the performance of typical bearings of modest size and duty, particularly in the field of tilting pad thrust bearings where simple boundary conditions apply. Journal bearing implementations are more difficult to create but even very simple models give fundamentally correct steady state performance predictions. In general the boundary conditions applied to the internal film boundaries have a local effect and the type of boundary condition used is not an overriding factor governing the predicted fluid pressure in the bulk of the lubricating film.

2.2 CAVITY EQUATIONS

Cavitation is a phenomenon that is restricted to liquids and is not applicable to systems with gaseous working fluids. Since this thesis is concerned with the effect of cavitation on bearing dynamics the lubricant must be a liquid. In these circumstances the relative fluid density $'\varrho''$ is normally set to unity, to reflect the effective incompressibility of the working fluid. In order to maintain the general nature of the equations in this chapter the non-dimensional lubricating fluid density $'\varrho''$ and viscosity $'\mu''$ have been retained. For all subsequent chapters a liquid lubricant and isoviscous solutions have been assumed. Thus for the following chapters the relative density and viscosity parameters have been given a value of one, and have disappeared from the continuity expressions.

Studies aimed at observing oil film cavitation behaviour have usually considered steady state operation and have shown the formation of a finite number of cavities separated by relatively thin streamers of oil such as those shown on figure 2.3. The nature of the cavities is such that it is easy to conceptually divide the clearance space into two distinct regions, the full film region and the cavitation region. Typically the film ruptures at intervals across most of the bearing width, but at one angular location. Thus the film rupture, or cavitation boundary between the two regions is sensibly defined by the noses

of the cavities. The cavities normally extend to a well defined position where the lubricating film reforms. Whereas the cavities usually form a substantial continuous film of cavity fluid, the streamers are for most of their length an order of magnitude narrower than the cavities, and can not be considered as significant expanses of continuous fluid. Later the cavitation region will be shown to be effectively an area of constant pressure.

Observations reported in chapter 7 of this thesis show that during the dynamic motion of whirl onset, the cavities formed during the preceding steady state condition can be expected to maintain their basic steady state structure as they oscillate at the frequency of the journal motion. Hence a model of the cavitation region with the ability to allow for small boundary movements during dynamic conditions is suitable for stability analyses. Whereas the estimated steady state performance of a bearing is relatively insensitive to the boundary conditions used, instability is a clearly defined condition which can be expected to be sensitive to the cavitation model.

Surface tension effects have a significant influence on the form of the cavity boundaries. Fall(13) and others have shown correlations between the number of streamers, the film thickness and the parameter 'μU/T', where 'T' represents the surface tension of the working fluid. Surface tension phenomena are the

result of an inbalance of cohesive and adhesive atomic forces. Because these forces are very short range in comparison to bearing clearances there is a balance of force throughout most of the load bearing film. However there is a very large inbalance of intermolecular forces in the first few layers of molecules near the surface of the lubricant. This inbalance forms a dominant mechanism determining the shape of the cavity boundaries. As a result surface tension effects are normally treated as a boundary condition, hence the surface tension parameter does not appear in Reynolds equation.

The streamers of oil passing through the cavitation region being relatively narrow are dominated by surface tension effects which play an important role in maintaining the long side surfaces. Observation shows that surface tension also causes significant turning of the fluid at the nose of the cavities, channelling fluid into the streamers. Similarly surface tension is significant at the reformation boundary where surface tension maintains the film formation front inbetween the streamers. But these effects are local and do not affect the bulk of the film. Thus the body forces in the Navier-Stokes equations which represent surface tension effects, are only significant for fluid in the streamers or adjacent to the film boundaries. Consequently Reynolds equation can not be expected to be a good model for the flow of lubricant through the cavitation region.

In contrast the cavities represent significant continuous volumes of low viscosity gaseous fluid. As such, Reynolds equation is applicable to the flow and pressure inside a cavity, just as Reynolds equation is used for the prediction of gas bearing performance. However a bearing designed to operate with a high viscosity lubricant is unlikely to develop significant pressures in a region of low viscosity gas. A bearing operating at steady state has stationary cavity boundaries and a constant cavity volume. Observations reported in chapter 7 show that the process of releasing gas from solution in the lubricant is relatively slow, and the process of reabsorption to be even slower. Hence the cavities tend to have a constant mass content and there must be a circulation of gas within each cavity as shown on figure 2.4. Applying continuity in the 'x' direction for the 'x-y' plane gives the following expressions for the velocity profile and pressure gradient in a one dimensional system.

$$u = 3 (U_1 + U_2) \left(\frac{y}{h}\right)^2 - 2 (2U_1 + U_2) \left(\frac{y}{h}\right) + U_1$$

$$\frac{\partial P}{\partial x} = \frac{6\mu}{h^2} (U_1 + U_2) \tag{2.8}$$

$$\frac{\partial p'}{\partial \phi} = H \frac{\mu'}{h'^2}$$

However since the gases of the cavity fluid are normally orders of magnitude less viscous than the lubricant, the cavity pressure gradients will be small compared to the gradients in the full

film. This hypothesis is supported by results published by Etsion and Ludwig(14) which show very little change in pressure over the cavitation region. Experience with short bearing solutions for Reynolds equation also show that narrow streamers of fluid are incapable of supporting large pressures. Thus apart from the step changes in pressure due to surface tension effects at the cavity boundaries, the whole of the cavitation region is likely to be close to a uniform pressure.

The Reynolds number for the flow of cavity fluid will normally be slightly greater than that for the lubricant, hence inertia effects will appear in the cavity before the full film. Also figure 2.4 shows that there will be considerable velocity components and gradients across the clearance space near the cavity boundaries. Consequently not all the conditions for Reynolds equation are necessarily satisfied by the whole of each cavity.

Whilst it is possible to use Reynolds equation for a model of flow in the cavitation region, difficulties will be encountered in dividing the region between cavities and streamers, and a numerical technique would be the only practical method of solution. A much simpler approach incorporating the essential features of the cavitation region is required so that the results are suitable for an algebraic treatment of stability.

Early work by Swift(15) and Steiber(16) identified a cavitation boundary condition that provided for continuity of lubricant across the film rupture surface. More recent work by Jakobsson(17), Floberg(18) and Olsson(19) has lead to a single equation for both the formation and cavitation boundaries, and includes a model for lubricant flow through the cavitation region. For the rest of this thesis the theories presented by Jakobson, Floberg and Olsson will be refered to as the J.F.O. boundary conditions. This later work is based upon the following assumptions. First that where the film ruptures all the lubricant flow is channeled into the streamers, the whole of the cavitation region is at a uniform pressure and that this pressure is the lowest pressure in the clearance space. The cavity gas is assumed to have negligible mass, to be inviscid and perfectly elastic, hence the properties of the cavity gas are eliminated from the theory. This streamer model of cavitation complies with observed streamer patterns but does not prescribe all the boundary conditions.

The cavitation normally experienced in hydrodynamic machinery is usually the formation of voids in the working fluid when the local film pressure drops below a critical value. Taking a simple view of the cavitation process, the critical pressure is the saturated vapour pressure of the working fluid. This type of cavitation condition must normally be associated with the initial formation of the cavitation region in a lubricating film. The

typical steady state situation for a journal bearing is that voids are not continuously created but that existing cavities maintain their equilibrium position in the clearance space against the flow of lubricant. Since the steady state cavities in a lubricating film usually contain air rather than oil vapour, the pressure in a closed cavity is governed by the equation of state for air, not the saturated vapour pressure of oil. Alternatively, if the cavitation region is ventilated the cavity pressure will be the ambient value.

There is an alternative model available for predicting the location of the cavitation boundary which is based upon the phenomenon of separation. This model does not predict the formation of streamers but requires that all the lubricant be carried away from the boundary on a moving surface. The separation model predicts that the boundary occurs with a positive pressure gradient just downstream of a small sub-cavity pressure loop in the load bearing film. However the low pressure region tends to be very small. Fall(13) in his measurements of the cavity pressures also shows sub-cavity film pressures existing before the rupture surface. The better performance prediction of the separation model at some operating conditions, as shown by Taylor(20), is outweighed by its difficulty of use.

The J.F.O. streamer model has been developed to an advanced state so that there is a simple boundary equation for both types

of region interface, and an easy interpretation leading to manageable expressions for the boundary equations. But in order to make the theory workable the fluid film is assumed to rupture into an infinite number of infinitesimally narrow streamers and cavities. The state of the cavitation region is described by the streamer density function 'D' and the cavity pressure. The streamer density function is defined as the proportion of an elemental cross-sectional area, at right angles to the surface motion, which is occupied by lubricant. Since there are no pressure gradients in the region the lubricant velocity profiles are simply :-

$$u = (U_2 - U_1) \left(\frac{y}{h}\right) + U_1$$

$$v = 0 \qquad\qquad (2.9)$$

$$w = 0$$

Following the derivation of Reynolds equation, continuity of lubricant mass is applied to an elemental volume bridging the clearance between journal and bearing surfaces. The mass of lubricant contained in the elemental volume at any given time is given by the following expression:-

$$\varrho \; D \; h \; R\delta\phi \; L\delta\zeta \qquad\qquad (2.10)$$

Since cavity fluid is assumed to have negligible density and be infinitely compressible, the mass of cavity fluid in the control volume can be neglected. Since there are no pressure gradients

in the fluid a significant mass flow can not exist at rightangles to the direction of motion. Hence the mass flow rate through the cavitation region is given by the following expression for mass flow in the phi direction through an elemental section.

$$\rho \ D \ \frac{\omega_o}{2} \ R \ h \ L d\zeta \tag{2.11}$$

Thus equating the rate of change of mass content, to the net mass flow of lubricant into the elemental volume, and rearranging to make non-dimensional terms gives the following expression for the streamer state in the cavitation region.

$$\frac{\partial(Dh')}{\partial\phi} = \frac{-2}{\omega_o} \frac{\partial(Dh')}{\partial t} \tag{2.12}$$

Again this formula has been derived in a fixed coordinate system and the functions 'D' and 'h'' must be expressed in terms of the coordinates 'ø' and 'ζ'. The streamer model for the cavitation region is very simple, eliminating not only the fluid properties of the cavity fluid but also surface tension. As a consequence the only parameter used in the cavitation equations that does not appear in Reynolds equation is the streamer density function 'D'. The cavitation model requires uniform pressure over the region which is a reasonable approximation to observed film behaviour. The surface tension parameter has been neglected because its effect on the number of streamers is of secondary importance, and there is currently no evidence available to indicate that surface tension has a significant effect on film pressures.

Thus a simple differential equation has been derived which reflects the important characteristics of the cavitation region. The combination of Reynolds equation (2.6) and the streamer equation (2.12) provide models of the lubricant flow in the full film and cavitation regions respectively, which between them cover the whole of the clearance space.

2.3   BOUNDARY EQUATIONS

The simplest boundary condition to be applied to the governing differential equations is that the lubricant pressure should be the same as that of the ambient atmosphere where the fluid film extends to the sides of the bearing. Similarly if the bearing surface contains a lubricant supply groove then fluid at the edge of the groove must be at the pocket pressure. The interior boundaries not attached to a supply slot require a more detailed approach.

The equations for continuity at the boundary between the full film and cavitation regions can be developed from an approach similar to that used by Olsson(19). The effect of boundary surface curvature in elevation is assumed to be negligible, so that the boundary interface is perpendicular to the bearing surfaces, and can be represented by a line on a plan of the clearance space as shown by figure 2.5. Since the cavitation

region is assumed to be at a uniform pressure the film boundaries must also be constant pressure contours. The following relation for pressure at the boundary surface is derived from the condition that the boundary pressure is constant.

$$\left(\frac{R}{L}\right) \frac{\partial p'}{\partial \zeta} = \frac{\partial p'}{\partial \phi} \tan(\beta) \qquad (2.13)$$

Since the boundary surface has no volume a boundary condition must be that the full film and cavitation region solutions predict a continuity of mass across each part of the bounding surface. The general expression for mass flow across a surface moving with a normal velocity $'V_n'$ at any part of the clearance space is :-

$$\varrho \int_0^h u \, dy \, \delta s \cos(\beta) + \varrho \int_0^h w \, dy \, \delta s \sin(\beta) - \varrho \, V_n \, h \, \delta s \qquad (2.14)$$

Using the expressions (2.3) and (2.9) for the fluid velocity components, the mass flow crossing an element of the boundary surface at the full film side is :-

$$\frac{\varrho \omega_o R h}{2} \left(\left(1 - \frac{h^2}{\mu' H} \frac{\partial p'}{\partial \phi} (1+\tan^2(\beta)) \right) \cos(\beta) - \frac{2 \, V_n}{\omega_o R} \right) \delta s \qquad (2.15)$$

The corresponding expression for the cavity side of the boundary is:-

$$\frac{\varrho \omega_o R h}{2} \, D \left(\cos(\beta) - \frac{2 \, V_n}{\omega_o R} \right) \delta s \qquad (2.16)$$

The following boundary condition is found when the two

expressions above are constrained to have the same value.

$$(1-D)\left(\cos(\beta) - \frac{2}{\omega_0}\frac{V_n}{R}\right) - \frac{h^2}{\mu' H}\frac{\partial p'}{\partial o}(1+\tan^2(\beta))\cos(\beta) = 0 \qquad (2.17)$$

The pressure gradient in the boundary equation above is always the pressure gradient at the full film side of the boundary surface, and similarly the streamer density is the density of the streamers on the cavity side of the boundary.

This expression of the boundary condition becomes inadequate if the boundary surface turns to become parallel to the circumferential direction. For this case the product of the pressure gradient and the trigonometric expression is indeterminate. A better behaved version of the relationship is found using the pressure gradient normal to the boundary surface, as follows:-

$$(1-D)\left(\cos(\beta) - \frac{2}{\omega_0}\frac{V_n}{R}\right) - \frac{h^2}{H}\frac{R}{\mu'}\frac{\partial p'}{\partial n} = 0 \qquad (2.18)$$

This single equation is completely general in that it applies to both the film rupture where flow is into the cavity, and the reformation boundary where the flow is out of the cavity into the full film region. Olsson(19) has shown how this equation can be interpreted so that different constraints are applied to the two types of boundary. The key is the assumption that the lowest pressure in the clearance space is always the cavity pressure. The simplified case of steady state is best for demonstrating the

interpretation.   The steady state version of the boundary
condition is :-

$$(1-D) \cos(\beta) \quad - \quad \frac{h^2}{H} \frac{R}{\mu'} \frac{\partial p'}{\partial n} \quad = \quad 0 \qquad\qquad (2.19)$$

Considering first the cavitation boundary, which is the surface
that generates streamers of oil, the cavitation region must be
downstream of the boundary.   Consequently   the   lowest pressure
condition requires   that the pressure gradient in the fluid film
approaching the cavity must be negative or zero.   To satisfy
equation (2.19) the streamer density function at the boundary
must have a value of one and the pressure gradient be zero.   Thus
making each term in the equation equal to zero, which corresponds
to the well known Swift-Steiber condition of no pressure gradient
at the film rupture boundary.   At the film reformation surface
the cavities must be upstream of the boundary and the pressure
gradient in the full film must be positive or zero.   Then the
streamer density function at the boundary surface   must have a
positive value less than one to balance the equation.   Thus the
boundary condition is interpreted as giving a zero pressure
gradient and unity streamer density function at a boundary that
generates streamers, and specifies a relationship between the two
variables at a film formation surface.

When a dynamic situation is studied the effect of internal
film boundary velocities must be taken into account.   It is

assumed that the cavity pressure remains constant and uniform over the cavitation region, whilst remaining the lowest pressure in the clearance space for the whole of the motion. For modest motions with small velocities the coefficient of the streamer density function $'\cos(\beta)-2V_n/\omega_a R'$ in equation (2.17) remains positive, and the above interpretation derived for steady state is still applicable. However if this factor changes sign the interpretation must be revised. For periods when the film boundary surfaces have sufficiently large forward velocities for the expression $'\cos(\beta)-2V_n/\omega_a R'$ to become negative, the relationships between streamer density and pressure gradient functions are reversed. The physical limitations on the value of the streamer density function, and the restrictions imposed on the pressure gradient by the minimum pressure condition, require that the moving film boundaries change type when a critical boundary velocity is reached. The critical velocity is given by the rate at which the lubricant can be transported through the cavitation region.

As shown above the mean velocity at which the lubricant is predicted to travel through the cavitation region depends upon the cavitation model that is used. The streamer model has a mean velocity equal to half the effective surface speed, whereas the separation model gives a velocity equal to the speed of the surface that transports the fluid away from the full film. A refined boundary model may allow for transport of lubricant in

streamers and as a surface film, in which case the critical boundary velocity component will be between the critical velocities of the two mechanisms.

2.4 FILM EQUATIONS IN THE RELATIVE COORDINATE SYSTEM

So far the three basic equations of continuity have been expressed in a fixed coordinate system. A useful alternative presentation can be generated by transformation into a relative coordinate system based upon the line joining the instantaneous journal and bearing centres. The radial and axial coordinates are retained but a new angular coordinate $'\phi_r'$ as shown on figure 2.2, is required. The two systems are linked by the relationship :-

$$\phi = \phi_r + \Theta \qquad (2.20)$$

Thus the appropriate Galilean transformations to be applied to the continuity equations are :-

$$\left(\frac{\partial}{\partial \phi} \right)_{\zeta, t} = \left(\frac{\partial}{\partial \phi_r} \right)_{\zeta, t}$$

$$\left(\frac{\partial}{\partial \zeta} \right)_{\phi, t} = \left(\frac{\partial}{\partial \zeta} \right)_{\phi_r, t} \qquad (2.21)$$

$$\left(\frac{\partial}{\partial t} \right)_{\phi, \zeta} = \left(\frac{\partial}{\partial t} \right)_{\phi_r, \zeta} - \frac{d\Theta}{dt} \left(\frac{\partial}{\partial \phi_r} \right)_{\zeta, t}$$

Applying these transformations creates three new basic equations

for which all variables should be expressed in terms of the coordinates 'ϕ_r' and 'ς'.

$$\frac{\partial}{\partial\phi_r}\left(\frac{\rho'h'^3}{\mu'}\frac{\partial p'}{\partial\phi_r}\right) + \left(\frac{R}{L}\right)^2 \frac{\partial}{\partial\varsigma}\left(\frac{\rho'h'^3}{\mu'}\frac{\partial p'}{\partial\varsigma}\right)$$

$$= H\left(\frac{\partial(\rho'h')}{\partial\phi_r}\left(1-\frac{2\dot{\theta}}{\omega_o}\right) + \frac{2}{\omega_o}\frac{\partial(\rho'h')}{\partial t}\right) \quad (2.22)$$

$$\left(1-\frac{2\dot{\theta}}{\omega_o}\right)\frac{\partial(Dh')}{\partial\phi_r} = \frac{-2}{\omega_o}\frac{\partial(Dh')}{\partial t}$$

$$(1-D)\left(\left(1-\frac{2\dot{\theta}}{\omega_o}\right)\cos(\beta) \frac{-2}{\omega_o}\frac{V_n}{R}\right) - \frac{h'^2}{H}\frac{R}{\mu'}\frac{\partial p'}{\partial n} = 0$$

In particular the film thickness should be expressed as :-

$$h = C\left(1 + \epsilon\cos(\phi_r)\right) \quad (2.23)$$

Comparing this set of equations with the originals (2.6), (2.7), (2.12) and (2.19) it can be seen that where the rotational speed occurred, either in its own right or as a part of the compressibility number 'H', it has been multiplied by the factor '$1-2\dot{\theta}/\omega_o$'. Hence the fixed version of Reynolds and the streamer equations can be transformed into the relative equations by replacing 'ω_o' by '$\omega(1-2\dot{\theta}/\omega_o)$'. Thus setting '$\dot{\theta}$' to zero in the relative equation will give exactly the same form of relationships as the fixed coordinate equations. Therefore the set of pressure fields and streamer density functions that satisfy the fixed equations for plain journal bearings, will also be the solution set for the system of relative equations. For steady state operating conditions this equivalence is shown more

clearly in the next chapter. Unfortunately most liquid lubricated journals are not plain in that axial slots are machined into the bearing surface to aid the flow of lubricant into the working section.

The crucial importance of the expression $'\omega_o(1-2\dot{\theta}/\omega_o)'$ is shown by the expression of the continuity equations in relative coordinates. If either $'\omega_o'$ is zero, or $'\dot{\theta}'$ is equal to $'\omega_o/2'$ the steady state film pressure solution is a constant value equal to atmospheric conditions, and the bearing is incapable of supporting a load. The first condition typically represents a bearing under a fixed direction load and no journal or bearing rotation, no hydrodynamic pressure is generated and the journal sits in the bottom of the bearing. No damage results since there is no sliding taking place. The second condition can be represented by a rotating load precessing at half the effective surface speed. Again no hydrodynamic pressure is generated to support the load. Since the journal and bearing surfaces will normally be in relative motion, sliding contact will take place generating excessive amounts of heat energy and cause damage to the bearing.

If the term $'1-2\dot{\theta}/\omega_o'$ has a small value during all or part of a dynamic motion, the generation of hydrodynamic film pressure is largely dependent upon the time derivative terms in Reynolds equation. The bearing can then be expected to exhibit a

stiffness much less than that at the steady state condition. This lack of stiffness is observed close to the half speed whirl condition when motions with a small value for the angular velocity expression, appear in the absence of significant exciting forces.

The equations predict that any combination of journal, bearing and load rotation will lead to the generation of hydrodynamic forces, provided that the two exceptional cases are avoided. Thus experimental apparatus need not be restricted to systems having fixed bearings and loads, with only the journal rotating.

3 STEADY STATE SOLUTIONS

The most important class of solution to Reynolds and the streamer equations represent the steady state equilibrium operating condition. For these solutions all the variables are independent of time, hence all the time derivative terms in the continuity equations are identically equal to zero. Thus the simplified Reynolds and streamer equations for a steady system are:-

$$\frac{\partial}{\partial \phi}\left(h_o'^3 \frac{\partial p_o'}{\partial \phi}\right) + \left(\frac{R}{L}\right)^2 \frac{\partial}{\partial \zeta}\left(h_o'^3 \frac{\partial p_o'}{\partial \zeta}\right) = H \frac{\partial(h_o')}{\partial \phi}$$

$$\frac{\partial(D_o h_o')}{\partial \phi} = 0 \tag{3.1}$$

and the equation for continuity across the cavity boundary is:-

$$(1-D_o)\cos(\beta_o) - \frac{h_o'^2}{H} R \frac{\partial p_o'}{\partial n} = 0 \tag{3.2}$$

All variables representing steady state solutions have been given a subscript of zero. The same equations expressed in the relative coordinate system defined at the end of the last chapter are :-

$$\frac{\partial}{\partial \phi_r}\left(h_o'^3 \frac{\partial p_o'}{\partial \phi_r}\right) + \left(\frac{R}{L}\right)^2 \frac{\partial}{\partial \zeta}\left(h_o'^3 \frac{\partial p_o'}{\partial \zeta}\right)$$

$$= H \left(1 - \frac{2\dot{\phi}}{\omega_o}\right) \frac{\partial(h_o')}{\partial \phi_r} \tag{3.3}$$

$$\frac{\partial(D_o h_o')}{\partial \phi_r} = 0$$

and for the boundary surface:-

$$(1-D_o) \quad \cos(\beta_o) \quad - \quad \frac{h_o'}{H} R \frac{\partial p_o'}{\partial n} \quad = \quad 0 \tag{3.4}$$

The similarities between the equations for the fixed and relative coordinate systems are now apparent. The steady state operating condition in the relative coordinate system is defined to be the journal centre orbiting around the centre of the bearing at a constant eccentricity and a steady angular velocity. Thus a single expression for each of the field variables $'p_o''$, $'D_o'$ and $'h_o''$ will satisfy both sets of equations for bearings of the same geometry, provided that the following condition is satisfied:-

$$H \left(1 - \frac{2\dot\theta}{\omega_o}\right)\Bigg|_{\text{relative}} \quad = \quad H \Bigg|_{\text{fixed}} \tag{3.5}$$

In all the following work the fixed coordinate system has been used in preference to the relative system . The fixed direction for the basis of the coordinate system has always been chosen to be the line joining the steady state line of journal and bearing centres, this is expressed mathematically as $'\theta_o'$ identically equal to zero. This choice considerably simplifies the algebra associated with the governing continuity equations. For steady state operating conditions $'\dot\theta'$ is identically equal to zero, which makes $'\phi'$ equal to $'\phi_r'$, thus under these conditions the fixed and relative equations are equivalent.

3.1   CONGRUENT OPERATING CONDITIONS

Normally the independent variables $'\epsilon_o'$ and $'\omega_o'$ are considered as positive, but negative values of both parameters represent real operating conditions. If a typical journal comes to rest and starts to rotate in the opposite direction, the angular velocity has changed sign. Any algebraic expression for bearing performance ought to be able to correctly predict the result of such a change in the direction of motion. Similarly the journal eccentricity need not be exclusively positive. If the algebraic expressions derived for the pressure and streamer density become invalid when either independent variable is negative, then the appropriate limit should be placed on the allowable range for that variable. Figure 3.1 shows the typical steady state condition and the congruent systems with negative eccentricity and rotation. By inspection it can be seen that the negative rotation system is a mirror image of the usual operating condition, about an axis defined by the line of journal and bearing centres. Consequently an algebraic solution to the steady state equations ought to satisfy the following conditions.

$$p_o'(\phi_r, -H) = p_o'(2\pi - \phi_r, H)$$
$$D_o(\phi_r, -H) = D_o(2\pi - \phi_r, H)$$

$$(3.6)$$

Similarly two systems of equal eccentricity but of opposite sign have point symmetry about the bearing centre. Hence the appropriate conditions for the complete solution to satisfy are:-

$$p_o'(\phi, -\epsilon_o) = p_o'(\pi + \phi, \epsilon_o)$$

$$D_o(\phi, -\epsilon_o) = D_o(\pi + \phi, \epsilon_o)$$

(3.7)

3.2 SHORT BEARING SOLUTION

The short bearing or Ocvirk solution to the continuity equations is applicable for cases where the bearing width 'L' is small compared to the radius 'R'. Usually good agreement between theory and experimental results are obtained for length to diameter ratios of less than one half. For these cases the rate of change of pressure in the circumferential direction must be insignificant compared with the corresponding rate of change in the axial direction, because of the relative fluid film extent in these axes. Reynolds equation is integrated with ease once the circumferential pressure gradient term has been eliminated. But it should be noted that the modified equation only satisfies continuity in the limiting case of zero bearing width. The short bearing Reynolds equation and its general solution are:-

$$\left(\frac{R}{L}\right)^2 \frac{\partial}{\partial \zeta}\left(h_o'^3 \frac{\partial p_o'}{\partial \zeta}\right) = H \frac{\partial(h_o')}{\partial \phi}$$

(3.8)

$$p_o' = \left(\frac{L}{R}\right)^2 H \left(\frac{-\epsilon_o \sin(\phi)}{2 \, h_o'^3} \zeta^2 + \frac{C_{o1}}{h_o'^3}\zeta + C_{o2}\right)$$

The constants of integration 'C_{o1}' and 'C_{o2}' must be evaluated using a suitable set of boundary conditions. Taking the usual

operating condition that there should be ambient pressure at the sides of the bearing, and defining 'p'' to be a non-dimensional gauge pressure, the boundary conditions are:-

$$p_o' \; = \; 0 \quad at \quad \zeta \; = \; \pm 0.5 \tag{3.9}$$

This condition alone provides sufficient information to evaluate both constants and fully define the pressure field without any flexibility left to apply the J.F.O. cavity boundary conditions. The resulting expression for film pressure is as follows.

$$p_o' \; = \; \left(\frac{L}{R}\right)^2 \; H \; \frac{\varepsilon_o \sin(\phi)}{2 \; h_o'^3} \left(\frac{1}{4} - \zeta^2\right) \tag{3.10}$$

This expression for pressure is a continuous function in the coordinates 'ø' and 'ζ' but the bearing surfaces are only defined in a small region of this mathematical space. The area of interest is always between zeta equal to plus and minus one half, but any continuous region of two pi radians in the phi direction is suitable. Normally a region defined between plus and minus pi, or zero to two pi is taken. Thus the expression for fluid pressure outside the region between zeta equal to plus and minus one half is defined to be invalid and parts of the solution lying outside a continuous region of two pi radians are chosen to be discarded.

Further selection takes place as the expression predicts sub-atmospheric pressures and even tensile states which most

engineers are unwilling to accept, since cavitation would normally be expected to intervene. In order to allow cavitation to take place the region of validity for the pressure expression has to be declared as smaller than the actual region occupied by the working surfaces. Since the region of cavitation is nominally at a uniform pressure, a constant pressure contour is usually chosen as the cavity boundary. The lower pressure region bounded by the chosen contour being defined as the cavitation region. Any sub-ambient pressure contour may be chosen as the cavity boundary but the most easily managed contour is that of ambient pressure. It is important to note that the boundary condition is defined as film rupture and formation taking place at a given value of film pressure. Since continuity within the pressure field is not satisfied there will always be apparently more lubricant flowing out of the cavity than entering. Hence no profit can be gained from attempting to calculate the streamer density function for the chosen cavity region.

The usual short bearing steady state solution assumes a ventilated cavity and atmospheric pressure in the cavitation region. The resulting boundary positions are film rupture at the minimum clearance height and film formation at the maximum clearance. The corresponding values of $'\phi_r'$ are pi and two pi respectively across the whole of the bearing width. These boundary angles have been used in subsequent chapters as the limits of the steady state lubricating film.

The solution for pressure can be tested by the appropriate congruency conditions. The expression (3.10) does satisfy the conditions, but a pressure field solution that includes a region of cavitation does not satisfy either of the congruency conditions. This situation arises because of the logical selection of the cavitation region. Thus expressions for Ocvirk type solutions that include a region of cavitation are only valid for positive values of 'ϵ_o' and 'ω_o'.

3.3   THE LONG BEARING SOLUTION

The long bearing solution, often referred to as the Sommerfeld solution is applicable to bearings of width much greater than the radius. In the limit that the bearing is infinitely long or that a seal mechanism prevents the formation of side effects, there will be no change of field variables in the axial direction. Neglecting the derivatives with respect to 'ζ' simplifies the continuity equations and again they become easily integrable. The steady state Reynolds equation for a long bearing is:-

$$\frac{\partial}{\partial\varnothing}\left(h_o'^3 \frac{\partial p_o'}{\partial\varnothing}\right) = H \frac{\partial(h_o')}{\partial\varnothing} \qquad (3.11)$$

Although analytic expressions are available for the various integrals, the mass of algebra soon becomes unmanageable. The generation of pressure in the lubricating film can be expressed

more concisely by using the notation shown below devised by Booker[21]. Making use of symbols for the indefinite integrals, the general solution for the long bearing equation is:-

$$p_o' = H (\epsilon_o I_3^{01} + C_{o1} I_3^{00} + C_{o2})$$
(3.12)

$$\text{where} \quad I_\ell^{m \wedge} = \int \frac{\sin^m(\emptyset) \cos^{\wedge}(\emptyset)}{h_o'^{\ell}} \, d\emptyset$$

The streamer equation does not require numerical evaluation, and has the following general solution.

$$D_o = \frac{C_{o3}}{h_o'}$$
(3.13)

Again $'p_o''$ is interpreted as a non-dimensional gauge pressure. The choice of definition is possible since the pressure variable in Reynolds equation only appears differentiated. Once more the solution is defined for an infinite range of values for $'\emptyset'$, but the region of interest is by definition the space between the formation and cavitation boundaries, and values outside the assumed full film region are discarded. Because there is no variation in the axial direction the cavitation boundaries are aligned with the axis. Hence the boundary angle $'\beta_o'$ is identically equal to zero, and the boundary equation simplifies to:-

$$(1-D_o) - \frac{h_o'^2}{H} \frac{\partial p_o'}{\partial \emptyset} = 0$$
(3.14)

If the steady state cavity boundaries are defined to exist at

angles of 'ϕ_{co}' for the cavitation boundary and 'ϕ_{fo}' for the formation surface, then the cavitation boundary conditions derived from equation (2.17) are:-

$$p_o' \Big|_{\phi_{co}} = p'_{CAV}$$
$$\frac{\partial p_o'}{\partial \phi} \Big|_{\phi_{co}} = 0 \qquad\qquad (3.15)$$
$$D_o \Big|_{\phi_{co}} = 1$$

and the continuity conditions for the formation surface are:-

$$p_o' \Big|_{\phi_{fo}} = P'_{CAV}$$
$$(1-D_o) - \frac{h_o^2}{H} \frac{\partial p_o'}{\partial \phi} \Big|_{\phi_{fo}} = 0 \qquad (3.16)$$

The first basic configuration that will be developed is for a plain bearing with no oil supply slots to disturb the bearing surfaces. This configuration is not very practical but is mathematically possible since there is no side leakage from a long bearing, but the results are relevant to some real two dimensional cases with portions of the film formation boundary not located at an oil supply groove. This configuration can have only one full film and one cavitation region, hence the expressions for film pressure and streamer density are bounded by single pair of cavitation and formation boundaries. Substituting the general solutions for the field variables 'p_o'' and 'D_o' into the boundary equations, gives five linear equations in three undefined constants.

$$
\begin{bmatrix}
I_3^{oo} \big|_{\phi_{co}} & 1 & 0 \\
1 & 0 & 0 \\
0 & 0 & 1 \\
I_3^{oo} \big|_{\phi_{fo}} & 1 & 0 \\
1 & 0 & 1
\end{bmatrix}
\begin{bmatrix}
C_{o1} \\
C_{o2} \\
C_{o3}
\end{bmatrix}
=
\begin{bmatrix}
\left(\dfrac{p'_{cav}}{H} - \epsilon_o I_3^{o1} \right) \Big|_{\phi_{co}} \\
-\epsilon_o \cos(\phi) \big|_{\phi_{co}} \\
h'_o \big|_{\phi_{co}} \\
\left(\dfrac{p'_{cav}}{H} - \epsilon_o I_3^{o1} \right) \Big|_{\phi_{fo}} \\
1
\end{bmatrix}
\qquad (3.17)
$$

Even if the unknown boundary angles are considered to make the problem five non-linear equations in five unknowns, a unique solution is still not defined. The redundancy is explained by the fact that all five equations are derived from the condition of continuity. As a result any pressure function that satisfies the cavitation boundary conditions, the formation boundary pressure condition and Reynolds equation will define the solution of the streamer density equation and automatically satisfy the formation boundary relationship between the pressure gradient and the streamer density function.

There is a continuous sequence of possible solutions to the field and boundary equations that ranges from pressure films extending for an arc of 0 radians to arcs of 2π radians. The possible set of boundary angles is shown on figure 3.2, and a sample set of pressure solutions for an operating eccentricity ratio of 0.5 are presented on figure 3.3. Each solution to the equations represents a possible equilibrium condition but not

necessarily a realistic lubrication situation.

Traditionally the equilibrium solution featuring a film formation boundary placed at the position of maximum clearance height has been favoured because it has a property of minimising some potential energy functions and is insensitive to small changes of the formation boundary position. It also simplifies some of the algebra. These usual solutions are marked on figures 3.2 and 3.3. The well known full Sommerfeld solution is a member of the solution set presented, but the half Sommerfeld solution which has an allowance for cavitation is not. This is because the half Sommerfeld solution is the long bearing equivalent of the Ocvirk solution with a very simple boundary condition that does not satisfy the J.F.O. boundary criteria.

The second kind of bearing configuration studied includes oil supply pockets. These are normally used to ensure an adequate supply of fresh oil to the clearance space for lubrication and cooling purposes. The lubricant supply to the oil pocket is taken to be at the ambient pressure, as typical bearing designs have a low pressure feed compared to the mean pressure on the loaded surface. The position of the load bearing film in relation to the supply pockets must be considered. The possible cases which have a film ending at a supply slot are not considered since this condition will normally severely limit the load carrying capacity of a bearing and are avoided during

bearing design.

This leaves two distinct film configurations, the lubricating film starting at the oil supply slot and the film forming downstream of the slot. Both of these cases have the film terminating at a cavitation boundary according to the boundary continuity condition (3.2). The latter situation is most unlikely since it is the purpose of the pocket to flood the clearance space and give a local streamer density function equal to one.

The case of the oil film starting at a supply pocket is a subset of the first case since the pocket pressure satisfies the film formation pressure condition of the first configuration. In fact the possible set of solutions is equal to first solution set. But a proportion of the solutions with the oil supply slot in the divergent section of the clearance space are normally regarded as being unrealistic. The subset of solutions that represent the typical case of a vertical load and two oil supply slots on the horizontal centreline are indicated on figure 3.2.

When compared with the usual solutions, the cases representing the typical bearing geometry are seen to have substantially different film formation boundary angles. The two types of solution diverge as the operating eccentricity ratio increases. The corresponding film pressure profiles have been marked on

figure 3.3 which is for a medium eccentricity ratio of 0.5. The difference in film boundary angles leads to a difference in peak pressure but does not significantly alter the pressure profile of the curves.

All the above solutions can be tested against the congruency conditions, but only one special case will fulfill the requirements. The one case is the full Sommerfeld solution with the constant $'C_{o\lambda}'$ equal to zero, which will satisfy the test for negative rotation but not for negative eccentricity. Again the presence of a cavitation region introduces an irregular feature which prevents the solutions satisfying the congruency conditions. Hence the full solution will in most cases be valid for only positive values of $'\epsilon_o'$ and $'\omega_o'$.

3.4 FINITE WIDTH BEARINGS

Finite width solutions to the continuity equations offer the opportunity of modelling typical bearings in detail. The usual boundary conditions are ambient pressure at the sides of the bearing, oil supply pockets and the cavity boundaries. Since the flow of oil out of the bearing sides is modelled, it is necessary to provide for oil supply slots so that the mass content of the film can be maintained. Various methods for solving the equations of continuity are available but all of them rely on

numerical evaluation at some stage. The major problem to be faced is the location of the cavity boundaries. Since numerical techniques have to be used, a common solution method is to use a finite difference representation of the differential equations. With this method there is a simple means of locating the cavitation area based upon setting calculated values of fluid pressure less than the cavitation value, equal to that value. This constrains the solution surface for pressure to pass through a ring of calculation points at the cavity pressure, and the boundary surface is normally assumed to be that ring. The solution surface normally exhibits a minimum type turning point close to the nodes assumed to be the cavitation boundary, and consequently approximates to the Swift-Steiber condition.

A finite difference method has been used to generate pressure fields for finite width bearings operating at an eccentricity ratio of 0.5. In order that the different curves may be compared with similar Ocvirk and long bearing solutions, film formation at the maximum clearance height and cavitation at ambient pressure have been assumed. The centreline values of the calculated pressure fields are presented on figure 3.4 against both the long and short bearing solutions. The results have been multiplied by a function of aspect ratio, as shown on the figure, to prevent the pressure curves tending to zero as the length to diameter ratio is reduced to small values.

The cavitation boundary has not been located by the method described above because of the coarseness of the results that the method produces. The technique used was to solve the finite difference equations, but not to constrain the cavitation boundary to lie at calculation nodes. Solutions were generated over a fixed calculation grid, sized to be slightly larger than the expected full film region. Then, as has been described for the long and short bearing solutions, parts of the solution that were deemed to lie in the cavitation region were discarded.

The extent of the fluid film is governed on three sides by the oil supply groove and the sides of the bearing. Three sides of the calculation grid were placed on the boundaries governed by the above bearing geometry, and the fourth side placed downstream of the expected cavitation boundary position. The technique used to find the required solution to Reynolds equation can be envisaged as finding values for the fluid pressure on the fourth side of the calculation grid that generate the required coincidence of zero pressure and pressure gradient across the width of the calculation grid. The film boundary was then assumed to exist where the correct cavitation boundary conditions appeared.

The required pressure field was found by breaking the problem into parts and summing two types of solution for Reynolds equation. The first solution was found by solving Reynolds

equation with a boundary value of zero around the whole of the calculation grid perimeter. This first solution formed the fundamental pressure field to which multiples of the second set of solution fields were added, to form the film pressure field. Each of the second set of boundary values were for zeros around the calculation grid except for one perimeter node which was set to unity. A solution for Reynolds equation was then generated when each of the boundary nodes on the fourth side of the calculation grid was set in turn to unity. Examination of the finite difference equations shows that a sum of the fundamental pressure field and multiples of the second series of fields satisfies Reynolds equation, and the values of the multipliers gives the nodal pressures along the fourth side of the calculation grid.

The cavitation boundary conditions were located by using curve fits to generate pressure values inbetween the calculation points in the region where the cavitation boundary was expected to lie. Then the proportions of the second set of solutions in the summation were adjusted until a zero pressure gradient was calculated to coincide with zero pressure. The cavitation boundary was then assumed to be at the points of zero pressure, and calculated film pressure values beyond the cavitation boundary were discarded. The calculated cavitation boundaries for the film pressure curves shown on figure 3.4 are presented on figure 3.5. A smooth variation in the location of the cavitation

boundary is demonstrated as the length to diameter ratio is changed, and the two dimensional solutions are seen to tend towards the limiting long and short bearing values.

The scaling factor used on figure 3.4 has hidden the wide range of peak pressures presented, but serves to highlight the fact that very little change takes place in the profile of the pressure curves as the length to diameter ratio changes. Thus some of the film characteristics for the usual and typical long bearing solutions, and finite width solutions with comparable boundary conditions can be expected to exhibit broadly similar properties.

4 DYNAMIC SOLUTIONS TO THE FILM EQUATIONS

The solutions to the steady state equations presented in the previous chapter serve only to define equilibrium conditions, a further dynamic analysis is required to determine whether the equilibrium position is a stable state or an unattainable unstable situation. The assessment of stability requires a general dynamic solution to the full continuitiy equations. If large amplitude dynamic displacements from the equilibrium positions are considered, the non-linear behaviour of the load bearing film is such that the dynamic solution cannot be related to the associated steady equilibrium condition. To analyse such large amplitude dynamic operating states the usual time marching techniques have to be used. For very large dynamic orbits approaching a circular path about the centre of a plain journal bearing, the dynamic state can be approximated by a steady state condition in the rotating coordinate system. Since whirl is normally expected at about half the running speed, the expression $'1-2\dot{\theta}/\omega_a'$ is likely to have a small value. Thus very little hydrodynamic pressure will be generated to support the journal, hence the large amplitude of fully developed whirl orbits.

Motions involving small dynamic displacements can be analysed using perturbation techniques to give first order approximations for the lubricating film behaviour as deviations from the equilibrium state. The evaluation of stability is normally based

on the estimation of a system's dynamic behaviour after being displaced by a small amount from its equilibrium state. Thus a perturbation analysis is a suitable technique to use in determining the dynamic characteristics of a lubricating film with respect to stability.

The small scale dynamic orbits of typical journals have been observed to be approximately elliptical in shape and centred upon the steady state equilibrium position. A first order approximation to an elliptical orbit can be achieved in the fixed polar coordinate system by using the following equations.

$$\epsilon = \epsilon_o + \text{Real}(\epsilon_1\, e^{\lambda t}) \qquad \text{where} \quad \epsilon_1 << \epsilon_o$$
$$\theta = \theta_o + \text{Real}(\theta_1\, e^{\lambda t}) \qquad \text{and} \quad \epsilon_o\, \theta_1 << \epsilon_o$$

$$(4.1)$$

The complex variables 'ϵ_1' , 'θ_1' and 'λ' allow the elliptical orbit to have an undefined growth time constant, orbital time period and phase angle between motions in the two coordinate directions. This technique has been used by Marsh(22) to predict the stability performance of gas bearings.

The steady state solutions developed in chapter 3 have already demonstrated that the film pressure and streamer density fields depend upon the journal position, but the time derivative terms in the field equations dictate that the solutions will also be a function of translational journal velocity. Therefore the pressure generated in the lubricating film can be expressed as

two Taylor series in each coordinate direction, one series in journal displacement about the equilibrium position, and the other in terms of velocity. The exponential description of the journal displacement implicitly carries with it the velocity information in an accessible form. As a result the dynamic pressure field can be expressed as a single Taylor series expansion in terms of the complex displacement variables $'\epsilon, e^{\lambda t}\,'$ and $'\epsilon_o \Theta, e^{\lambda t}\,'$ multiplied by complex coefficients. Each term in the series is composed of the complex displacement vector raised to a power and a complex variable representing the pressure field derivatives.

If the analysis is restricted to small displacements and velocities the Taylor series can be truncated to the first two terms leaving a first order approximation to the dynamic pressure field. The streamer density field can also be treated in the same way to give the following equations, expressed first in series form then in vector notation.

$$p' = p_o' + Real(\ p_1'\epsilon_1\, e^{\lambda t} + p_2'\epsilon_o \Theta_1\, e^{\lambda t}\ )$$
$$D = D_o + Real(\ D_1\, \epsilon_1\, e^{\lambda t} + D_2\, \epsilon_o \Theta_1\, e^{\lambda t}\ )$$

$$p' = p_o' + Real(\ [\ p_1'\ ,\ p_2'\ ].[\ \epsilon_1\ ,\ \epsilon_o \Theta_1\ ]\ e^{\lambda t}\ ) \quad\quad (4.2)$$
$$D = D_o + Real(\ [\ D_1\ ,\ D_2\ ].[\ \epsilon_1\ ,\ \epsilon_o \Theta_1\ ]\ e^{\lambda t}\ )$$

where p_1' , p_2' , D_1 and D_2 are complex

The journal displacement expressions can be substituted into the

formula for film thickness to obtain an equation in terms of the complex dynamic displacement variables. Neglecting second order terms the result is:-

$$h' = 1 + \epsilon_o \cos(\emptyset - \Theta_o)$$
$$+ \text{Real}(\epsilon_i e^{\lambda t} \cos(\emptyset - \Theta_o) + \epsilon_o \Theta_i e^{\lambda t} \sin(\emptyset - \Theta_o)) \qquad (4.3)$$

A useful simplification to the following algebra can be achieved if at this stage the fixed coordinate axes are chosen to be aligned with the equilibrium state journal and bearing centres, as in the steady state solutions already described. Then the value of 'Θ_o' is zero and the expression for film thickness reduces to:-

$$h' = 1 + \epsilon_o \cos(\emptyset)$$
$$+ \text{Real}(\epsilon_i e^{\lambda t} \cos(\emptyset) + \epsilon_o \Theta_i e^{\lambda t} \sin(\emptyset)) \qquad (4.4)$$

$$h' = h_o' + \text{Real}([\cos(\emptyset) , \sin(\emptyset)].[\epsilon_i , \epsilon_o \Theta_i] e^{\lambda t})$$

Now that expressions have been derived for all the independent variables in terms of the dynamic displacement vector, they can be substituted into the field equations. Considering Reynolds equation first the differential equation becomes:-

$$\text{Real}\left[\frac{\partial}{\partial\phi}\left(h_o^3\,\frac{\partial p_o'}{\partial\phi}\right) + \frac{\partial}{\partial\phi}\left(h_o^3\,\frac{\partial}{\partial\phi}([\,p_1',\,p_2'\,].[\,\epsilon_1,\,\epsilon_o\theta_1\,]\,e^{\lambda t})\right)\right.$$

$$+\;3h_o^2\,[\,\cos(\phi)\,,\,\sin(\phi)\,].[\,\epsilon_1,\,\epsilon_o\theta_1\,]\,e^{\lambda t}\,\frac{\partial p_o'}{\partial\phi}$$

$$+\left(\frac{R}{L}\right)^2\left(\frac{\partial}{\partial\zeta}\left(h_o^3\,\frac{\partial p'}{\partial\zeta}\right) + \frac{\partial}{\partial\zeta}\,h_o^3\,\frac{\partial}{\partial\zeta}([\,p_1',\,p_2'\,].[\,\epsilon_1,\,\epsilon_o\theta_1\,]\,e^{\lambda t})\right)$$

$$\left. +\;3h_o^2\,[\,\cos(\phi)\,,\,\sin(\phi)\,].[\,\epsilon_1,\,\epsilon_o\theta_1\,]\,e^{\lambda t}\,\frac{\partial p_o'}{\partial\zeta}\right] \tag{4.5}$$

$$=\;\text{Real}\left[H\left(\frac{\partial h_o'}{\partial\phi} + \frac{\partial}{\partial\phi}([\,\cos(\phi)\,,\,\sin(\phi)\,].[\,\epsilon_1,\,\epsilon_o\theta_1\,]\,e^{\lambda t})\right.\right.$$

$$\left.\left. +\;\frac{2\lambda}{\omega_o}\,[\,\cos(\phi)\,,\,\sin(\phi)\,].[\,\epsilon_1,\,\epsilon_o\theta_1\,]\,e^{\lambda t}\right)\right]$$

Since the variables dependent on the operating condition should satisfy this equation for all $'\epsilon_1'$, $'\theta_1'$ and $'t'$, the equation can be divided into three independent parts which must be satisfied simultaneously. The three parts are:-

(i)
$$\frac{\partial}{\partial\phi}\left(h_o^3\,\frac{\partial p_o'}{\partial\phi}\right) + \left(\frac{R}{L}\right)^2\frac{\partial}{\partial\zeta}\left(h_o^3\,\frac{\partial p_o'}{\partial\zeta}\right) = H\,\frac{\partial h_o'}{\partial\phi}$$

(ii)
$$\frac{\partial}{\partial\phi}\left(h_o^3\,\frac{\partial p_1'}{\partial\phi} + 3h_o^2\cos(\phi)\,\frac{\partial p_o'}{\partial\phi}\right)$$

$$+\left(\frac{R}{L}\right)^2\frac{\partial}{\partial\zeta}\left(h_o^3\,\frac{\partial p_1'}{\partial\zeta} + 3h_o^2\cos(\phi)\,\frac{\partial p_o'}{\partial\zeta}\right) \tag{4.6}$$

$$=\;H\left(\frac{\partial}{\partial\phi}\cos(\phi) + \frac{2\lambda}{\omega_o}\cos(\phi)\right)$$

(iii)
$$\frac{\partial}{\partial\phi}\left(h_o^3\,\frac{\partial p_2'}{\partial\phi} + 3h_o^2\sin(\phi)\,\frac{\partial p_o'}{\partial\phi}\right)$$

$$+\left(\frac{R}{L}\right)^2\frac{\partial}{\partial\zeta}\left(h_o^3\,\frac{\partial p'}{\partial\zeta} + 3h_o^2\sin(\phi)\,\frac{\partial p_o'}{\partial\zeta}\right)$$

$$=\;H\left(\frac{\partial}{\partial\phi}\sin(\phi) + \frac{2\lambda}{\omega_o}\sin(\phi)\right)$$

The first equation can be seen to be identical to the steady state equation (3.1), for which solutions have already been found. The remaining two equations can be combined into a single equation using the convenient complex notation below.

$$\frac{\partial}{\partial\phi}\left(h_o^3\frac{\partial p_T'}{\partial\phi} + 3h_o^2 e^{i\phi}\frac{\partial p_o'}{\partial\phi}\right) + \left(\frac{R}{L}\right)^2 \frac{\partial}{\partial\zeta}\left(h_o^3\frac{\partial p_T'}{\partial\zeta} + 3h_o^2 e^{i\phi}\frac{\partial p_o'}{\partial\zeta}\right)$$
$$= H\left(ie^{i\phi} + \sigma e^{i\phi}\right) \qquad (4.7)$$

$$\text{where} \quad p_T' = p_1' + i p_2'$$
$$\text{and} \quad \sigma = 2\lambda / \omega_o$$

It must be noted that the complex notation has been used twice and that these two uses are strictly independent. The first use was to describe the motion of the journal and provides information about time periods and phase relationships. The second use is simply a convenient method of simplifying the presentation of the problem by combining two similar equations, and conveys no information concerning time. The two different uses must not be confused and mixed during solution of the equation.

The streamer density field equation can also be transformed by the same techniques to give the following steady state and dynamic equations.

$$\frac{\partial}{\partial\phi}(D_o\, h_o') \;=\; 0$$

$$\frac{\partial}{\partial\phi}(D_o\, e^{i\phi} \;+\; h_o' D_T) \;=\; -\sigma\, (\, D_o\, e^{i\phi} \;+\; h_o' D_T\,) \tag{4.8}$$

where $\quad D_T \;=\; D_1 \;+\; i\, D_2$

So far the mathematical description of the boundary surfaces between the full film and cavitation regions has been very basic because of the simple requirements of steady state. The dynamic state requires a much more detailed description of the boundary position and its movements. Since the mathematical representation of the boundary surface is a line in a plane, the instantaneous position of the boundary can be expressed as a single equation. This equation can then be parameterised to give an expression for the boundary position in each coordinate direction. Because the boundary will oscillate in time with small orbital journal motions, the surface position can be expressed as a function of the complex journal displacement vector.

The remaining theoretical work on cavitation in this thesis considers only the special case of both the formation and cavitation boundaries extending from one side of the bearing to the other, and the boundary slope angle 'β' does not approach a value of $\pm\pi/2$ radians. Under such conditions the boundary position is adequately described by the circumferential

coordinate of the boundary surface as a function existing across the whole of the bearing width. Thus a first order expression for the boundary location during a small orbital motion of the journal is :-

$$\phi_B = \phi_{Bo} + \text{Real}([\phi_{B1} , \phi_{B2}].[\epsilon_1 , \epsilon_o \theta_1] e^{\lambda t}) \qquad (4.9)$$

The subscript 'B' has been used to indicate a boundary of arbitrary type since the equation is applicable to both formation and cavitation boundaries. The real function 'ϕ_{Bo}' describes the steady state boundary position for the underlying equilibrium condition, and the variables 'ϕ_{B1}' and 'ϕ_{B2}' are complex functions indicating the dynamic motion of the boundary. All the boundary angle variables are expressed in the fixed coordinate system.

This first order representation has been used to derive first order expressions to describe the boundary surface geometry and motion. These expressions when substituted into the boundary continuity equation (2.17) give the following boundary equation in terms of the complex journal displacement vector and must be satisfied at the instantaneous boundary position.

$$(1 - D) (1 - \sigma [\phi_{B1} , \phi_{B2}].[\epsilon_1 , \epsilon_o \theta_1] e^{\lambda t})$$
$$- \frac{h^2}{H} \frac{\partial p'}{\partial \phi} (1 + \tan^2 (\beta_o)) \qquad (4.10)$$
$$- 2\left(\frac{R}{L}\right)\tan(\beta_o) [\frac{\partial \phi_{B1}}{\partial \zeta} , \frac{\partial \phi_{B2}}{\partial \zeta}].[\epsilon_1 , \epsilon_o \theta_1] e^{\lambda t}) = 0$$

Since the calculation of the boundary movement is a part of the

dynamic solution, the instantaneous boundary position is not known, hence the boundary values of the field variables $'p''$, $'D'$ and $'h''$ must be translated into values at the steady equilibrium boundary position as below.

$$p'\Big|_{\phi_B} = p'\Big|_{\phi_{Bo}} + \frac{\partial p_o'}{\partial \phi}\Big|_{\phi_{Bo}} [\ \phi_{B1}\ ,\ \phi_{B2}\ ] . [\ \epsilon_1\ ,\ \epsilon_o \Theta_1\ ]\ e^{\lambda t}$$

$$D\Big|_{\phi_B} = D\Big|_{\phi_{Bo}} + \frac{\partial D_o}{\partial \phi}\Big|_{\phi_{Bo}} [\ \phi_{B1}\ ,\ \phi_{B2}\ ] . [\ \epsilon_1\ ,\ \epsilon_o \Theta_1\ ]\ e^{\lambda t} \qquad (4.11)$$

$$h'\Big|_{\phi_B} = h'\Big|_{\phi_{Bo}} - \epsilon_o \sin(\phi)\Big|_{\phi_{Bo}} [\ \phi_{B1}\ ,\ \phi_{B2}\ ] . [\ \epsilon_1\ ,\ \epsilon_o \Theta_1\ ]\ e^{\lambda t}$$

Substituting these expressions into the boundary equation and expressing the result in the complex notation gives the following static and dynamic equations to be solved at the steady state boundary position.

(i) $\qquad (1 - D_o) - \frac{h_o^2}{H} \frac{\partial p_o'}{\partial \phi} (1 + \tan^2(\beta_o))\ =\ 0$

(ii) $\qquad \left(\sigma(1 - D_o) + \frac{\partial D_o}{\partial \phi} \right) \phi_{BT} + D_T - \frac{h_o^2}{H} \frac{\partial p_o'}{\partial \phi} 2\left(\frac{R}{L}\right)\tan(\beta_o) \frac{\partial \phi_{BT}}{\partial \varsigma}$

$\qquad + \frac{h_o^2}{H} (1 + \tan^2(\beta_o)) \frac{\partial}{\partial \phi}\left(p_T' + \frac{\partial p_o'}{\partial \phi} \phi_{BT} \right) \qquad (4.12)$

$\qquad + 2 \frac{h_o'}{H} \frac{\partial p_o'}{\partial \phi} (1 + \tan^2(\beta_o)) (e^{i\phi} - \epsilon_o \sin(\phi)\ \phi_{BT})$

$\qquad = 0$

where $\quad \phi_{BT} = \phi_{B1} + i\ \phi_{B2}$

The dynamic equation can be simplified slightly by making use of the steady state streamer and boundary equations to give :-

$$\left(\left(1 - D_o \right) \sigma + D_o \frac{\epsilon_o \sin(\phi)}{h_o'} \right) \phi_{BT} + D_T$$

$$+ \left(1 - D_o \right) \left(- 2\left(\frac{R}{L}\right)\frac{\tan(\beta_o)}{\left(1 + \tan^2(\beta_o) \right)} \frac{\partial \phi_{BT}}{\partial \zeta} \right. \qquad (4.13)$$

$$+ \frac{\partial}{\partial \phi}\left(p_T' + \frac{\partial p_o'}{\partial \phi} \phi_{BT} \right) \Big/ \frac{\partial p_o'}{\partial \phi}$$

$$\left. + \frac{2}{h_o'} \left(e^{i\phi} - \epsilon_o \sin(\phi) \phi_{BT} \right) \right) \qquad = \quad 0$$

The simple interpretation of the boundary equation shown in chapter 2 to distinguish between the cavitation and formation boundaries has been obscured by the mass of algebra but is still valid. The boundary conditions found for the film rupture surface are that there should be a film pressure equal to the cavity pressure, zero pressure gradient and a streamer density function of one. The three corresponding boundary equations for the dynamic components of the solutions can be deduced from the above equations and simplified by using the steady state boundary conditions to give the following three equations in terms of the parameter values at the steady state cavitation boundary position.

$$p_T' \qquad = \quad 0$$

$$\frac{\partial p_T'}{\partial \phi} + \frac{\partial^2 p_o'}{\partial \phi^2} \phi_{cT} = \quad 0 \qquad (4.14)$$

$$D_T + \frac{\epsilon_o \sin(\phi)}{h_o'} \phi_{cT} = \quad 0$$

The formation boundary is again described by equations representing two conditions. The first is the boundary

continuity equation (4.13), which cannot be simplified. The other condition is that the film pressure should have the prescribed cavitation value at the instantaneous boundary position. This second condition can be transposed to the steady state boundary location to give to the following equation:-

$$p_T' + \frac{\partial p_o'}{\partial \phi} \phi_{fT} = 0 \qquad (4.15)$$

In the remaining sections of this chapter the long and short bearing solutions to these equations are presented, but numerical solutions for finite length bearings have not been attempted.

4.1 SHORT BEARING SOLUTION

The short bearing solution to the dynamic part of Reynolds equation follows the course of the steady state solution method described in the previous chapter. Neglecting the pressure derivatives in the circumferential direction reduces Reynolds equation for the dynamic pressure fields to the following form.

$$\left(\frac{R}{L}\right)^2 \frac{\partial}{\partial \zeta}\left(h_o'^3 \frac{\partial p_T'}{\partial \zeta} + 3h_o'^2 e^{i\phi} \frac{\partial p_o'}{\partial \zeta} \right) = H \left(ie^{i\phi} + \sigma e^{i\phi} \right) \qquad (4.16)$$

Integrating twice gives:-

$$p_T' = \left(\frac{L}{R}\right)^2 H \left(ie^{i\phi} + \sigma e^{i\phi}\right)\frac{\zeta^2}{2h_o'^3} + C_1 \frac{\zeta}{h_o'^3} + C_2 - \frac{3e^{i\phi}p_o'}{h_o'} \qquad (4.17)$$

where C_1 and C_2 are constants of integration

Substituting the usual boundary conditions of ambient pressure at the sides of the bearing is sufficient to evaluate both constants of integration to give the following general solution.

$$p_T' = -\left(\frac{L}{R}\right)^2 \frac{H}{2h_o'^3} \left(ie^{i\phi} + \sigma\ e^{i\phi} + \frac{3e^{i\phi}\epsilon_o \sin(\phi)}{h_o'} \right)\left(\frac{1}{4} - \zeta^2\right) \quad (4.18)$$

Again there is no flexibility left to consider the application of cavitation boundary conditions, as a result the J.F.O. relationships can not be used. The steady state boundary condition for internal cavity boundaries as stated in the previous chapter is applicable to both the static and dynamic states. The steady state cavity pressure of ambient has been used in the following calculation of the dynamic pressure fields, but exactly the same static and dynamic analyses can be applied using other cavity pressure values.

The cavities have been assumed to be bodies of air at ambient pressure because of the relatively free access the surrounding atmosphere has to the cavitation region in typical bearing installations. Thus the boundary condition for dynamic motions is film rupture and formation at ambient pressure. The values of the boundary movement parameters $'\phi_{cT}'$ and $'\phi_{fT}'$ are found by substituting the steady and dynamic pressure field solutions (3.10) and (4.18) into the first order approximation for the boundary pressure given by equations (4.11). The single expression relating to both cavitation and formation boundaries

is a feature of only the case of cavitation at ambient pressure.

$$\emptyset_{BT} = p_T' \bigg/ \frac{\partial p_o'}{\partial \emptyset} = \frac{\sigma}{\epsilon_o} + \frac{i}{\epsilon_o} \qquad\qquad (4.19)$$

$$\emptyset_B = \emptyset_{Bo} + \text{Real}(\frac{\sigma}{\epsilon_o} \epsilon_1 e^{\lambda t} + \Theta_1 e^{\lambda t})$$

Hence the short bearing solution with cavitation at ambient pressure, predicts that in general the cavitation and formation boundaries will oscillate with a finite amplitude in response to journal motions. As could be expected, problems will arise when the steady state operating eccentricity is very small and the presence of the eccentricity parameter in the denominator of one term will predict large amplitude boundary motions in response to small journal motions. However the perturbation solution is only valid for small values of the ratio 'ϵ_1 / ϵ_o', thus a finite boundary motion is predicted for all small amplitude journal motions that will satisfy the limits of validity for the analysis.

4.2   THE LONG BEARING SOLUTION

The long bearing type of solution results from assuming that the film and cavity characteristics remain unchanged along the axis of a bearing. Thus all differentials with respect to 'ς', and the boundary slope angle 'β' in the governing equations for this type of bearing are identically equal to zero. The long

bearing equation for film pressure and streamer density, and their general solutions are given below.

$$\frac{\partial}{\partial\phi}\left(h_o'^3 \frac{\partial p_T'}{\partial\phi} + 3h_o'^2 e^{i\phi} \frac{\partial p_o'}{\partial\phi}\right) = H\left(ie^{i\phi} + \sigma\, e^{i\phi}\right)$$

$$\frac{\partial}{\partial\phi}\left(D_o\, e^{i\phi} + h_o' D_T\right) = -\sigma\left(D_o\, e^{i\phi} + h_o' D_T\right)$$

$$p_T' = H\left(\left(I_3^{o'} + i\, I_3^{'o}\right)\left(1 - i\sigma\right)\right. \tag{4.20}$$

$$\left. - 3\left(\epsilon_o\left(I_4^{o2} + i\, I_4''\right) + C_{o1}\left(I_4^{o1} + i\, I_4^{'o}\right)\right)\right)$$

$$+ C_{T1}\, I_3^{oo} + C_{T2}$$

$$D_T = C_{T3}\, \frac{e^{-\sigma\phi}}{h_o'} - D_o\, \frac{e^{i\phi}}{h_o'}$$

All the general cavitation boundary equations (4.14), and the formation boundary pressure value condition (4.15) remain unaltered by the assumption of invariance in the axial direction. But the relationship between the pressure gradient and streamer density function (4.13) simplifies to the following equation.

$$\left(\left(1 - D_o\right)\sigma + D_o\epsilon_o\frac{\sin(\phi)}{h_o'}\right)\phi_{fT} + D_T$$

$$+ \left(1 - D_o\right)\quad\left(\frac{\partial}{\partial\phi}\left(p_T' + \frac{\partial p_o'}{\partial\phi}\phi_{fT}\right)\middle/\frac{\partial p_o'}{\partial\phi}\right. \tag{4.21}$$

$$\left. + \frac{2}{h_o'}\left(e^{i\phi} - \epsilon_o \sin(\phi)\,\phi_{fT}\right)\right) = 0$$

Thus there are three cavitation and two formation boundary equations to describe the boundary values of the dynamic pressure and streamer density fields, representing the same five boundary

conditions governing the steady state solutions. Since the above equations have already been transformed from the instantaneous boundary positions they must be evaluated at the steady state boundary locations.

The steady state solutions presented in the previous chapter considered three different arrangements of the full film and cavitation regions. The first arrangement analysed had no oil supply pocket to constrain the position of either the cavitation or formation boundaries. Hence the dynamic solution for this type of geometry must evaluate the motion of both boundary surfaces. Since there was only one full film region and one cavitation region the equations to be solved are found by substituting the general long bearing field equations (4.20) into the five boundary conditions. The five unknowns in the set of equations are complex variables, two of which describe the dynamic pressure fields and the remaining three describe the streamer density, formation and cavitation boundaries. The set of equations are presented below in matrix form where a zero represents an element having a value of zero, a '+' sign represents a non-zero constant and a '*' sign represents a function of 'σ'.

$$
\begin{bmatrix}
+ & + & O & O & O \\
+ & O & O & + & O \\
O & O & * & + & O \\
+ & + & O & O & + \\
+ & O & * & O & *
\end{bmatrix}
\begin{bmatrix}
C_{T1} \\
C_{T2} \\
C_{T3} \\
\phi_{cT} \\
\phi_{fT}
\end{bmatrix}
=
\begin{bmatrix}
* \\
* \\
+ \\
* \\
*
\end{bmatrix}
\tag{4.22}
$$

The solution of these equations during a stability analysis is complicated by the fact that the value of ' ' is unknown at the time the solution is required. The arrangement of the various functions of ' ' within the set of equations implies that the five unknowns will also be functions of ' '. Working through the matrix solution shows that the streamer density function must have the following relationship with 'σ'.

$$
\frac{C + D\sigma + E\sigma^2}{F\, e^{-\sigma\phi_{fo}} + (G + H\sigma)\, e^{-\sigma\phi_{co}}}
\tag{4.23}
$$

The remaining four variables have the following more complicated form of functional relationship with 'σ', where the capital letters represent constants to be evaluated for each variable.

$$
\frac{(A + B\sigma)\, e^{-\sigma\phi_{fo}} + (C + D\sigma + E\sigma^2)\, e^{-\sigma\phi_{co}}}{F\, e^{-\sigma\phi_{fo}} + (G + H\sigma)\, e^{-\sigma\phi_{co}}}
\tag{4.24}
$$

The form of the solutions show that at any given operating condition the constants in the dynamic stiffness matrix are functions of the ratio between orbital and rotational frequencies. The non-linear nature of these results makes this bearing arrangement more difficult to analyse than the Ocvirk

solution, and no further work has been performed on this type of bearing model.

The second type of bearing arrangement considered in chapter 3 was for the film formation boundary fixed at an oil supply slot. This arrangement is simpler than the above solution because the most complicated boundary condition has been removed from the set of equations which have to be solved. There is no change to the film rupture mechanisms so the same three cavitation boundary equations have to be solved. There is only one formation boundary condition which is that the dynamic pressure fields must have zero values at the steady state boundary position. Thus the dynamic pressure field is constrained to be zero at both the steady state formation and cavitation boundaries. These two conditions are sufficient to determine the values for the constants of integration in the general solutions (4.20). The zero pressure gradient condition serves to define the cavitation boundary movement variable $'\phi_{c\tau}'$, and the remaining cavitation boundary equation serves to fix the streamer density function.

Since the dynamic pressure fields are now constrained to be zero at both the steady state film boundary locations, the dynamic performance predictions will be equivalent to the results obtained from analyses that have neglected the possibility of boundary movement.

The solution of the two boundary pressure equations is straight forward since none of the elements in the matrix of coefficients are functions of $'\sigma'$. However the right hand side of these two equations are linear functions of $'\sigma'$ so the constants in the general equation for the dynamic pressure fields will also be the expected linear functions of $'\sigma'$.

The constants of integration in the dynamic pressure field equation have been solved for two sets of boundary conditions. First for the usual long bearing solution that assumes there is an oil supply slot at the steady state maximum clearance position, and also for the more typical case of an oil supply at the horizontal bearing centreline. The resulting dynamic pressure fields are presented on figure 4.1 against the Ocvirk solutions. The Ocvirk results show the predicted centreline pressure values for a bearing of width to diameter ratio equal to one half.

As for the steady state pressure fields, the usual long bearing solutions are similar in shape to the Ocvirk predictions. However there is a significant difference in the peak pressure values between the long and short bearing solutions. Because the pressure profiles are broadly similar, comparable predictions for bearing dynamic performance can be expected. The cavitation boundary movement parameter $'\phi_{c\tau}'$ has also been calculated for each of the three solutions. Since $'\phi_{c\tau}'$ is not only a complex

number but also a function of the journal motion, only the
component parts of the parameter can be evaluated and presented.
The boundary movement parameter has been split up into component
parts as shown in the following equations.

$$\phi_{cr} \quad = \quad \phi_{c_1} \quad + \quad i \ \phi_{c_2}$$

$$\phi_{c_1} \quad = \quad A \quad + \quad \sigma \ B \qquad\qquad (4.25)$$

$$\phi_{c_2} \quad = \quad C \quad + \quad \sigma \ D$$

For both the long and short bearing solutions 'D' is equal to
zero for all values of operating eccentricity ratio. In addition
the short bearing solution gives 'A' equal to zero, and 'B' equal
to 'C'. The results are presented on figure 4.2 and show similar
values for the parameter components despite their different
origins.

The curves presented on figures 4.1 and 4.2 have been derived
from the Ocvirk solutions which demonstrate a floating formation
boundary position based upon unrealistic boundary conditions, and
the long bearing solutions with a fixed film formation boundary
position. Despite the fundamental differences in the governing
differential and boundary equations the curves have basically the
same shape. Since the calculated dynamic pressure fields for
finite width bearings can be expected to tend to the long and
short bearing solution fields for extreme values of the length to
diameter ratio, the finite width solutions can be expected to
exhibit broadly similar results for the dynamic film behaviour.

The dynamic equations (4.22) for a long bearing with a film formation boundary free to find its equilibrium position have been shown to generate non-linear expressions for the dynamic pressure fields. Since short and medium finite width bearings are heavily influenced by the axial flow of lubricant, the dynamic solutions for typical short and medium width bearings can be expected to produce results similar to the predictions generated by the Ocvirk solutions.

5   JOURNAL DYNAMICS

The dynamic motion considered in the previous chapter is the result of the journal moving in response to the forces acting upon its mass. These forces belong to either of two categories, the pressure force generated by the lubricating film, or the applied load. Whereas the applied load is usually known in advance of the bearing design, the film force is normally calculated by integrating the pressure field around the clearance space. If the journal motion is defined, the changing pressure field can be calculated. But for stability analysis the small orbital motion is undefined, consequently the film force components must be evaluated in terms of the dynamic displacement vector.

The resultant force exerted on the journal is found by integrating the fluid pressure around the whole of the bearing. Since the direction in which the pressure force acts is always at right angles to the local surface, the integration must also define the direction in which the resultant force acts. The usual way of finding both the direction and size of the net force is to integrate the components of the local pressure forces in convenient coordinate directions, and find the resultant by vector addition of the force components.

Because the fluid pressure is exerted on a continuous surface encircling the shaft, any hydrostatic component of the pressure distribution will not contribute to the net force on the journal. Hence the lubricating film forces can be calculated by integrating the difference between the pressure field and any arbitrary value. Since the cavitation region has been defined to be a region of constant pressure, the integration can be simplified by summing the difference between film and cavity pressures. Then the integrand is identically equal to zero over the whole of the cavitation region. Hence all that is required is to integrate the function $'P - P_{CAV}'$ over the full film region.

A fixed cartesian coordinate system has been used for the analysis of journal dynamics, with $'r'$ and $'s'$ axes along and at right angles to the steady state line of centres shown on figure 5.1. Dimensional and non-dimensional film force components acting in the fixed cartesian system are defined by the following equations.

$$F_r = \int_A (P - P_{CAV}) \cos(\phi) \, dA$$

$$F_s = \int_A (P - P_{CAV}) \sin(\phi) \, dA$$

$$f_r' = \int_A (p' - p_{CAV}') \cos(\phi) \, dA \qquad (5.1)$$

$$f_s' = \int_A (p' - p_{CAV}') \sin(\phi) \, dA$$

where $\quad f' = F / P_a RL$

and $\quad A = $ full film region

Since the cavity boundaries have been allowed to oscillate in time with the journal motion, the integration must be evaluated between the instantaneous boundary positions. If the symbol 'A,' is used to represent the steady state full film region and 'δA' the instantaneous difference between the dynamic and steady state regions, the integration can be subdivided into two parts as follows.

$$\int_{A} (\ p' - p'_{cAV}\ )\ f(\phi)\ dA\ =\ \int_{A_0} (\ p' - p'_{cAV}\ )\ f(\phi)\ dA$$
$$+ \int_{\delta A} (\ p' - p'_{cAV}\ )\ f(\phi)\ dA \qquad (5.2)$$

where $f(\phi)$ represents the sine and cosine functions

When small boundary motions are considered, the difference between the instantaneous field and the cavity pressures at the steady state boundary, is a first order sized term. Thus the integral over the area 'δA' will be a second order term which can be neglected. Substituting the first order expression for film pressure into the remaining integral gives the following general approximation for the film forces using the steady state boundary positions.

$$\int_{A_0} (\ p' - p'_{cAV}\ )\ f(\phi)\ dA$$
$$+\ \ Real(\ \int_{A_0} [\ p'_1,\ p'_2\ ].[\ \epsilon_1,\ \epsilon_0\ \Theta_1\ ]\ e^{\lambda t}\ f(\phi)\ dA\ ) \qquad (5.3)$$

Thus for the small scale motions expected during whirl onset, it is sufficient to integrate the expression for film pressure over the steady state full film region, and neglect the boundary motion. To simplify the following algebra it is convenient to

use symbols representing the pressure field integrals, to give the following first order expressions for the film force components.

$$f_r' = f_{ro}' + [f_{r\epsilon}' , f_{r\theta}'].[\epsilon_, , \epsilon_o \theta_,] e^{\lambda t}$$

$$f_s' = f_{so}' + [f_{s\epsilon}' , f_{s\theta}'].[\epsilon_, , \epsilon_o \theta_,] e^{\lambda t}$$

(5.4)

5.1 EQUATIONS OF MOTION FOR THE JOURNAL

The equations of journal motion have been derived from Newton's second law expressed in the 'r-s' cartesian coordinate system. Previously the journal position has been expressed in polar coordinates, but is easily transformed into the cartesian system by the usual set of transformation equations. The expressions describing the journal position, and their first order approximations for small journal motions are:-

$$r = Real(C \epsilon \cos(\theta - \theta_o))$$

$$s = Real(C \epsilon \sin(\theta - \theta_o))$$

(5.5)

$$r = Real(C (\epsilon_o + \epsilon_, e^{\lambda t}))$$

$$s = Real(C \epsilon_o \theta_, e^{\lambda t})$$

Hence Newton's second law of motion for the journal is as follows, where the subscript 'A' indicates force components of the applied load.

$$P_a RL \left(f'_{Ar} + f'_r \right) = \text{Real}\left(MC \overline{\lambda^2 \epsilon_, e^{\lambda t}} \right)$$

$$P_a RL \left(f'_{As} + f'_s \right) = \text{Real}\left(MC \overline{\lambda^2 \epsilon_o \theta_, e^{\lambda t}} \right) \tag{5.6}$$

Substituting the first order expressions (5.4) for the film forces into the equations of motion, and expressing the resulting equation in matrix form gives:-

$$\begin{bmatrix} f'_{Ar} & + & f'_{ro} \\ f'_{As} & + & f'_{so} \end{bmatrix} + \begin{bmatrix} f'_{r\epsilon} & f'_{r\theta} \\ f'_{s\epsilon} & f'_{s\theta} \end{bmatrix} \begin{bmatrix} \epsilon_, \\ \epsilon_o \theta_, \end{bmatrix} e^{\lambda t} = \begin{bmatrix} \epsilon_, \\ \epsilon_o \theta_, \end{bmatrix} e^{\lambda t}$$

$$\tag{5.7}$$

where $\quad \gamma = \dfrac{M_R C \omega_o^2}{4 P_a RL} \quad$ and $\quad \sigma = \dfrac{2\lambda}{\omega_o}$

When the bearing is operating under a steady load the sum of the applied load and the steady film force components is identically equal to zero. Thus the left hand matrix of this last equation vanishes to leave an eigenvalue problem.

Chapter 4 has shown that the Ocvirk and the common long bearing dynamic pressure field solutions to Reynolds equation are linear functions of 'σ'. Hence the result of integrating these pressure fields is to generate dynamic film force components that are also linear functions of 'σ'. The coefficients of 'σ' in these first order expressions are equivalent to stiffness and damping parameters in an ordinary mass spring damper system. It should be noted that the mathematical concept of stiffness has been used for these coefficients which is equal to minus one times the normal engineering definition of stiffness. Because of

the similarity between the film equations and spring damper systems, the matrix of film force components expressed as functions of $'\sigma'$, as set out below, is often called the dynamic stiffness matrix of a bearing.

$$\begin{bmatrix} f'_{r\epsilon} & f'_{r\vartheta} \\ f'_{s\epsilon} & f'_{s\vartheta} \end{bmatrix} = \begin{bmatrix} A_{11} + \sigma B_{11} & A_{12} + \sigma B_{12} \\ A_{21} + \sigma B_{21} & A_{22} + \sigma B_{22} \end{bmatrix} \qquad (5.8)$$

$$= [A(\sigma)]$$

Substituting the dynamic stiffness matrix for the film force components into the matrix equation of motion, gives the following equation for unforced journal motion.

$$\begin{bmatrix} A_{11} + \sigma B_{11} & A_{12} + \sigma B_{12} \\ A_{21} + \sigma B_{21} & A_{22} + \sigma B_{22} \end{bmatrix} \begin{bmatrix} \epsilon_1 \\ \epsilon_2 \Theta_1 \end{bmatrix} = \gamma \sigma^2 \begin{bmatrix} \epsilon_1 \\ \epsilon_2 \Theta_1 \end{bmatrix} \qquad (5.9)$$

Since the parameter $'\sigma'$ appears in both the expression for the eigenvalue and the dynamic stiffness matrix, the common solution techniques for finding eigenvalues are not appropriate. The unknown variables in this equation are $'\gamma'$ and $'\sigma'$, hence the solution requires pairs of these parameters that satisfy the equation. The condition for solving the eigenvalue problem and hence the equations of motion is:-

$$\text{Det} \begin{bmatrix} A_{11} + \sigma B_{11} - \gamma \sigma^2 & A_{12} + \sigma B_{12} \\ A_{21} + \sigma B_{21} & A_{22} + \sigma B_{22} - \gamma \sigma^2 \end{bmatrix} = 0 \qquad (5.10)$$

This determinant forms the characteristic equation for the

dynamic system comprising the rotor mass and the lubricating film. In general there are two modes of dynamic motion since the system has two degrees of freedom. Each mode shape is defined by the eigenvector and its relationship with time is defined by the non-dimensional time constant $'\sigma'$. The particular solution of most interest is the case when $'\sigma'$ is wholly imaginary, as this condition defines a neutrally stable state that normally exists at the stability boundary between stable and unstable operating regions. By substituting a wholly imaginary variable for $'\sigma'$ in the equations of motion, forces the characteristic equation to yield the mode of vibration relating to the stability boundary.

The solutions derived by this method define only one mode of vibration whilst the second mode remains unknown. Since there is normally no simple algebraic link between the coefficients of the characteristic equation and the resulting non-dimensional time constants, numerical techniques must be used to find time constants for all the modes of vibration at each operating condition. For a simple assessment of journal stability it is not necessary to check all the modes of vibration, since Routh's criterion links the coefficients of the characteristic equation with the system stability.

In the equation below $'ik'$ has been substituted for the variable $'\sigma'$. The parameter $'k'$ will be referred to as the non-dimensional frequency ratio since it is equal to the orbital

frequency divided by half the rotational frequency.

$$\text{Det} \begin{bmatrix} A_{11} + i\, kB_{11} + \gamma k^2 & A_{12} + i\, kB_{12} \\ A_{21} + i\, kB_{21} & A_{22} + i\, kB_{22} + \gamma k^2 \end{bmatrix} = 0 \quad (5.11)$$

where $k = \dfrac{2\omega}{\omega_o}$,

Since the solutions to this equation describe important atributes of the lubricating film relating to the critical condition of whirl onset, the set of values satisfying the equation have been given the symbols $'\gamma_c'$ and $'k_c'$. Expanding the determinant gives two equations of real variables to be solved simultaneously.

$$A_{11}\, A_{22} - A_{12}\, A_{21} - k^2 (B_{11}\, B_{22} - B_{12}\, B_{21})$$
$$+ \gamma k^2 (A_{11} + A_{22}) + (\gamma k^2)^2 = 0$$
$$\quad (5.12)$$
$$k ((A_{11}\, B_{22} + A_{22}\, B_{11} - A_{12}\, B_{21} - A_{21}\, B_{12})$$
$$- \gamma k^2 (B_{11} + B_{22})) = 0$$

The general solution to these equations can be expected to give a value of about one for $'k'$, since the usual behaviour of a bearing on the stability boundary is to exhibit a small orbital motion at half the journal running speed. There is also the trivial solution which requires that $'k'$ is equal to zero and the stiffness coefficients of the dynamic stiffness matrix form a matrix with a zero determinant.

$$k = 0 \quad \text{and} \quad A_{11}\, A_{22} - A_{12}\, A_{21} = 0 \quad (5.13)$$

5.2   SIGNIFICANCE OF THE DYNAMIC STIFFNESS MATRIX EIGENVALUES

The eigenvalues of the dynamic stiffness matrix represent the lubricating film's resistance to motion as the journal performs an orbit defined by the associated eigenvector.   For the particular case of a real eigenvalue, the equations describe a simple mechanical system consisting of springs but not dampers. Thus as the journal performs the prescribed orbit at the prescribed frequency ratio $'k_c'$ the film acts in the same manner as two springs acting at right angles to each other, each with a non-dimensional stiffness equal to minus one times the real eigenvalue.   The previous section has shown that when a journal is operating at the stability boundary, its non-dimensional dynamic stiffness matrix does have a real eigenvalue which is equal to $'-\gamma_c k_c^2'$.   Hence at this whirl onset condition the dynamic performance of the film can be completely represented by an axisymmetric spring with a stiffness equal to $P_a RL \gamma_c k_c^2 / C$.

In general increasing the steady component of the applied load generates a journal movement which has a component at right angles to the direction of the applied load.   The shape of typical steady state operating curves show that there is always one particular operating eccentricity at which increasing the magnitude of the applied load causes a journal displacement in the direction of the load line.   This condition will be called the nose of the steady state running curve and is an example of

an operating condition with a principal direction of loading. The incremental static stiffness of the lubricating film at the nose of the steady state curve can be described by the following matrix equation. The displacements $'x_V'$ and $'x_H'$ are in directions along and at right angles to the applied load, and the terms $'S''$ represent the stiffness of the lubricating film to incremental loads $'f_V''$ and $'f_H''$.

$$
\begin{bmatrix} f_V' \\ f_H' \end{bmatrix} = \begin{bmatrix} S_{VV}' & S_{VH}' \\ 0 & S_{HH}' \end{bmatrix} \begin{bmatrix} x_V' \\ x_H' \end{bmatrix}
\tag{5.14}
$$

The definition of a principal direction of loading has been taken to be any direction for which the journal displacement is along the line of action of the incremental load producing the displacement. The situation is characterised by an incremental static stiffness matrix with a zero on the minor diagonal. Such a matrix has two real eigenvalues $'S_{VV}''$ and $'S_{HH}''$. By definition the above matrix of static stiffness terms is equal to the dynamic stiffness matrix for a motion with zero time constant and orbital frequency $'k_c'$, transformed by rotation through an angle equal to the attitude angle. The occurrence of a real eigenvalue for the dynamic stiffness matrix has been shown to be associated with a neutrally stable operating condition. Thus the nose of the steady state operating curve may exhibit some special dynamic characteristics, particularly as most stability results have been obtained for operating eccentricities less than the value at which the nose occurs.

If the steady state stiffness characteristics of journal bearing systems can be shown to have principal directions of loading over a wide range of operating eccentricities, the nose of the steady state curve will only be a particular example of a more general phenomenon. Since this phenomenon is determined by only the stiffness elements of the dynamic stiffness matrix, and is independent of the damping coefficients, the fact that principal directions of motion exist is unlikely to imply any special dynamic characteristics.

If a principal direction of loading exists there must be a rotational transformation of the dynamic stiffness matrix which produces a zero stiffness term on the minor diagonal. If $'\alpha'$ represents the angle through which the dynamic stiffness matrix is transformed, the condition for a principal direction of loading is:-

$$(A_{12} + A_{21}) \cos(2\alpha) - (A_{11} - A_{22}) \sin(2\alpha)$$
$$\pm(A_{12} - A_{21}) = 0 \tag{5.15}$$

The general solution to this equation is:-

$$\alpha = \frac{1}{2} (n\pi \pm \delta - \beta)$$

where   n is an arbitrary integer

$$\cos(\alpha) = \frac{A_{12} - A_{21}}{\sqrt{(A_{12} + A_{21})^2 + (A_{11} - A_{22})^2}} \quad (5.16)$$

$$\cos(\beta) = \frac{A_{12} + A_{21}}{\sqrt{(A_{12} + A_{21})^2 + (A_{11} - A_{22})^2}}$$

$$\sin(\beta) = \frac{A_{11} - A_{22}}{\sqrt{(A_{12} + A_{21})^2 + (A_{11} - A_{22})^2}}$$

The nose of the steady state operating curve is known to satisfy this condition when the transformation angle $'\alpha'$ is equal to the attitude angle. But for small operating eccentricities the journal displacement is always approximately at right angles to the direction of the applied load, thus a principal direction does not exist for lightly loaded operating conditions.

Figure 5.2 shows the principal directions of loading when the Ocvirk solution values are substituted for the elements of the dynamic stiffness matrix. The curves show that there are no principal directions of loading for operating eccentricity ratios of less than about 0.6. The nose of the steady state operating curve is predicted to occur at an eccentricity ratio of approximately 0.663, which is within the operating range that exhibits principal directions of loading. In the next section this eccentricity value is compared with the operating eccentricity for which the short bearing theory predicts a

critical frequency ratio equal to zero. Thus the Ocvirk solution demonstrates that the nose of the steady state curve is not a singularity but part of a continuous series of principal directions of loading.

Further the condition for the angle $'\delta'$ to exist is also the condition for there to be real eigenvalues for the incremental static stiffness matrix. Thus if an operating condition exists for which the orbital frequency on the stability boundary is zero, there must be a principal direction of loading at that condition, but the converse is not necessarily true.

5.3   SHORT BEARING STABILITY

The previous chapters have developed simple algebraic expressions for the short bearing steady state and dynamic pressure field solutions to Reynolds equation. Integrating the pressure fields between the steady state film boundaries, as shown above, gives the following expressions for the steady state and dynamic force components.

$$f'_{ro} = \left(\frac{L}{R}\right)^{2}\frac{H}{12}\,\epsilon_{o}\,\frac{(-2\epsilon_{o})}{(1-\epsilon_{o}^{2})^{2}}$$

$$f'_{so} = \left(\frac{L}{R}\right)^{2}\frac{H}{12}\,\epsilon_{o}\,\frac{\pi}{2\,(1-\epsilon_{o}^{2})^{3/2}}$$

$$f'_{r\epsilon} = \left(\frac{L}{R}\right)^{2}\frac{H}{12}\left(\frac{-4\epsilon_{o}\,(1+\epsilon_{o}^{2})}{(1-\epsilon_{o}^{2})^{3}}\quad-\sigma\,\frac{\pi\,(1+2\epsilon_{o}^{2})}{2\,(1-\epsilon_{o}^{2})^{5/2}}\right) \quad (5.17)$$

$$f'_{r\rho} = \left(\frac{L}{R}\right)^{2}\frac{H}{12}\left(\frac{-\pi}{2\,(1-\epsilon_{o}^{2})^{3/2}}\quad+\sigma\,\frac{2\epsilon_{o}}{(1-\epsilon_{o}^{2})^{2}}\right)$$

$$f'_{s\epsilon} = \left(\frac{L}{R}\right)^{2}\frac{H}{12}\left(\frac{\pi\,(1+2\epsilon_{o}^{2})}{2\,(1-\epsilon_{o}^{2})^{5/2}}\quad+\sigma\,\frac{2\epsilon_{o}}{(1-\epsilon_{o}^{2})^{2}}\right)$$

$$f'_{s\rho} = \left(\frac{L}{R}\right)^{2}\frac{H}{12}\left(\frac{-2\epsilon_{o}}{(1-\epsilon_{o}^{2})^{2}}\quad-\sigma\,\frac{1}{2}\frac{\pi}{(1-\epsilon_{o}^{2})^{3/2}}\right)$$

The congruent operating conditions shown on figure 3.1 suggest that both the steady state force components should be odd functions of eccentricity, and that the radial and tangential components should be respectively even and odd functions of the compressibility number 'H'. However since the steady state pressure fields have been shown to be valid for only positive values of both eccentricity and compressibility number, the steady state force components will only be valid over the same ranges. Hence the algebraic expressions need not exhibit the function relationships described.

Substituting the expressions for the dynamic force components into the equations for the stability boundary, and solving for the critical values of the stability parameter and non-dimensional frequency ratio, gives the following results.

$$\gamma_c =$$

$$\left(\frac{L}{R}\right)^2 \frac{H}{12} \frac{2\epsilon_o(2+\epsilon_o^2)(3+\epsilon_o^2)(\pi^2(1+2\epsilon_o^2)-16\epsilon_o^2)}{(1-\epsilon_o^2)(\pi^2(4+8\epsilon_o^2-3\epsilon_o^4-7\epsilon_o^6-2\epsilon_o^8)-16\epsilon_o^2(1+8\epsilon_o^2+3\epsilon_o^4))}$$

$$k_c = \frac{(\pi^2(4+8\epsilon_o^2-3\epsilon_o^4-7\epsilon_o^6-2\epsilon_o^8)-16\epsilon_o^2(1+8\epsilon_o^2+3\epsilon_o^4))}{(2+\epsilon_o^2)^2(1-\epsilon_o^2)(\pi^2(1+2\epsilon_o^2)-16\epsilon_o^2)}$$

<div align="right">(5.18)</div>

$$\gamma_c k_c^2 = \left(\frac{L}{R}\right)^2 \frac{H}{12} \frac{2\epsilon_o(3+\epsilon_o^2)}{(1-\epsilon_o^2)^2(2+\epsilon_o^2)}$$

These results are equivalent to the expressions derived by Holmes(7), who used a different solution technique. The values of these functions and the associated critical eigenvalues are plotted on figure 5.3.

There is a particular value of operating eccentricity for which the frequency of the neutrally stable orbit has tended to zero. At this operating condition the critical eigenvalue has remained non-zero since the critical stability parameter has tended to infinity. Because the eigenvalue has remained finite the solution is not the trivial solution referred to at the end of section 5.1, but the critical eigenvalue is equal to one of the eigenvalues of the static stiffness matrix. Whereas the stability boundary comes to an end at an eccentricity ratio of about 0.756, the nose of the Ocvirk steady state running curve occurs at an eccentricity of about 0.663, emphasising the difference between the two conditions.

Experience with the solutions to the characteristic equation has shown that if one mode of vibration has a wholly imaginary non-dimensional time constant, the other mode of vibration has a time constant with a negative real part. This indicates that the second mode is stable and that the stability boundary for the first mode can be observed. In the operating region for eccentricities greater than 0.756 experience shows that the equations predict both modes of vibration will always be stable.

Adding together the steady state force components gives the following expressions for the applied load and attitude angle predicted by the short bearing theory.

$$f_o' = \left(\frac{L}{R}\right)^2 \frac{H}{12} \epsilon_o \frac{\sqrt{\pi^2 + (16 - \pi^2)\epsilon_o^2}}{2(1 - \epsilon_o^2)^2} \qquad (5.19)$$

$$\propto = \tan^{-1}\left(\frac{-\pi(1 - \epsilon_o^2)^{1/2}}{4\,\epsilon_o}\right)$$

Since the solutions to the governing equations for incompressible lubricants predict the pressure fields and force components to be proportional to the shaft speed, a simple design chart can be constructed to show the steady state running relationship and the stable running limit of a bearing. Using the Ocvirk solutions the following simple expressions can be derived for the operating speed and whirl onset speed in terms of the bearing geometry, oil viscosity and known functions of eccentricity.

$$\omega_o = \left(\frac{\text{LOAD } 2C^2}{\mu RL} \right) \frac{1}{f_{ss}(\epsilon_o)}$$

$$\omega_{oc} = \left(\frac{2\mu RL^3}{M_R C^3} \right) f_D(\epsilon_o)$$

(5.20)

The functions of eccentricity $'f_{ss}'$ and $'f_D'$ are defined by the Ocvirk solutions (5.18) and (5.19). Thus curves for various values of the parameters $'\text{LOAD } 2C^2 / \mu RL'$ and $'2\mu RL^3 / M_R C^3'$ can be drawn against axes of eccentricity and rotational speed. Figure 5.4 shows the resulting design chart. The steady state operating curve for a particular installation can be found by interpolation, and followed from low speed high eccentricity up to the stability limit predicted by the Ocvirk solutions. The chart has been drawn for low rotational speeds, but can be extended to higher values by successively adding one to the vertical scale values and multiplying the curve labels by ten.

5.4   LONG BEARING STABILITY

The previous chapter has shown that the expressions for the dynamic pressure fields generated by a long bearing with a fixed film formation boundary are also linear functions of $'\sigma'$. Hence integrating these pressure fields will produce constants for the stiffness and damping coefficients in the bearing's dynamic stiffness matrix. Thus the analysis of bearing stability with these coefficients will follow the equations set out at the

beginning of this chapter, and demonstrated on the short bearing solution. However the floating film formation boundary case identified, but not pursued, would produce functions of $'\sigma'$ for the stiffness and damping coefficients.

The long bearing pressure fields presented in the last chapter were generated using numerical techniques, consequently numerical integration has been used to evaluate the long bearing stiffness and damping coefficients. The stability parameters resulting from substituting the stiffness and damping coefficients into the stability equations, are shown on figure 5.5. The general shape of the curves are similar to the short bearing results, with the critical stability parameter tending to infinity for eccentricities in the range 0.7 to 0.8, but a significant variation in the critical frequency ratio is shown. The long bearing results are not directly comparable with the Oovirk solutions because of the length to diameter ratio effect, but when compared on the same basis as the steady state pressure fields shown on figure 3.4, the long bearing stability parameters take values significantly less than the Oovirk solutions.

The effects of changing the film formation boundary position on the film's critical stability parameters are shown for an operating eccentricity ratio of 0.5, on figure 5.6. Generally the critical stability parameter values are seen to fall as the lubricating film length is decreased, indicating a reduction in

the stable operating range. The critical frequency ratio parameter is seen to rise steadily to values that are not normally observed, but this may be because a journal operating with such short lubricating films have not been tested. Thus operating a severely starved bearing or decreasing the working surface in the loaded arc of a bearing can be expected to have a destabilising effect.

6   JOURNAL AND BEARING DYNAMICS

The equations of motion for a bearing mounted on a flexible support structure are a simple extension to the system of equations describing journal motion. The equations which will be derived have a wide range of application since they are similar to those representing a flexible shaft supported by journal bearings on firm foundations. Thus the equations of journal and bearing dynamics describe simplified forms of two common shaft and bearing arrangements.

The coordinate system that has been used for the analysis of journal dynamics has its origin at the geometric centre of the bearing. Thus the film force expressions derived in the last chapter are applicable to the study of journal and bearing dynamics, provided that displacements in the $'\epsilon-\Theta'$ polar coordinate system are recognised as journal displacements relative to the bearing, and are not assumed to be absolute journal displacements. Thus the absolute journal position is the vector sum of the bearing displacement, and the relative journal position in $'\epsilon-\Theta'$ coordinates. If the symbols $'R_G'$ and $'S_B'$ are used to represent the bearing position in the fixed $'r'$ and $'s'$ axes, as shown by figure 5.1, the equations for journal and bearing motions are as follows.

$$M_R \begin{bmatrix} C\ddot{\epsilon} & + & \ddot{R}_B \\ C\epsilon\ddot{\Theta} & + & \ddot{S}_B \end{bmatrix} = - P_a RL \begin{bmatrix} f'_{Ar} & + & f'_r \\ f'_{As} & + & f'_s \end{bmatrix}$$

$$M_B \begin{bmatrix} \ddot{R}_B \\ \ddot{S}_B \end{bmatrix} = - P_a RL \begin{bmatrix} f'_r \\ f'_s \end{bmatrix} - \begin{bmatrix} S_{Mr} R_B \\ S_{MS} S_B \end{bmatrix} - \begin{bmatrix} C_{Mr} \dot{R}_B \\ C_{MS} \dot{S}_B \end{bmatrix} \qquad (6.1)$$

where

M_R = Rotor mass

M_B = Bearing mass

S_{Mr} = Mounting stiffness in the 'r' direction

S_{MS} = Mounting stiffness in the 's' direction

C_{Mr} = Mounting damping in the 'r' direction

C_{MS} = Mounting damping in the 's' direction

Since the bearing and journal displacements will normally have the same functional relationship with time, the bearing position can be expressed as follows.

$$R_B = R_{Bo} + \text{REAL}(C R'_{B1} e^{\lambda t})$$
$$S_B = S_{Bo} + \text{REAL}(C S'_{B1} e^{\lambda t}) \qquad (6.2)$$

For unforced motions of the system, the steady component of the film force will be equal and opposite to the applied load and the steady component of the mounting reaction. Thus the dynamic characteristics of the system are described by the following set of equations.

$$\text{REAL} \left[M_R C \lambda^2 \begin{bmatrix} \epsilon_1 + R'_{\theta 1} \\ \epsilon_o \Theta_1 + S'_{\theta 1} \end{bmatrix} e^{\lambda t} \right] = \overline{\text{REAL}} \left[P_a RL \begin{bmatrix} f'_{r\epsilon} & f'_{r\theta} \\ f'_{s\epsilon} & f'_{s\theta} \end{bmatrix} \begin{bmatrix} \epsilon_1 \\ \epsilon_o \Theta_1 \end{bmatrix} e^{\lambda t} \right]$$

$$\text{REAL} \left[M_\beta C \lambda^2 \begin{bmatrix} R'_{\theta 1} \\ S'_{\theta 1} \end{bmatrix} e^{\lambda t} \right] = \text{REAL} \left[\left[-P_a RL \begin{bmatrix} f'_{r\epsilon} & f'_{r\theta} \\ f'_{s\epsilon} & f'_{s\theta} \end{bmatrix} \begin{bmatrix} \epsilon_1 \\ \epsilon_o \Theta_1 \end{bmatrix} \right. \right.$$
$$\left. \left. - \begin{bmatrix} S_{Mr} & C R'_{\theta 1} \\ S_{Ms} & C S'_{\theta 1} \end{bmatrix} - \begin{bmatrix} C_{Mr} & C\lambda R'_{\theta 1} \\ C_{Ms} & C\lambda S'_{\theta 1} \end{bmatrix} \right] e^{\lambda t} \right] \quad (6.3)$$

These two equations can be made non-dimensional and combined to form the following matrix equation.

$$\begin{bmatrix} \gamma_R \sigma^2 & 0 & \gamma_R \sigma^2 & 0 \\ 0 & \gamma_R \sigma^2 & 0 & \gamma_R \sigma^2 \\ 0 & 0 & \gamma_\beta \sigma^2 & 0 \\ 0 & 0 & 0 & \gamma_\beta \sigma^2 \end{bmatrix} \begin{bmatrix} \epsilon_1 \\ \epsilon_o \Theta_1 \\ R'_{\theta 1} \\ S'_{\theta 1} \end{bmatrix} =$$

$$\begin{bmatrix} f'_{r\epsilon} & f'_{r\theta} & 0 & 0 \\ f'_{s\epsilon} & f'_{s\theta} & 0 & 0 \\ -f'_{r\epsilon} & -f'_{r\theta} & -S'_{Mr} & -C'_{Mr}\sigma \\ -f'_{s\epsilon} & -f'_{s\theta} & 0 & -S'_{Ms} & -C'_{Ms}\sigma \end{bmatrix} \begin{bmatrix} \epsilon_1 \\ \epsilon_o \Theta_1 \\ R'_{\theta 1} \\ S'_{\theta 1} \end{bmatrix} \quad (6.4)$$

where $\quad \gamma_X = \dfrac{M_X C \omega_o^2}{4 P_a RL}, \quad S'_{Mx} = \dfrac{S_{Mx} C}{P_a RL}, \quad C'_{Mx} = \dfrac{C_{Mx} C \omega_o}{P_a RL2}$

This equation is too general for significant simplifications to be made by algebraic manipulation. However the matrix representing an axisymmetric mounting can be expressed in a more convenient form making use of the dynamic stiffness matrix.

$$
\begin{bmatrix} [A] - \gamma_R \overline{\sigma^2} \, I & - \gamma_R \sigma^2 I \\ - \gamma_R \sigma^2 I & -(\gamma_{RB} \sigma^2 + C_M' \sigma + S_M') \, I \end{bmatrix} \begin{bmatrix} \epsilon_1 \\ \epsilon_u \, \Theta_1 \\ R_{B1}' \\ S_{B1}' \end{bmatrix} = 0 \qquad (6.5)
$$

The characteristic equation for the system is derived from the determinant of the matrix of coefficients. The general solution gives up to four orbital modes of vibration with their associated values of non-dimensional time constant $'\sigma'$.

There are three basic stability conditions that can be observed. If all the four values of $'\sigma'$ have negative real parts, the equations represent a stable operating condition, and small disturbances to the system will result in a decaying orbital motion as the system returns to its equilibrium position. If three values have negative real parts and the fourth is wholly imaginary the system will be operating at the stability boundary. In this state a small random disturbance will initiate an orbital motion that persists indefinitely. The third condition is for one or more of the real parts to have a positive value, in which case the system will be unstable. Upon reaching this final type of operating condition the system will rapidly develop large amplitude motions and settle at a new condition of fully developed whirl. Due to the non-linear nature of lubricating film behaviour, the characteristic equation is only applicable for small amplitude motions about the steady equilibrium position. The system response to a large disturbance cannot be

predicted by these equations, nor the growth of small whirl orbits into fully developed whirl.

As in the case of journal dynamics, substituting the variable 'ik' for the non-dimensional time constant 'σ' will force the equation (6.5) to yield the modes of vibration which define the stability boundary. Further dramatic simplification results from examination of a system with no mounting damping. The characteristic equation for an undamped system can be expressed as:-

$$(S_M' - \gamma_{RB} k^2) \, \text{Det}\left[[A(ik)] + \gamma_R k^2 \left(\frac{S_M' - \gamma_B k^2}{S' - \gamma_{RB} k^2} \right) I \right] = 0 \quad (6.6)$$

The coefficient of the unit matrix 'I' in this equation is composed of real variables, hence the coefficient itself is a real number. Comparing this equation with the corresponding equation (5.11) for journal motion, shows that the mathematical problem has already been presented and solved. The real coefficient must have the same value as the real eigenvalues of the dynamic stiffness matrix. In particular the value of the frequency ratio parameter for a neutrally stable orbit is equal to the film's critical frequency ratio at the same eccentricity ratio. Thus a stability boundary exists at operating conditions that satisfy the following equations.

$$k = k_c \quad \text{and} \quad \gamma_c k_c^2 = \gamma_R k_c^2 \left(\frac{\gamma_B k_c^2 - S_M'}{\gamma_{RB} k_c^2 - S_M'} \right) \quad (6.7)$$

Since all the variables in this equation, with the exception of the mounting stiffness parameter $'S'_M'$, are predefined functions of the operating condition, the equation is best presented to define the critical mounting stiffness at which the stability boundaries lie.

$$S'_{MC} \quad = \quad \gamma_c \, k_c^2 \, \left(\, \frac{\gamma_B}{\gamma_c} \quad + \quad \frac{\gamma_R}{\gamma_c - \gamma_R} \, \right) \tag{6.8}$$

Thus the right hand side of this equation can be evaluated for a range of eccentricity ratios to find the critical mounting stiffnesses for various operating conditions. Examining equation (6.8) shows that the critical mounting stiffness values will be negative if the operating stability parameter $'\gamma_R'$ lies in the range $'\gamma_c < \gamma_R < (\gamma_c \, \gamma_{RB} / \gamma_B)'$. The upper and lower limits represent a zero stiffness and an infinitely stiff mounting respectively. Thus there is an operating region for which the theory predicts that there are no critical mounting stiffness values.

The rigid mounting case lies at the lower side of this region for which no neutrally stable operating conditions are predicted to exist. Hence progressively reducing the mounting stiffness can not make the system more stable. Both the long and short bearing stability solutions which have been presented, show the lubricating film's critical stability parameter tending to infinity at a certain eccentricity ratio, whilst the dynamic

stiffness remains finite. Substituting an infinite critical
stability parameter ' δ_c ' and a finite value for the dynamic
stiffness ' $\delta_c k_c^2$ ' into equation (6.8), shows that this condition
is associated with a zero critical mounting stiffness. These two
limiting cases form the operating conditions at the extremes of
the lower whirl onset boundary shown on figure 6.1.

The upper boundary of the region which does not exhibit a
stability boundary is marked by a zero mounting stiffness
condition. Therefore the stability boundary curve originating
from this point must rise with increasing mounting stiffness.
This second critical operating condition has been marked on
figure 6.1 as the second whirl onset boundary. If this were the
real situation then the second critical condition could never be
observed, as the theory does not predict a stable operating
region immediately below the second whirl onset boundary.

The sketch 6.1 can be compared with figure 6.2 which depicts
the typical observed behaviour for self acting plain gas bearings
reported by Marsh(23) and Simmons(24). The fact that the first
onset boundary does not extend to the zero mounting stiffness
case is explained later. Results presented in chapter 8 of this
thesis show that oil lubricated bearings also exhibit the type of
behaviour shown on figure 6.2. Clearly the theory in its present
state is not complete as it does not predict the presence of a
third boundary between the first and second onset boundaries.

But the theory does predict the two whirl onset operating conditions.

Since the second boundary is attainable, a system supported on a very soft suspension will have a greater stable operating range than if it were rigidly mounted on its foundations. A measure of the improvement in performance is given by the fact that the journal acts as if it possessed a mass equal to $'(M_B + M_R)/M_B'$ times its actual value.

Figure 6.2 demonstrates that the critical running speed at which a bearing goes unstable can be changed by varying the mounting stiffness. This feature of a flexibly mounted bearing can be used to control the operating condition at which whirl onset occurs. Hence a bearing can be made to give critical stability parameter information covering a range of eccentricity ratios. When a bearing is supported upon an axisymmetric spring it will normally go unstable before the operating stability parameter $'\delta_R'$ reaches the rigid critical value $'\delta_c'$. However the stability boundary equation (6.7) can be rearranged to show the relationship between the operating stability parameter $'\delta_R'$ at which whirl onset is encountered, and the critical stability parameter $'\delta_c'$ which is a lubricating film property. The relationship is:-

$$\gamma_c \;=\; \gamma_R \left(\frac{1 - (\omega_1 / \omega_B)^2}{1 - (\omega_1 / \omega_{RB})^2} \right) \tag{6.9}$$

The symbols $'\omega_{RB}'$ and $'\omega_B'$ respectively represent the natural frequencies of the rotor and bearing supported on the mounting springs and the bearing only on the mounting. Consequently, if a stability boundary is encountered with a bearing system that is supported on an flexible axisymmetric mounting, the value of the lubricating film property $'\gamma_c'$ called the critical stability parameter, can be calculated from the operating stability parameter value $'\gamma_R'$. The natural frequencies of the mounting system $'\omega_{RB}'$ and $'\omega_B'$ must be known, and the frequency of the whirl orbit $'\omega_1'$ has to be measured.

Thus a bearing mounted on a symmetrical flexible mounting can be made to go unstable over a range of operating conditions simply by changing the stiffness of the mounting. Further a few simple measurements enables the operating stability parameter at which whirl onset occurs, to be converted into the critical stability parameter of the lubricating film. The resulting information can then be used as design data for similar bearing systems with or without flexibility in the mounting or shaft.

6.1 WHIRL CESSATION

The equations of motion above have been interpreted to show two stability boundaries for a flexibly mounted bearing. The shape of the predicted stability curves shown on figure 6.1, can be compared with the type of air bearing behaviour shown on figure 6.2 observed by Marsh and Simmons (24). These sketches show that the linear theory tends to predict whirl onset boundaries in the appropriate places but does not give the whirl cessation boundary. Based on a limited number of whirl cessation observations, Marsh and Simmons found the following expression to predict the whirl cessation speeds reasonably accurately.

$$\omega_a = \omega_\beta / k_c$$
$$\text{or} \quad \omega_1 = \omega_{R\beta}$$

(6.10)

This condition has some theoretical justification in equation (6.7), since the denominator's value changes sign through zero as the rotor speed passes through the critical value. However this support is based on the assumption that the non-dimensional frequency ratio and the running speed are independent parameters. The system's characteristic equation is an eighth order polynomial in the complex time constant $'\sigma'$. Thus for each operating condition there are up to four periodic modes of vibration, each with its associated complex time constant. Since the coefficients of the polynomial representing the characteristic equation are functions of the operating

condition, the rotor speed and the non-dimensional frequency ratio 'k' are not independent. Numerical solutions generated for the modes of vibration on the proposed whirl cessation boundary show that none of the modes are predicted to be neutrally stable. Thus all the conditions for the proposed whirl cessation boundary are never simultaneously satisfied. Consequently the whirl cessation condition proposed is not supported by the linear theory of bearing performance.

Experimental observations from both the air bearings tested by Marsh and Simmons, and the oil bearings tested during the work performed for this thesis showed that the characteristics of the whirl cessation boundary, the lower boundary of the upper stable operating region, are quite different to those of the first and second whirl onset boundaries. The onset boundaries are characterised by a very sharp rise in whirl amplitude as the boundary is traversed from the stable operating region into the unstable area. The onset of instability generates small orbital motions of the centrebody, which remain modest even after fully developed whirling has commenced.

In contrast, if the whirl cessation boundary is crossed with decreasing speed, a gradual rise in orbital amplitude is observed as the unstable operating region is penetrated, a rapid unstable rise in orbit amplitude is not generally observed. In addition, comparatively large and strong vibratory motion of the centrebody

is experienced. Thus the two types of stability boundary tend to exhibit significantly different characteristics. The whirl onset boundaries tend to show true unstable behaviour whereas the whirl cessation boundary tends to show features associated with resonance.

6.2   ALTERNATIVE SYSTEM MODELS

Some of the assumptions used to simplify the dynamic analysis may have caused the above form of solution which is plainly at odds with observed bearing performance. One such simplification was to neglect the effects of damping in the mounting system. Reintroducing the damping term into the characteristic equation destroys the simple relationship (6.7) between the flexible and rigidly supported arrangements. Typical curves for the calculated critical stiffness for a damped system are shown on figure 6.3. These curves have been drawn from computed solutions using a constant value for the damping coefficient at all operating conditions and values of the mounting stiffness.

Figures 6.1 and 6.3 show that the major effect of the mounting damping is to cause the first critical speed at low mounting stiffnesses to tend to infinity, otherwise the damping has very little effect on the stability boundary condition. The most important aspect of this result is that part of the stable

running area now extends up to the second whirl onset boundary, enabling bearing performance at this critical condition to be observed. Thus it appears that additional damping in the system external to the lubricating film prevents the lower unstable operating region from extending to very low mounting stiffness values. If the damping coefficient used in the numerical solutions is varied with both mounting stiffness and operating condition then a stability map more in line with current results can be produced.

The long bearing solution that allowed the film formation boundary position to be determined by the J.F.O. boundary conditions, produced non-linear expressions for the film stiffness and damping coefficients. Since the coefficients generated by this solution are functions of the non-dimensional time constant, the resulting dynamic film characteristics can be expected to be significantly different. The corresponding dynamic equations for self acting air bearings also give functions of the orbital frequency for the stiffness and damping coefficients. The solutions to these equations for gas bearings show a stable operating region below the second whirl onset boundary. Thus pursuing the more difficult theoretical long bearing solution may lead to a more representative prediction of dynamic performance. But more detailed experimental data obtained from whirl cessation conditions is required before the performance predictions of these models can be assessed.

7   CAVITATION OBSERVATION EXPERIMENTS

7.1   TEST APPARATUS DESIGN

An experimental apparatus was designed so that the behaviour of typical lubricating films could be observed under controlled conditions representing a variety of operating regimes. The main objective was to study the nature of the lubricating film and cavitation region at steady state conditions, and note their behaviour as dynamic situations were introduced. A requirement was that the test bed should be sufficiently flexible to not only model the usual bearing installation of a rotating journal operating under a fixed load in a stationary bearing, but also alternative situations with a rotating bearing outer member and rotating loads.

In order to achieve the primary goal of being able to view the phenomena occurring inside the clearance space, the test bearings were made of clear perspex to run in conjunction with aluminium journals. The flexibility of operation was achieved in two ways, first by mounting both the journal and bearing on shafts capable of being driven independently, and also by providing two different mechanisms for loading the test bearing. The two types of load generated by the rig were a load acting in a constant

direction, and a load rotating at a steady angular velocity about the axis of the bearing. As with normal bearing installations the journal was allowed to take up the operating eccentricity that balanced the applied load and resulting film forces.

Two sets of test bearing parts were built to give differing boundary conditions at the sides of the clearance space. The first set was designed for flooded operation, that is the journal fully submerged in lubricant. Thus lubricant could enter the clearance space from both sides of the bearing. The excess fluid provided a barrier between the clearance space and the ambient atmosphere, denying air free access to the cavitation region. The alternative parts were shaped so that oil leaving the bearing would drain away from the sides of the clearance space allowing the surrounding atmosphere relatively free access to the working section, as is often the case for typical installations. This second arrangement is referred to as the drained configuration.

The apparatus was designed with a vertical axis, primarily to avoid the necessity for oil seals, but also to allow reasonable all round viewing. If standard oil seals had been used to keep the lubricant inside the apparatus, the natural journal motion would have been restricted by the stiffness of the sealing rings. The perspex bearing outer members were mounted on shafts from below whilst the journals were suspended inside the bearings from above, as shown on figure 7.1. Thus the perspex bearings and the

steel discs upon which they were mounted naturally formed a vessel suitable for containing the lubricant. Access to the test section for feeding additional lubricant to the system and removing used oil was gained through the shaft supporting the bearing outer member.

A reasonably large working section was produced by having a bearing of width and diameter equal to 100.0 mm. Hence difficulties in observation resulted from the rapid random motion of the boundary surfaces within the clearance space rather than the size of the image. The forces required to produce large operating eccentricities with the intended shaft speeds of about 100 rpm were kept within reasonable bounds by using a thin oil of 7.0 mPas (7.0 cP) at 20°C and a relatively large clearance ratio of 0.01. Table 7.1 gives details of the basic parameters of the test bed.

The height of the test stand was such that it was convenient and safe to use a compressed air reaction drive to turn the journal. Allowing the journal to float in the bearing inevitably resulted in the occasional periods of surface contact under high loads and low sliding speeds. Sliding contact caused scuffing and scoring damage to the bearing surfaces. The scores in the surface generated local areas of large film thickness which disturbed the cavity boundary shapes. The response of a D.C. motor drive to the onset of scuffing would have been to generate

more driving torque and keep the shaft turning at a reduced speed. The resulting periods of scuffing could have been prolonged and would have caused excessive damage to the bearing. The main advantage of the reaction drive was that the driving torque generated was effectively constant throughout the working speed range, even if the turbine was being driven backwards. Thus for the reaction drive, the period of scuffing was governed by the journal shaft's moment of inertia. In practice the moment of inertia was low and the large increase in drag at the onset of sliding contact was sufficient to quickly bring the journal shaft to rest. Thus the turbine drive was a safety feature designed to minimise scuffing damage to the bearing surfaces.

The turbine consisted of a pair of nozzles fixed to the ends of arms 0.7 m long attached to the top of the journal shaft. The drive proved sufficient to give journal speeds of several hundred rpm but had a long time period for settling to steady state, and was very sensitive to changes in load. The outer member of the bearing was driven by a conventional belt drive from an electric motor.

Because of the need for flexibility, all round visibility and the larger than typical clearance ratio, the equipment was designed for qualitative observation rather than a quantitative assessment of performance.

7.1.1   Flooded Test Bearing Assembly

The first test parts were for a plain bearing with no oil supply facilities. The journal was designed to be submerged in lubricant, allowing oil to enter the clearance space from above and below. The perspex outer member was machined whilst mounted on its shaft and supporting plate to give a plain cylindrical bore. Similarly the journal was also machined to a plain cylindrical shape after mounting on its shaft. The upper journal shaft was designed to swing freely from a spherical roller bearing fixed ten journal widths above the test bearing. Consequently the test journal performed a conical rather than translational motion as it found its equilibrium position. The resulting misalignment caused severe distortion of the cavitation patterns, as the cavities tended to take on a size and appearance corresponding to the local eccentricity. But for steady state conditions with the fixed direction load, it was possible to eliminate cavitation region distortion by offsetting the spherical support bearing an appropriate amount.

7.1.2   Drained Test Bearing Assembly

Because of the conical misalignment problem with the first set of parts, a different suspension was devised for the drained bearing. A special double thrust bearing, as shown on

figure 7.2, was made for supporting the journal, by turning the thrust races from two standard ball bearings inside out. The resulting flat surfaces allowed the shaft to move at right angles to its axis, enabling the journal to have rotary and translational motion whilst preventing conical misalignment.

The second journal to be manufactured was mounted on a much shorter shaft with the special thrust bearing located between the test journal and the load insertion bearings. Drive to the journal was provided by the reaction turbine described above, with the torque transmitted by a flexible coupling joining the turbine and journal shafts. The upper and lower journal faces were machined concave to encourage lubricant expelled from the bearing to drain away, instead of remaining at the side of the clearance space to be drawn back into the lubricating film. The base plate supporting the perspex bearing outer member was also machined concave and several holes drilled right through its thickness to allow used oil to be removed from the test section. Grooves were cut along the length of the bearing support shaft to house the oil supply and return pipes, enabling a limited amount of bearing rotation.

The supply of fresh lubricant was introduced to the clearance space through a 4.0 mm hole in the bearing wall, to create a minimum of disturbance to the cylindrical bore. This particular arrangement was chosen to model the bearing geometry used for the

stability experiments described in the next chapter. Lubricant was supplied to the clearance space from a reservoir mounted 1.0 m above the test section.

7.1.3   Applied Loads

Both the applied loads were transmitted to the journal through ball races on the journal shaft, mounted as close as possible to the test bearing. The fixed direction load, which will be referred to as just the 'fixed load', was derived from the weight of masses placed on a scale pan. A cable attached to the outer race of the lower load insertion bearing was passed over a pulley allowing the scale pan to be suspended adjacent to the lower shaft. Since the pulley was mounted on a minature ball race and the typical fixed load applied to the shaft was 10 to 20 kgf, the frictional resistance associated with the pulley could be neglected.

The other type of load which will be described as the 'rotating load' was derived from a helical coil spring stretched between the upper load insertion bearing and a windlass. The windlass was mounted on a rotating table so that it could perform a circular orbit around the axis of the test bearing. Thus the table could be turned to produce a steady load acting in a variable direction, or the table could be driven at constant

speeds to produce the desired rotating load capability. An electric motor and belt drive were capable of turning the rotating table at speeds of up to 200 rpm.

7.2   MODES OF OPERATION

Reynolds equation has been shown to predict the generation of a steady pressure field and cavitation region for any set of steady bearing surface speeds and a steady load, provided that the combined surface motion relative to the load line is non-zero.   Typical journal bearing applications are for a steady unidirectional load and motion of only the journal surface.   This was the mode of operation normally used for observing the steady state film behaviour. But for operation at high eccentricities the usual practice was to drive the bearing outer member and allow the journal to run at the same speed.   This avoided scuffing damage to the bearing surfaces. All the possible modes of combined journal and bearing rotation with a fixed load were successfully tried.

The loss of load carrying capacity whilst the bearing surfaces moved with equal velocities in opposite directions was easily demonstrated. As the condition was approached, surface contact would cause the journal to be brought to rest, and then driven in the same direction as the bearing. Hence the singular condition

could be approached but not observed in this type of apparatus with a floating journal.

Steady conditions under the action of the fixed load were relatively easy to study, because the cavitation regions were stationary relative to the fixed observer. When generating steady conditions with the rotating load, the usual mode of operation was for the journal and bearing surfaces to be stationary. Since this situation generated a cavitation region that precessed around the clearance space, sweeping past a fixed observer, interpreting the image was much more difficult. High speed photography was required to reveal the detail of the cavity shapes and motions.

Dynamic conditions were generated by simultaneously applying fixed and rotating loads to any combination of journal and bearing rotation. The usual procedure for generating a dynamic state was to start from any steady condition and then to apply the disturbing dynamic load, otherwise a confused operating state often resulted. Because of the difficulty in observing a rotating cavitation region, the usual experimental method was to obtain a fixed load steady state operating condition and then apply a smaller rotating load.

The relative magnitude of the applied loads had a marked effect on the dynamic behaviour. If the fixed load was dominant,

a steady state like cavity was formed, and the smaller rotating load caused a cyclic disturbance to the cavity's shape and position. Similarly if the rotating load was dominant, the fixed load could be expected to produce a cyclic variation to the precession of the cavitation region around the bearing. But this second orbiting cavity behaviour is not easily detected by a fixed observer. If the two loads were of a comparable size no such simple characterisation was possible and a much more complicated situation existed.

The relative velocity of the two load lines compared to the effective sliding speed was also important. A very low orbital frequency resulted in effectively a cycle of steady state conditions, whereas a high relative speed generated large squeeze film forces opposing the journal motion. Relative load line velocities giving orbital frequencies in the region of half the effective surface rotational value, were expected to give relatively large orbit sizes about the steady state equilibrium position. This is because of the characteristics of Reynolds equation noted in chapter two. For periods when the angular velocity of the journal about the bearing centre, is in the region of half the effective surface angular velocity, there is very little surface motion to draw fluid into the convergent hydrodynamic wedge. Consequently the generation of film pressure during such periods was mainly dependent on the squeeze film action of the bearing.

7.3 STEADY STATE FLOODED OBSERVATIONS

The first series of experiments were performed with the flooded lubrication parts. At all times the journal was fully immersed with a sufficient barrier of oil to prevent the direct entry of air into the clearance space. The typical operating procedure was to set the journal turning and then introduce some fixed load. At first there would be no cavitation apparent but after a minute or so, careful inspection about the region of the load line would reveal three or four very small narrow cavities. The cavitation would normally start in a region of locally very thin film thickness due to misalignment of the journal. Typically over a period of about ten minutes the cavitation region would grow to a limiting size. First of all the number of cavities but not their size would increase as the region spread across the width of the bearing. Then the size of the cavities would increase and their number diminish as the circumferential extent of the region grew.

Upon stopping the journal rotation, the cavities would rapidly change shape to form a smoother boundary surface, and slowly rise through the clearance space to the free surface. This behaviour indicates that gases at about ambient pressure filled the voids in the lubricant film. Since the direct entry of air to the cavitation region was prevented, the gases must have been released from the lubricant as it passed through the low pressure

region downstream of the minimum film clearance.

Once the cavities had become established, changing the operating condition would normally involve a change of cavity volume. An increase in volume would be accommodated by a lowering of the cavity pressure and the release of further air from solution. If a decrease in volume was required then the change of mass content appeared to be accomplished not by reabsorption back into the oil but by the generation of small bubbles at the film reformation boundary. These bubbles would then be swept away downstream to be cast out of the clearance space at the sides of the bearing.

The basic appearance of an established cavitation region is as shown on figure 2.3. This figure shows cavities with smooth sides, but typical gaseous cavities in mineral oil normally had a certain amount of random surface rippling and branching of the cavities superimposed on this basic shape. Streamers were generated at the cavitation boundary and became narrower towards the film formation surface, where they normally occupied a very small proportion of the cross-sectional area. The sections of formation boundary inbetween the streamers usually appeared to be disconnected segments of a smooth curve, hence it is very easy to visualise a continuous line along the segments of formation surface cutting through the streamers. This line can reasonably be taken as the demarcation between the cavitation and full film

regions.

As shown, the flooded configuration had the film formation boundary turning round to become parallel to the sides of the bearing and continuing to form the nose of the outermost cavities. More difficulty was usually found in defining a precise location for the cavitation boundary. The streamers rapidly narrowed in a short distance about the nose of the cavities, from occupying the whole of the bearing width to a much smaller proportion. Because this area of film rupture and induction into the streamers had a finite length, cavitation could be said to have occurred over an area rather than at a position. However the noses of the cavities tended to form a straight line across the film, which has been taken to represent the cavitation boundary.

Superimposed on top of the basic streamer structure there was normally a random dendritic pattern. This was the result of the formation of secondary noses at the sides of the main cavities, and produced the ragged appearance of typical streamers. The secondary noses would push forward against the surface motion and sideways away from the parent cavity but usually for only a small distance. This action of forming secondary noses appeared to be an important mechanism concerning the number and position of the oil streamers and cavities. The basic structure of the cavitation region shown on figure 2.3, is similar to the

photographs presented by Cole and Hughes(25), and Etsion and Ludwig(14) in similar studies with journal bearings. Several of the papers presented at the first Leeds-Lyon symposium(1) also present a similar picture of cavity forms. However the shapes of the cavities observed during the present study were rarely so smooth, nor were they as steady as the above photographic records would suggest. Figure 8 of Cole and Hughes' presentation, shows a few cavities with side noses that form a dendritic pattern. This type of appearance was more typical of the structures found in the present test bearings.

The general appearance of a typical cavitation region is shown by figure 7.3 which shows observations for the usual steady state mode of journal bearing operation. The sequence of images starts with a high eccentricity operating condition when there was a very narrow band of small thin cavities close to the load line. The cavities and streamers were numerous with a limited amount of distortion due to side effects. As the operating speed was increased the length of the cavitation region increased, the cavities moved downstream away from the load line, and the number of cavities decreased. At high speeds the number of cavities and the scale of the dendritic action decreased until one primary cavity with relatively smooth sides was flanked by much smaller cavities. A further increase in speed would cause the cavities to be swept away downstream to break into smaller pockets of gas which were quickly expelled at the sides of the bearing. This

action is caused by the local pressure gradients being insufficient to propel the cavity against the surface motion and the flow of lubricant.

The movement of the cavitation boundary away from the load line as eccentricity was decreased is predicted by the usual long and short bearing solutions for Reynolds equation. But the observed cavities always subtended an angle of less than $45°$ which is much smaller than the $90°$ to $180°$ of the usual solutions.

As the operating eccentricity ratio was decreased the number of cavities and streamers decreased, concentrating the cavity fluid into fewer larger cavities, consequently a mechanism for reducing the number of streamers was acting. The converse was also true in that as the eccentricity ratio was increased additional streamers and cavities were generated. The dendritic action of creating secondary cavity noses appeared to enable the change in the number of streamers to take place. The mechanism for generating a new cavity streamer pair seemed to be the appearance of a secondary nose sufficiently strong to develop into a cavity in its own right. The new nose would have to make a significant penetration towards the full film region in order to create a new streamer between itself and its parent cavity. Thus cavity fluid of the parent would be divided between the two new small cavities. This behaviour is illustrated on figure 7.4,

alongside two other related behaviour patterns observed.

A development of this mechanism was observed when the secondary nose broke through into an adjacent cavity. Then in addition to a streamer being created, another is lost. The result is that a portion of cavity fluid is transferred from one streamer to the next. This transfer of fluid was much more common than the simple generation of an extra cavity, and often involved a 'knock on' effect causing a chain reaction of similar events along the line of cavities.

In a third variation of this theme a streamer could be lost by a secondary nose breaking through into an adjacent cavity but not forming a new streamer between itself and its parent. Hence the action of secondary cavity nose formation can explain the means by which a cavitation region maintains its equilibrium during fundamental changes such as a variation in the number of cavities.

The flow of oil in the lubricating film was normally invisible but occasionally an accumulation of fluff would be swept into the clearance space to briefly indicate the currents of oil before being swept out again. A more consistent mechanism for indicating the flow pattern occurred at high journal speeds, when there tended to be a plentiful supply of small gas bubbles being swept through the clearance space.

The most significant path taken by these bubbles was along a strong jet of fluid entering the clearance space just downstream of the film formation boundary. Bubbles entrained in these jets penetrated to the centre of the bearing, then travelled with the surface motion along the centreline. On approaching the cavitation boundary, they would be swept out of the lubricating film at the side of the bearing. This path is shown on figure 7.5 along with the rest of the family of routes taken by fluid entering the side of the clearance space. The bubbles would tend to maintain a constant velocity of about half the journal surface speed along each of the three segments comprising the route described. The fact that bubbles were swept into the centre of the bearing indicates that not only is there a significant sub-ambient pressure region downstream of the cavitation region, but also that most of the oil flow through the film was bypassing the cavitation region, rather than pass along the streamers or ride as a film on the journal surface.

A secondary circulation was also observed when bubbles followed the first leg of the path already described, but then slowed down rapidly as they approached the bearing centreline. Having lost all their axial velocity they would creep against the surface motion and join a cluster of similar small bubbles near the film formation boundary. The movement of these bubbles against the surface and fluid motion could be due to the positive pressure gradient away from the film formation boundary which

would normally be expected in this area. Occasionally one of the cluster of bubbles would be drawn away from the rest and accelerate rapidly away from the cavitation region to follow the final two legs of the path described above. Thus bubbles tended to migrate in both directions through the body of fluid immediately downstream of the film formation boundary.

Since the bubbles tended to have a diameter approaching the local film thickness, it is unlikely that they travelled upstream in the flow of oil adjacent to the stationary bearing surface to be swept away by transferring to the flow next to the journal. An alternative explanation is that the bubbles were swept away from the film formation boundary in the current generated by a streamer entering the full film, and its progress against the surface motion was between two such currents. However such an alignment of the bubble paths with the streamers was not noted when the experiments were performed, and does not appear to be a more plausible explanation.

Driving the bearing in addition to, or instead of the journal did not reveal any obvious performance phenomena related to these alternative modes of operation. Rotating steady state cavitation regions were generated by using the rotating load and they appeared to have the general characteristics already described. As noted above detailed observation was not easy, but a limited amount of high speed cinematography did not show any features

that could not be generated with the fixed load.

7.4   DYNAMIC FLOODED OPERATION OBSERVATIONS

As described above dynamic states were produced by the combined use of fixed and rotating loads. As was expected, when a small rotating load was introduced to a fixed load steady state condition, there was no dramatic change to the basic structure of the cavitation region, but a small oscillatory motion in time with the disturbing force was observed. The general size, shape and the number of cavities did not change but the dendritic action appeared to be more prominent as the boundaries moved against the surface motion.

For moderate dynamic loads the amplitude of the film boundary motion decreased as the angular velocity of the rotating load was increased from speeds comparable to the surface motion to higher values. Non-linearities in the motion became apparent for large boundary movements when the boundary surfaces moved more rapidly against the surface motion than with it. But any phase difference between the motion of the cavitation and formation boundaries was not pronounced.

In extreme cases the cavitation region could be made to perform very large oscillations with an amplitude of more than

180°. Under such large amplitude motion and certain combinations of relative speeds, the boundary surfaces appeared to change type as described in chapter 2. The boundaries could be seen to change their appearance in a manner that suggested that the critical boundary speed had been reached and that the surfaces were for a short period changing their nature from formation to cavitation and viceversa.

If the dynamic load was increased to become comparable to the load producing the steady condition, the amplitude of boundary motion increased until the steady state type cavitation region broke down. The breakdown mechanism can be described as part of the cavity close to the film formation boundary switching from an oscillatory motion about a steady state position to a rotational motion orbiting around the bearing, but the part of the cavity close to the film rupture boundary remaining in an oscillatory mode of motion. Usually this breakdown occurred when the cavitation region reached an extremity of its oscillatory motion. Thus during the period of the breakdown the cavitation boundary would be swept around the bearing with the surface motion, to an extremity of its oscillation, perform the usual about turn and proceed to move against the surface motion. As the cavitation boundary reached the extremity of its cyclic motion, the film formation boundary would not be able to perform the usual reversal, but would continue to move with the journal surface. Thus for a short period the cavity boundaries would be moving

apart causing a large increase in the cavitation region extent.

This process of stretching the cavitation region resulted in the cavities being divided into a large number of smaller cavities and bubbles dispersed around the bearing. Immediately after the start of the cavity region breakdown, the increase in local film thickness due to the passing of the minimum film position, would draw lubricant into the clearance, forcing the cavities towards the centreline of the bearing. Under these conditions the bubbles of gas were not expelled at the sides of the clearance space, as was observed for the breakdown of steady state cavitation at high operating speeds, but remained distributed through the film. This behaviour appears to be the same as observed by White(26) for squeeze film bearings.

7.5   DRAINED STEADY STATE OBSERVATIONS

The small oil supply hole and the low supply pressure of the drained journal parts meant that only a relatively low rate of oil flow could be supplied to maintain the oil film, hence the bearing could be expected to run in a starved condition. As the mass content of a steady state film is constant, the flow of lubricant at the supply pocket can be expected to determine the circumferential length of the film. Since the usual oil supply arrangement is to have supply slots across most of the bearing

width, to give an ample supply of lubricant, the test bearing can-
not be considered as representative of typical bearing
installations.

The typical steady state fluid film appearance for the drained
test bearing is shown on figure 7.6. The most striking feature
of the results is the short length of the full film region which
was always less than 100°. The usual solutions to Reynolds
equation predict films about twice as long, but these solutions
assume a more appropriate supply of lubricant. The high
eccentricity, short film length observations show that the load
line was biased towards the formation boundary rather than the
cavitation boundary, this is probably a false indication. As
expected reducing the head available to drive lubricant into the
bearing resulted in the load bearing film becoming shorter.

The cavitation boundary had a similar appearance to the
surfaces observed in the flooded tests, but tended to produce
fewer streamers. All the streamers were affected by gravity
which caused them to descend through the clearance space as the
distance from their source increased. Only some of the streamers
extended right through the cavitation region to return lubricant
to the load bearing film through the formation boundary. Because
of gravity a few of the streamers generated near the lower
surface of the journal terminated at the lower edge of the
clearance space, but far more appeared to end part way across the

cavitation region. Due to the increase in clearance space height and loss of fluid over the bearing surfaces, most of the streamers reached a stage where they could no longer continue to span the bearing clearance. At this point the J.F.O. type of streamer ended and the fluid formed thin films on each of the bearing and journal surfaces.

As with the flooded results the formation boundary formed a very smooth curve across the bearing width, punctuated at intervals by streamers entering the film. The usual behaviour of the supply pocket was to form a streamer of oil rather than initiate the load bearing film. Consequently sweeping the supply hole through the cavitation region had no noticeable effect on the system. It was only at very low journal speeds that the oil supply system was able to develop sufficient pressure at the pocket, to generate a region of hydrostatic film which would then form the leading edge of the full film region.

7.6   DYNAMIC DRAINED OBSERVATIONS

Again the addition of a small dynamic load to disturb the steady state condition did not cause a fundamental change to the film structure, the only significant development being the oscillation of the film in time with the disturbing force. Whereas placing the oil supply hole inside the steady state film

region caused a reduction in the film region size, the dynamic film could pass over the oil supply hole without any untoward effects. Modest rotating loads were sufficient to cause large amplitude oscillation of the film region, and continuous operation with the film boundaries sweeping through angles of greater than 180° was possible.

If the two applied loads became comparable, the working film would breakdown and become distributed around the bearing. Since the volume of lubricant in the steady state load bearing film was small compared to the clearance space volume, the dispersal of the working fluid around the bearing resulted in the formation of lubricant filaments spanning the clearance space. Because of the compressibility of air there was very little tendency for the lubricant to be expelled from the clearance space as the journal orbited under the action of the applied loads. As for the steady state oil streamers, the narrow filaments would not be able to generate any significant fluid pressures. Hence large amplitude journal orbits were observed since there were no significant hydrodynamic forces generated to oppose the motion.

Alternatively with a rapid transition to a dominant rotating load, it was possible to retain the same load bearing film, and maintain the film precessing around the bearing.

7.7 SEMI-FLOODED OPERATION

Interpretation of the images generated by the usual bearing configurations was helped by observing the film behaviour at unusual conditions. One of these conditions was generated by allowing the atmosphere a limited amount of access to the clearance space. If the barrier of lubricant above the journal was reduced to about 2.0 mm then there would be insufficient head available to transport oil across the top of the journal and maintain the flow into the fluid film. The result was that the free surface would be drawn into the clearance space, forming a tongue of air as shown on figure 7.7. Whilst this penetration of air into part of the clearance space existed, the formation of cavities as described for the flooded operation would still take place.

If sufficient oil had been removed and the tongue of gas penetrated about a third of the way across the clearance space. The upstream surface of tongues of this size were likely to form ripples as shown on figure 7.7. Occasionally such a ripple would develop a finger of air extending far in advance of the original surface position, and the oil film close in on the base of this finger to form a detached pocket of air. Sometimes the resulting closed pocket would then migrate against the surface motion to augment the cavities that had already developed. The result would be the creation of cavities larger than those observed for

the flooded tests. It is assumed that the bubble of air was driven towards the cavitation region by the prevailing pressure gradient, indicating that the cavities were at a sub-ambient pressure. But this can not be considered as an exact model of the flooded case because of the disturbance due to the loop of atmosphere penetrating the clearance space.

The results of gradually reducing the volume of oil in the test section are shown on figures 7.8 to 7.11. The first change to the lubrication system would be the tongue of air extending from the upper side of the clearance space. As soon as this tongue extended by about a third of the distance across the bearing, boosting of the cavitation region would take place. As described above the boosting took the form of quantities of air breaking free from the tongue and migrating into the cavitation region. At this stage the jet of lubricant entering the bearing from above took the form of a broad streamer of oil, but much weaker than the jets observed during the flooded tests.

As the lubricant level was further reduced this broad streamer marking the upper boundary of the cavitation region, became thinner and weaker, until eventually no more than a typical streamer originating from the cavitation boundary. As the standing oil level approached the lower side of the journal, the lubricating system appearance began to resemble the drained bearing arrangement. During the transition from fully flooded to

the drained type of condition, the full film region gradually changed from occupying most of the journal circumference to only a small part. At the same time the cavity pressure obviously rose from a sub-ambient value to atmospheric pressure.

Initially the dendritic action became more pronounced as the cavity was boosted by additional air from the atmosphere, with considerable secondary noses forming at the sides of the main cavity noses. Photographs presented by Jacobson and Hamrock(27) of cavities in a dynamically loaded bearing, show cavity patterns typical of those in the present bearing operating with an inflated cavitation region. Observation of the cavitation region whilst the bearing was running in the usual fixed load steady state mode showed that although the region remained stationary patterns within the region travelled in the direction of the moving surface. High speed cinematography of this condition generated by a rotating load revealed more detail of the dendritic behaviour.

As the rotating cavitation region swept around the bearing, the patterns formed by the cavity boundaries and oil filaments remained stationary. Once a secondary nose had formed it advanced with the cavitation boundary and away from its parent cavity, leaving in its track a finger of cavity fluid. This long finger of cavity remained at the place it was formed since only the nose of the cavity advanced as the cavitation region swept

by. At first cavity fluid flowed into the finger, causing it to expand at right angles to its length, finally the approach of the film formation boundary would cause the side cavity to collapse. The fluid driven out of the collapsing cavity passed back through the root of the side cavity and forward along the parent cavity to feed freshly formed and developing side cavities. This behaviour is illustrated on figure 7.12 which has been simplified to show primary cavities with smooth sides and only one or two side cavities. The usual patterns formed by inflated cavities normally displayed many more side cavities than are shown on the figure.

The typical ragged appearance of streamers is explained by the random formation of the secondary noses. As the cavitation boundary advanced the noses of secondary side cavities from adjacent parent cavities would approach each other. Since their formation was due to random events they would not be symmetrically displaced either side of the streamer between adjacent parent cavities. Eventually the side cavities would overlap slightly to produce a small kink in the streamer, thus producing the curved streamer sides and centreline.

7.8 OBSERVATIONS WITH COMBINATIONS OF IMMISCIBLE FLUIDS

Particles of foreign matter and bubbles of air in the flooded experiments demonstrated ways of indicating the flow of lubricant through the load bearing film. Since the intrusion of foreign matter in the form of balls of fluff were infrequent, and the air bubbles were only generated at high shaft speeds, a more controllable means of providing flow visualisation was desireable. Because of the thin film thicknesses near the cavitation boundary, flow visualisation was attempted by the introduction of an immiscible fluid into the clearance space. Hence the requirement was for a pair of immiscible fluids of similar density that could be made visibly distinguishable.

Various combinations of fluids including water, methylated spirits, oil and glycerine were tried with the following general result. If a small amount of more viscous fluid was added to the system, the indicator fluid did form small bubbles but they were not sufficiently mobile in the clearance space to follow the local flow of the lubricating fluid, and often became attached to one of the bearing surfaces. For a small amount of less viscous fluid added to the lubricant, small bubbles would be formed in the more turbulent areas at the side of the bearing but the indicator would collect in the cavitation region and behave like cavity fluid. Thus it was possible to have oil as the lubricant and have both air and water in the cavities.

A workable combination of fluids proved to be glycerine and a light mineral oil. The glycerine was used in bulk as the lubricant and small amounts of oil were introduced as the indicator. The pair proved to act like oil and air except that because of their higher viscosities and the lower surface speeds used, there was much less dendritic action and transient random motion took place at a much slower pace. Thus observation of the dendritic action was made much more easily when this combination of fluids was used. The general appearance of the liquid filled cavities were much closer to the smooth sided structures observed by Cole and Hughes(25), than those normally obtained with gaseous cavities.

Since the two working fluids were immiscible the normal cavity formation mechanism was not available and the region of cavitation was often initiated by forcing a small volume of oil into the clearance space. As before increasing the operating eccentricity caused a reduction in the equilibrium volume of the cavity, which resulted in the shedding of small bubbles of cavity fluid from the formation boundary. Very slow cavity growth was possible by absorption of small oil bubbles circulating in the glycerine, but this mechanism was limited by the scarcity of small oil bubbles. The description of dendritic action in the section on flooded observations is mainly due to the observations made with this unusual combination of fluids.

Unfortunately no combination of fluids was found to be suitable for the intended purpose of flow visualisation in the fluid film. In general consistently good performance was not obtained.

7.9 ESTIMATED FILM PERFORMANCE AT WHIRL ONSET

The experiments performed with the perspex bearings have enabled the film behaviour to be observed for a medium length device. As found by other workers the clearance space is divided between the full film and cavitation regions. The full film region tends to be very uninteresting until the flow of lubricant through the film can be studied. In contrast the cavitation region is a dynamic area of random motion which immediately attracts the eye.

The fundamental structure of cavities divided by streamers was present for all the tests performed, giving confidence in the J.F.O. streamer model of the cavitation region. There was no evidence to suggest that there was a thin film of lubricant on the rotating journal which would support the alternative separation theory of cavitation. However this is not proof that separation was not taking place at the cavitation boundary.

One obvious conclusion of the study is that the extent of the full film region is dependent upon the volume of oil passing through the film, whether it enters through the formation boundary or at the sides of the clearance space. Thus the usual simple solutions to the one dimensional Reynolds equations may not be the most appropriate for typical bearing geometries.

The tests with a dynamic operating condition demonstrated that moderate disturbances did not change the fundamental structure of either full film or cavitation regions. By the use of a small rotating load in addition to a larger steady load, the journal was made to perform small orbits around its steady equilibrium position in a manner similar to the type of motion that occurs during whirl onset. The resulting behaviour suggests that at whirl onset a journal is most likely to be supported on a film essentially the same as the steady state film but performing a steadily increasing oscillation in the circumferential direction. As the whirl condition develops the system can be expected to suddenly switch to a rotating field system to support the journal. Thus the theory of dynamic lubrication based upon the J.F.O. model which has been developed in the previous chapters represents the major features observed.

8. STABILITY EXPERIMENTS

The primary objectives for the work reported in this thesis were to develop an apparatus capable of indicating the stability characteristics of journal bearings and to test a number of different bearing geometries. The ultimate objective for the experimental investigation of bearing dynamics must be to evaluate the eight coefficients of the dynamic stiffness matrix over a wide range of bearing operating conditions. But determining all eight coefficients is a difficult task requiring the use of different techniques to find first the stiffness and then the damping terms. The scope of the experimental work reported was limited to investigate performance at the stability boundary, and to calculate the most significant eigenvalue of the dynamic stiffness matrix, from measurements taken at whirl onset.

The fundamental requirement was therefore to design and build an apparatus capable of driving bearings into unstable operating conditions. However when a bearing is operating close to its stability boundary, the hydrodynamic film tends to have very little dynamic stiffness in comparison to its static value. Thus small disturbances to the test bearing whilst it is running at the required operating condition, will lead to significant journal orbits and even instability. Similarly damping in the system external to the test bearing will have a significant stabilising influence and cause errors in locating the stability

boundary. Consequently minimising the external interferences acting on the moving parts is an important aspect of the test apparatus design. Normally two journal and two thrust bearings are necessary to adequately support a shaft, but Holmes(28) has shown that the interaction between the two journals in such an arrangement is likely to produce a stabilising influence. Hence there are advantages for a test configuration that has only one journal bearing.

The single bearing type of system has severe disadvantages in that the load on the bearing and the driving torque have to be derived from forces acting at a distance. Consequently typical means of loading and driving shafts can not be used. The most convenient and reliable means of loading a single bearing system is to use the force of gravity. This implies that the load on a bearing will be constant, which in turn implies instability will always occur at one running speed. Such a system would be of limited use as it yields a strictly limited amount of information. But Chapter 6 has shown that the critical running speed of any bearing can be changed by varying the stiffness of its supporting structure. Since the results gained from a bearing mounted on an axisymmetric spring have been shown to yield the required critical eigenvalue of the dynamic stiffness matrix, a test bed was designed based upon a single journal bearing supported on a mounting structure of variable stiffness.

There are a number of advantages to be gained from turning a single bearing system inside out, to have a rotor running on a stationary centrebody as shown on figure 8.1, rather than a journal located inside a bearing. Marsh(22) has shown that a bearing rotor will be gyroscopically stabilised, and conical whirl at low speeds will be suppressed, if its transverse moment of inertia is less than twice the polar moment. This condition effectively limits the length of a shaft or rotor if transverse whirl is to be studied. Since the loading on the bearing will be restricted by the value of gravity, typical bearing pressures of one or two megaPascals are not normally possible for bearings of a sensible small laboratory scale. Because a rotor is capable of possessing several times more mass than a shaft of equivalent size, a rotor on centrebody configuration will give bearing loadings closer to typical values found in practice.

Marsh and Simmons(23) have successfully used the single bearing layout sketched on figure 8.1 for their stability experiments with air bearings. The present work has developed the single bearing layout for studying the stability of oil lubricated bearings. Sections through the test assembly used in this study of half speed whirl are detailed on figures 8.2 and 8.3. The design of the various parts of the test arrangement are discussed in the following sections.

8.0.1 Test Rotor

The primary function of the rotor is to provide the rotating surface of the test bearing. Thus the internal surface of the rotor as shown on figure 8.4 was bored and ground to a close tolerance cylindrical shape. Keeping the bore constant right through the rotor had two advantages. A wide range of bearing geometries could be tested with the one rotor because both the bearing width and clearance ratio could be changed by a variation in the size and shape of the centrebody. The cylindrical bore also provided a suitable target surface for the displacement measuring instrumentation. The major disadvantage was the comparatively long distance the oil squeezed out of the clearance space had to travel before escaping from the system. But the high rotational speed ensured an even distribution of the escaping oil in a thin film around the bore.

As shown on figure 8.4, the sides of the rotor were machined to form oil flingers to direct the flow of waste oil, and thrust faces so that the rotor's centre of mass could be kept over the centreline of the bearing. The axial location function was performed by aerostatic thrust bearings which were designed with large working clearances to minimise their influence on the rotor's dynamic behaviour. The torque needed to accelerate the rotor up to and maintain the working speed was generated by an impulse turbine consisting of thirty slots milled into the

outside diameter of the rotor. Finally twelve machine screws were fitted to the periphery of the rotor to facilitate balancing. The basic details of the rotor geometry are given on table 8.1.

8.0.2   Test Centrebodies

The centrebodies not only provided the stationary bearing surface and the means of supplying oil to the bearing, but the detail of their shape also defined the test bearing geometry. The centrebody maximum diameter, as shown on figure 8.5, governed the bearing clearance, and the axial length of this surface defined the bearing width. Table 8.1 lists the basic centrebody details for all the bearing geometries tested.

Since it was the purpose of the test bed to drive bearings into half speed whirl, subsequent periods of running with very large amplitude orbital motions were expected. Hence the centrebodies were designed to ensure that the fully developed whirl did not cause excessive wear to the bearing surfaces. The most favourable circumstances for maintaining a hydrodynamic film to support the rotor are achieved by having a maximum of continuous centrebody bearing surface. To minimise the disturbance to the cylindrical bearing shape, the oil supply was implemented by drilling a single small hole on the bearing

centreline of each centrebody. As an additional precaution the centrebodies were made from phosphor bronze to minimise damage to the steel rotor.

The large centrebody and rotor masses, combined with the wide range of mounting stiffnesses, produced large variations in the static and dynamic displacements of the centrebody. Thus it was much more convenient for all the instrumentation and services to be mounted on the centrebody rather than fixed to the bed plate. The distance probe mountings were machined as shown on figure 8.5 on both sides of the raised bearing surface. The combined oil catchers and thrust bearings were made to be secured to the ends of the centrebody as shown on figure 8.2, and the turbine nozzles were mounted with the tachometer probe on rods secured to the oil catchers.

A special centrebody with two aerostatic bearings, as shown on figure 8.5, was made for the task of balancing the rotor. The unit was designed to replace the normal centrebodies so balancing could be performed using the standard test bed equipment.

8.0.3   Flexible Mounting

The flexible support structure required to vary the critical whirl onset speeds was implemented using two hollow stainless

steel tubes, one screwed into each end of the centrebody. The tubes were designed to be bolted down onto movable support pillars, so that the active length of the beams could be varied. Increasing the distance between the supporting pillars, which are shown schematically on figure 8.1, decreased the effective stiffness of the tubular supports and hence the natural frequencies of the flexible mounting system.

The relative values for the mounting system's first two natural frequencies are important, since translational whirl is associated with the first mode of vibration, and the second mode is excited by conical whirl. Even though the rotor was sufficiently short to be gryoscopically stabilised, a high natural frequency for the second mode of vibration was desireable to keep the conical whirl onset speed as high as possible. The simple mass and beam system used did not have a great separation between the first two natural frequencies, but conical whirl was only experienced for one test bearing. The presence of conical whirl did not prevent the acquisition of translational whirl data since the rotor was already running above the limiting speed of the data gathering electronics.

The tubular suspension gave a working range of natural frequencies, 'ω_{AB}', from 10 to 100Hz. In addition the support pillars could be brought right up to the ends of the centrebody structure to provide a rigid mounting.

8.1 SERVICES TO THE TEST BEARING

A pumped oil supply was used to provide lubricant at about
20°C and a pressure of 0.35 bar to the test bearing. For all
experiments a light mineral oil was used having the viscosity
relationship plotted on figure 8.6. The oil was assumed to have
a nominal viscosity of 7.0 mPas, (7.0 cP), for all calculations.
The pressure of 0.35 bar was found to be the minimum necessary to
give smooth running at stable operating conditions. Setting the
centrebody with the oil supply hole facing directly downwards,
then turning it through 15° to 20° against the direction of rotor
rotation, was found to be the best orientation for consistently
smooth running. Increasing the supply pressure by modest amounts
was found not to affect the whirl onset speeds. The used oil
escaping from the test bearing was allowed to drain into a sump
before being filtered and recycled.

The test bed's high pressure air requirements were all
provided by the laboratory compressed air supply. A filtered and
regulated supply was used for the aerostatic thrust bearings and
the centrebody used for balancing. A separate regulated supply
was used to feed one pair of forward facing drive nozzles. Fine
control of the rotor speed was achieved by adjusting the pressure
ratio across these nozzles, and hence the quantity of air
entering the drive turbine. Unregulated supplies were connected
to the remaining drive nozzles, one pair forward facing and a

similar pair facing backwards, to provide rapid acceleration through unstable operating regions and rapid deceleration to bring the rotor out of the fully developed whirl condition.

Both the oil and the compressed air were fed directly to the centrebody through lengths of PVC tubing, which allowed the the test assembly unrestricted movement on its flexible mounting.

8.2   INSTRUMENTATION

The analysis of the test bearing behaviour has been shown to require the measurement of the rotor speed and orbital frequency at whirl onset, along with two natural frequencies of the mounting system. As is normal practice, instrumentation was also provided to indicate the journal position within the clearance circle. However the eccentricity and attitude angle which define the rotor position are two of the most difficult parameters to measure. This is due to the small displacements involved, the lack of a fixed datum, the relative motion between components and thermo-elastic distortion of both surfaces. Not only must non-contacting measuring devices be used but they are subjected to a comparatively harsh environment.

Traditionally either capacitive or inductive techniques have been used to sense journal position, and both types of equipment

were available for use in this project. The capacitive equipment whilst being a much more mature technology is more difficult to use. The sensors have to be placed very close to the target surface, which should be earthed, and are sensitive to the dielectric constant of the medium in the clearance. The alternative eddy current type of probe has severe problems in sensitivity to the electrical properties of the target surface and the ambient temperature, but have compensating advantages with large operating clearances, insensitivity to the fluid in the clearance, and small size. These advantages meant that the eddy current probes could be safely mounted on the centrebody using the rotor bore as a target. The eddy current sensors were so versatile that they were used for the source of all electrical signals to come from the test assembly. Since the standard eddy current transducers tend to be very bulky, compared to the size of the radiating coil, special probes were developed and manufactured by the University staff to fit in the confined space between the rotor and centrebody.

Two probes were mounted on the centrebody, 90° apart and to one side of the bearing surface, so that their readings gave the rotor position in cartesian coordinates. Thus displaying the signals on an X-Y oscilloscope recreated the journal motion. Since the probes effectively scanned a track in the rotor bore, a cyclical variation in the output signal arose due to the spatial variation of the rotor's surface properties. The unwanted signal

component could originate from two types of surface feature, the geometric shape of the surface, and the electro-magnetic properties of the material. Both the shape of the signature and its relative invariance along the rotor bore, combined with experiments on various test pieces, indicated that the signal disturbance was largely due to the electro-magnetic properties of the target surface.

Typical false distance readings were of the order of 15 μm, which is significant compared to the 50 to 100 μm range of diametral clearances tested. Both probes used for measuring the journal position were affected by the variation of surface properties, but their relative position on the centrebody generated a phase difference between the two surface signal components. This caused a characteristic closed loop figure to be presented on the oscilloscope display. Because the figure was very distinctive and constant for each bearing build, it was called the rotor signature. Although the presence of this signature obscured the exact rotor position, it did not prevent the detection of whirl onset. Since the orbital frequency is typically about half of the rotational value, whirl onset was indicated on the oscilloscope display as the formation of a double image. The two component parts of the double image would continue to separate as the orbit grew in size.

A third distance sensing probe was always mounted on the centrebody in line with one of the previously mentioned pair, but at the other side of the raised bearing surface. The additional signal was used to categorise the mode of whirl as either translational or conical. Tests with various specimens showed the rotor signature remained comparatively constant in the axial direction whilst changing markedly in the circumferential direction. Thus displaying the signals from the two probes at opposite sides of the bearing surface and axially in line, on an oscilloscope set at high gain in X-Y mode, produced a straight line at 45° to the horizontal. Translational whirl onset caused an elongation of this line. In contrast conical whirl produced a thickening of the line which degenerated into a confusion of traces covering the whole screen. The effectiveness of this technique was demonstrated during one series of tests, when a conical whirl condition intervened before the second translational whirl onset boundary could be reached.

Once a large amplitude translational whirl condition had been established the first oscilloscope display showed a roughly circular trace. Superimposed on the general circular shape was a characteristic pattern occurring twice in one circuit of the circle. This pattern was due to the rotor signature and the fact that it appeared twice per orbit indicated that large amplitude whirl was also performed at about half the rotor speed. The basic circular shape was apparent because the bearing clearances

tested were always larger than the false displacement signals of the signature. Measurement of the trace showed that the circular orbit amplitude was approximately equal to the clearance circle diameter, suggesting that during fully developed whirl the rotor was performing an orbit almost equal to the clearance circle supported by a very thin lubricating film.

The rotor speed was determined by measuring the frequency at which the buckets of the turbine drive passed a fixed point. An electrical signal was generated by placing an eddy current probe adjacent to the turbine. The probe's output signal was fed directly to a timer counter which provided a continuous display of the bucket passing frequency. A one second counting period proved sufficient to give the required accuracy and a rapid updating of the rotor speed.

The natural frequencies of the mounting system were found by inducing resonance with an electro-mechanical vibrator. Again eddy current probes were used to monitor the centrebody response. Since the system's natural frequencies were of the order of 10Hz, a phase locked loop type of low frequency meter was used to give readings to an accuracy of 0.01Hz with a cycle time of only one second.

8.3   DATA RECORDING AND REDUCTION

The major signal processing problems to be overcome were the isolation of the whirl frequency signal components and to relate the displacement information they contain to the bearing's clearance circle. Finding the orbital frequency also presented difficulties since the small amplitude whirl signal was always heavily masked by the larger synchronous surface property signals. Separation of these two signal components using analogue equipment would not have been easy, since they were typically only one octave apart.

If analogue instrumentation is used to measure the bearing performance, two different signal processing techniques are necessary to derive the positional and frequency information. Marsh and Simmons used analogue instrumentation for their air bearing experiments to process the output signals from the capacitive transducers they used. The positional information was derived from the time averaged values of the source signals. The fact that they were using symmetrical centrebodies helped them find the centre of their bearings. The transformation from average signal levels to steady state journal position was easily determined and checked by successively rotating the centrebody through 90° and taking readings, whilst the bearing was operating at a steady state constant speed condition. When measuring the orbital frequency they attenuated the synchronous signal

component using a variable frequency notch filter, to leave the signal from the whirl motion as the dominant component. Since a timer counter was used for the frequency measurement, the small scale whirl orbit had to be held for several seconds whilst the reading was taken.

The centrebodies used for this study of oil lubricated bearings were not axially symmetric because of the oil supply arrangement, and turning the centrebody through reasonable angles was found to cause significant changes to the operating eccentricity. Thus the technique used by Marsh and Simmons for defining the centre of the clearance circle could not be used for this type of oil bearing. To overcome calibration problems and perform a more detailed analysis of the displacement signals, the work reported in this thesis used digital equipment to perform a numerical analysis.

The high analogue to digital conversion rates the test apparatus required were achieved by dedicating a microprocessor to driving a converter chip. The recorded information was then down-loaded to a microcomputer system for ease of performing the numerical analysis. In order to obtain sufficient information to make the numerical analysis a reasonable proposition, a sampling rate of at least ten coordinate pairs was required for each time around the whirl orbit. Since the whirl frequency was expected to be about half of the running speed, only five coordinate data

pairs were required for each turn of the rotor. A standard trigger circuit was used to generate a data conversion timing signal from the rotor speed sensor. Thus thirty samples per revolution were obtained and the sampling rate automatically adjusted itself to suit the orbital frequency. Using the bucket passing signal also had the benefit that the false signal components apparent in the rotor signature appeared as repeating sequences of fixed values throughout each data set.

The analogue to digital conversion cycle time limited the maximum working rotor speed to about 13,000 rpm. At this speed the interval between timing signals was approximately equal to two conversion periods. As each timing signal was received the signal levels were frozen by 'sample and hold' circuits in order not to generate errors due to the conversion delays. The result of each conversion was stored in the memory attached to the microprocessor. The finite size of the processor memory meant that data could be recorded for a period of up to 17 revolutions. The electronics associated with the data conversion and storage were designed and assembled by the Durham University Microprocessor Centre. For all the experiments reported, the signals from two displacement sensors were recorded and data was acquired in a continuous period of 17 revolutions. Once the microprocessor memory was full the data was then down-loaded to the microcomputer for signal analysis.

The microcomputer had several different signal processing functions to perform. For each test session images of the rotor signature and the clearance circle had to be generated before the steady state and dynamic peformance could be analysed. The technique used to analyse whirl onset data was to fit the the generalised journal motion given by equations (4.1) to the rotor positional information contained in the data set. Thus information was gained not only for the steady state position and the whirl frequency but also the orbit size, shape and growth constant. Details of the numerical algorithms used to analyse the whirl orbit data are given in appendix one.

A discrete fourier transformation was performed on a limited number of data sets by a mainframe computer. Since the frequency information is contained in the data sets from both probes, the signal values in the two coordinate directions were combined to form a series of complex numbers. The series of complex numbers was then transformed into a set of complex fourier coefficients. The moduli of the resulting coefficients are presented on figures 8.7 and 8.8 for a typical set of test results. The first figure is for the data as recorded and shows the dominance of the synchronous signal component. The second figure is the result of performing the analysis after subtraction of the rotor signature. The fourier analysis has drawbacks since it requires substantial computing power and can only produce frequency values to a limited accuracy.

8.4   OPERATING PROCEDURE

Before running on an oil film, the rotor was balanced to minimise synchronous excitations due to out of balance. The processs must be performed with care since synchronous vibrations are thought to have a stabilising affect on the oil film. Balancing was performed with the aerostatic centrebody fitted to the suspension system, and the rotor running at speeds which excited the first and second modes of vibration. The position and magnitude of the out of balance masses was judged from traces of the rotor signature and centrebody motion displayed on an oscilloscope. The machine screws set into the rotor were adjusted so that the centre of mass lay on the bearing centreline, and the axis giving the maximum moment of inertia lay along the axis of the rotor bore.

Once the rotor had been balanced, the first test bearing was assembled and the relationship between the mounting frequencies $'\omega_{RB}'$ and $'\omega_{B}'$ determined. Theoretically the ratio should be equal to the following function of the rotor and bearing masses.

$$\frac{\omega_{B}}{\omega_{RB}} = \sqrt{\frac{M_R + M_\beta}{M_\beta}} \qquad (8.1)$$

Substituting the weights of the test assembly parts into the formula indicated that the frequency ratio should have been about 0.744. By using a mechanical vibrator to find the system's

resonant frequencies, the ratio was found to remain constant at a value of 0.746 over the working range of the suspension.

After these preliminary experiments were completed, the measurement of bearing performance could begin. At the beginning of each test session the suspension was set to a relatively soft value, so that the rotor could be run up to and left to warm through at a speed of seven or eight thousand rpm. After about ten minutes the signal amplifiers associated with the data recording equipment were set so that the whole of the clearance circle lay within the operating range of the analogue to digital converter. The gain was then adjusted to make the diameter equivalent to approximately three thousand digits.

The first five sets of readings were recorded whilst the test bearing was running at a steady operating condition. The signature image was derived from these data sets as detailed in the appendix. Tests showed that the signature image remained constant throughout the working speed range of apparatus. Having determined the signature, three data sets were taken from fully developed whirl conditions. The clearance circle centre and diameter were calculated from these circular orbits, using the assumption that the rotor was whirling on a negligible lubricating film thickness. All subsequent data sets were transformed into journal displacements by subtracting the signature image and mapping the resulting data onto the clearance

circle.

Having performed the system setting up and calibration procedure, measurement of the bearing performance could commence. The bearing's steady state behaviour was determined by taking readings at a series of stable states, from very low rotor speeds up to the range of whirl onset speeds. Finally tests at the whirl onset boundaries were performed.

For each whirl onset experiment the distance between the suspension supports was set to the desired length, and the natural frequency ' ω_{RB} ' measured. The rotor was then accelerated to a stable operating condition below a whirl onset boundary. The whirl onset boundary was approached slowly by allowing the rotor speed to rise by about two rpm per second. When close to the stability boundary, random influences would initiate small journal motions which would slowly decay. The critical running speed was judged to have been reached when such random disturbances produced a strong orbit that showed no signs of decaying. Occasionally the stable system would be disturbed by a large influence which would cause premature whirl onset and instability at an otherwise nominally stable operating condition.

Some parts of the second whirl onset boundary could only be reached by passing through the lower unstable operating region. As already described a pair of unregulated drive nozzles were

used to give rapid acceleration through the unstable operating region. To aid passage through these conditions the first whirl onset boundary could be temporarily displaced to larger values of the operating stability parameter. The system characteristics were changed by grasping one end of the centrebody, increasing both the mounting stiffness and damping. However in the region of the whirl cessation boundary the vibrations were always very strong, and could not be suppressed by such simple means. As a result the unstable operating region was always traversed as quickly as possible.

For the stiffer settings of the suspension, and particularly at the second whirl onset boundary, the small whirl orbit would very quickly grow into fully developed whirl. The extent to which the upper stability boundary could be followed whilst increasing the mounting stiffness, was often limited by the ability to initiate the data recording before the small amplitude orbit had become fully developed whirl. At the other end of the mounting stiffness range and particularly for the first whirl onset boundary, the test bearing often demonstrated a great reluctance to go unstable, exhibiting small steady orbital motions over a wide speed range. For most cases the data analysis showed that the orbit recorded had an amplitude of between 1 and 5 percent of the clearance circle radius.

Usually the whirl orbit would have turned into a fully
developed whirl condition before the rotor speed could be reduced
to less than the critical value. Then the rotor speed had to be
decreased by about a thousand rpm before the bearing would return
to a steady operating condition. Hence the usual operating
procedure was to cycle around a hysteresis loop, but very careful
control of the operating speed could prevent the orbit developing
into a large amplitude motion. If the rotor speed was held
constant at a value very close to the stability boundary, an
occasional random influence would cause the formation of a small
stable orbit which could be maintained for an extended period of
time. A slight reduction of the rotor speed would then cause the
orbit to decay and return the system to a steady stable state.
However when operating at these conditions the system could
always be made to go unstable by disturbing the centrebody with a
sufficiently large impulsive force.

In general when running in the stable region immediately below
a whirl onset boundary, the closer the running speed was to the
critical value, the smaller the disturbance required to send the
system unstable. This suggests that for some operating
conditions there are limiting values for the journal
displacement, below which the system will remain stable. Since
fully developed whirl is associated with a rotating pressure
field system, and stable states are associated with oscillation
of the pressure field, the disturbance limits might be associated

with the transition of the oscillatory mode of cavity motion to a
rotating condition.

8.5   RESULTS

The experimental results have been grouped into three
sections.   The first deals with the steady equilibrium operating
positions found from both the steady and dynamic tests.   These
are followed by plots of the whirl onset performance indicated by
the microcomputer.   The final group consists of the dynamic
lubricating film characteristics calculated from the whirl data.
The results for each section are presented and interpreted in
turn.

8.5.1   Steady Equilibrium Positions

All the steady state rotor positions and whirl orbit centres
have been collected onto figures 8.9 to 8.23, one for each test
session.   The left hand graph of each figure shows the recorded
rotor position marked on the large amplitude whirl orbit which
has been assumed to indicate the clearance circle.   The
horizontal and vertical axes represent the coordinate directions
of the two distance measuring probes used for each test.   The
direction in which gravity was acting on each of these figures,

is always displaced from the vertical axis by about 20° in an anticlockwise direction. This is because one of the distance probes was always placed in line with the oil supply hole. As described above, the hole was always displaced from the bearing's vertical axis. The right hand plot on each figure shows the indicated eccentricity against running speed.

All the test sessions show a tendency for the indicated eccentricity ratio to become larger than a value of one at low speed running conditions. Figure 8.21 shows the worst set of results in this respect, and all the test sessions with the smallest clearance on the 20.0 mm wide bearing are poor. The fact that figures 8.21 to 8.23, which are for the same bearing geometry, exhibit this effect to different degrees, combined with observations made during fully developed whirl, indicate that the initial fully developed whirl could be supported by a lubricating film of significant thickness. Thus the large amplitude whirl orbit used to represent the clearance circle was always slightly less than the actual clearance circle diameter. However other instrumentation errors have probably combined with this effect to produce the observations shown on figure 8.21.

The bearing geometries of smaller clearance and greater width can be expected to develop relatively more hydrodynamic action and generally operate at lower values of eccentricity ratio. Typically their steady state curves approach the assumed centre

of the clearance circle as the rotor speed increases, but then pass beyond the centre. The curves on figures 8.17 and 8.18, for the bearing of 30.0 mm width, clearly demonstrate this action. The indicated behaviour is not realistic, and is probably due to inadequacies of the instrumentation and analysis techniques.

Some inaccuracy can be explained by considering the thermo-elastic distortion of the bearing members. Substituting the rotor geometry into Lamé's equations for a rotating disc gives a value of $1.41 \times 10^{-10} \omega_o$ for the strain in the material at the rotor bore. For the smallest clearance ratios tested, the bearing clearance is predicted to have increased by about 8% due to expansion of the rotor bore after acceleration from 0 to 10,000 rpm. Since the numerical description of the clearance space was gained from tests performed at whirl onset speeds, the elastic rotor distortion should not have significantly affected the mapping of whirl orbit data onto the assumed clearance circle. However the elastic distortion of the rotor bore will have had a much greater affect on the indicated low speed steady state running eccentricity and attitude angle.

Since the shear rate in the lubricating film is proportional to the rotational speed, both the power losses and the bearing temperature can be expected to rise as the operating speed is increased. Again for the smallest clearances tested, the rate of change of clearance ratio with operating temperature is about

-1.0% per degree centigrade due to the expansion of the centrebody, and +0.6% per degree for the rotor. Experience operating the test bearings showed that prolonged running at very high speeds could cause the centrebody temperature to rise to about 40°C. The figures above show that a rise of 20°C in both members of the bearing produces in the worst case about a -8.0% change in the clearance ratio.

Further work on inductive displacement probes similar to those used in these tests, has suggested that the transducer sensitivity probably decreased markedly with increasing temperature. Thus the large errors in the indicated rotor position shown by figure 8.17 are probably due to an accumulation of thermo-elastic distortion, change in transducer characteristics and lack of precision in determining the clearance circle. The scale of these effects was not appreciated when the experiments were performed, otherwise the additional instrumentation necessary to assess the changes would have been fitted. By placing an additional pair of displacement transducers diametrically opposite those used in the tests, the speed and temperature effects could have been estimated and the results corrected during the numerical analysis.

Figures 8.14 and 8.19 show a large amount of scatter for the rotor location within the clearance circle, but generally there is much better repeatability for the relationship between speed

and eccentricity. Figure 8.11 demonstrates a dual behaviour that the test bearings often exhibited. The rotor sometimes appeared to be able to operate on either of two steady state operating curves, but generally this was not apparent in the curves of running speed against eccentricity.

The 10.0 mm wide bearing performed well with a clearance ratio of two thousandths but could not be made to run steadily when the clearance ratio was increased to three thousandths, and no measurements were taken at this larger clearance. Similarly the 20.0 mm wide bearing ran unsteadily when its clearance ratio was increased to four thousandths. Although no sensible steady state readings could be taken, some dynamic results were recorded. Hence the limited number of points for this bearing geometry. Upon reflection these two bearings were probably running severely starved of lubricant, and increasing the supply hole diameter would probably have enabled them to run in a satisfactory manner.

The indicated eccentricity values from all the test sessions have been corrected to give a realistic interpretation of the bearing performance. All the eccentricity values from each test session have been multiplied by a constant scaling factor so that the corrected eccentricities tend to a value of one as the rotor speed tends to zero. The steady state relationships showing a tendency towards the assumed centre of the clearance circle have been corrected a second time to make the high speed eccentricity

values approach zero. The corrected results for each bearing geometry are presented on figures 8.24 to 8.31. In general the correction of the indicated eccentricity values gives a more acceptable indication of the bearing performance.

The graphs to the right hand side of figures 8.24 to 8.31 have been marked with the Ocvirk steady state performance predictions. These curves of theoretical behaviour have been calculated using the nominal values of lubricant viscosity and bearing geometry. Since the bearing operating temperature can be expected to increase with rotor speed, the effective oil viscosity will become progressively less as the rotational speed rises. Thus the Ocvirk steady state performance predictions can be expected to over estimate the load carrying capacity of the test bearings at high operating speeds. This type of behaviour would appear as a divergence between the test results and the predicted steady state performance with increasing operating speed. However the test results demonstrate a clear trend opposed to that expected from such a change in viscosity.

The same trend of developing less load carrying capacity than expected at low operating speeds, was also noted by White(26). Based upon his observations of cavitation in squeeze film bearings, White suggested that this might be due to the formation of a low pressure region at the mid-section of his test bearings. Alternatively the observed trend may be explained by oil

starvation. There are two features common to the bearing designs tested during the present work and by White. One is that the formation boundaries of the lubricating films were free to find their equilibrium positions. The other is that the supply of lubricant to the clearance space was severely restricted in both designs, when compared to typical journal bearing geometries which have oil supply grooves.

The ratio of oil expelled at the sides of a bearing, to that entering the lubricating film at the formation boundary, will increase as the operating eccentricity ratio rises. Thus for the bearings tested in the present work and those used by White, the film formation boundary probably retreated as the operating eccentricity increased. Therefore starvation of the lubricating film in the test bearings can be expected to increase progressively with eccentricity ratio. As a result the steady state eccentricity will rise more rapidly with falling rotor speed, than predicted by the Ocvirk solution. It is this type of trend that is shown by the test results.

8.5.2   Whirl Onset Performance

Figures 8.33 to 8.40 show the running speeds at which whirl onset occurred, and the non-dimensional frequency ratios for the orbits analysed. All results obtained with a rigid mounting

setting have been marked on the upper plot of each figure as having a mounting stiffness of 1.0×10^7 N/m. In general two whirl onset boundaries were found over a range of mounting stiffnesses. Finding both the first and second whirl onset conditions was expected, since both boundaries have been observed for similar experiments with air bearings. After some initial exploratory tests no further attempts were made to locate the whirl cessation boundaries. Thus only the whirl onset boundaries have been plotted, and the upper boundary of the lower unstable operating region has not been marked.

Consistently repeatable results were obtained for the first whirl onset boundary, and as expected the mounting damping limited the extent of the low speed unstable operating region. The second whirl onset boundary was not so clearly defined and some scatter was experienced on a few tests. Figure 8.35 shows a marked difference between two sets of readings taken at low values of the mounting stiffness. The reason why the first test session with this bearing geometry produced such an unusual set of results is not known.

The 10.0 mm wide bearing gave a very scattered set of results with whirl onset occurring at operating eccentricities larger than the Ocvirk theory predicts. Since the bearing was probably running partially starved, due to the small diameter of the oil supply hole, results in line with the Ocvirk predictions cannot

be expected. As already described the 20.0 mm wide bearing ran very unsteadily with the largest clearance ratio of 4 thousandths, but the limited number of results do show a clear second whirl onset boundary position. The results for the bearing with a 40.0 mm width show only the first whirl onset boundary. The stable operating region at low values of the mounting stiffness was limited for this bearing by the onset of conical whirl. The conical whirl was encountered at running speeds of about 13,000 rpm.

A number of the bearing geometries show whirl onset conditions about the nose of the steady state operating curve. But figure 8.30 has some whirl onset points which can arguably be taken to be beyond the nose of the steady state curve. These points demonstrate that the extent of the stability boundary is not limited by the nose of the steady state operating relationship, as discussed in chapter 5.

The non-dimensional frequency ratio results generally show consistent trends in line with the predictions of the Ocvirk solution. Most bearings exhibited a ratio of slightly greater than unity for whirl onset at low eccentricity values, but the results do not rise to values as great as 1.05 that the Ocvirk solution predicts. The test results also show a rapid fall in the parameter value at eccentricities of about 0.6, in good agreement with Ocvirk. Values of the non-dimensional growth time

constant, which were calculated from the whirl data, are generally about 0.001, normally positive but occasionally negative. Thus the growth time constants for the orbital whirl onset motion were generally greater than 2 seconds.

The non-dimensional frequency results from each test bearing have been collected onto figure 8.41 to show the general agreement with the Ocvirk prediction. Although values do not rise substantially above unity, this level is maintained up to moderately high eccentricity ratios. For higher eccentricities both the Ocvirk prediction and the observed values fall rapidly. The only exception is the set of results gained from the 30.0 mm wide bearing running with a clearance ratio of 3 thousandths. For this one geometry the non-dimensional frequency ratio falls markedly throughout the range of eccentricities at which the bearing became unstable.

Figure 5.5 has shown that a steady fall in the value of the non-dimensional frequency parameter is a feature of the usual long bearing solution. The long bearing predictions presented on figures 5.5 and 5.6 show that maintaining a non-dimensional frequency ratio of about one through the range of small and moderate eccentricities is a feature of shorter film arcs down to about 90'. This tends to indicate that most of the bearings were operating at a partially starved condition. The extent to which the results were influenced by the freedom of the film formation

boundary to oscillated in time with the orbital journal motion is
uncertain.

The real and imaginary parts of the complex number $'\epsilon_i / \epsilon_o \theta_i'$
describing the shape of the whirl orbit are compared with the
Ocvirk predictions on figures 8.42 to 8.49. In general most of
the results are in good agreement with the theoretical values, an
exceptionally good correlation being demonstrated on figure 8.48
for the 30.0 mm wide bearing at a clearance ratio of 4
thousandths. Again the results for the test bearing having a
width of 10.0 mm are at odds with the short bearing predictions.

8.5.3 Lubricating Film Characteristics

The critical stability parameter and the dynamic film
stiffness derived from the test results have been plotted with
the Ocvirk predictions on figures 8.50 to 8.57. It should be
noted that the lubricant viscosity is not required either for the
calculation of the results from the test readings, or for the
predicted Ocvirk values. Journal bearing performance prediction
and the interpretation of experimental results are often
sensitive to the value used for the bearing clearance, since this
parameter often appears in formulae raised to a power of two or
more. The clearance in a bearing has usually to be determined by
calculating the difference between measurements of the journal

diameter and bearing bore, which leads to inaccuracy. Thus errors in the determination of the clearance can lead to large differences between the observed and predicted bearing performance. However for the critical stability parameter this is not the case, because the expressions used to generate the predicted performance and calculate the test results are both linear functions of the bearing clearance.

The critical stability parameter results generally hold a reasonably constant value for low eccentricities, and show signs of rising sharply at an eccentricity ratios of about 0.6, as do the Ocvirk predictions. However the Ocvirk predictions are up to six times greater than the test results. This factor of six is too large to be attributed to measurement errors. The results from the 10.0 mm wide bearing are of dubious value since they show an unexpected behaviour over the limited range of eccentricity ratios for which results could be obtained. The other occurrence of note is the falling stability parameter value shown on figure 8.57 for the 40.0 mm wide bearing. The same feature can be seen to a lesser extent on figure 8.54 for the 30.0 mm wide bearing, this seems to be associated with the low eccentricity results produced by the low clearance ratio geometries tested. This deviation from the trends exhibited by the other test bearings can not be explained.

The dynamic stiffness results are also up to a factor of six times less than the short bearing predictions. But where the Ocvirk prediction maintains a finite value whilst the critical stability parameter tends to infinity, the test results show the dynamic stiffness rising with the critical stability parameter. Although the non-dimensional frequency ratio readings fall as the critical stability parameter rises, the decrease is not sufficient to prevent the calculated dynamic stiffness value rising.

On most of the figures the sets of data obtained from the two different boundaries, the first whirl onset boundary at low speed high eccentricity, and the second boundary at low eccentricity, appear to form two segments of a continuous curve. This suggests that the behaviour at the two boundaries is due to the same phenomena, even though the observed characteristics are not fully supported by the theory.

The values of the stability and stiffness parameters are influenced by the basic bearing geometry, consequently they can not be presented directly on a single graph as a unique curve. However the short bearing theory suggests that when these parameters are divided by the compressibility number 'H' and the square of the width to diameter ratio, a unique curve should be formed. But bearings of large to medium width to diameter ratio are not expected to follow the trends predicted by the short

bearing solution.--

The dynamic film performance parameters from all the bearing geometries tested have been collected onto figures 8.58 and 8.59. The vertical axes of these graphs have been formed by dividing the film parameters by the compressibility number 'H', and multiplying by a function of the width to diameter ratio 'L/D'. The figures show that scaling the vertical axis has brought the results from all the bearing geometries into a narrow band. Apart from choosing width to diameter ratio instead of the width to radius ratio, and using the compressibility number in preference to the non-dimensional steady load value, no attempt has been made to fit these functions to the test results.

Figures 8.58 and 8.59 show that in general the scaled performance results are about a factor of ten times less than the short bearing predictions. Since the previous set of figures showed better agreement, the scaling by compressibility number and length to diameter ratio function has increased difference between the short bearing theory and test results. This is largely due to the test bearings running at greater values of compressibility number than the short bearing solution predicts.

Again the one exception is the set of results obtained from the bearing having a width of 30.0 mm and a clearance ratio of 3 thousandths. The results from this bearing are close to the

Ocvirk prediction, but there was no known change in the manufacture or operating procedures which would explain why this particular bearing should have exhibited a stability performance significantly better than all the other bearings tested.

8.6   COMPARISON WITH OTHER PUBLISHED WORK

The present results have been compared on figure 8.60 with recently published work by Mori, Okada and Mori(29), and Akkok and Ettles(30). The Japanese tests were performed using a two bearing test apparatus with bearings similar to those used in the present work. The bearings were plain bore cylindrical geometries with a single oil supply hole placed diametrically opposite to the load line. The Japanese work allowed for more oil to be fed into the clearance since their supply hole covered 40 percent of the bearing width, compared to the much smaller values used for the work reported in this thesis. The limited amount of whirl onset data presented by the Japanese generally show greater stability than the Ocvirk solution predicts. It should be noted that no indication has been given in their report that the whirl behaviour observed was always purely translational. Experience with a slow speed apparatus designed by Brown(31) has shown that great care has to be taken to eliminate conical components from the dynamic motion of a shaft supported by two journal bearings.

Only the critical stability parameter has been presented in the paper by Mori, Okada and Mori, hence it is not possible to compare their non-dimensional frequency ratios or film dynamic stiffnesses. Since the Japanese and the present test bearings are essentially similar, the results ought to be comparable, but the Japanese show a much more stable behaviour. Since their results show that moving the supply hole position towards the load line has a destabilising effect, their greater stability is probably due in part to larger lubricating film arcs.

The paper by Akkok and Ettles also presents information on a rigid bearing whirl onset stability parameter, but not frequency ratio or dynamic stiffness. In their paper Akkok and Ettles report very good agreement between test results and their finite width performance predictions. Their findings for two axial groove bearings have been plotted on figure 8.60. These results also indicate that bearings with typical oil feed arrangements exhibit stability performance comparable with the Ocvirk predictions. Tests performed on a bearing with large oil supply grooves, and hence a shorter lubricating film, show a reduced stability performance at about the same level as the majority the tests performed in the current work. This again suggests that the low stability performance of the bearings tested is largely due to the units running in a partially starved condition.

9 CONCLUSION

The foundations for Reynolds equation in its present form were produced in the last century from the study of lubrication by liquids. Although certain steady state journal bearing solutions have come into common use, the correct solution methods are still subject to debate.

The application of lubrication theory to gas bearings has shown a way to find dynamic solutions to Reynolds equation based on a perturbation analysis. By this technique a first order model of the lubricating film's dynamic behaviour is generated in terms of the journal motion. In the first part of this thesis the perturbation technique has been applied to the version of Reynolds equation used for incompressible lubricants. The result is one equation describing the generation of fluid pressure at steady operating conditions, and a second equation for the difference between the steady and dynamic pressure distributions.

The development of liquid lubrication theory has been held back by the difficulty in modelling the behaviour of the gaseous cavities that form in the clearance space. The model of cavitation made popular by Jakobsson, Floberg and Olsson has been used in the work presented to describe the lubricant flow through the cavitation region, and the boundary conditions between the cavitation and full film regions. Each of the parameters

describing the pressure generated in the lubricant, the fluid film boundary position and the state of the cavitation region have been approximated by using a perturbation series. The perturbation series are in terms of the journal displacement, and are truncated to leave the first two terms of the progression. Substituting these relationships into the lubrication equations generates linearised expressions describing the full film and cavitation region states, and the boundary conditions for the fluid film.

Although the present theory has been developed using the assumption that the lubricant viscosity is constant throughout the system, the work can be easily extended to allow for the variation of viscosity with fluid temperature. By consideration of the viscous losses in the lubricating film and the mechanisms by which the heat energy is dissipated, both steady state temperature and viscosity distributions can be calculated. To extend the same analysis to dynamic conditions in order to find the temporal variation of the viscosity distribution during whirl onset would considerably complicate the stability analysis.

The development of gas bearing theory has demonstrated that the temporal variation of the fluid density has to be included in the mathematical model of the system. The density and pressure of a gas are linked by the equation of state, and it is this link that makes the temporal variation of density an important factor

in gas lubrication. Since the lubricant viscosity does not appear in the equation of state for gases or liquids, the temporal variation of viscosity is unlikely to have a significant effect on the dynamic performance of either gas or liquid lubricated bearings. Thus keeping the calculated steady state viscosity distribution constant whilst solving for the dynamic performance of the bearing, will probably be sufficient to extend the theory beyond its present isoviscous state.

A large low speed test bearing was manufactured with a transparent outer member so that the basic nature of cavitation and its behaviour under under dynamic loading could be observed. Experiments performed at steady state conditions demonstrated the strong influence that the prevailing boundary conditions have on the extent of the full film region. Having the bearing fully submerged in oil resulted in the full film extending through arcs of about 300 degrees. However allowing the lubricant to drain away at the sides of the clearance space and feeding only a limited amount of oil into the bearing, resulted in the formation of load bearing films occupying about 60 degrees of arc. The dynamic characteristics of these two modes of operation can be expected to be substantially different. Thus the boundary conditions used in the lubrication equations must reflect the conditions prevailing in the type of bearing being studied, if an appropriate full film region extent is to be predicted.

Experiments were performed on the large low speed test bearing to simulate whirl onset conditions by introducing a small rotating load to disturb the steady state condition. Under these conditions the orbital motion of the journal and the cyclic cavity movements could be seen clearly. The effect of introducing a dynamic load to the system can be viewed at a simple level as causing the cavitation region to perform an oscillatory motion, since the basic structure of the steady state cavities was unaffected by the journal movement. Consequently the principal feature the cavitation region can be expected to exhibit during whirl onset, is a cyclic motion in time with the orbital journal movement.

Further experiments were performed with two immiscible liquids occupying the clearance space. These tests showed that if small amounts of the less viscous fluid were introduced into the bearing, the thinner fluid would tend to collect in that part of the clearance space where gaseous cavitation would be expected to form. In most respects the bodies of less viscous fluid acted in the same manner as a gaseous cavity. This suggests that some characteristics of cavitation in bearings can be studied using immiscible liquids instead of the usual combination of liquid and gas. The advantage of using a cavity fluid much more viscous than air, is that the random motion of the cavity side surfaces take place at a more easily observable pace.

The simplest class of solution to the lubrication equations arises when the short bearing simplification to Reynolds equation is used. The elementary treatment of the cavity boundaries has been shown to predict cyclic motions for both the film formation and rupture boundaries in response to orbital journal motions.

In contrast, the infinitely long solutions to the governing equations require the use of the boundary conditions derived in chapter 2, to describe the state of the boundary. As a result the possibility can be considered that the extent of the full film region is affected by the location of oil supply grooves. Using the full film boundary conditions which have been derived, has been shown to lead to either of two solution types. The first type is characterised by the formation boundary position being free to find its equilibrium position in the clearance space. This type of solution is similar to the short bearing solution in that both the film rupture and formation boundaries are free to oscillate in response to translational journal motion, but has been shown to lead to a much more complicated general solution for the pressure distribution around the bearing.

The second type of solution for the infinitely long bearing assumes that the film formation boundary is held at a fixed position by an oil supply groove. Thus only the film rupture boundary is free to move in response to journal motions. This

type of model is representative of typical bearing designs which have axial slots cut into the bearing surface at which the oil film is initiated.

These three types of solution produce two different types of expression for the dynamic forces generated by the lubricant film. The short and the second type of long bearing solutions produce linear expressions in terms of the journal motion for the elements of the film's dynamic stiffness matrix. The first type of long bearing solution which allowed the film formation boundary to find its equilibrium position, results in more complicated non-linear expressions in the dynamic stiffness matrix.

The similarity between the solutions for the long and short bearing pressure distributions and stability performance, suggest that the results to be obtained for finite width bearings will be broadly similar to the easier one dimensional solutions. The steady state finite width solutions presented in chapter 3 have already demonstrated that the major effect of bearing width is upon the magnitude of the pressure distribution, not its shape. Since typical journal bearings have modest length to diameter ratios, the distribution of pressure in the clearance space will be heavily influenced by the side leakage flow of lubricant. Consequently the performance of typical bearings will show a tendency towards the Ocvirk predictions.

Chapter 5 has shown how the linear expressions for the dynamic film forces are used to find the stability performance of the lubricating film. Three dynamic performance solutions have been generated. The usual theoretical long bearing solution, which features film formation at the position of maximum clearance, gives the greatest arc lengths for the full film extent. The short bearing solution gives film arcs of 180 degrees. Finally the long bearing solution with the film forming at the horizontal centreline, which is more typical of normal bearing designs, gives the shortest arc lengths for the full film. When due account is taken of the effect of bearing length to diameter ratio, these three types of solution demonstrate that decreasing the circumferential length of the lubricating film, over the range for which the solutions have been found, degrades the stability performance of the film.

Analysing the equations of motion representing a bearing mounted on an axisymmetric spring, reveals that the solution has features in common with the corresponding solution for a rigid rotor running in a rigidly mounted bearing. The equations can be made to show how whirl onset data gathered from a bearing mounted on an axisymmetric spring can be related to the dynamic properties of the lubricating film. The equations also predict that the critical running speeds of such a flexible system can be changed by varying the stiffness of the mounting. Thus flexibility in the bearing support structure can be used as a

means for controlling the running speed at which whirl onset occurs, thereby gaining bearing performance data over a range of operating conditions.

The solutions for the equations of motion representing a flexibly mounted system, indicate that there are always two critical running speeds. At each critical speed a mode of vibration is predicted to change, as the running speed is increased, from being stable to being unstable. Since there are two whirl onset speeds but no corresponding whirl cessation condition, the present model predicts that all running speeds above the first critical condition will be unstable. Experience with gas bearings and the experimental work reported in this thesis, both show that a stable operating region does exist immediately below the second critical condition. Hence the simple theory is incomplete. Modifications to the equations of motion which allow for damping in the bearing mounting, and non-linear film behaviour, can be made to give a performance prediction in line with observed test bearing performance. But further study is necessary to determine if these modified equations correctly predict the resonance type of behaviour observed at the upper boundary of the lower unstable operating region.

Stability data has been calculated from experiments performed with bearings on a high speed test apparatus designed for the

study of whirl onset. The test arrangement featured a single bearing system supported on axisymmetric springs. For most of the bearings tested, two critical whirl onset speeds were experienced over a range of mounting stiffnesses. This type of behaviour was expected from similar experiments performed with gas bearings but is not fully supported by the present theoretical analysis. The calculated dynamic performance of the lubricating film derived from the test results, indicate that it is the same phenomena that is being observed at the two critical operating speeds. But further work is necessary to categorise the whirl cessation behaviour observed at operating conditions inbetween the two whirl onset speeds.

The steady state performance readings obtained from the test arrangement have shown the inadequacies of the type of displacement sensors used. But sufficient data was gathered to enable a reasonable correction to be made to the results. The corrected steady state performance indicates that at most running speeds the test bearings were operating at larger operating eccentricities than would be predicted by the Ocvirk solution. Closer agreement between theory and results was generally apparent for high speed low eccentricity running conditions, a behaviour also observed by White. This characteristic is consistent with the proposition that the bearings were running at various degrees of a starved condition.

The film properties derived from readings taken at whirl onset conditions, show that the test bearings demonstrated a poorer stability performance than both the Ocvirk performance predictions and recent test results published by other workers. This behaviour is also consistent with the proposition that the bearings were normally running in a partially starved condition. There was one exception to this trend for a bearing in the middle of the range of those tested. This one particular bearing demonstrated both steady state and dynamic behaviour much closer to the Ocvirk predictions than any of the other units tested. The results for this bearing were all obtained at low operating eccentricity values, but the behaviour observed must be due to a fundamentally different film extent rather than being a feature of low eccentricity operation.

In general both the critical stability parameters and the film dynamic stiffnesses calculated from the test results are up to a factor of six times less than the Ocvirk predictions. Both parameter values show a rapid rise as eccentricities at the high end of the operating range are reached. Although this pattern is predicted for the critical stability parameter, both the Ocvirk and long bearing solutions show that the film's dynamic stiffness should not exhibit such a increase. This discrepancy might be due to inaccuracies in measuring the natural and orbital frequencies of the system, since the equations used to calculate the film properties become ill-conditioned for the high

eccentricity test results. Since the calculations performed during the analysis of the readings did not show signs of becoming significantly ill-conditioned, the rise in the calculated value for the dynamic stiffness may be another effect of damping in the mounting structure.

In general the orbital frequency results also exhibit trends in keeping with both the long and short bearing performance predictions. Similarly the complex numbers describing the whirl orbits recorded also demonstrate trends predicted by the Ocvirk solutions.

Dividing the calculated film properties by the compressibility number, and multiplying by a function of length to diameter ratio produces a band of results at a level of about ten times less than the Ocvirk prediction. The film parameter values on these plots show signs of rising at the low eccentricity end of each bearing's operating whirl onset range. This may be due to the film being less starved of oil at higher operating speeds, which is also indicated by the form of the steady state results.

Two conclusions can be drawn from comparing the Ocvirk performance predictions with the results obtained by Akkok and Ettles, and the present series of tests. The first conclusion is that the present work used bearings operating in a partially starved condition which caused the poor observed stability

performance. The second conclusion is that the Ocvirk predictions modified to take into account the effects of length to diameter ratio, give a quick and reasonably accurate indication of stability performance for typical plain journal bushes, despite certain aspects of the theory being fundamentally incorrect.

The eddy current type of probe used in the work reported was chosen because it enabled a simpler test apparatus to be designed and testing to start sooner than if capacitance probes had been used. Some of the drawbacks of the inductive devices were overcome by the use of a data-logger, and a micro-computer to analyse the readings. As the results have indicated, more sensors were required in order to provide adequate compensation of temperature and elasticity effects. Further work using better distance measuring devices, such as capacitance types of sensor, will undoubtedly give more accurate positional information. But at the same time, interpretation of the results would benefit from using a different oil feed arrangement that more closely controls the extent of the lubricating film. This would enable a direct comparison to be made between experimental results and the performance predicted by current theories. Such a successful comparison would give greater confidence in the results obtained from test bearings representing typical bearing geometries.

References

1   Dowson,D., Godet,M., and Taylor,C.M.,
        'Cavitation and related phenomena in lubrication',
        Leeds-Lyon symposium on tribology, 1st, Leeds, 1974.

2   DuBois,G.B., and Ocvirk,F.W., 'Analytical derivation and
        experimental evaluation of short bearing
        approximation for full journal bearing', N.A.C.A.,
        Report 1157,1953.

3   Harrison,W.J., 'The hydrodynamical theory of lubrication
        of a cylindrical bearing under variable load, and of
        a pivot bearing', Trans.Camb.Phil.Soc., 1919,
        vol 22, p373'

4   Newkirk,B.L., and Taylor,H.D., 'Shaft whipping due to
        oil action in journal bearings', Gen.Elect.Rev.,
        1925, p559.

5   Cameron,A., 'Principles of lubrication', Longmans, 1966.

6   Morrison,D., 'Influence of plain journal bearings on the
        whirling action of an elastic rotor',
        Proc.Inst.Mech.Engnrs., 1962, vol 176, no 22, p452.

7   Holmes,R., 'The vibration of a rigid shaft on short sleeve
        bearings', J.Mech.Engng.Sci., vol 2, no 4,
        1960, p337.

8   Lamb,H., 'Hydrodynamics', Cambridge, 1932.

9   Brand,R.S., 'Inertia forces in lubricating films',
        Trans.Amer.Soc.Mech.Engrs., J.Appl.mech.,
        1955, 22E, pp363-364.

10   Taylor,G.I., 'The stability of a visoous liquid contained
between two rotating cylinders', Phil.Trans.Roy.Soc.,
1923, 223(Series A), p289.

11   Cole,J.A., 'Experiments on the flow in rotating annular
clearanoes', Proc.Lub.Wear.Conf., 1957, p 16
Inst.Mech.Engrs.,London.

12   Vohr,J.H., 'An experimental study of Taylor vortices and
turbulenoe in flow between eccentric rotating
cylinders', Trans.Amer.Soc.Mech.Engrs., J.Lube.Tech.,
vol 90, no 1, 1968, p285.

13   Fall,C., 'A theoretical model of striated film-rupture',
Trans.Amer.Soc.Mech.Engrs., J.Lube.Tech.,
vol 104, no 2, 1982, p164.

14   Etsion,I., and Ludwig,L.P., 'Observation of pressure
variation in the cavitation region of submerged
journal bearings', Trans.Amer.Soc.Mech.Engrs.,
J.Lube.Tech., vol 104, no 2, 1982, p157.

15   Swift,H.W., 'The stability of lubricating films in journal
bearings', J.Inst.Civ.Engrs, 1931, 233(pt1), 267.

16   Steiber,W., 'Das Schwimmlager', 1933, (Verein Deutscher
Ingenieurre, Berlin).

17   Floberg,L., 'On hydrodynamic lubrication with special
reference to sub-cavity pressures and number of
streamers in cavitation regions',
Acta.Polytech.Scandanavia, MES, vol 19, 1965.

18   Floberg,L., and Jakobsson,B., 'The finite journal
bearing considering vapourisation',
Trans.Chalmers.Univ.Tech., 1957, Gotenborg.

19   Olsson,K., 'Cavitation in dynamically loaded journal
bearings', Trans.Chalmers.Univ.Tech., 1965,
Gotenborg.

20   Taylor,C.M., 'Separation cavitation solutions for the
        infinite width cylinder plane and journal bearing
        configurations', J.Mech.Engng.Sci., vol 15, no 3,
        1973, p237.

21   Booker,J.F., 'A table of the journal-bearing inte gral',
        Trans.Amer.Soc.Mech.Engrs., J.Basic Engng,
        vol 87D, no 2, 1965, p533.

22   Marsh,H., 'The stability of aerodynamic gas bearings',
        Mech.Engng.Sci. Monograph No 2, Inst.Mech.Engrs,
        London, 1965.

23   Marsh,H. and Simmons,J.E.L., 'An experimental method for
        the determination of journal bearing stability
        parameters Part 1:Theory', J.Mech.Engng.Sci.,
        vol 21, no 3, 1979, p179.

24   Simmons,J.E.L., 'An experimental method for the
        determination of journal bearing stability
        parameters Part 2:Experiment', J.Mech.Engng.Sci.,
        vol 21, no 3, 1979, p187.

25   Cole,J.A., and Hughes,C.J., 'Oil flow and film extent
        in complete journal bearings', Proc.Inst.Mech.Engrs.,
        London, 1956, vol 170, p499.

26   White,D.C., 'Squeeze film journal bearing', Ph.D. thesis,
        Cambridge, 1970.

27   Jacobson,B.O, and Hamrock,B.J., 'High-speed motion
        picture camera experiments of cavitation in
        dynamically loaded journal bearings',
        Trans.Amer.Soc.Mech.Engrs.,
        J.Lube.Tech., vol 105, no 3, 1983, p446.

28   Holmes,R., 'Instability phenomena due to circular bearing
        oil films', J.Mech.Engng.Sci.,
        vol 8, no 4, 1966, p419.

29   Akkok,M., and Ettles,C.M.M., 'The onset of whirl
          instability in journal bearings of various bore
          shapes and groove sizes',
          Trans.Amer.Soc.Mech.Engrs.,
          J.Lube.Tech., vol 105, no 3, 1983, p342.

30   Mori,A., Okada,K., and Mori,H., 'A study of the stability
          of a lightly loaded plain cylindrical journal
          bearing', J.Japan.Soc.Lub.Engrs., no4, 1983, p39.

31   Brown,T.E., 'Dynamic loading of journal bearings',
          Ph.D. thesis, Durham, 1976.

TABLE 7.1

Cavitation Test Bearing Details

Bearing dimensions

Diameter	100 mm
Width	100 mm
Clearance ratio	0.01

Journal

material – aluminium

speed – 0 – 200 rpm

loads – fixed – 0 – 20 kgf

rotating – 0 – 7 kgf at 0 – 100 rpm

Bearing

material – perspex

geometry – flooded parts – plain cylinder

– drained parts – plain cylinder with

4.0 mm dia oil supply hole

speed – 0 – 50 rpm

TABLE 8.1

Stability Test Bearing Rotor

material	–	EN 58	
bore	–	50.95	mm
axial length	–	90.0	mm
outside diameter	–	100.0	mm
mass	–	7.336	kg

Stability Test Bearing Centrebodies

material – bronze

width	nominal clearance ratio	clearance	feed hole dia
mm	–	mm	mm
10.0	0.002	0.11	1.0
10.0	0.003	0.16	1.0
20.0	0.002	0.10	2.0
20.0	0.003	0.15	2.0
20.0	0.004	0.20	2.0
30.0	0.002	0.11	3.0
30.0	0.003	0.15	3.0
30.0	0.004	0.21	3.0
40.0	0.002	0.11	3.0

COORDINATE SYSTEM

SURFACE VELOCITY COMPONENTS

V_2 W_2

U_2

SURFACE 2

SURFACE 1

FILM THICKNESS

h

FLUID VELOCITY COMPONENTS

v w

u

y z

x

FILM COORDINATE SYSTEM

FIGURE 2.1

FIXED
REFERENCE
DIRECTION

θ

ϕ

ϕ_r

BEARING
SURFACE

JOURNAL
SURFACE

$c\epsilon$

ω_a

LINE OF
CENTRES

$\delta\phi$
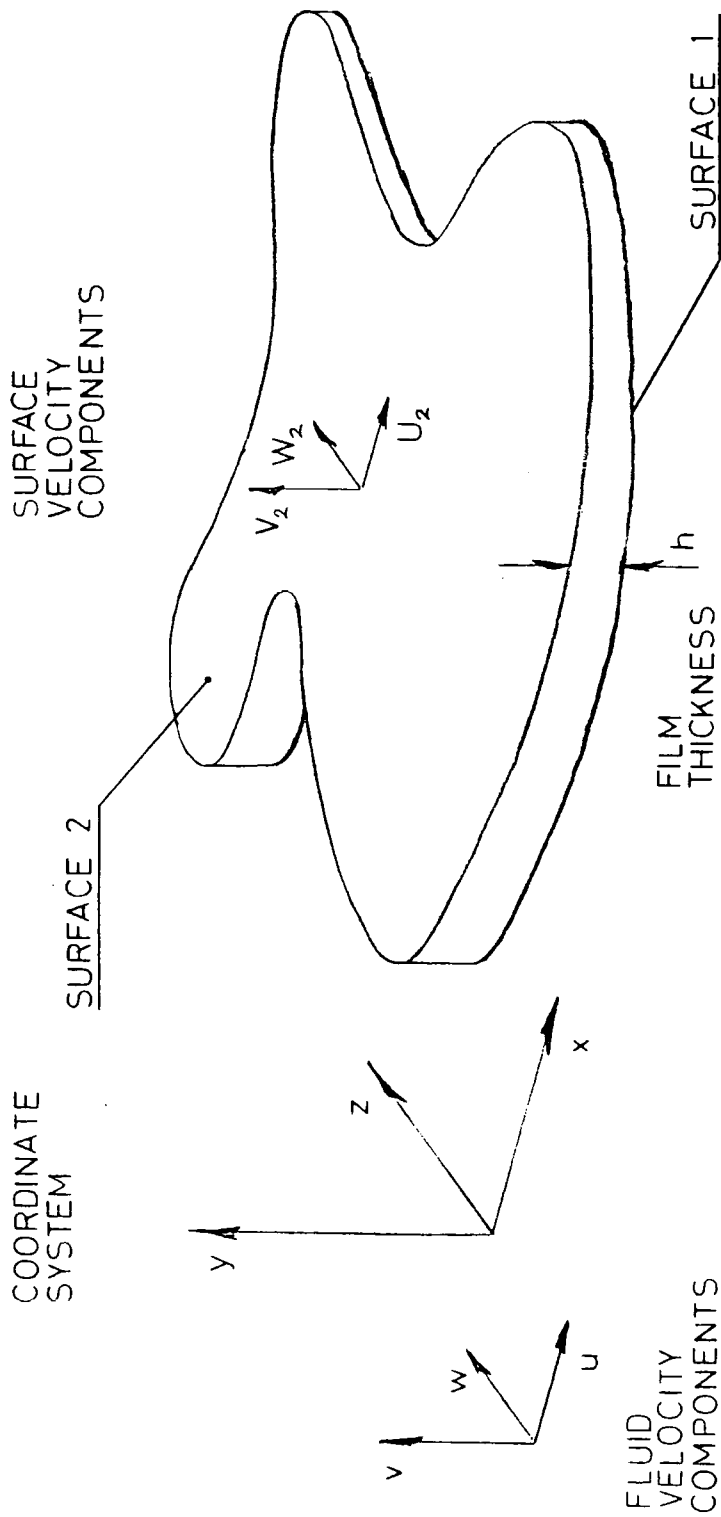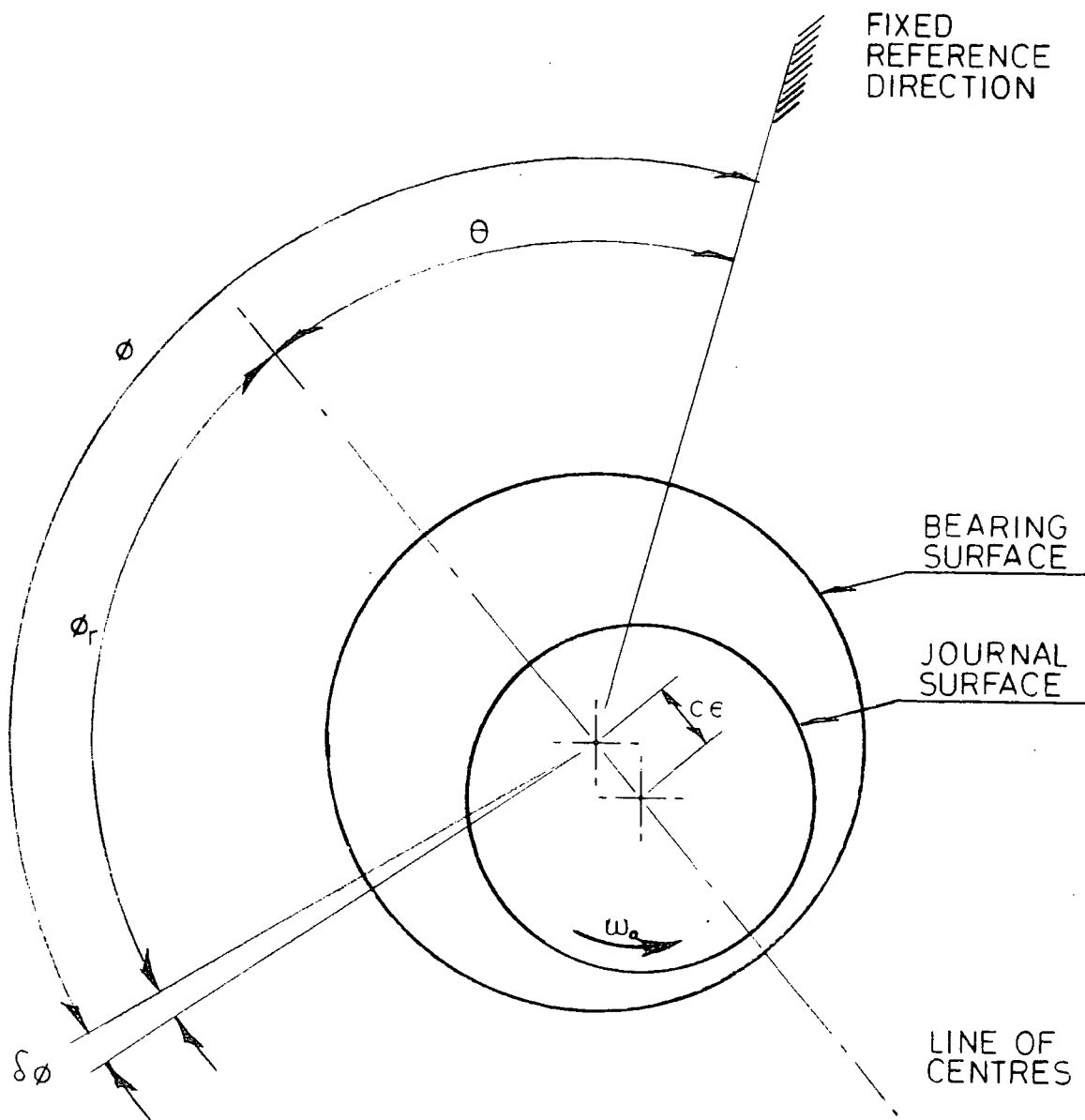
POLAR' COORDINATE SYSTEM

FIGURE 2.2

SIDE OF BEARING

CAVITIES

FORMATION
BOUNDARY

LUBRICANT
FILM

DIRECTION
OF MOTION

CAVITATION
BOUNDARY
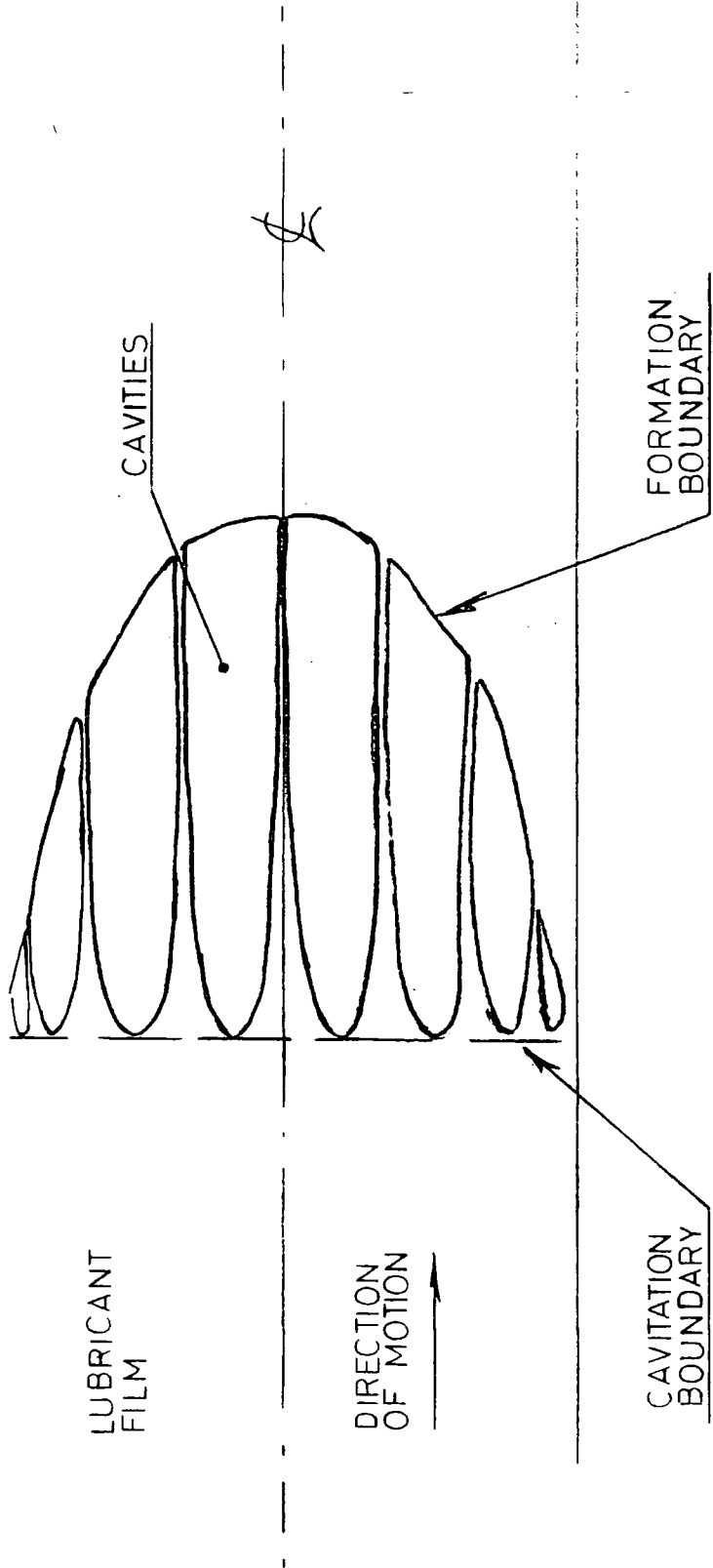
TYPICAL CAVITATION REGION

FIGURE 2.3

VELOCITY PROFILE

DIRECTION OF MOTION
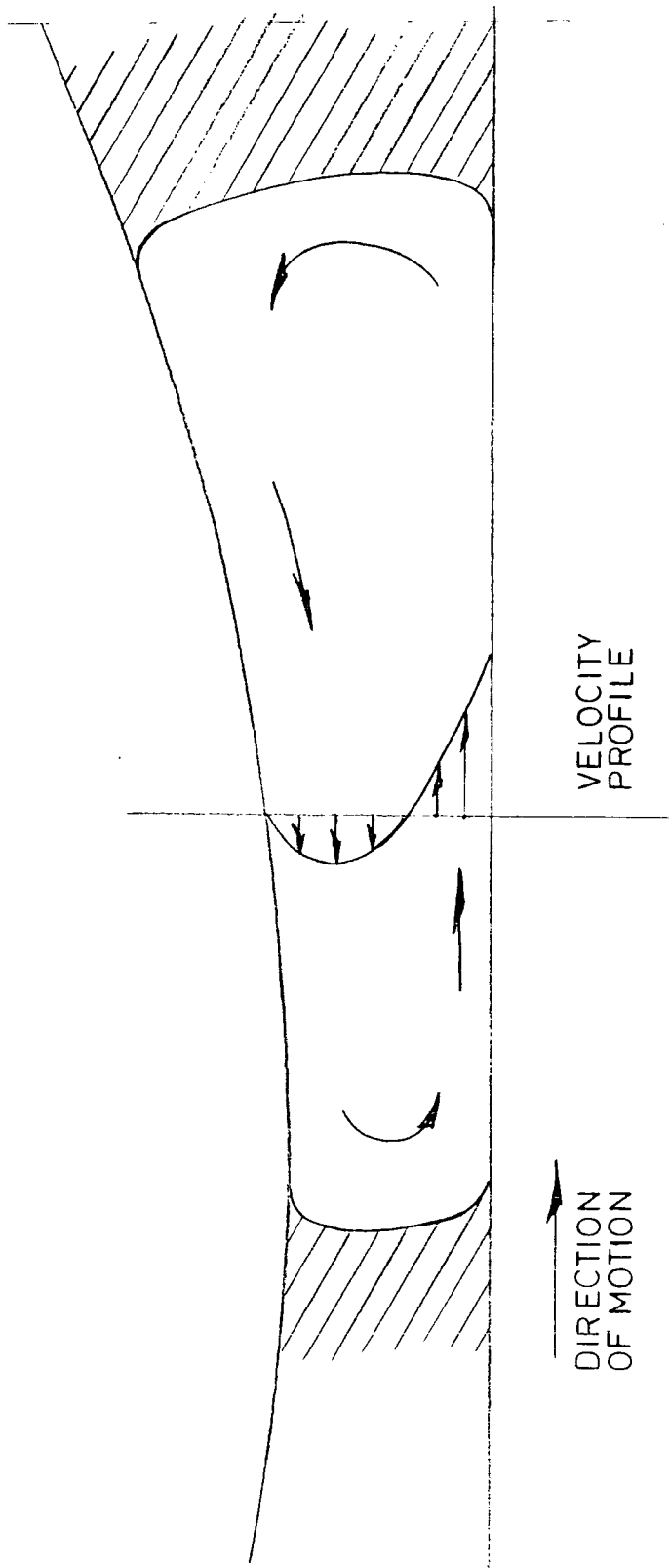
CAVITY FLUID CIRCULATION

FIGURE 2.4
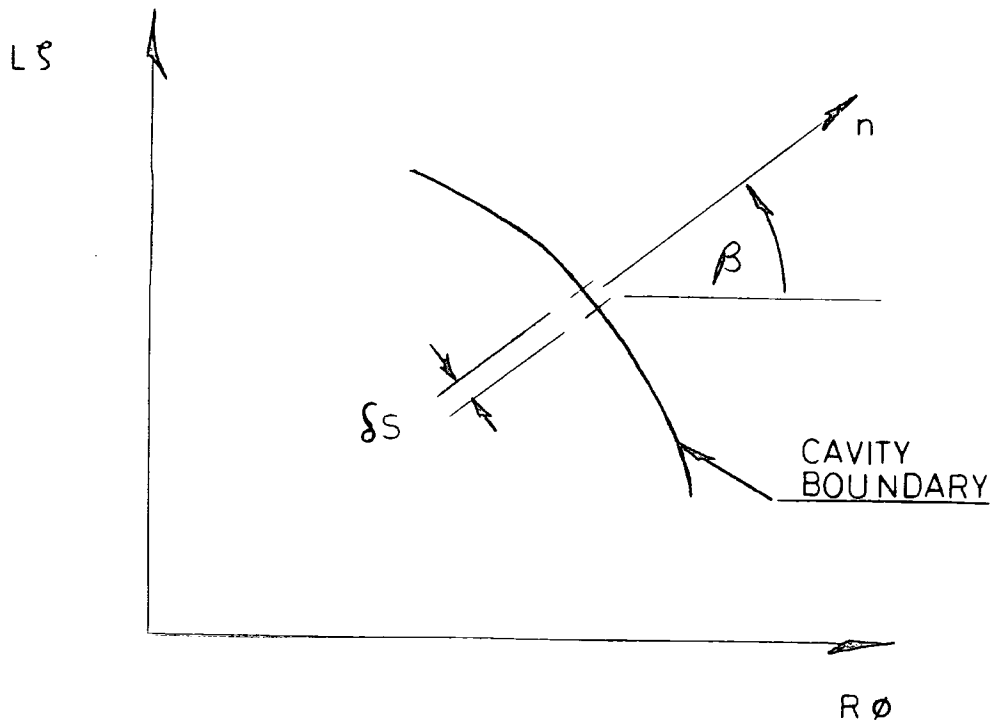
FILM – CAVITY
BOUNDARY ELEMENT

FIGURE 2.5
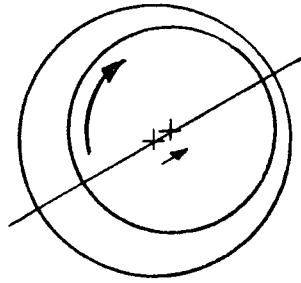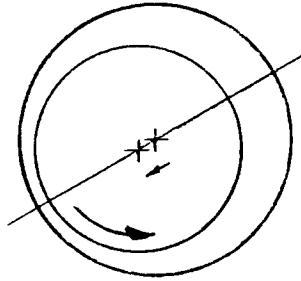
REFERENCE
SYSTEM

NEGATIVE
ECCENTRICITY

NEGATIVE
ROTATION
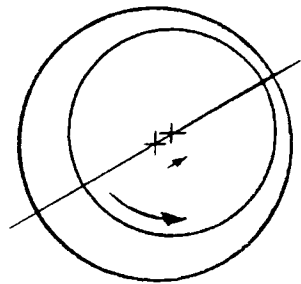
CONGRUENT BEARING SYSTEMS

FIGURE 3.1
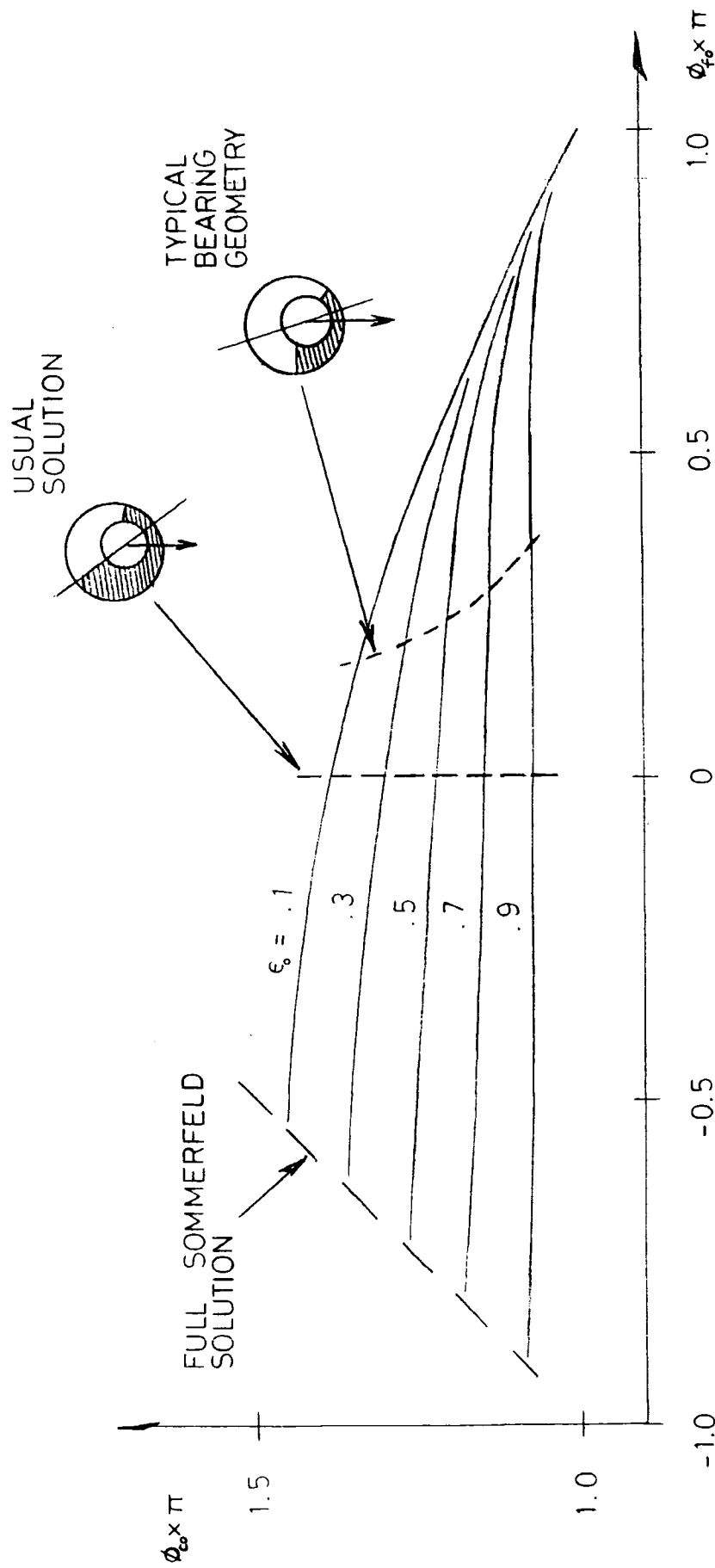
CAVITATION BOUNDARY ANGLES

LONG BEARING STEADY STATE

FIGURE 3.2

PRESSURE DISTRIBUTIONS

LONG BEARING STEADY STATE
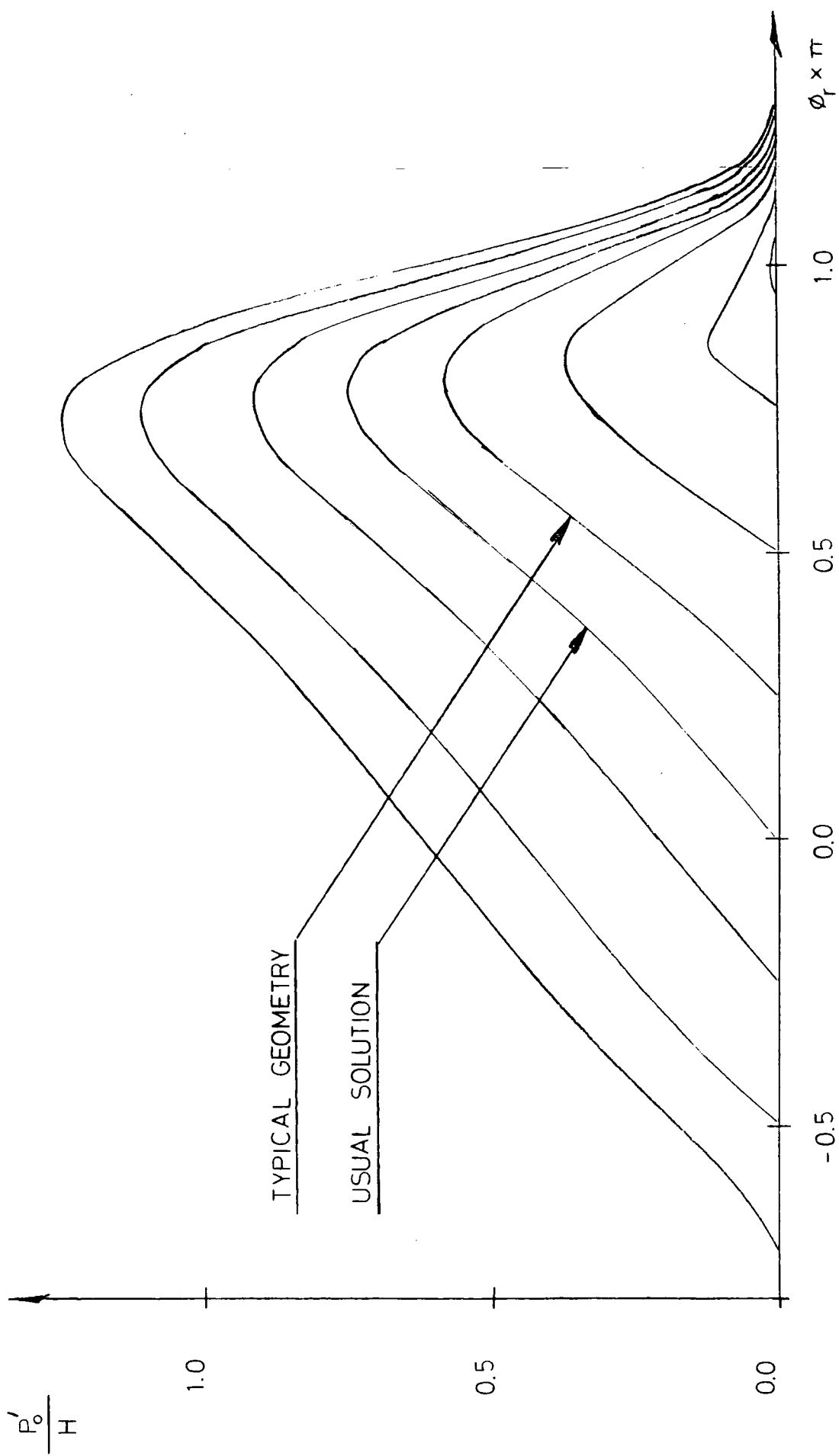
TYPICAL GEOMETRY

USUAL SOLUTION

$\frac{P_o'}{H}$

$\phi_r \times \pi$

FIGURE 3.3

FIGURE 3.4

CENTRE-LINE PRESSURE DISTRIBUTION

COMPUTED

SOMMERFELD LONG BEARING
OCVIRK SHORT BEARING

SYMBOL	L/D
□	0.1
△	0.25
○	0.5
+	1.0
•	2.0
◄	4.0
■	10.0

$\epsilon_o = 0.5$

$$\frac{P_o'}{H} \left[\frac{1 + (L/D)^2}{(L/D)^2} \right]$$

$\phi_r \times \pi$
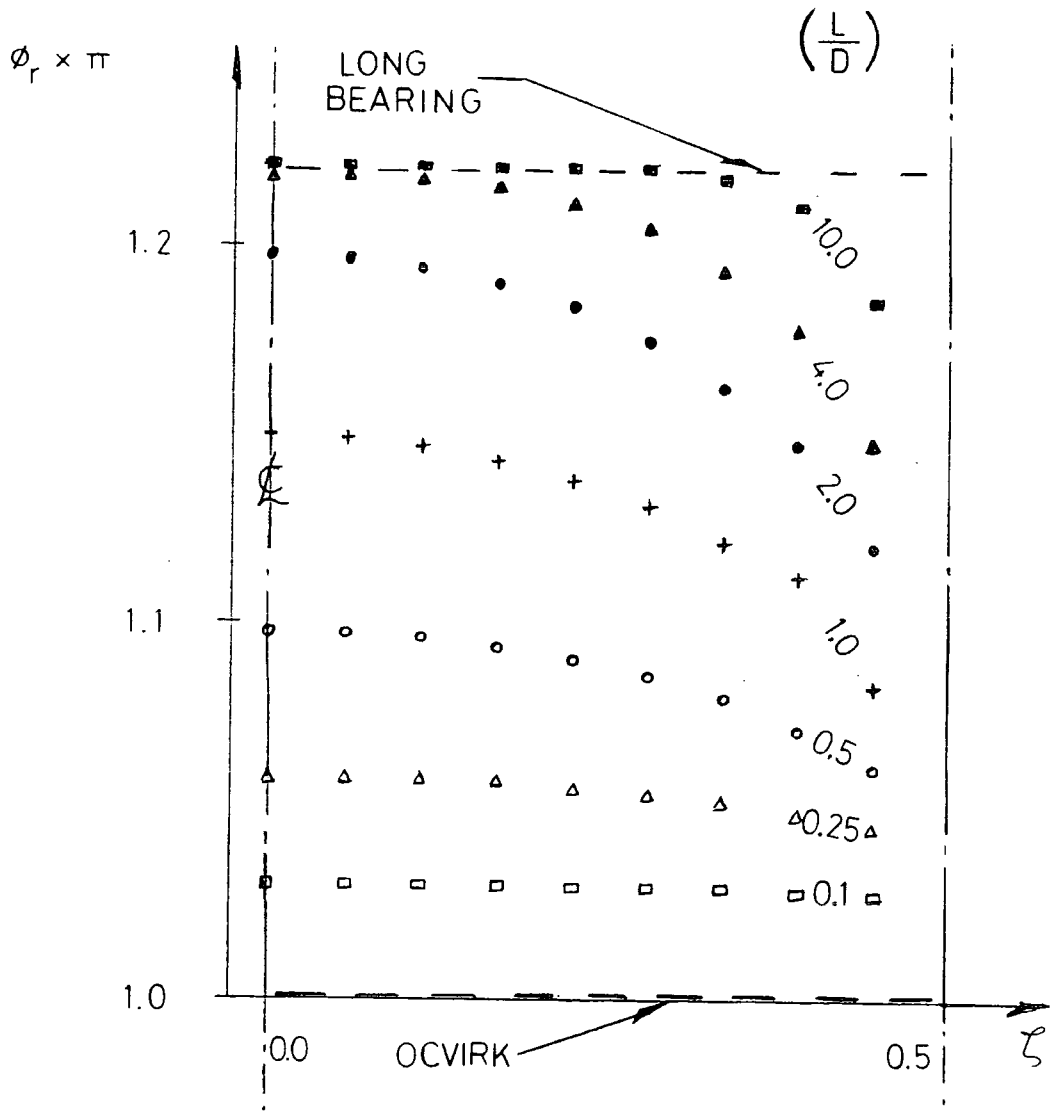
CAVITATION BOUNDARY LOCATION

COMPUTED

FIGURE 3.5
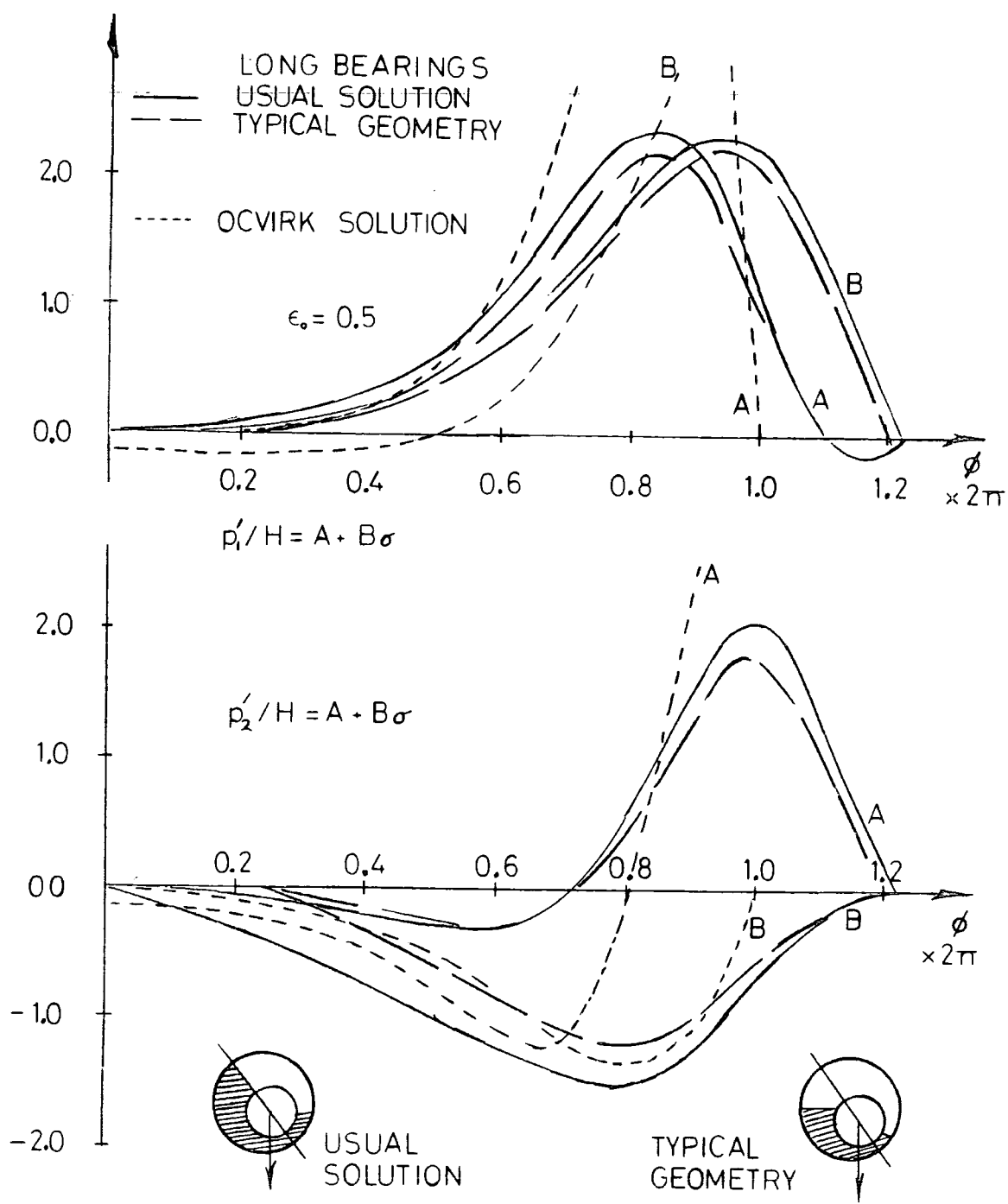
DYNAMIC PRESSURE
FIELD PROFILES

FIGURE 4.1
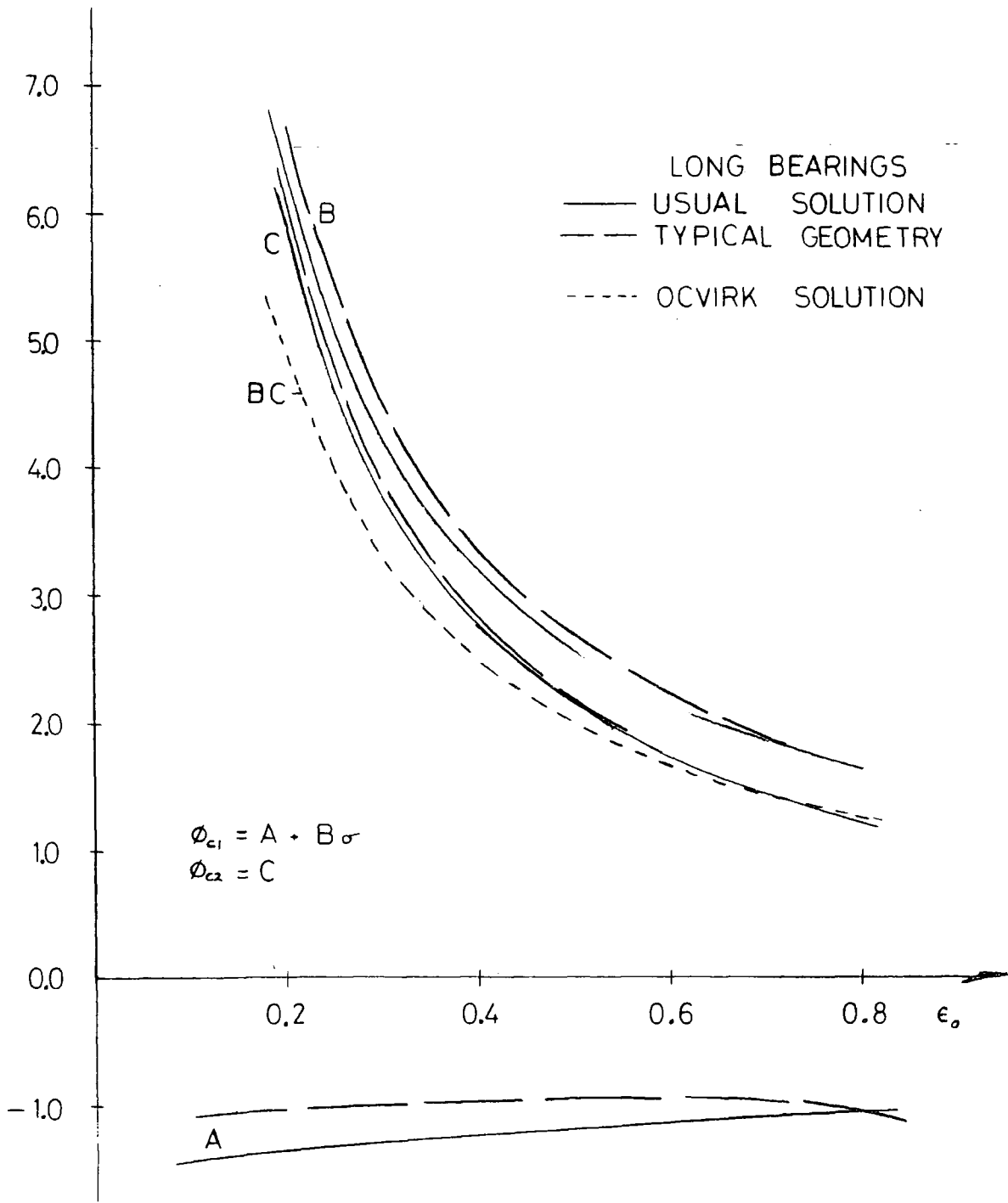
CAVITATION BOUNDARY
MOVEMENT PARAMETER

FIGURE 4.2

FIXED REFERENCE
DIRECTION AND
STEADY STATE
LINE OF CENTRES

θ

ϵ

r

s

ω_o

INSTANTANEOUS
JOURNAL
POSITION

STEADY STATE
JOURNAL POSITION
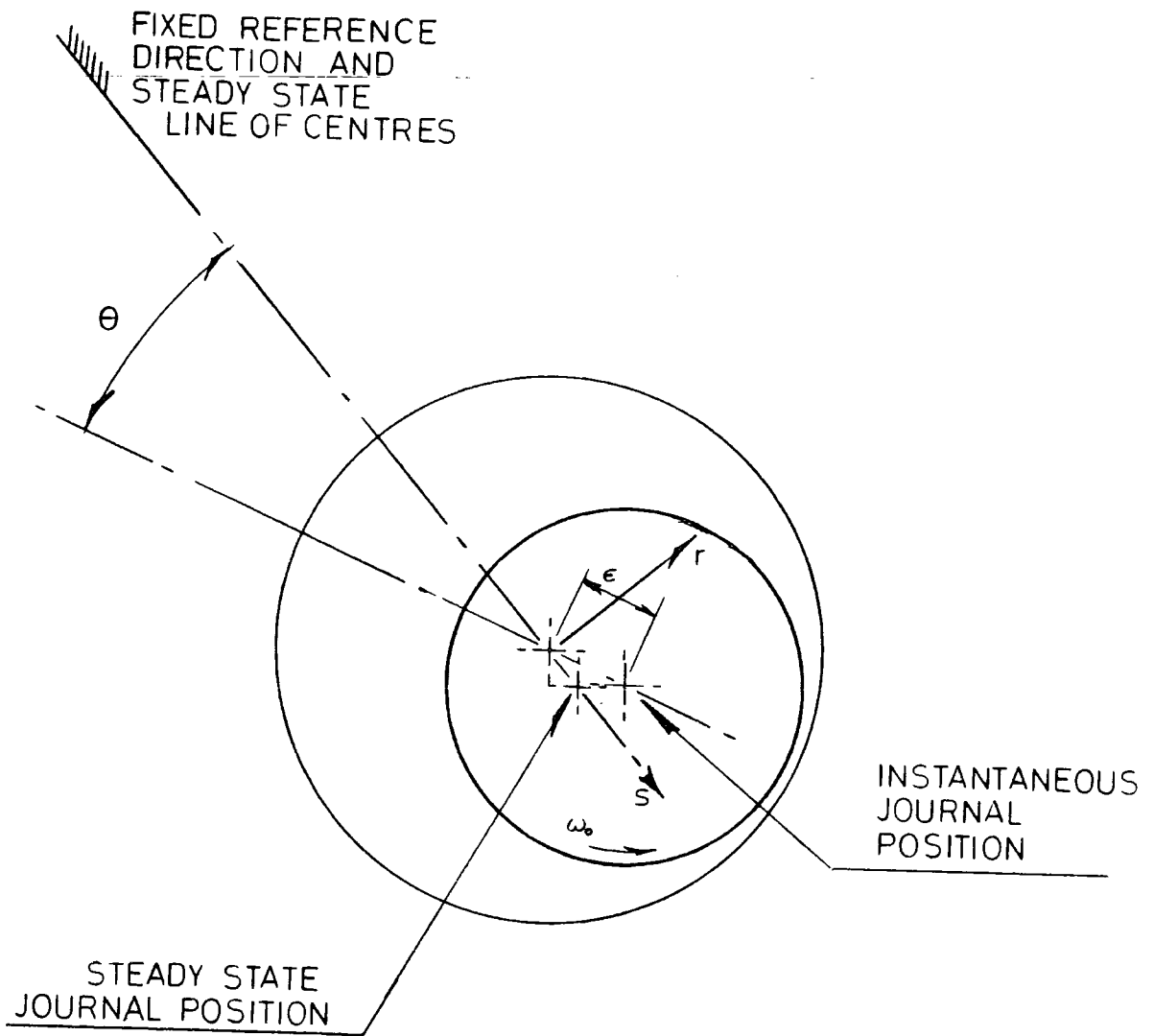
DYNAMICS COORDINATE SYSTEM

FIGURE 5.1
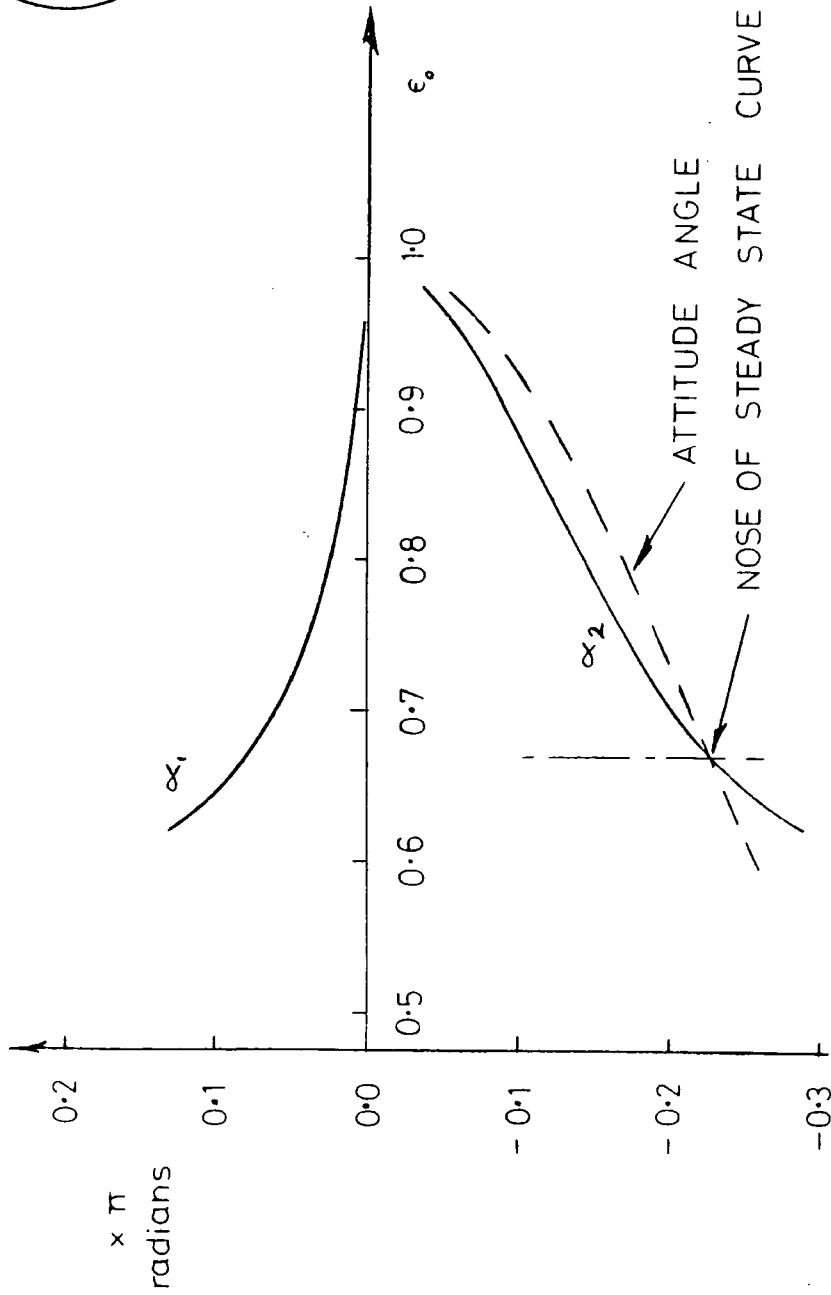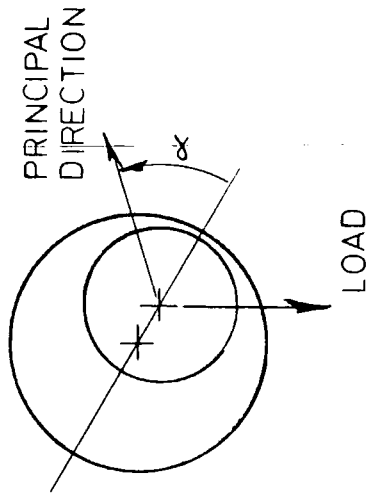
PRINCIPAL DIRECTIONS OF LOADING

(THEORETICAL — OCVIRK)
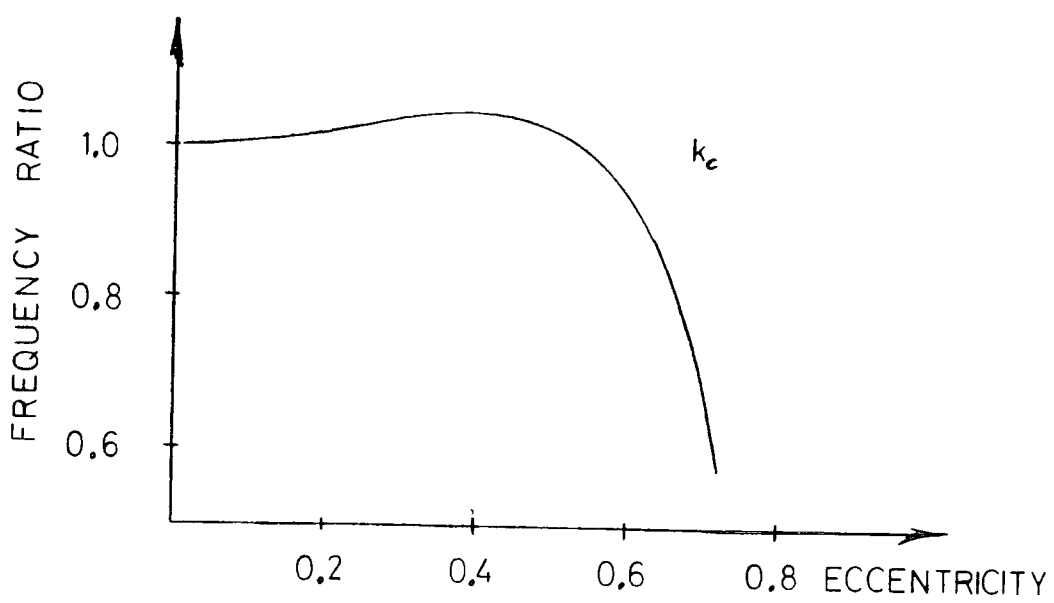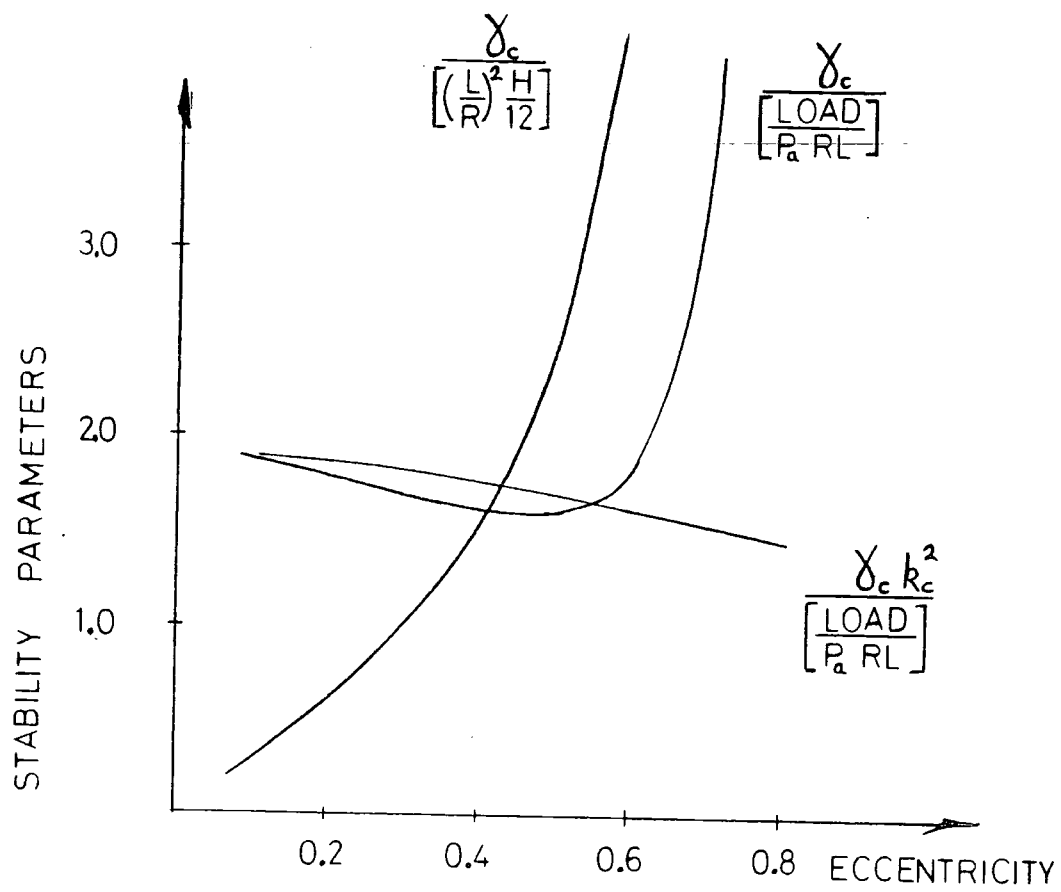
FIGURE   5.2

SHORT BEARING
CRITICAL FILM PARAMETERS

FIGURE 5.3
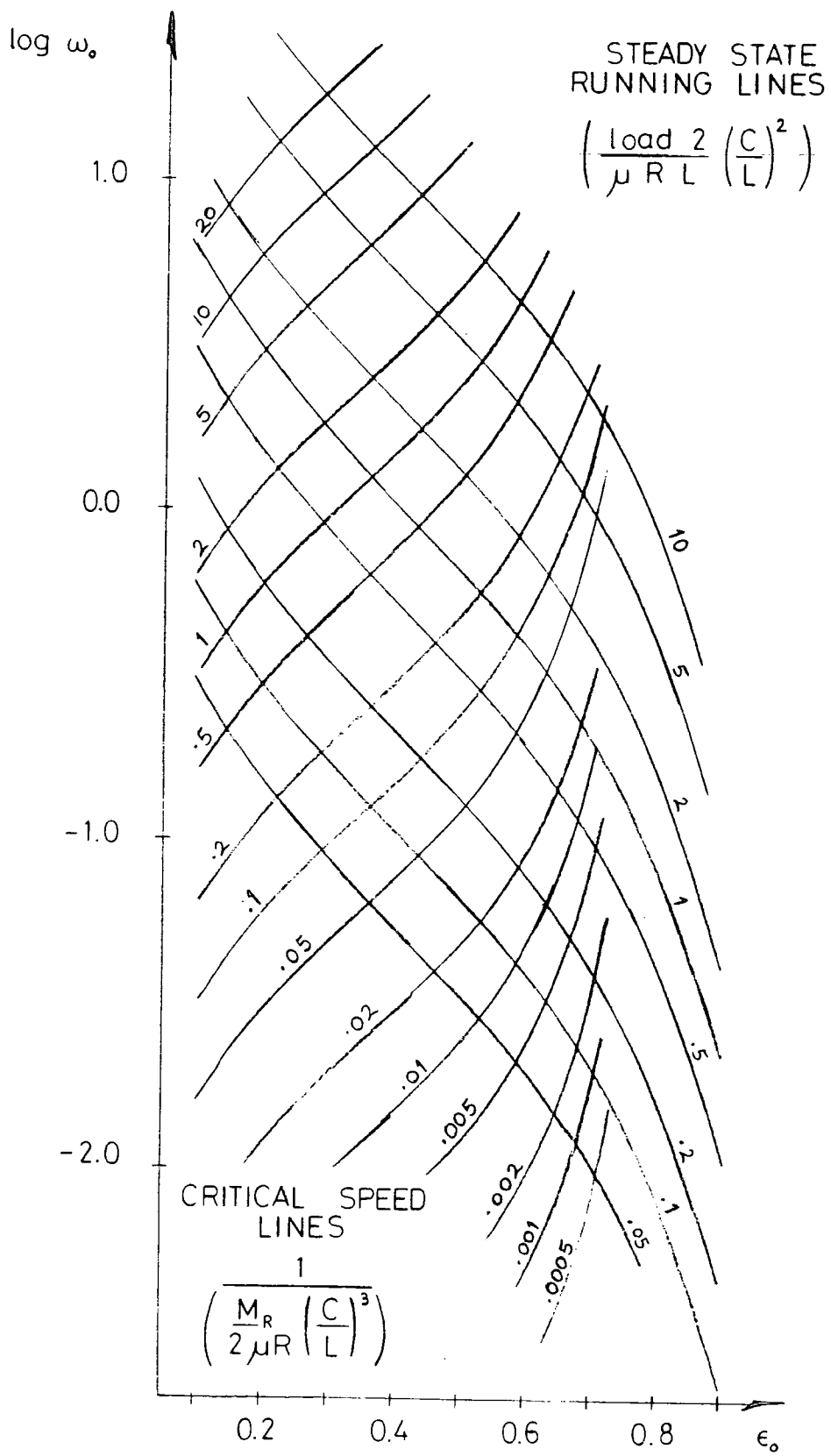
OCVIRK STABILITY PLOT

FIGURE 5.4
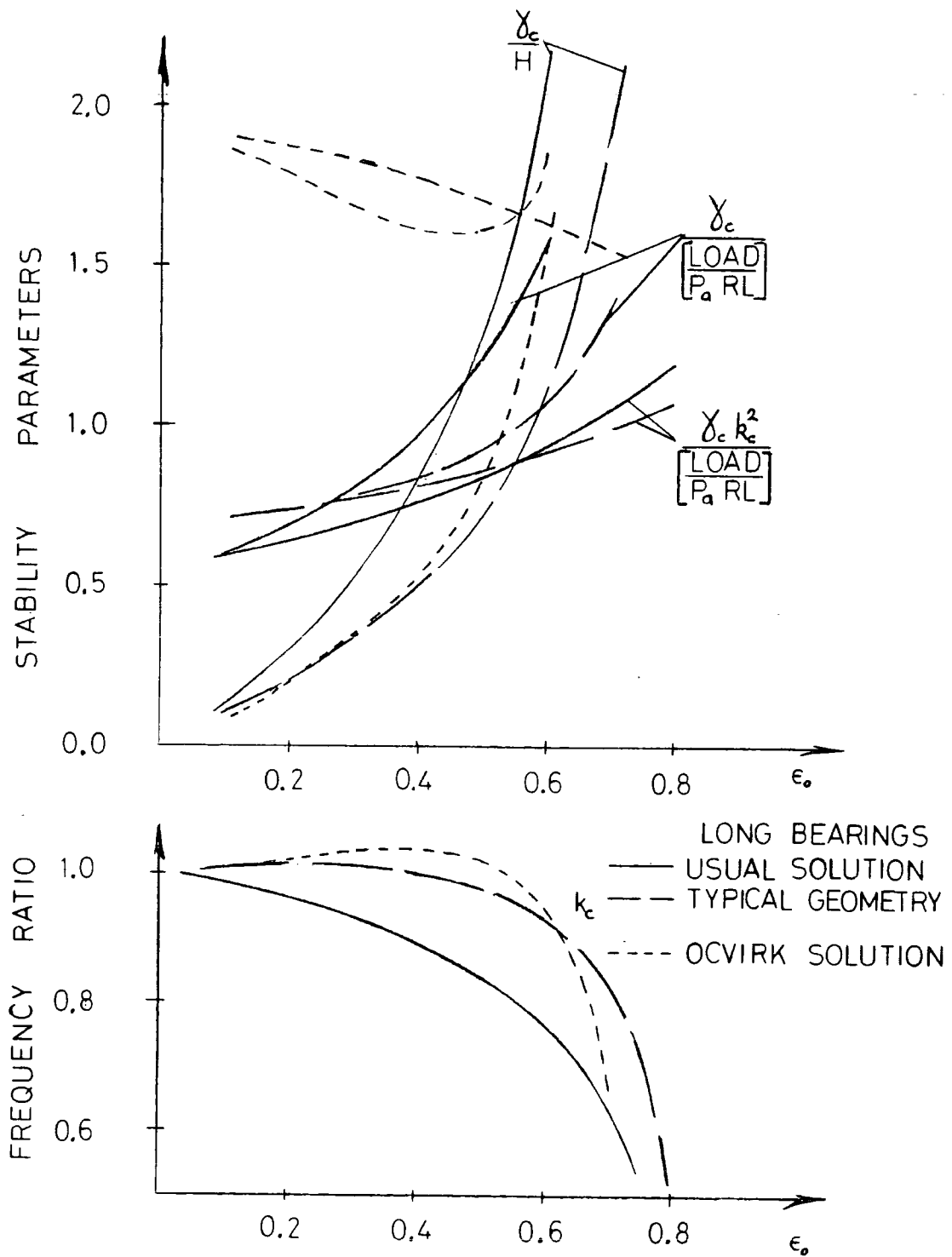
LONG BEARING
CRITICAL FILM PARAMETERS

FIGURE 5.5
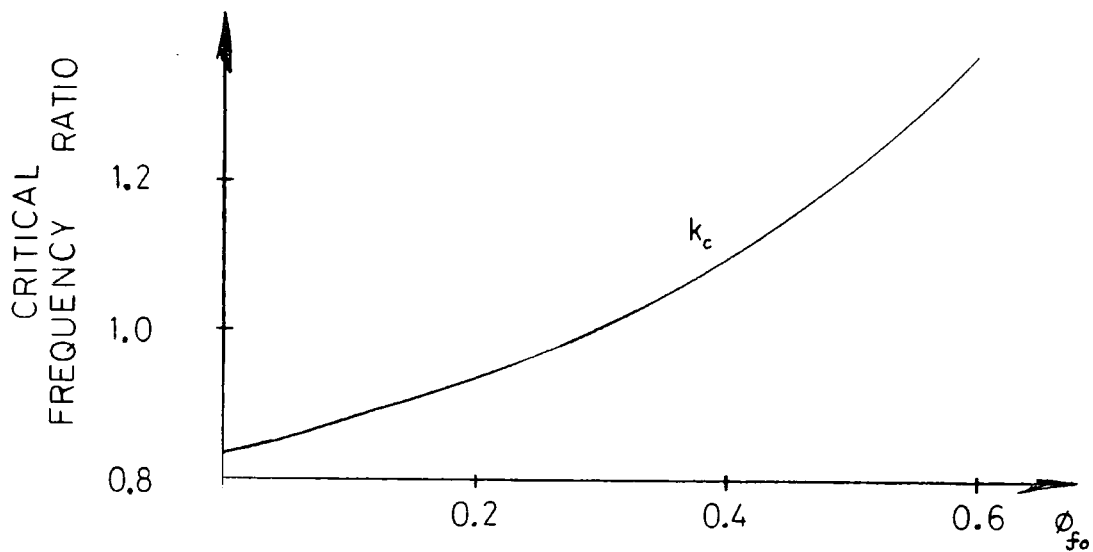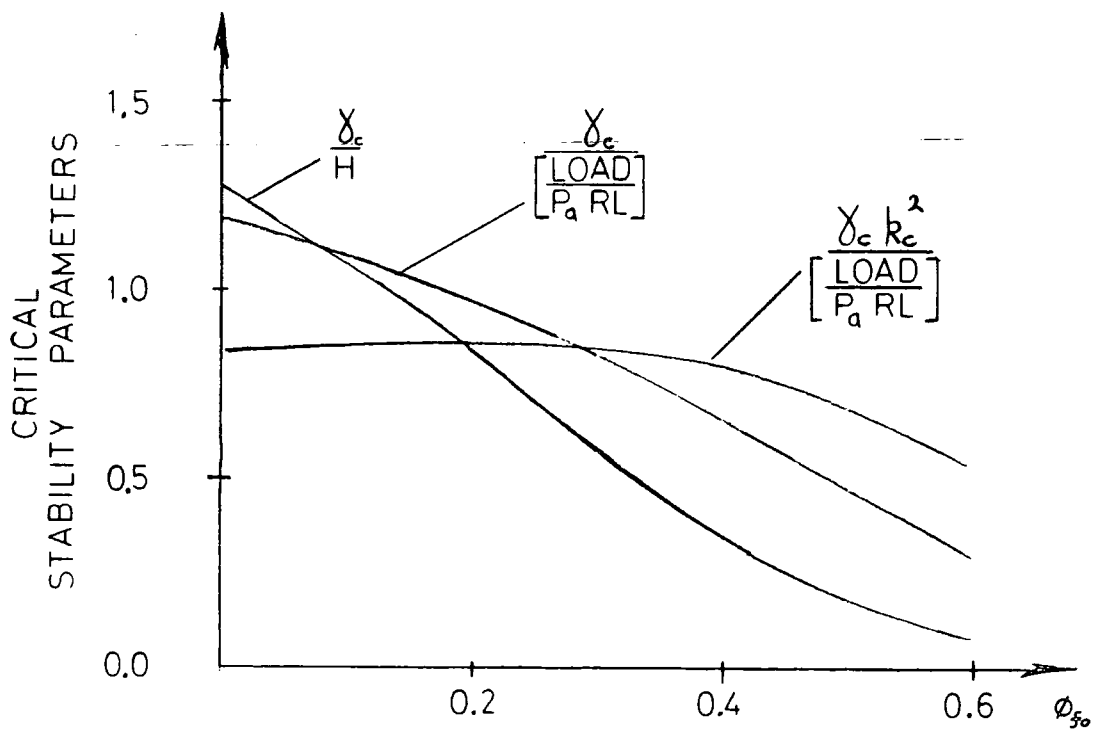
EFFECT OF FILM
FORMATION ANGLE

FIGURE 5.6

γ

STABILITY   PARAMETER

SECOND WHIRL ONSET BOUNDARY

$\gamma_c \dfrac{(M_B + M_R)}{M_B}$

γ_c

FIRST WHIRL ONSET BOUNDARY

MOUNTING   STIFFNESS
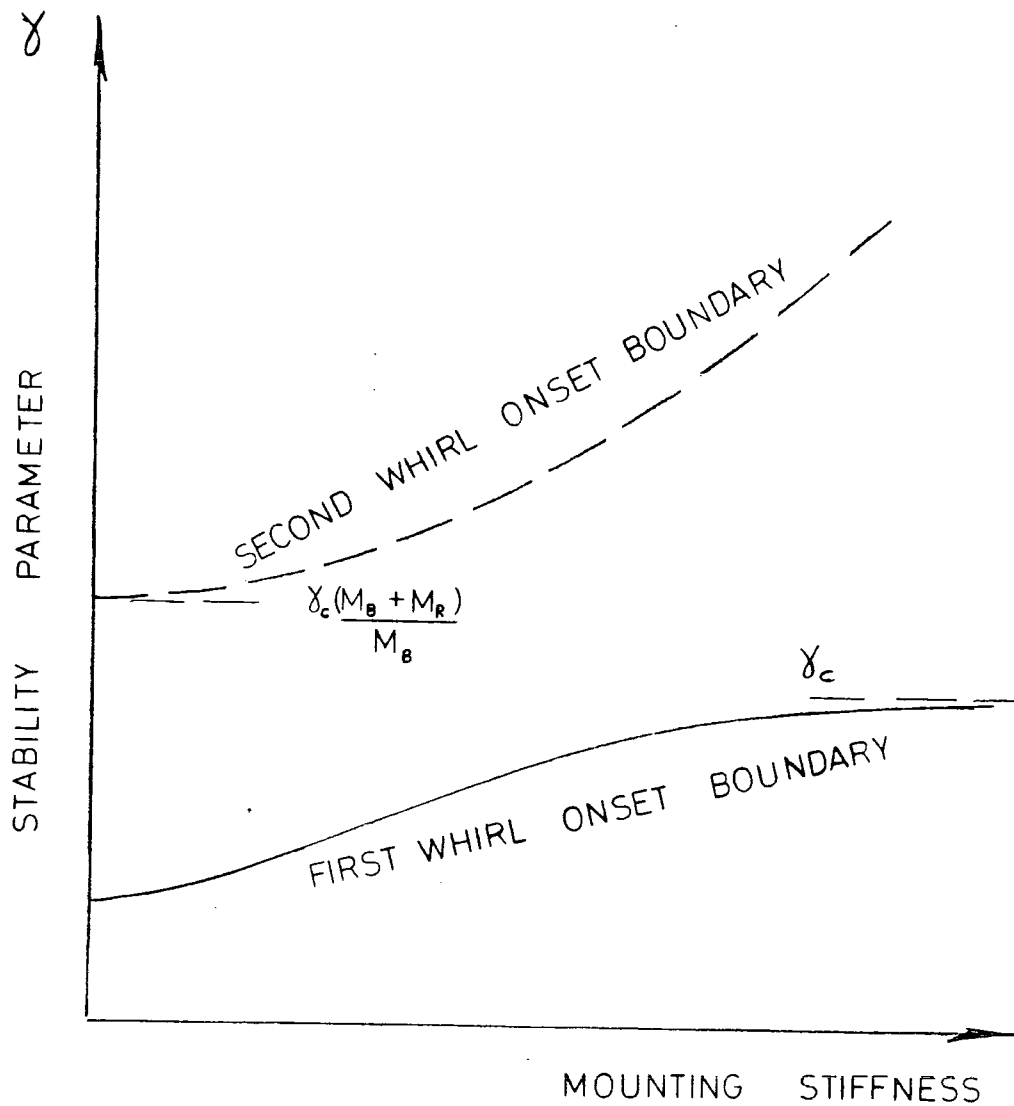
COMPUTED   BEHAVIOUR
USING   LINEAR   MODEL

FIGURE 6.1
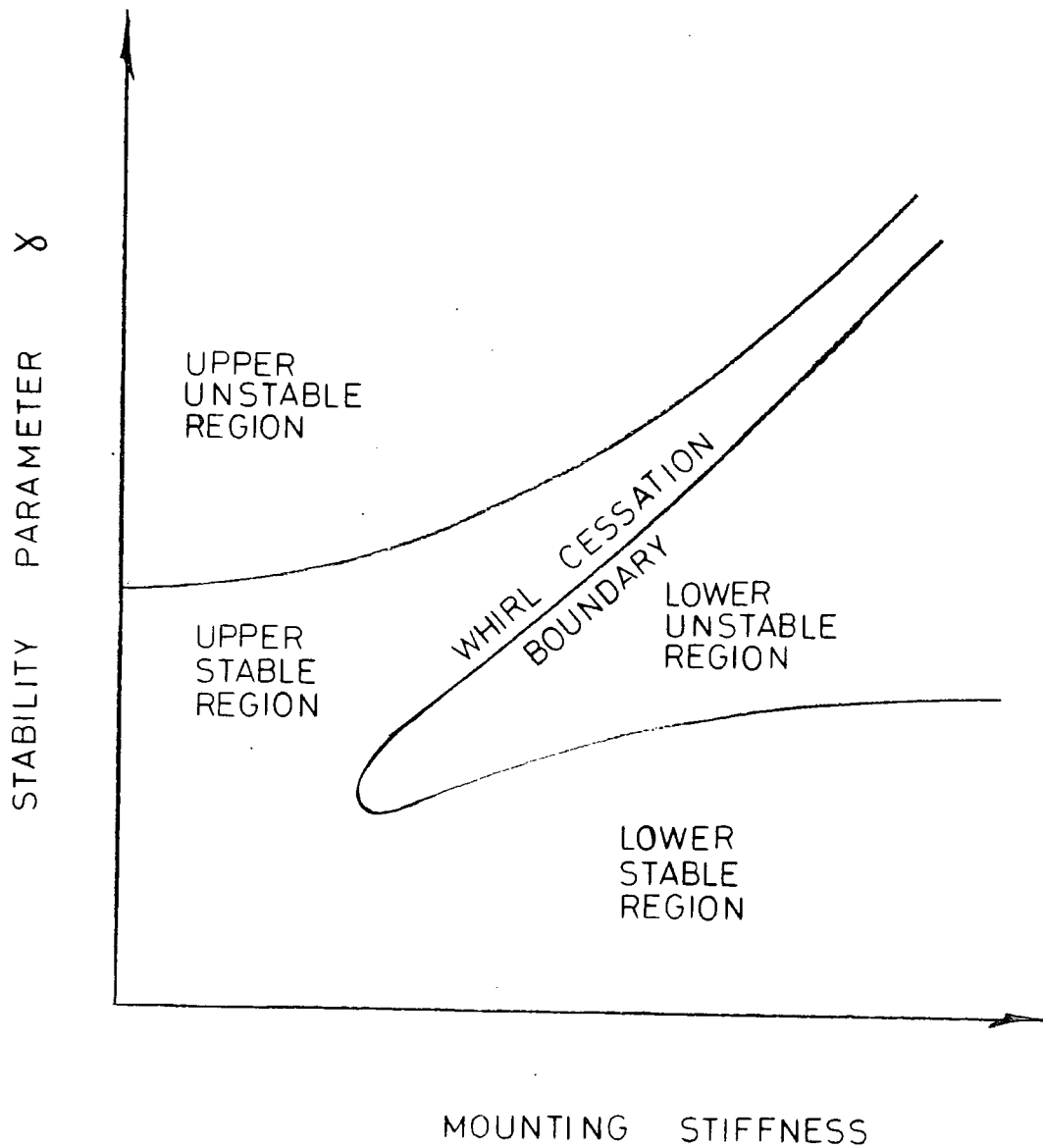
TYPICAL STABILITY RESULTS

FIGURE 6.2
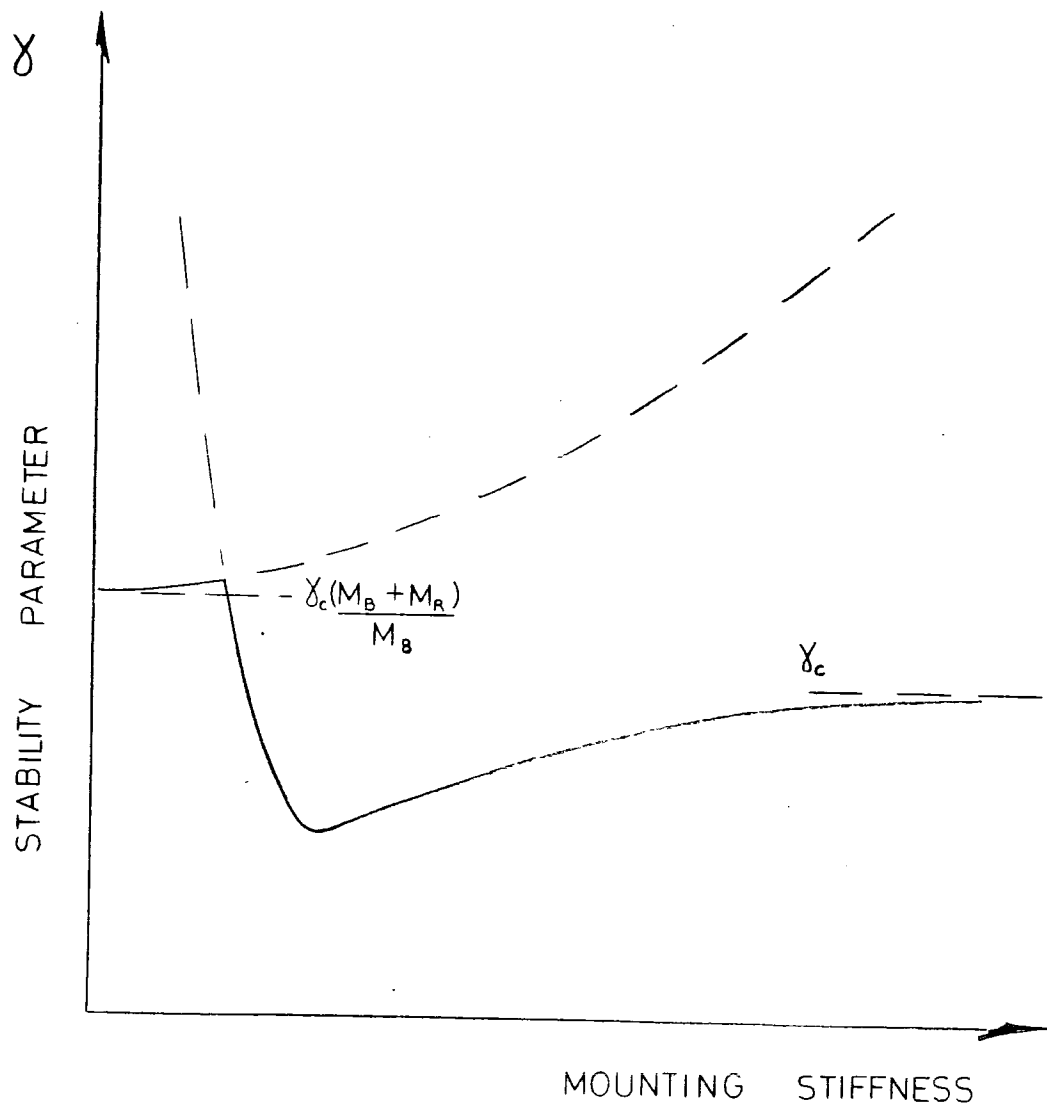
COMPUTED BEHAVIOUR
WITH MOUNTING DAMPING

FIGURE 6.3

CAVITATION
TEST ASSEMBLY

FLOODED CONFIGURATION
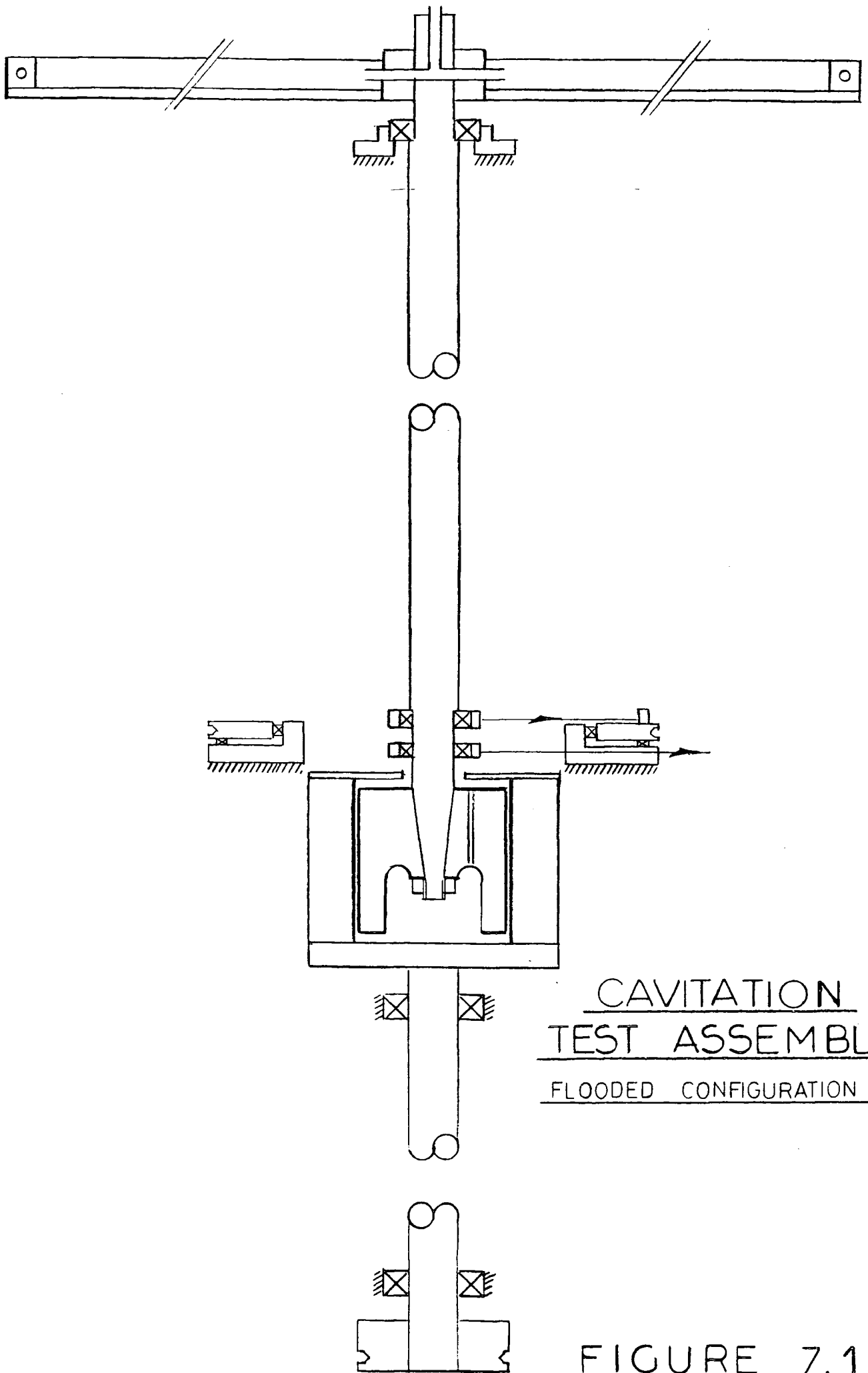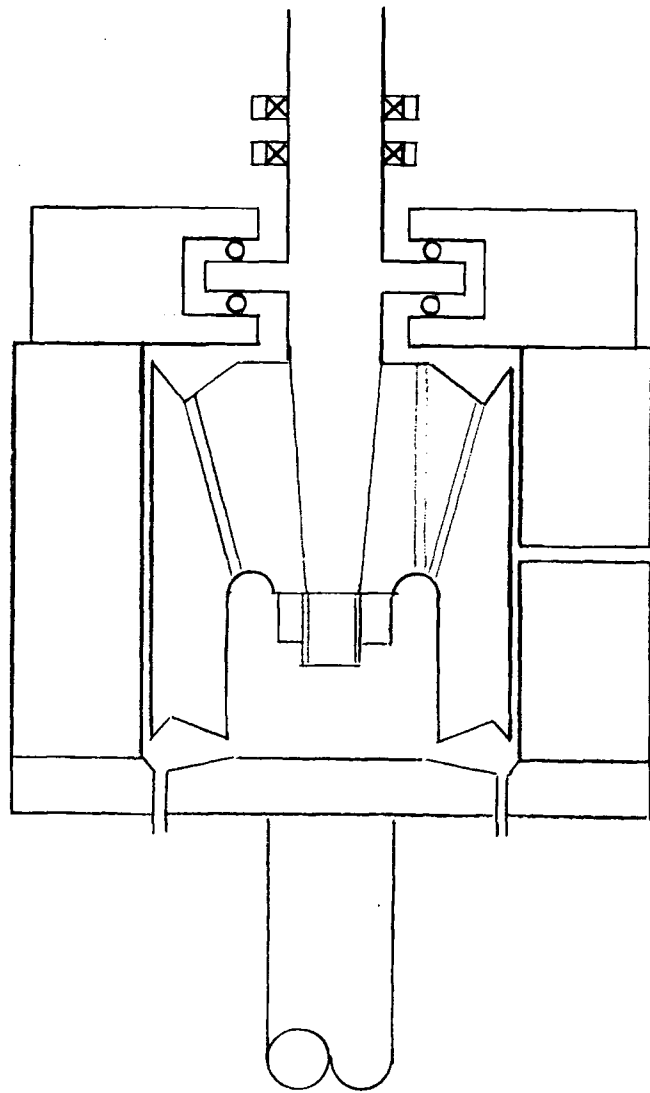
FIGURE 7.1

CAVITATION TEST BEARING

DRAINED   CONFIGURATION

FIGURE 7.2

LOAD
LINE

0

LOAD 12 Kg

π radians

RPM

¢

BEARING SIDE

2

5

10

20

30

40

CAVITATION APPEARANCE

FLOODED OPERATION

FIGURE 7.3

STREAMER
GENERATION

CAVITY
FLUID
TRANSFER

STREAMER
LOSS

TIME

SURFACE
MOTION

PRESSURE FIELD
MOVEMENT
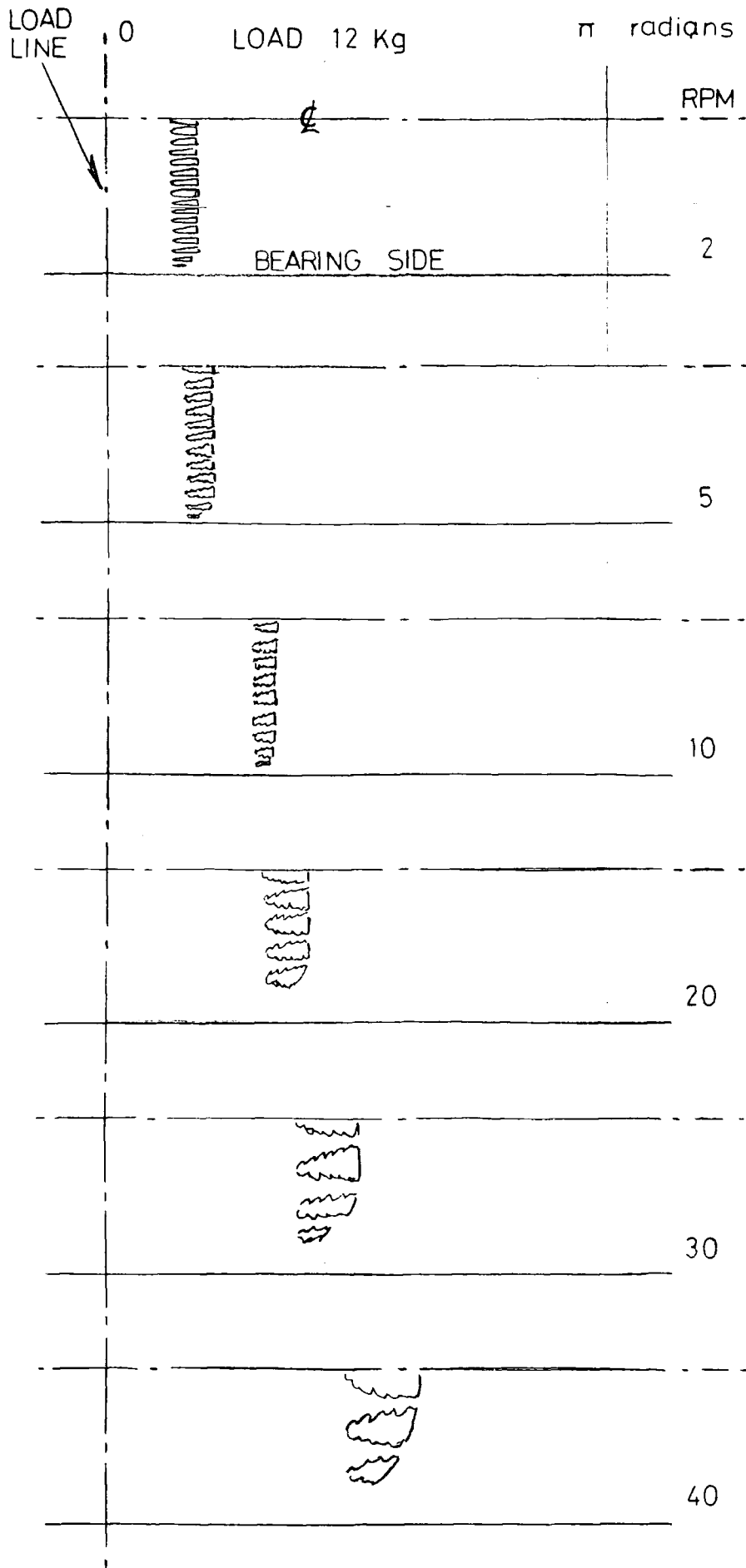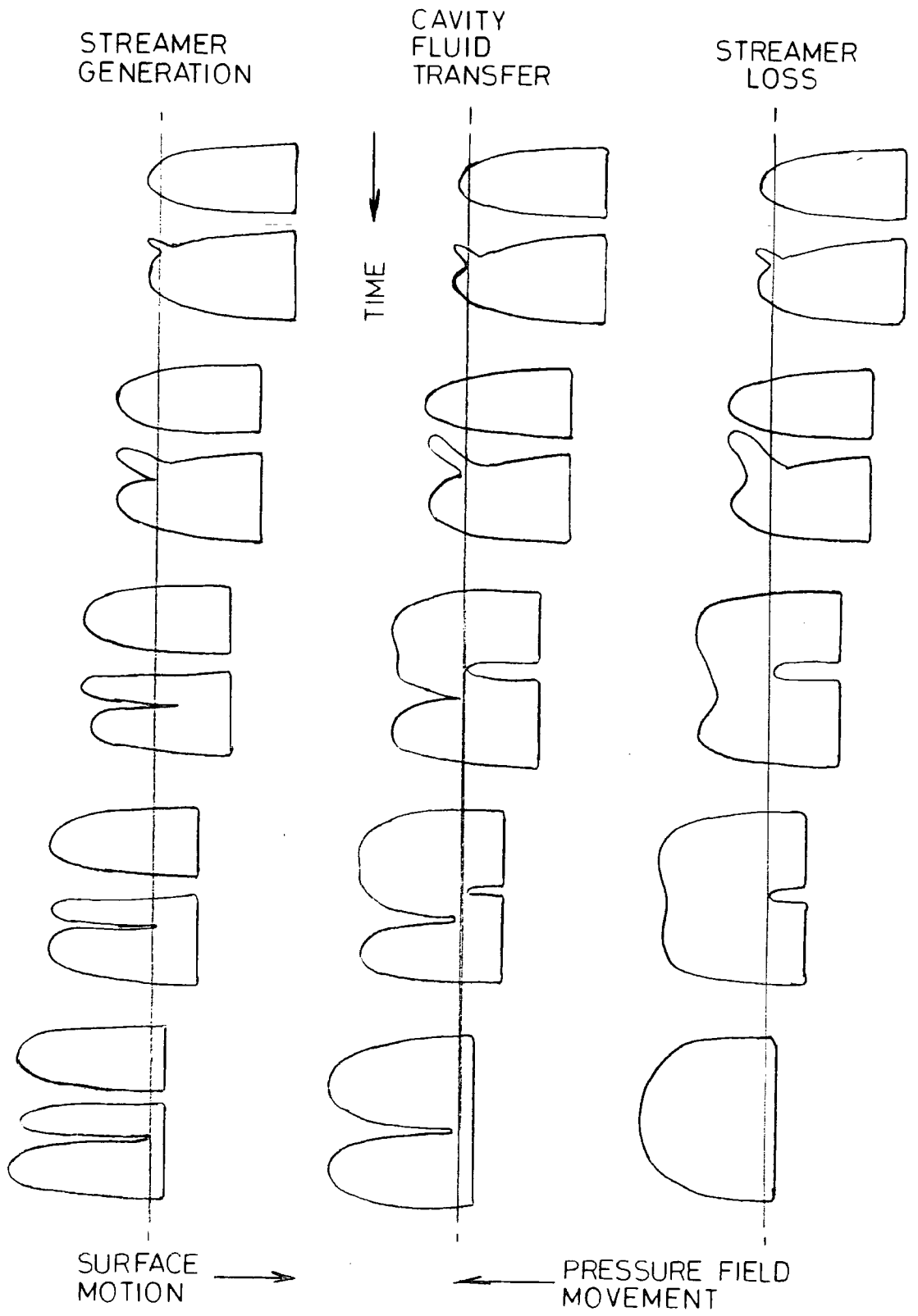
DENDRITIC ACTION

FIGURE 7.4
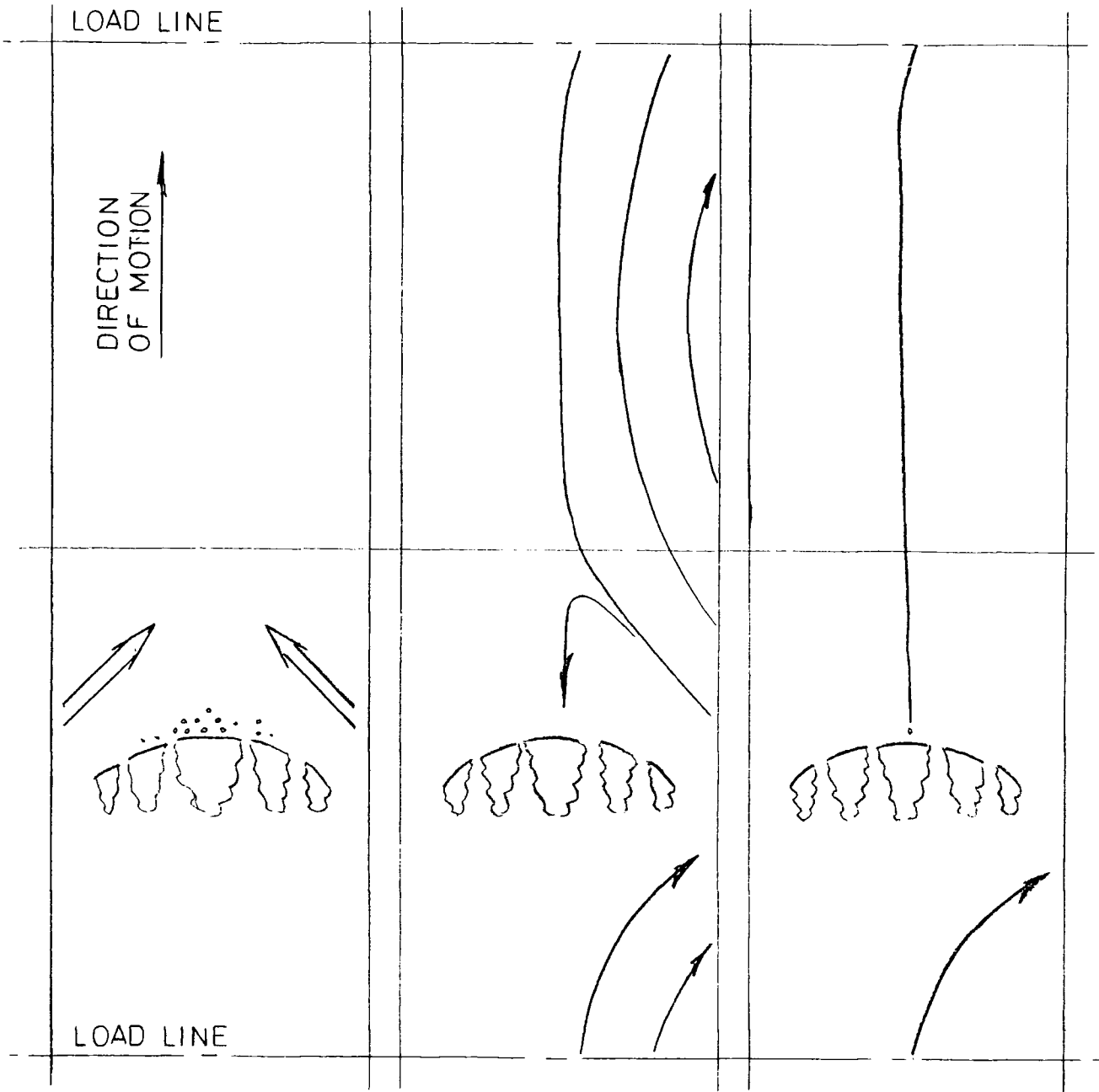
OIL FLOW FEATURES

FIGURE 7.5
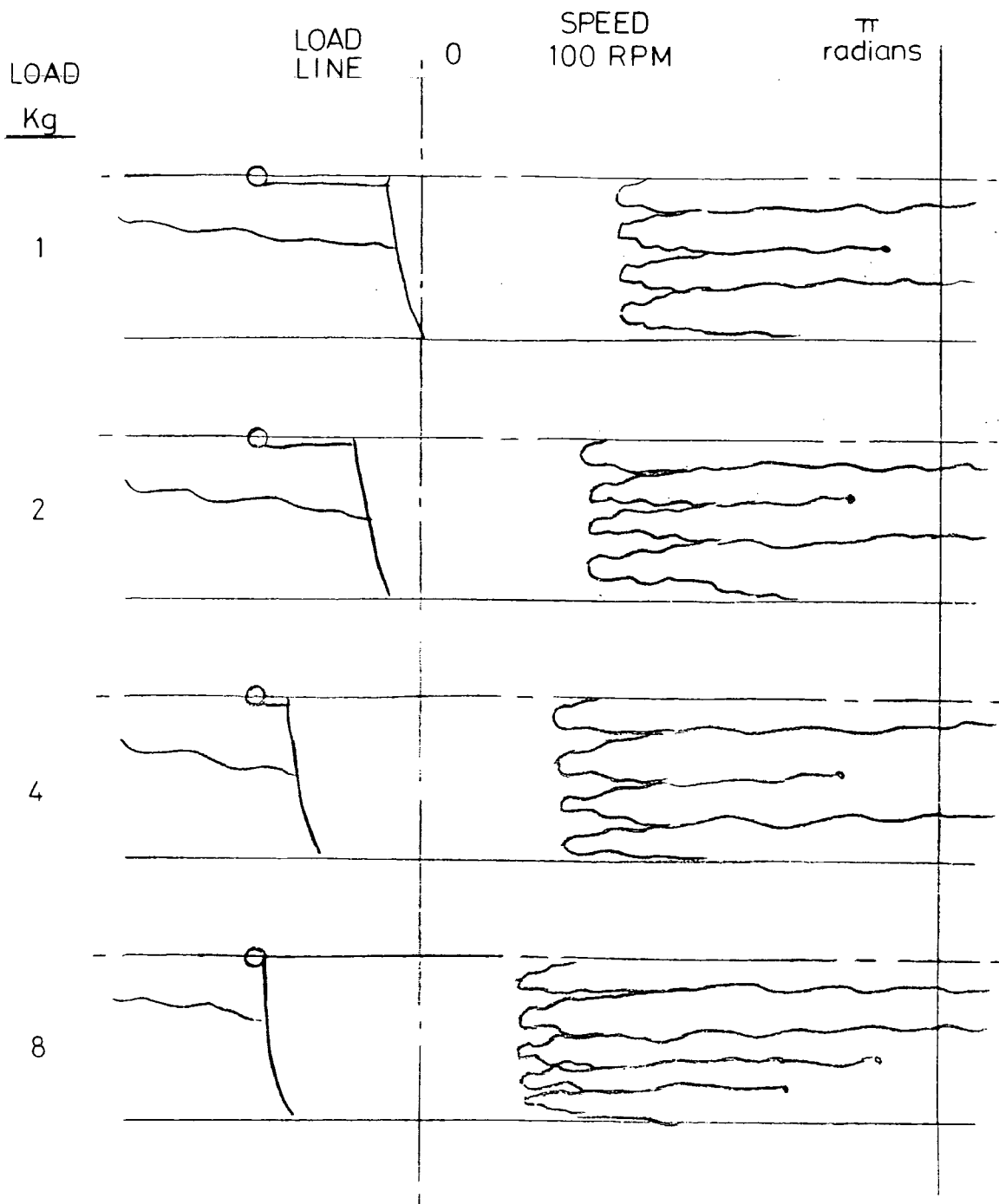
CAVITATION APPEARANCE

DRAINED OPERATION

FIGURE 7.6

LOAD
LINE   0   π radians
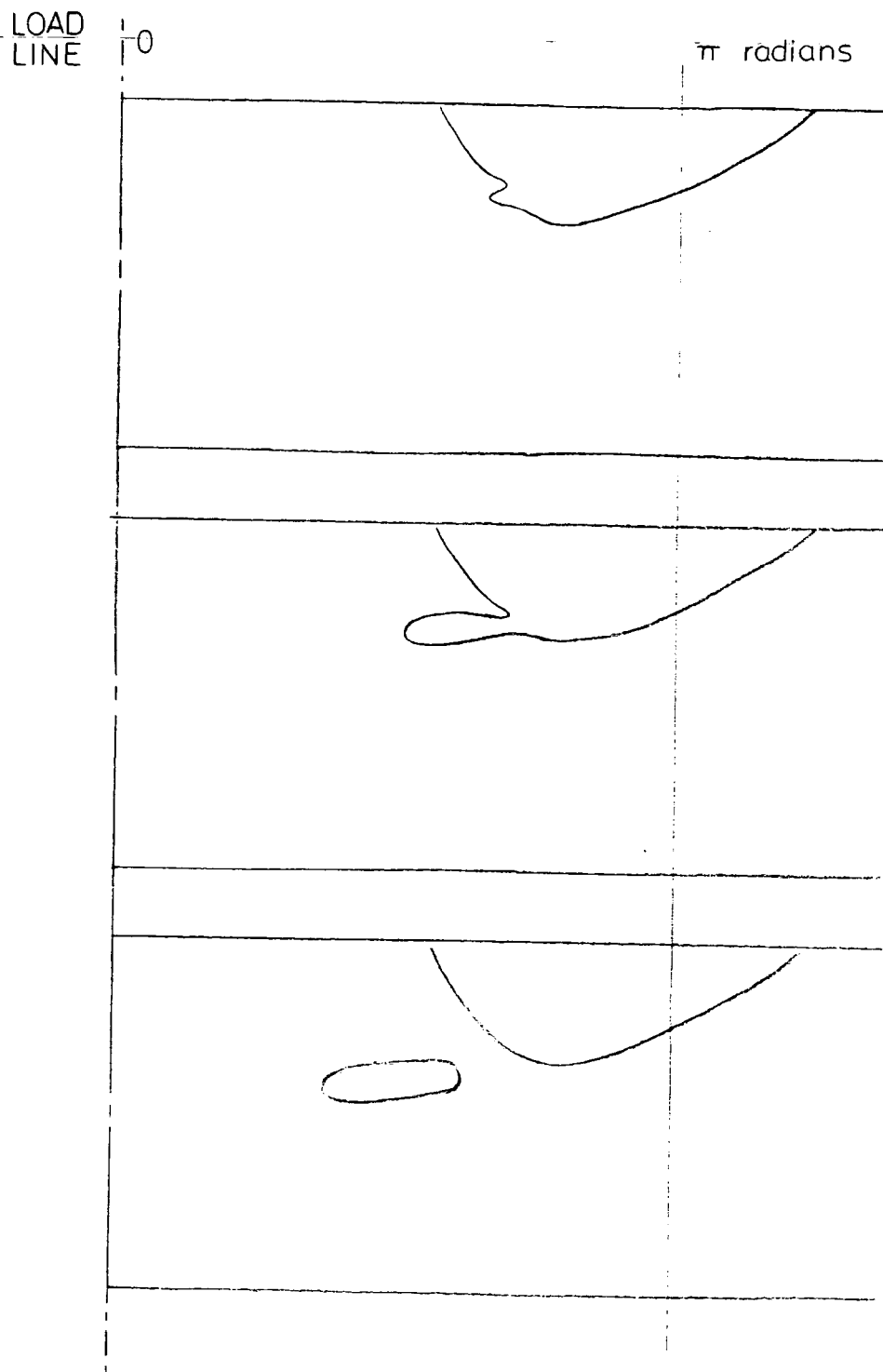
CAVITATION   BOOSTING

FIGURE   7.7
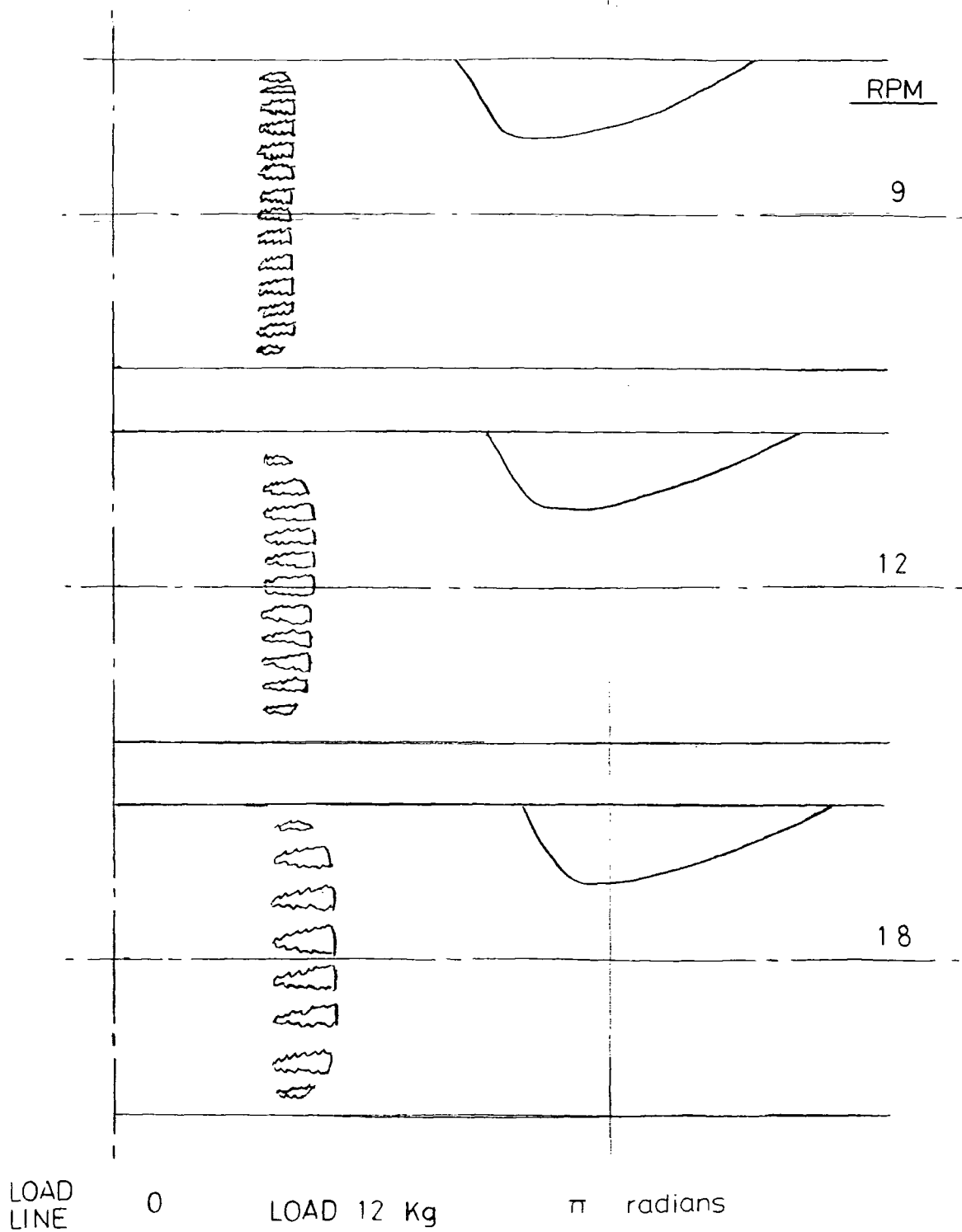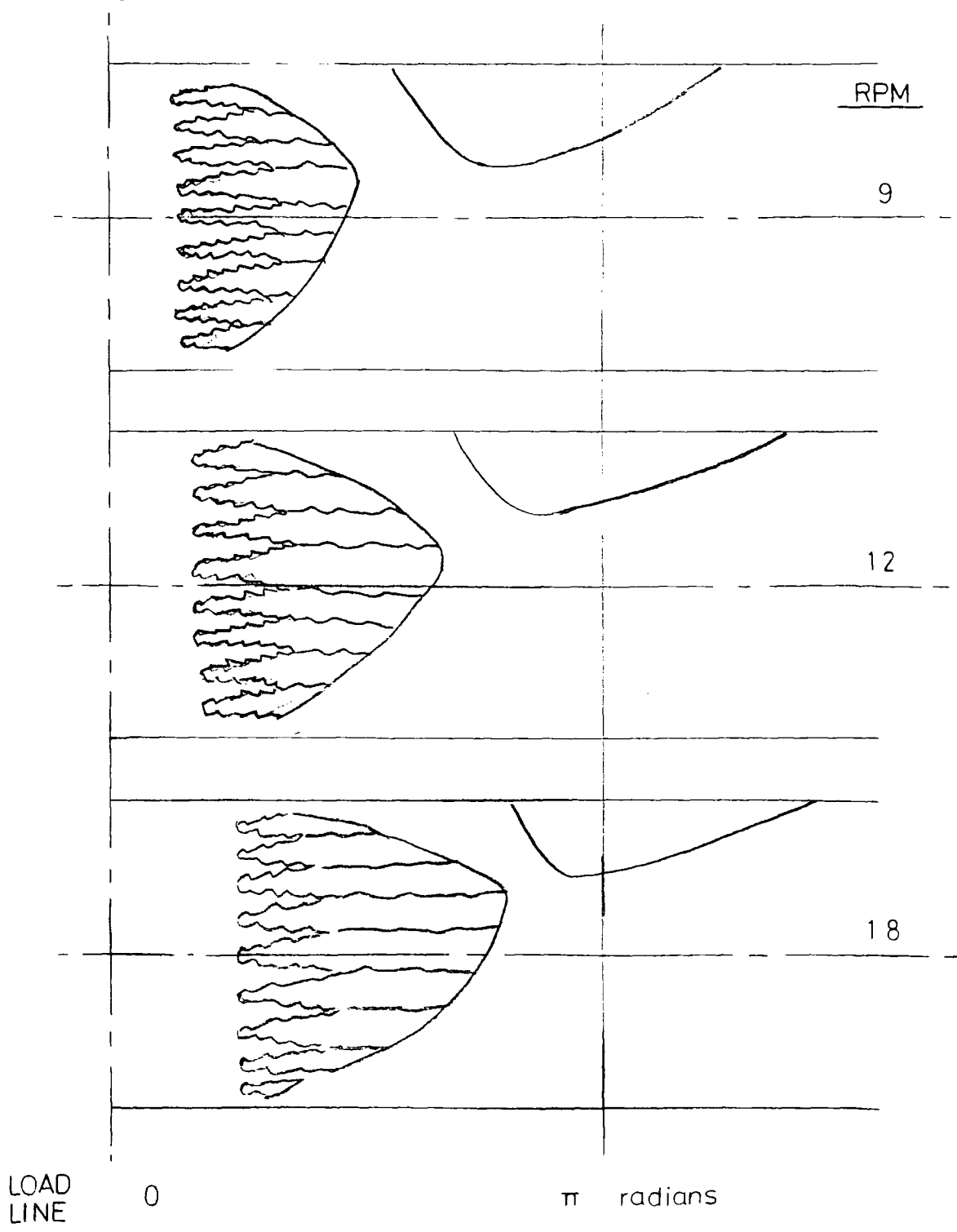
RPM

9

12

18

LOAD
LINE   0   LOAD 12 Kg   π   radians

CAVITATION   APPEARANCE

SEMI-FLOODED   OPERATION

FIGURE 7.8

RPM

9

12

18

LOAD
LINE   0   π   radians

CAVITATION   APPEARANCE
SEMI-FLOODED   OPERATION
FIGURE   7.9

RPM

4

9

12

LOAD
LINE

0   n   radians
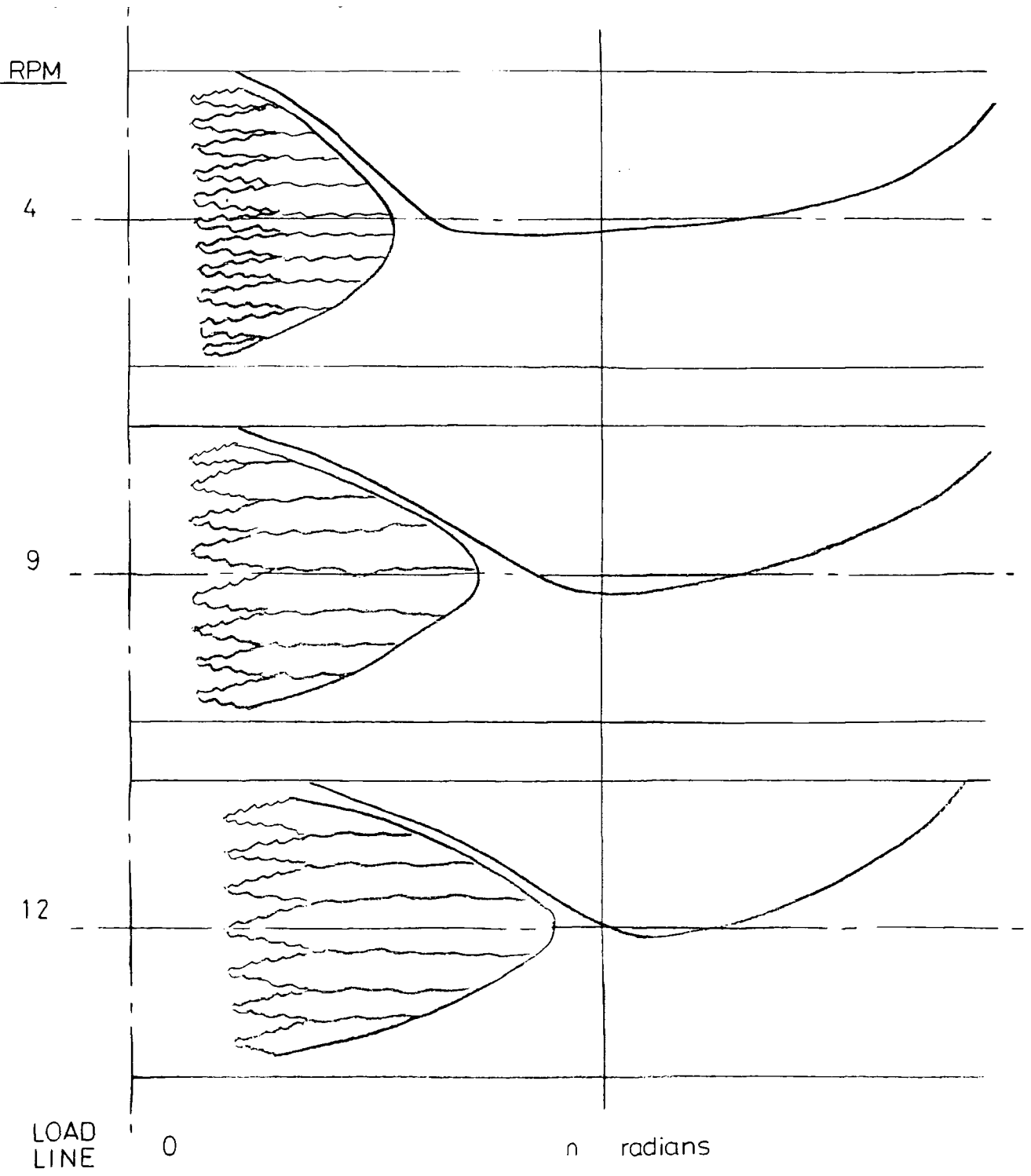
CAVITATION   APPEARANCE

SEMI FLOODED   OPERATION

FIGURE 7.10

CAVITATION APPEARANCE

SEMI-FLOODED OPERATION

FIGURE 7.11

PRESSURE FIELD
MOVEMENT

SURFACE
MOTION

TIME
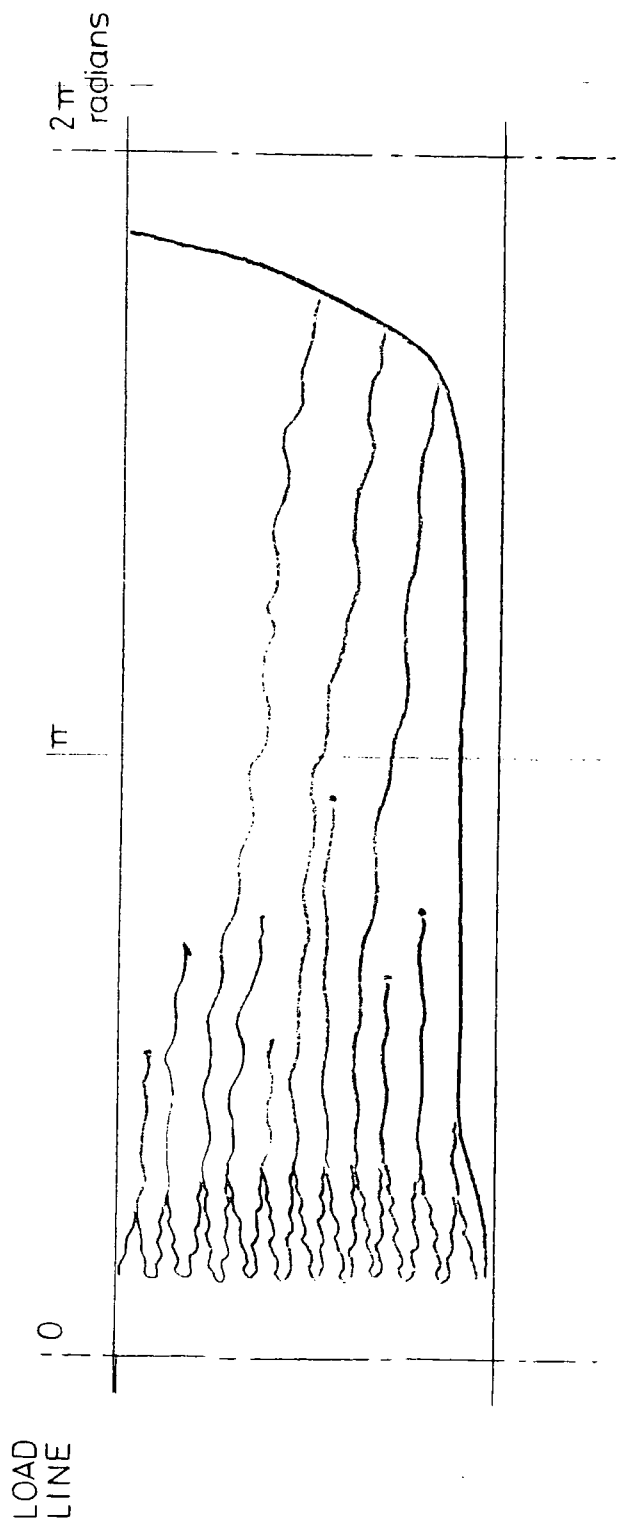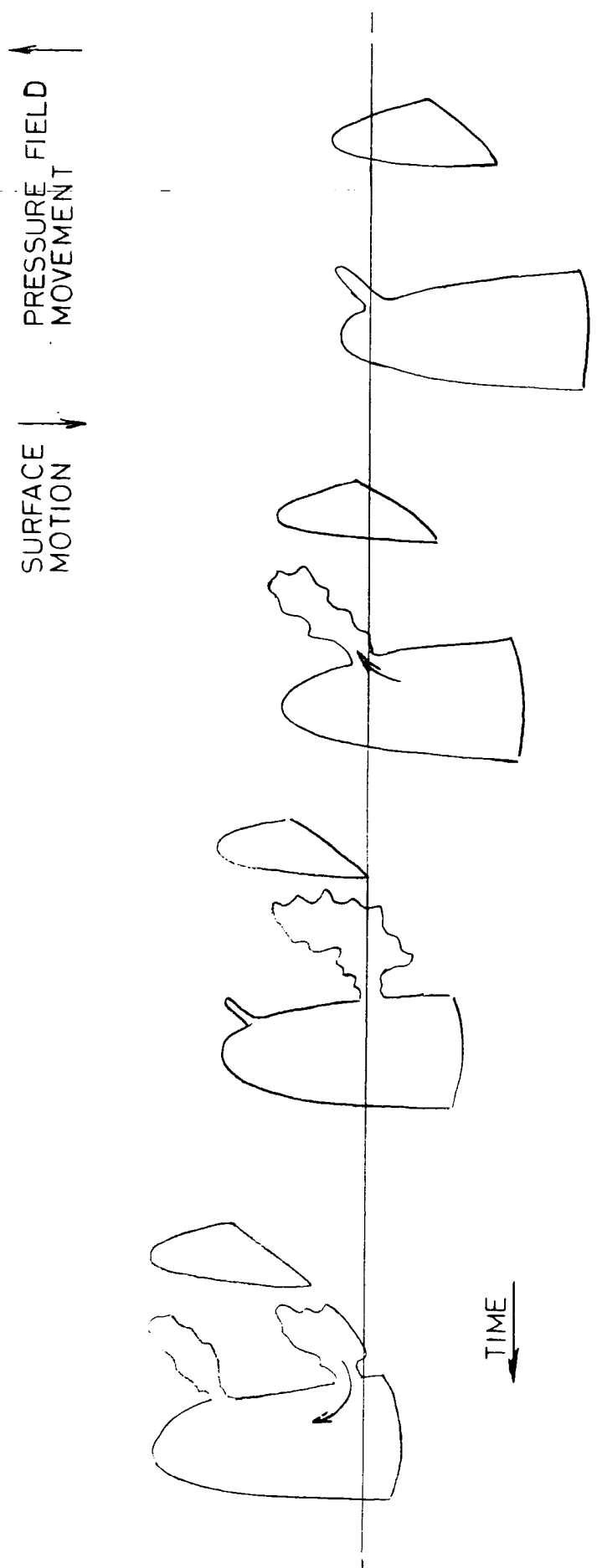
FLOW IN DENDRITIC CAVITIES

FIGURE 7.12

ROTOR
CENTRE BODY
FLEXIBLE MEMBER
ADJUSTABLE MOUNTING
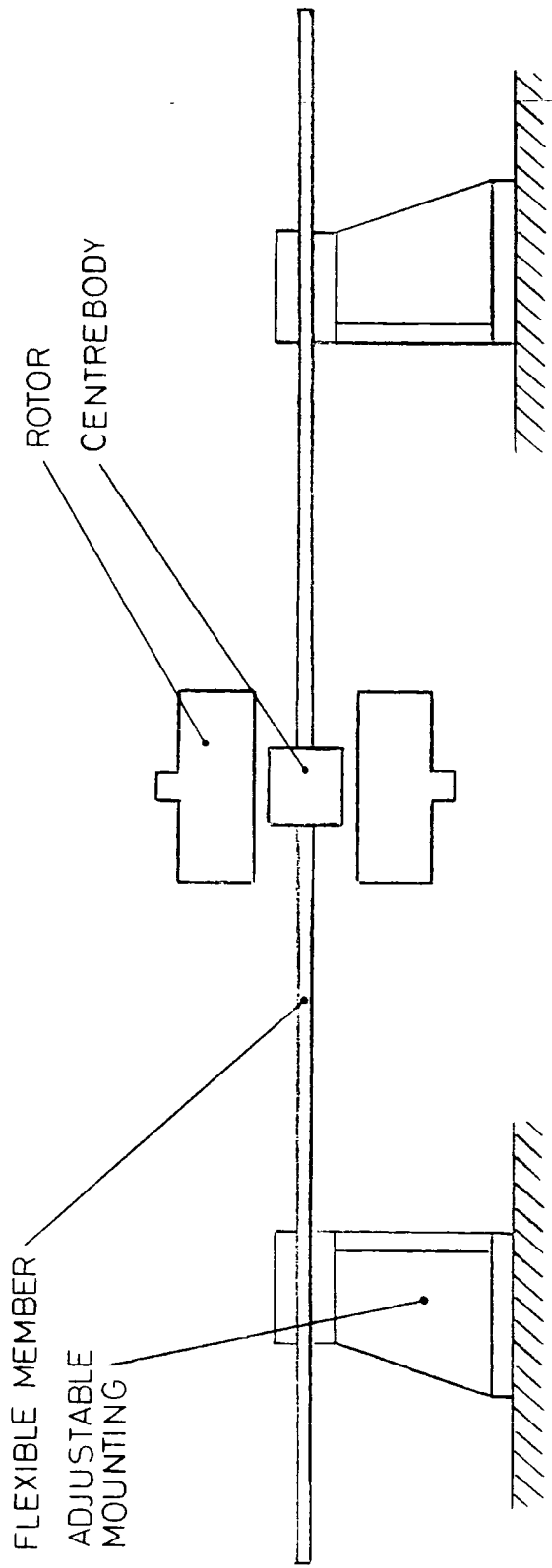
TEST ASSEMBLY SCHEME

FIGURE 8.1

ROTOR
DISPLACEMENT PROBE
CENTREBODY

SUSPENSION

COMBINED
THRUST BEARING
AND OIL CATCHER

SPEED PROBE AND
DRIVE NOZZLE
SUPPORT
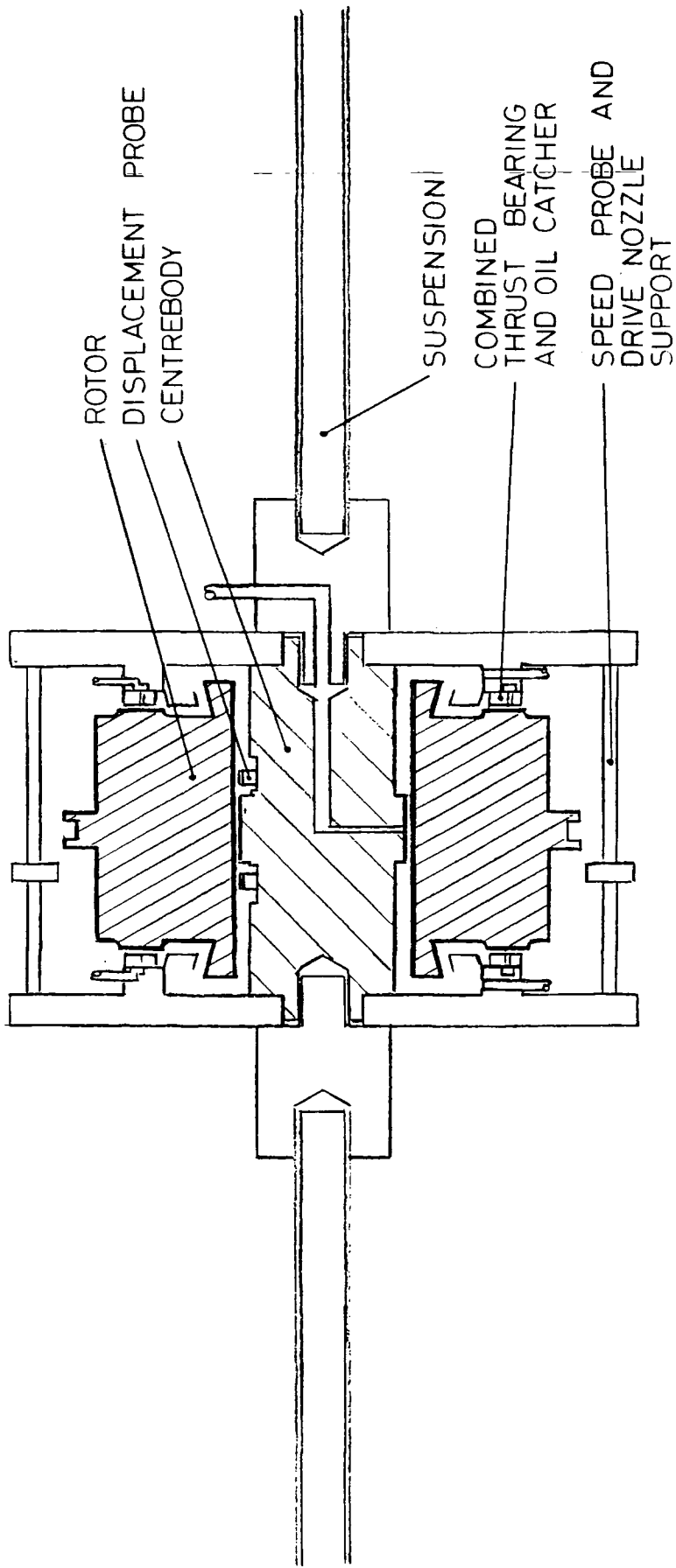
TEST BEARING ASSEMBLY

FIGURE 8.2

DISPLACEMENT PROBES

CENTREBODY

ROTOR

SPEED PROBE

DRIVE NOZZLES
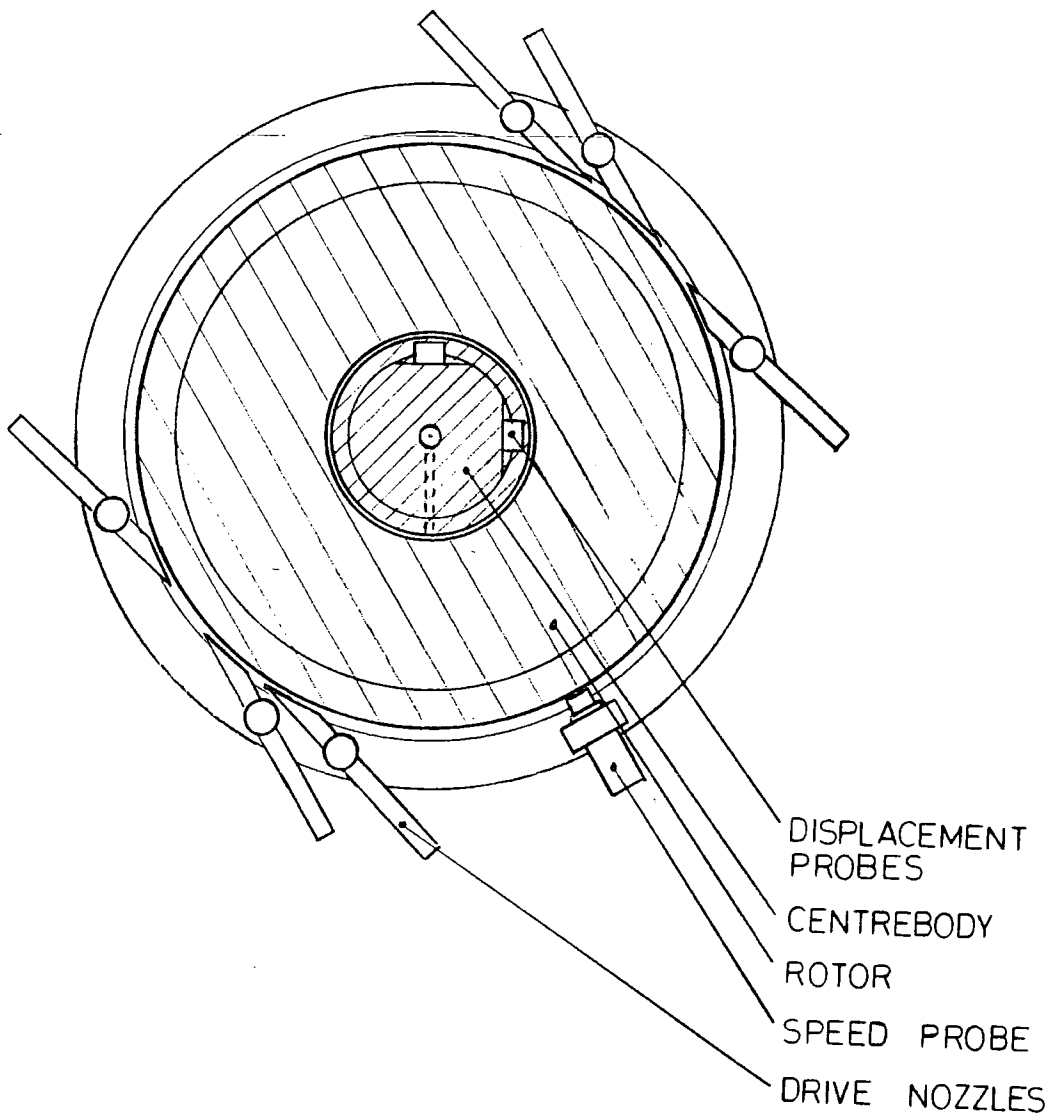
SECTION THROUGH TEST ASSEMBLY

FIGURE 8.3
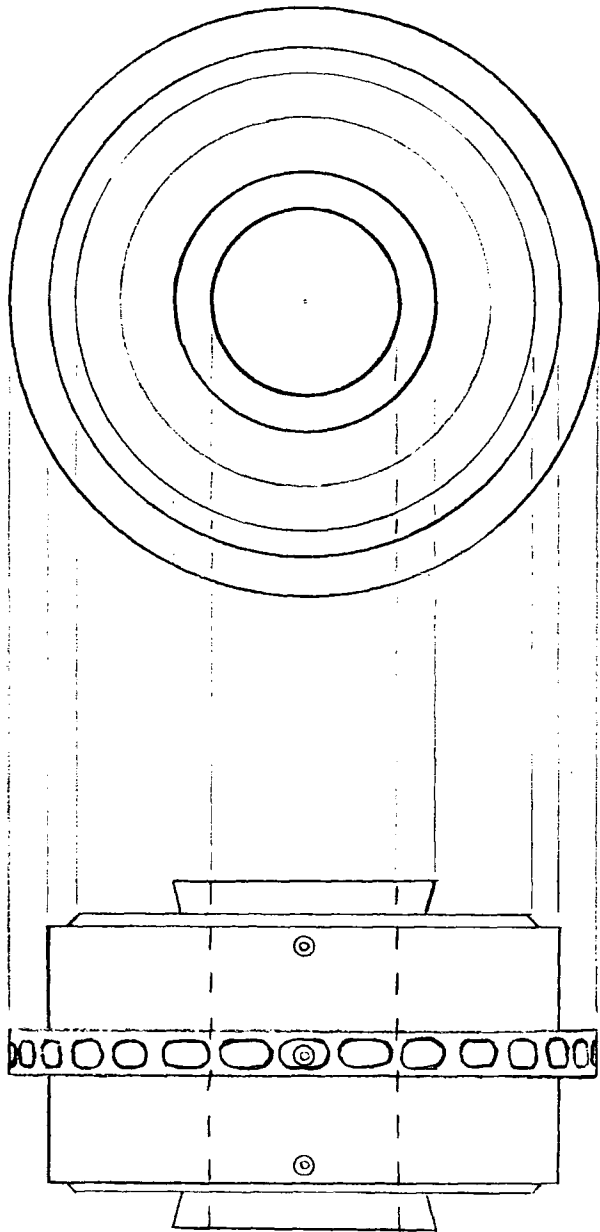
TEST ROTOR

FIGURE 8.4
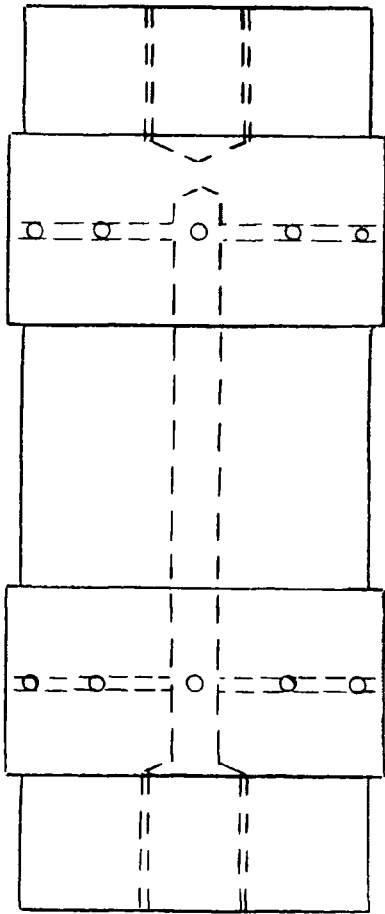
AIR BEARING
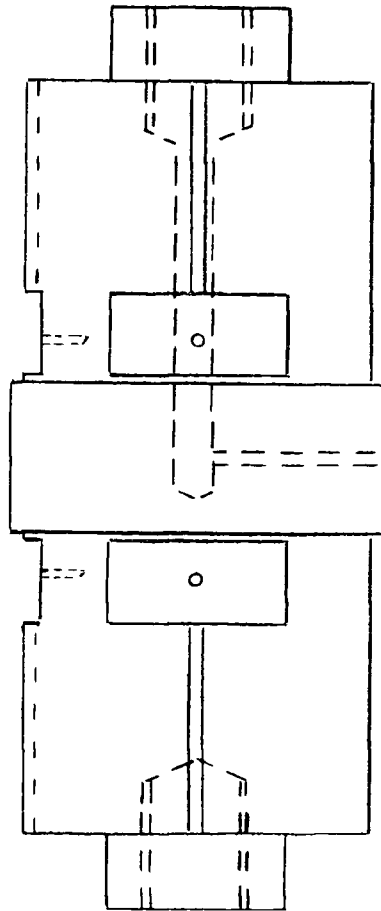
TEST BEARING

CENTRE BODIES

FIGURE 8.5

OIL VISCOSITY

FIGURE 8.6

AMPLITUDE

FREQUENCY

SYNCHRONOUS
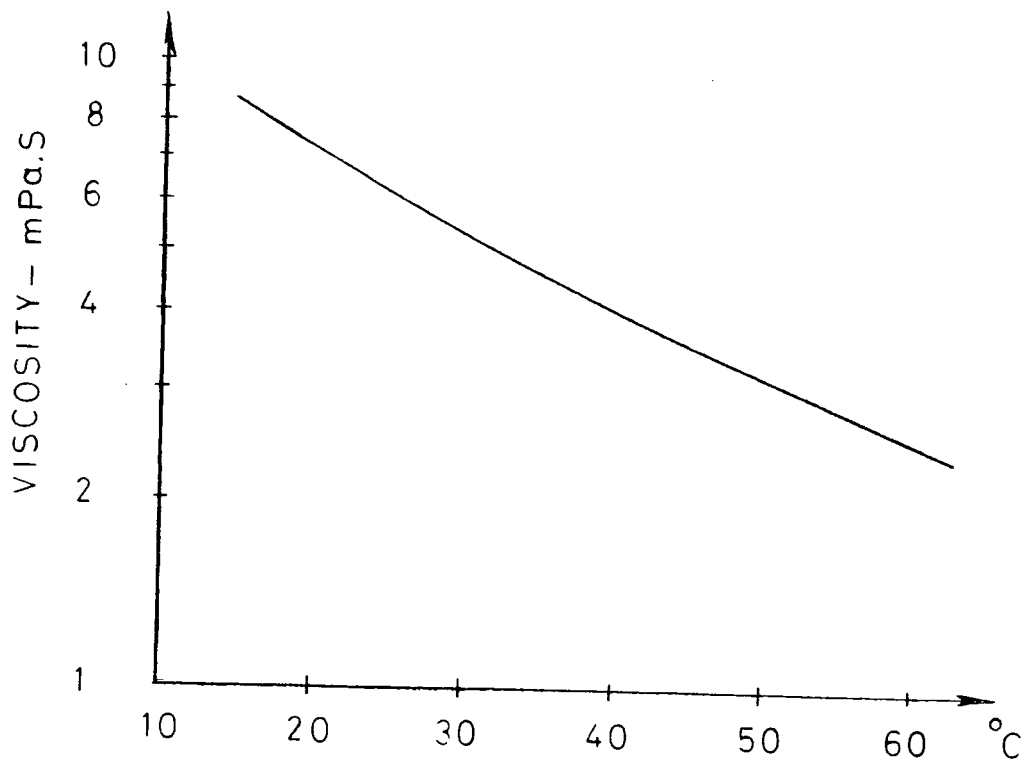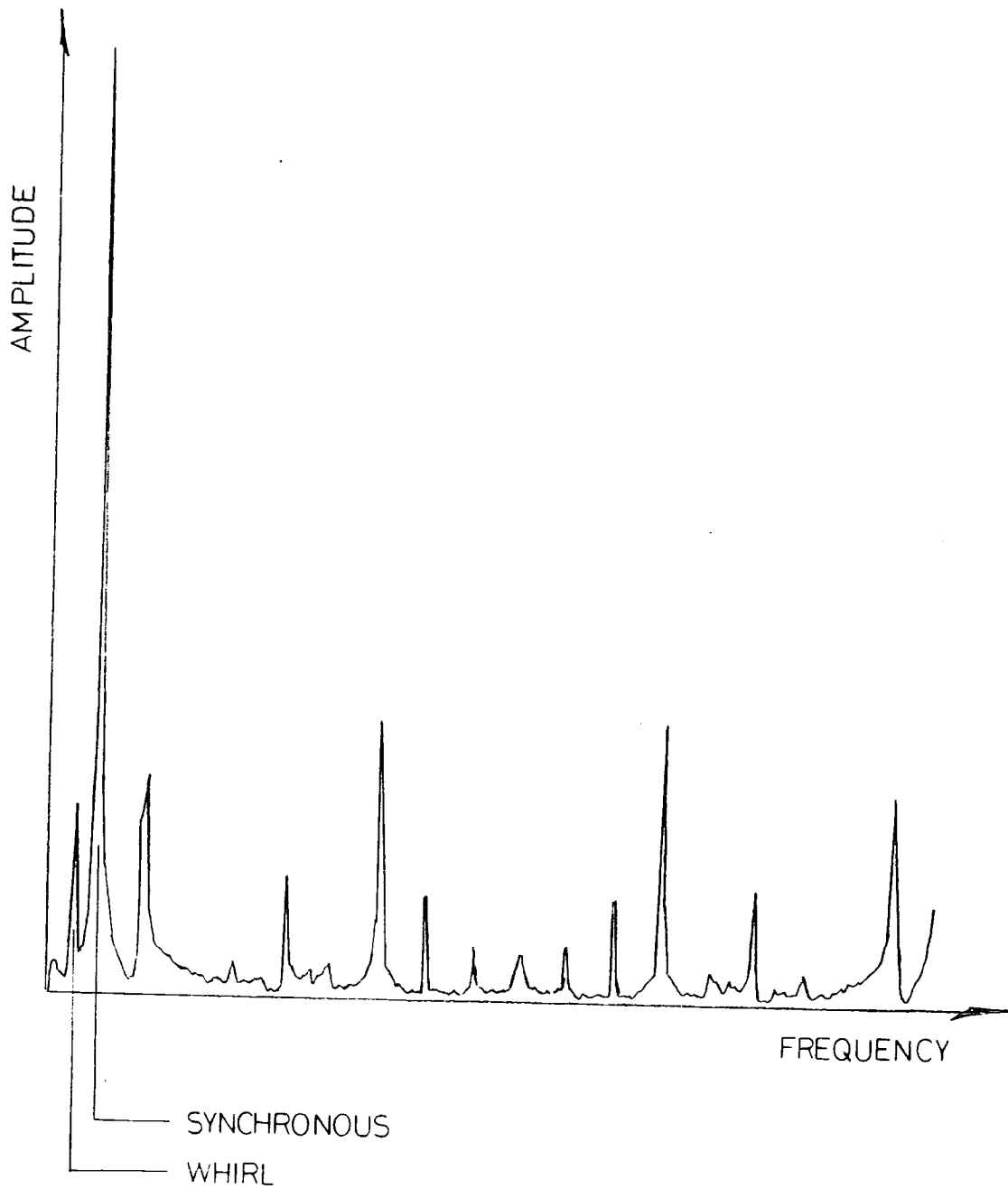
WHIRL

DISCRETE FOURIER TRANSFORM

ORIGINAL SIGNAL

FIGURE 8.7
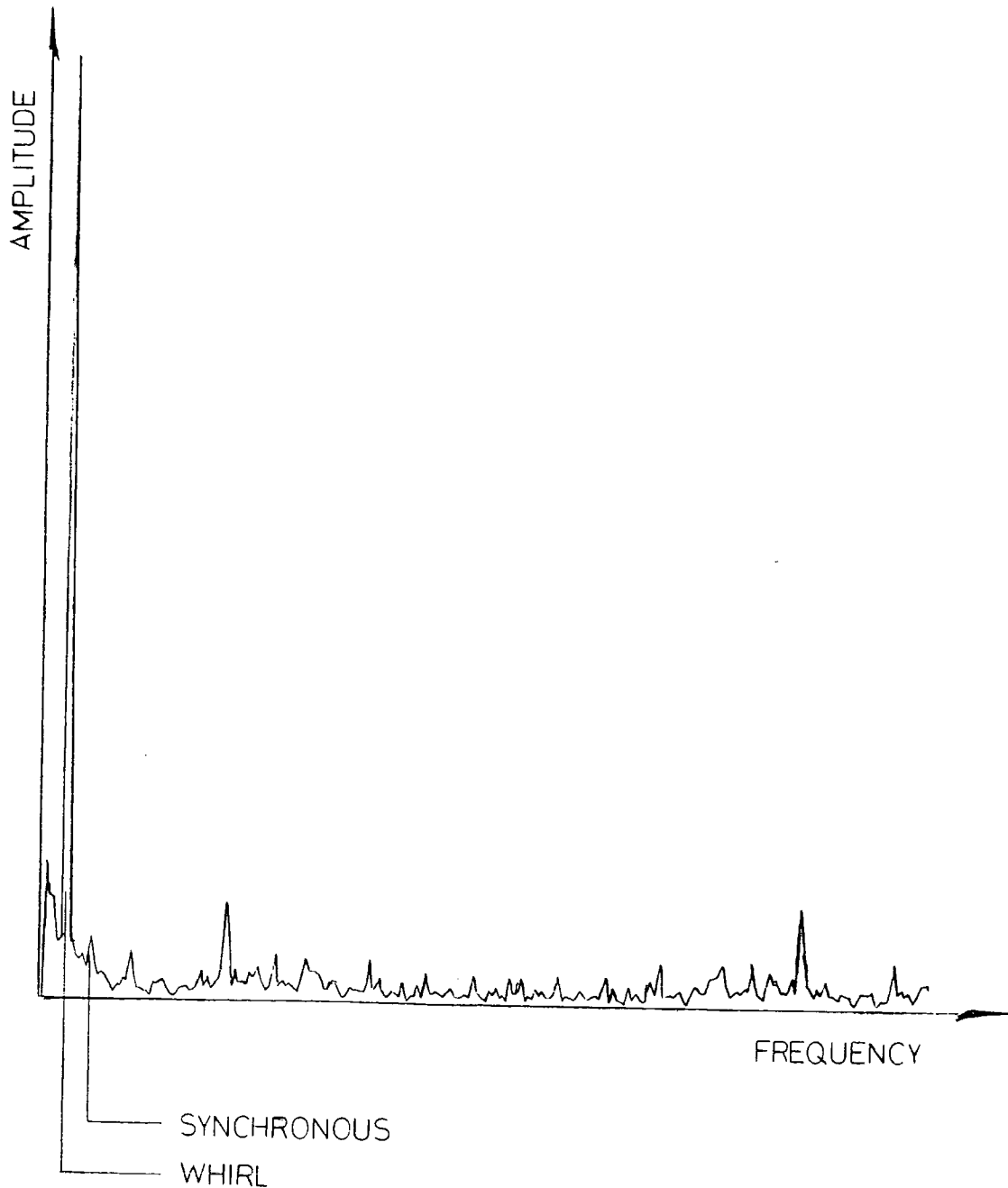
DISCRETE FOURIER TRANSFORM

SIGNAL LESS SIGNATURE

FIGURE 8.8

FIRST TEST SESSION

STEADY STATE RESULTS o
WHIRL ONSET RESULTS +

BEARING LENGTH 0.010 m
CLEARANCE RATIO 0.002

INDICATED STEADY STATE PERFORMANCE

FIGURE 8.9

INDICATED STEADY STATE PERFORMANCE

INDICATED ECCENTRICITY
ROTOR SPEED R.P.M.

SECOND TEST SESSION

STEADY STATE RESULTS   o
WHIRL ONSET RESULTS   +

BEARING LENGTH   0.010 m
CLEARANCE RATIO 0.002

FIGURE 8.10

FIRST TEST SESSION

STEADY STATE RESULTS   o
WHIRL ONSET RESULTS   +

BEARING LENGTH   0.020 m
CLEARANCE RATIO   0.002

INDICATED STEADY STATE PERFORMANCE

FIGURE 8.11

ROTOR SPEED R.P.M.

INDICATED ECCENTRICITY

SECOND TEST SESSION

STEADY STATE RESULTS   o
WHIRL ONSET RESULTS   +

BEARING LENGTH   0.020 m
CLEARANCE RATIO 0.002

INDICATED STEADY STATE PERFORMANCE

FIGURE 8.12

INDICATED ECCENTRICITY

ROTOR SPEED   R.P.M.

THIRD TEST SESSION

STEADY STATE RESULTS   o
WHIRL ONSET RESULTS   +

BEARING LENGTH   0.020 m
CLEARANCE RATIO 0.002

INDICATED STEADY STATE PERFORMANCE

FIGURE 8.13

INDICATED ECCENTRICITY

ROTOR SPEED R.P.M.

FIRST TEST SESSION

STEADY STATE RESULTS   o
WHIRL ONSET RESULTS   +

BEARING LENGTH   0.020 m
CLEARANCE RATIO 0.003

INDICATED STEADY STATE PERFORMANCE

FIGURE 8.14

INDICATED ECCENTRICITY

ROTOR SPEED   R.P.M.

10^3

SECOND TEST SESSION

STEADY STATE RESULTS   o
WHIRL ONSET RESULTS   +

BEARING LENGTH   0.020 m
CLEARANCE RATIO   0.003

INDICATED STEADY STATE PERFORMANCE

FIGURE 8.15

INDICATED STEADY STATE PERFORMANCE

STEADY STATE RESULTS o
WHIRL ONSET RESULTS +

BEARING LENGTH 0.020 m
CLEARANCE RATIO 0.004

FIGURE 8.16

FIRST TEST SESSION

STEADY STATE RESULTS o
WHIRL ONSET RESULTS +

INDICATED ECCENTRICITY

ROTOR SPEED R.P.M.

BEARING LENGTH   0.030 m
CLEARANCE RATIO 0.002

INDICATED STEADY STATE PERFORMANCE
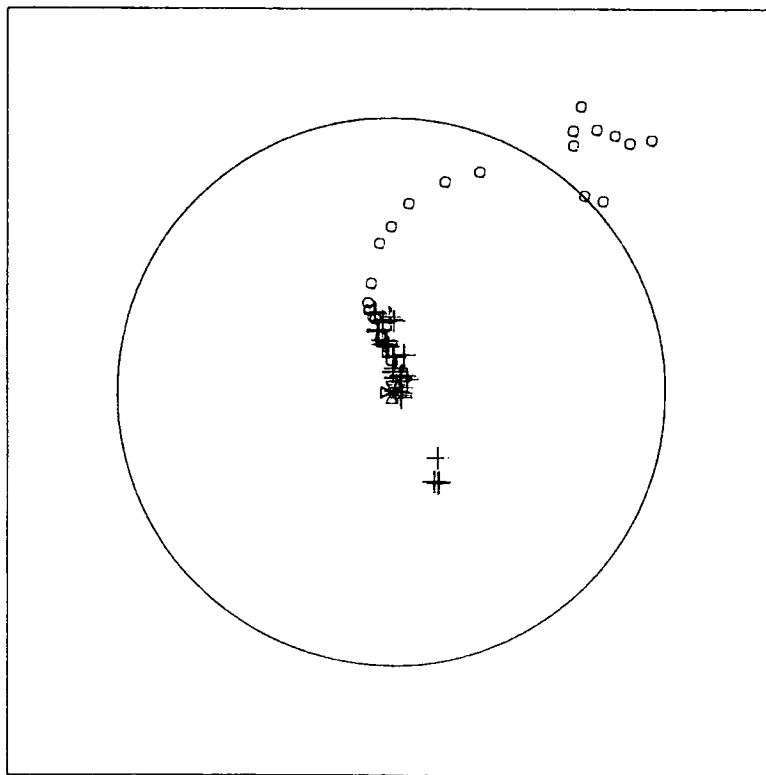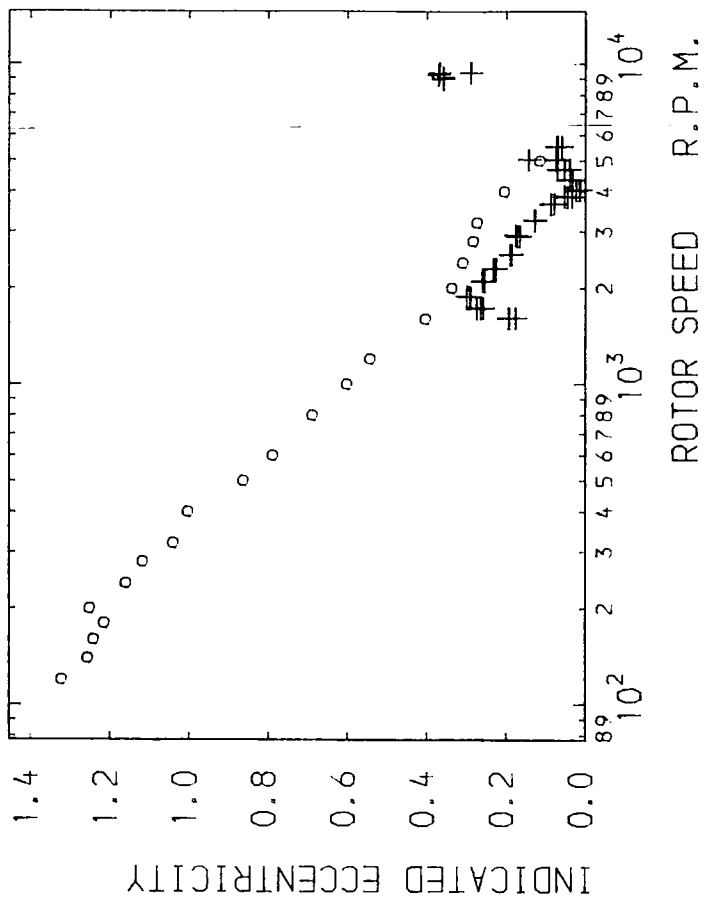
FIGURE 8.17

INDICATED STEADY STATE PERFORMANCE

SECOND TEST SESSION

STEADY STATE RESULTS   o
WHIRL ONSET RESULTS   +

BEARING LENGTH   0.030 m
CLEARANCE RATIO   0.002

FIGURE 8.18

INDICATED ECCENTRICITY

ROTOR SPEED R.P.M.

STEADY STATE RESULTS o
WHIRL ONSET RESULTS +

BEARING LENGTH 0.030 m
CLEARANCE RATIO 0.003

INDICATED STEADY STATE PERFORMANCE

FIGURE 8.19

INDICATED ECCENTRICITY

ROTOR SPEED R.P.M.

STEADY STATE RESULTS o
WHIRL ONSET RESULTS +

BEARING LENGTH 0.030 m
CLEARANCE RATIO 0.004

INDICATED STEADY STATE PERFORMANCE

FIGURE 8.20
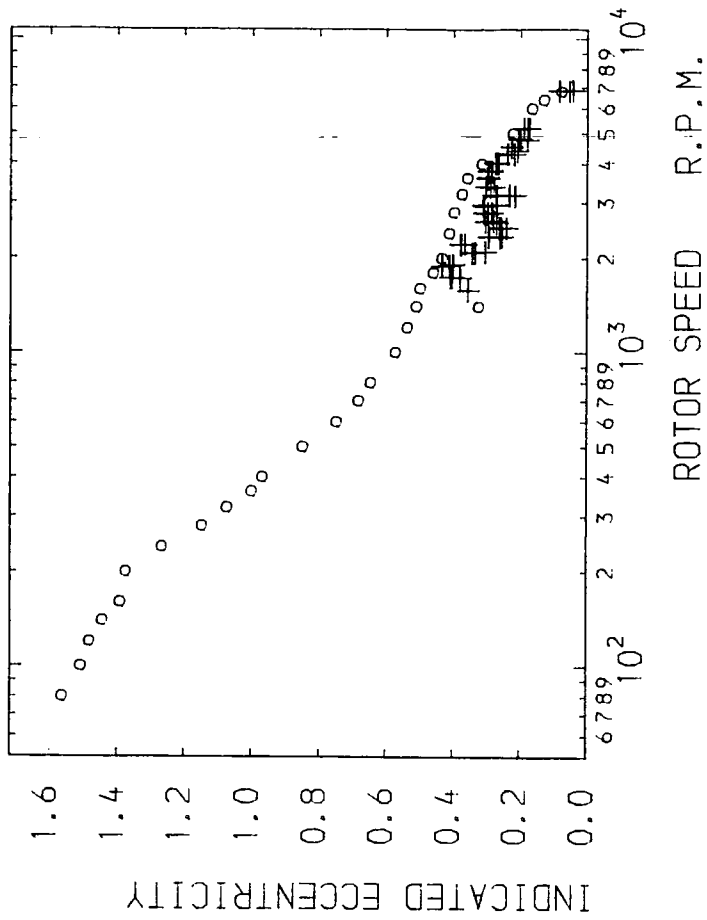
INDICATED ECCENTRICITY

ROTOR SPEED R.P.M.

FIRST TEST SESSION

STEADY STATE RESULTS   o
WHIRL ONSET RESULTS   +

BEARING LENGTH   0.040 m
CLEARANCE RATIO 0.002

INDICATED STEADY STATE PERFORMANCE

FIGURE 8.21

SECOND TEST SESSION

STEADY STATE RESULTS   o
WHIRL ONSET RESULTS   +

BEARING LENGTH   0.040 m
CLEARANCE RATIO   0.002

INDICATED STEADY STATE PERFORMANCE

FIGURE 8.22

INDICATED STEADY STATE PERFORMANCE

THIRD TEST SESSION

STEADY STATE RESULTS   o
WHIRL ONSET RESULTS   +

BEARING LENGTH   0.040 m
CLEARANCE RATIO   0.002

FIGURE 8.23

COMPRESSIBILITY NUMBER H

CORRECTED ECCENTRICITY

ALL TEST SESSIONS

STEADY STATE RESULTS   o
WHIRL ONSET RESULTS   +
OCVIRK PREDICTIONS   – –

BEARING LENGTH   0.010 m
CLEARANCE RATIO 0.002

CORRECTED STEADY STATE PERFORMANCE

FIGURE 8.24

ALL TEST SESSIONS

STEADY STATE RESULTS   o
WHIRL ONSET RESULTS   +
OCVIRK PREDICTIONS   – –

COMPRESSIBILITY NUMBER H

CORRECTED ECCENTRICITY

BEARING LENGTH   0.020 m
CLEARANCE RATIO 0.002

CORRECTED STEADY STATE PERFORMANCE

FIGURE 8.25

ALL TEST SESSIONS

STEADY STATE RESULTS   o
WHIRL ONSET RESULTS   +
OCVIRK PREDICTIONS   – –

BEARING LENGTH   0.020 m
CLEARANCE RATIO   0.003

CORRECTED STEADY STATE PERFORMANCE

FIGURE 8.26

CORRECTED STEADY STATE PERFORMANCE

FIGURE 8.27

ALL TEST SESSIONS

STEADY STATE RESULTS   o
WHIRL ONSET RESULTS   +
OCVIRK PREDICTIONS   – –

BEARING LENGTH   0.030 m
CLEARANCE RATIO   0.002

CORRECTED STEADY STATE PERFORMANCE

FIGURE 8.28

ALL TEST SESSIONS

STEADY STATE RESULTS   o
WHIRL ONSET RESULTS   +
OCVIRK PREDICTIONS   – –

BEARING LENGTH   0.030 m
CLEARANCE RATIO 0.003

CORRECTED STEADY STATE PERFORMANCE

FIGURE 8.29

COMPRESSIBILITY NUMBER H

CORRECTED ECCENTRICITY

ALL TEST SESSIONS

STEADY STATE RESULTS   o
WHIRL ONSET RESULTS   +
OCVIRK PREDICTIONS   - -

BEARING LENGTH   0.030 m
CLEARANCE RATIO 0.004

CORRECTED STEADY STATE PERFORMANCE

FIGURE 8.30

CORRECTED ECCENTRICITY

COMPRESSIBILITY NUMBER H

ALL TEST SESSIONS

STEADY STATE RESULTS   o
WHIRL ONSET RESULTS   +
OCVIRK PREDICTIONS   – –

BEARING LENGTH   0.040 m
CLEARANCE RATIO 0.002

CORRECTED STEADY STATE PERFORMANCE

FIGURE 8.31

THEORETICAL PERFORMANCE

EXPERIMENTAL RESULTS

NON-DIMENSIONAL FILM FORCE

10

1

0.1

0.01

0.0   0.2   0.4   0.6   0.8   1.0

ECCENTRICITY   RATIO

TYPICAL   RESULTS
OBTAINED   BY   WHITE

FIGURE 8.32

CRITICAL RUNNING SPEED

AND FREQUENCY RATIO

FIGURE 8.33

BEARING LENGTH   0.020 m   FIRST SESSION   ▫
CLEARANCE RATIO   0.002   SECOND SESSION △
                                 THIRD SESSION   ▽

CRITICAL RUNNING SPEED

AND FREQUENCY RATIO

FIGURE 8.34

BEARING LENGTH   0.020 m   FIRST SESSION   ▫
CLEARANCE RATIO 0.003   SECOND SESSION △

CRITICAL RUNNING SPEED

AND FREQUENCY RATIO

FIGURE 8.35

BEARING LENGTH   0.020 m   FIRST SESSION   ▫
CLEARANCE RATIO 0.004

CRITICAL RUNNING SPEED

AND FREQUENCY RATIO

FIGURE 8.36
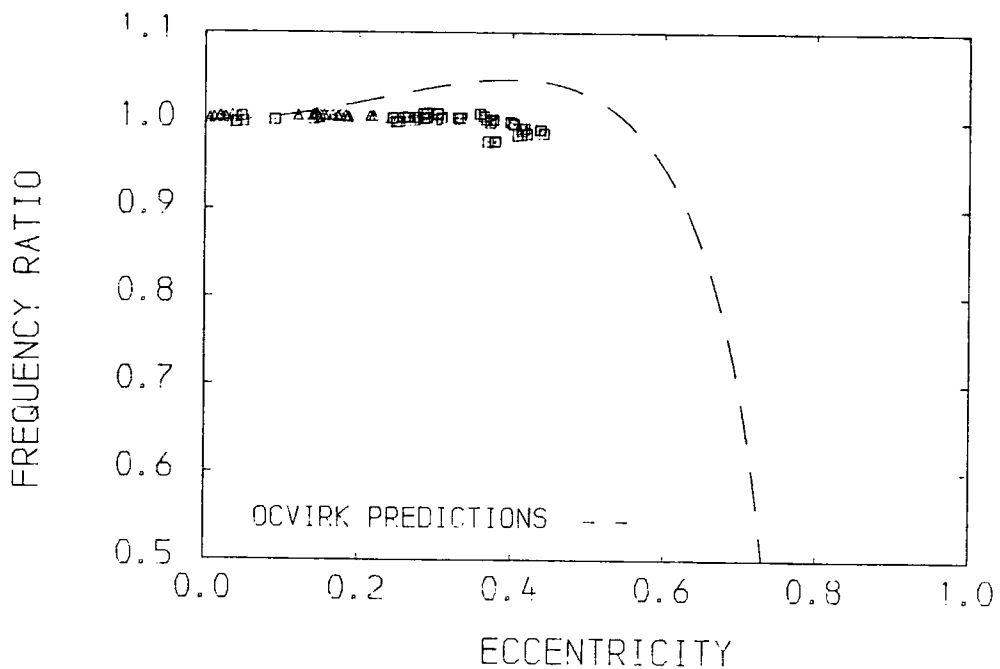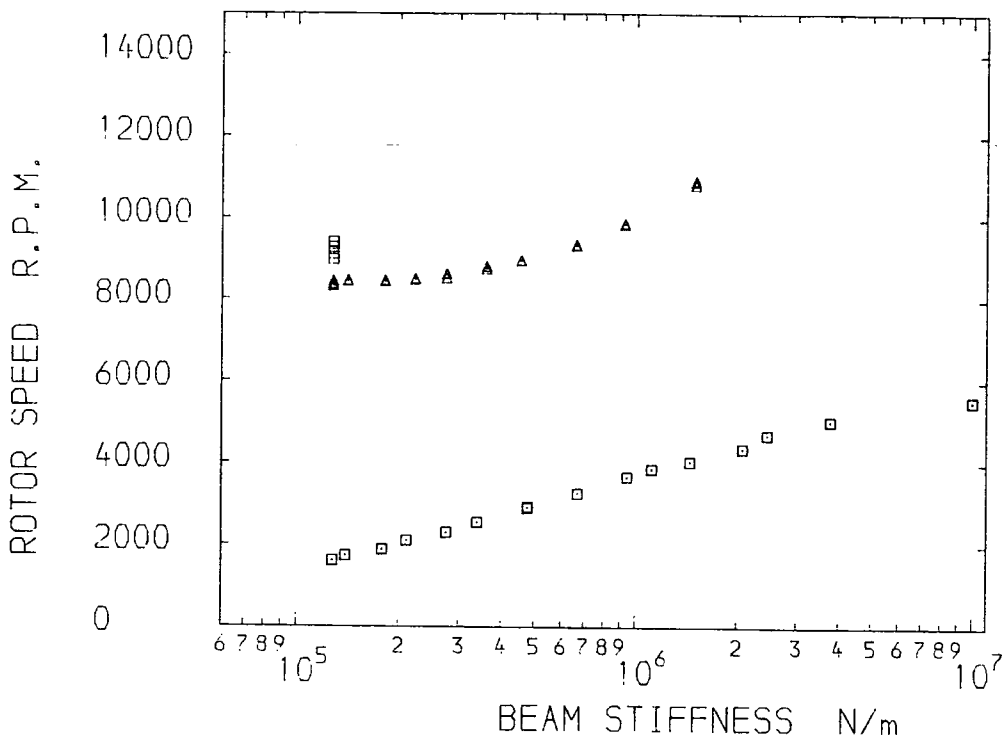
BEAM STIFFNESS   N/m

ECCENTRICITY

OCVIRK PREDICTIONS   — —

BEARING LENGTH   0.030 m   FIRST SESSION   ▢
CLEARANCE RATIO   0.002   SECOND SESSION △

CRITICAL RUNNING SPEED

AND FREQUENCY RATIO
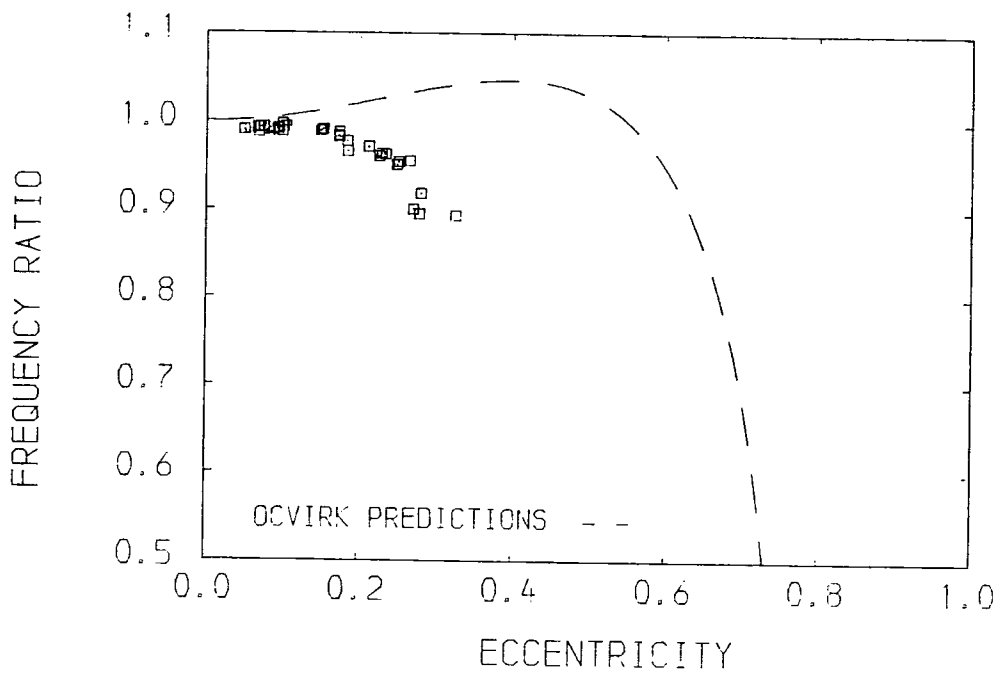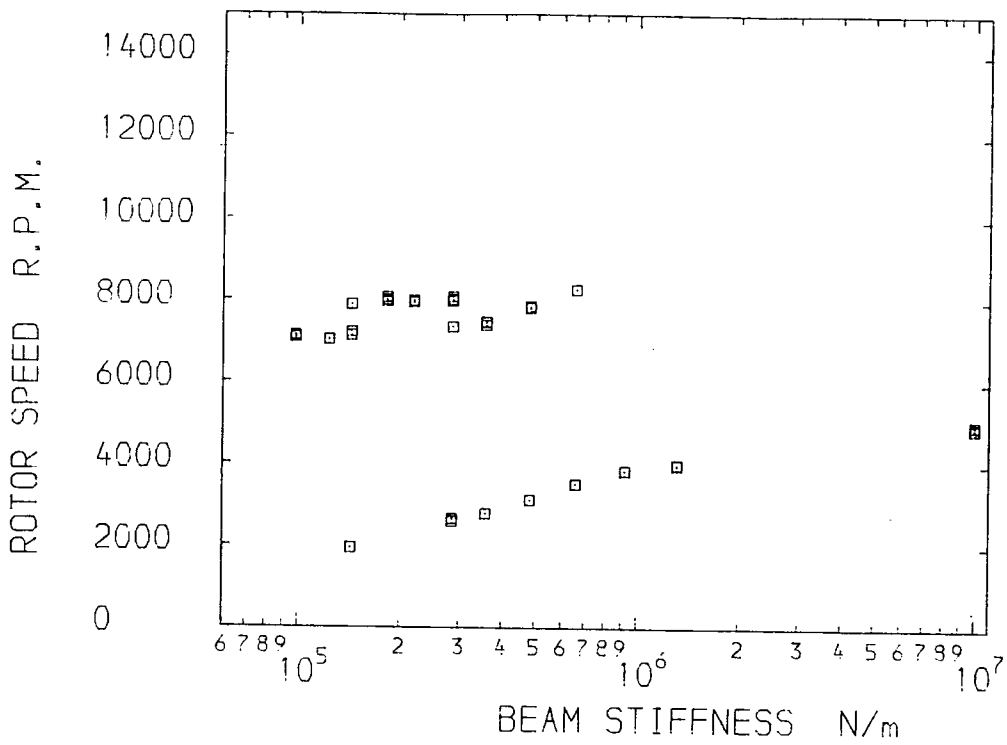
FIGURE 8.37

BEARING LENGTH   0.030 m   FIRST SESSION   □
CLEARANCE RATIO   0.003

CRITICAL RUNNING SPEED

AND FREQUENCY RATIO

FIGURE 8.38
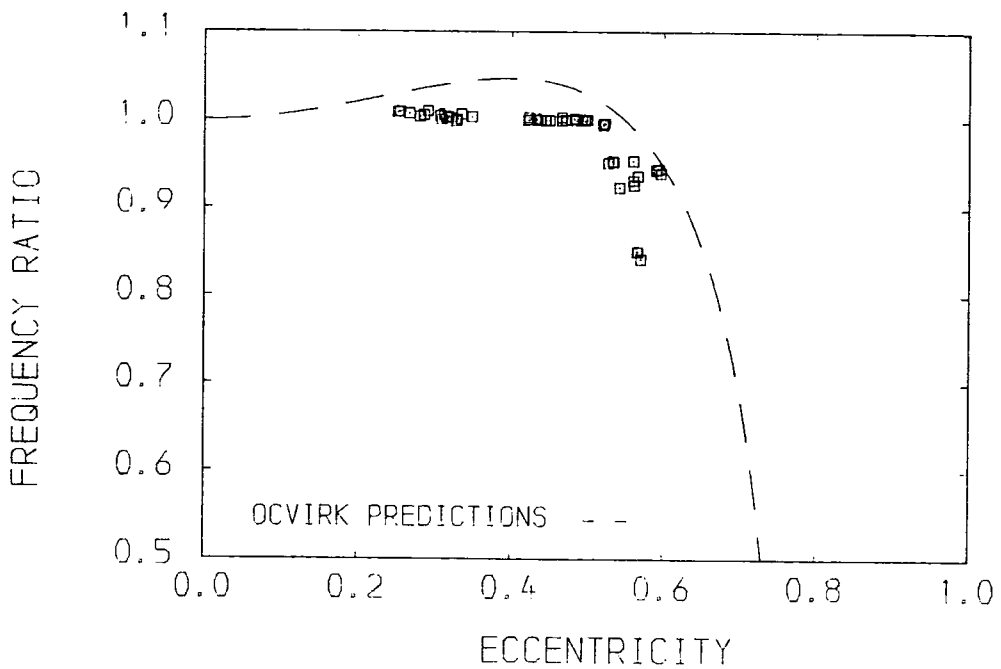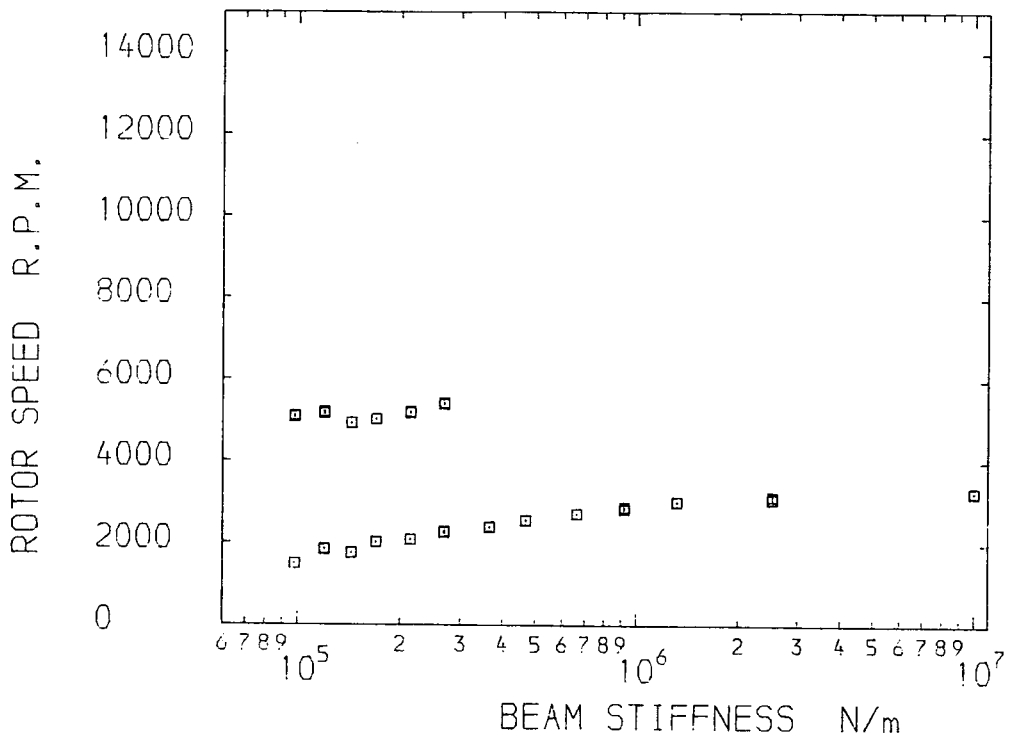
BEAM STIFFNESS   N/m

FREQUENCY RATIO

OCVIRK PREDICTIONS   - -

ECCENTRICITY

BEARING LENGTH   0.030 m   FIRST SESSION   ▫
CLEARANCE RATIO 0.004
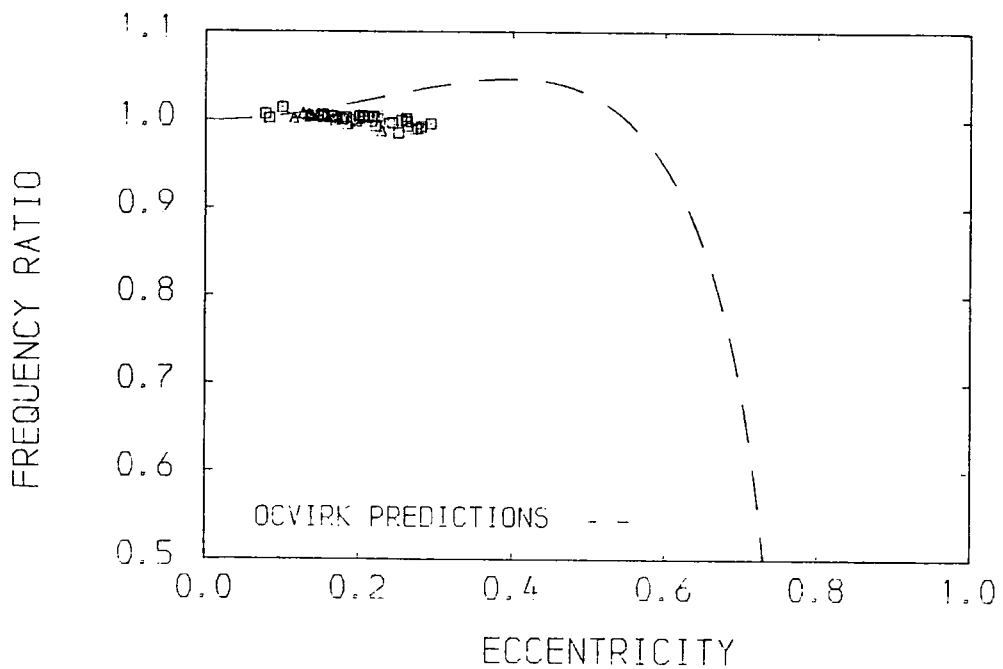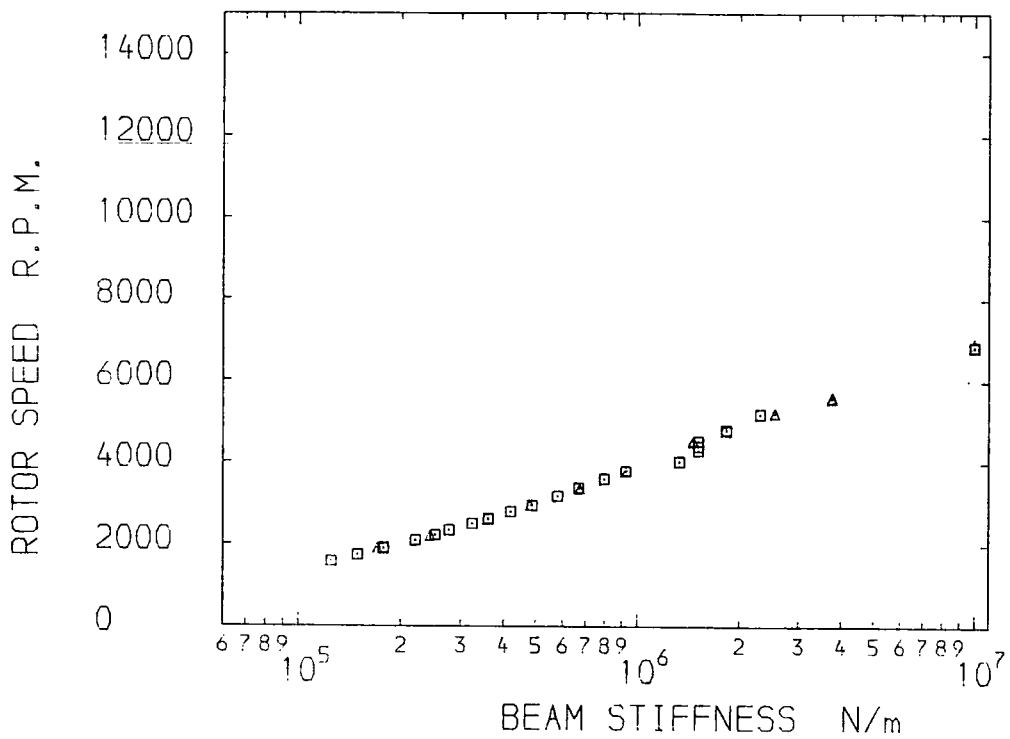
CRITICAL RUNNING SPEED

AND FREQUENCY RATIO

FIGURE 8.39

CRITICAL RUNNING SPEED

AND FREQUENCY RATIO

FIGURE 8.40
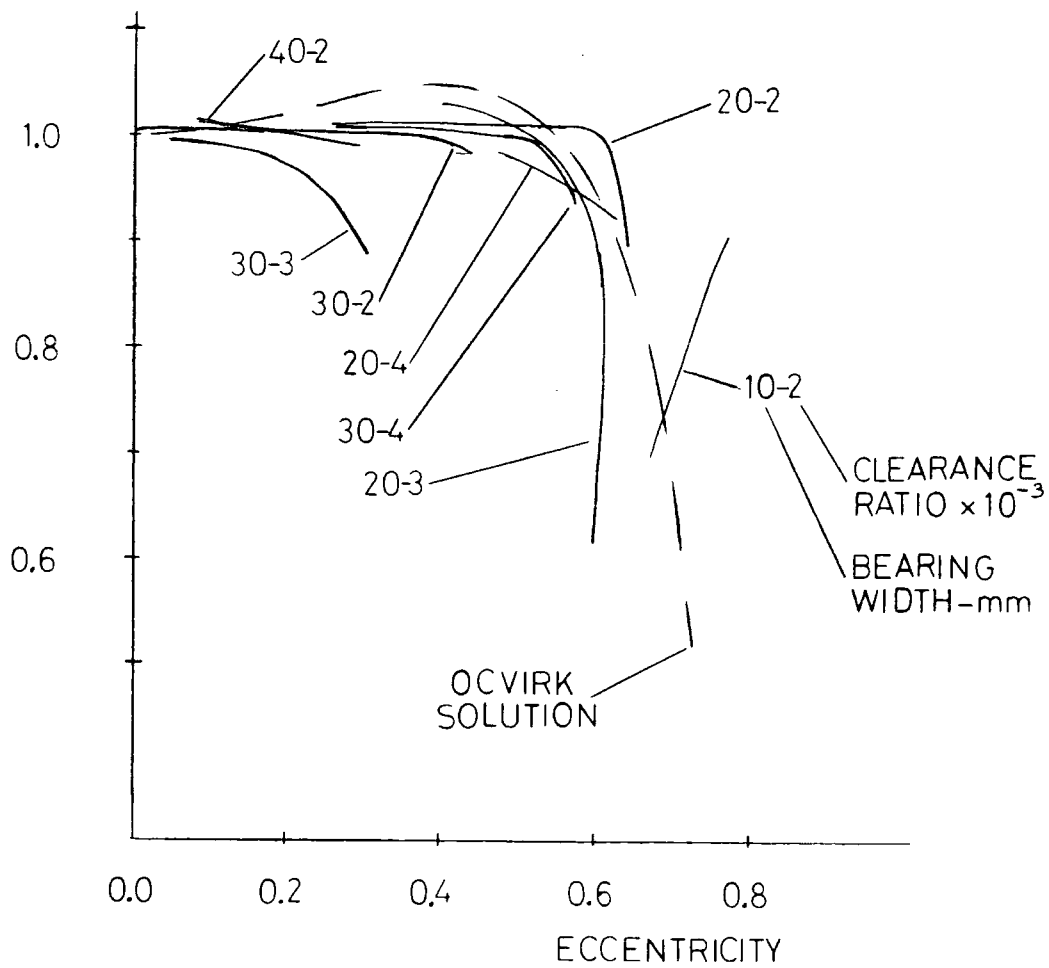
NON-DIMENSIONAL
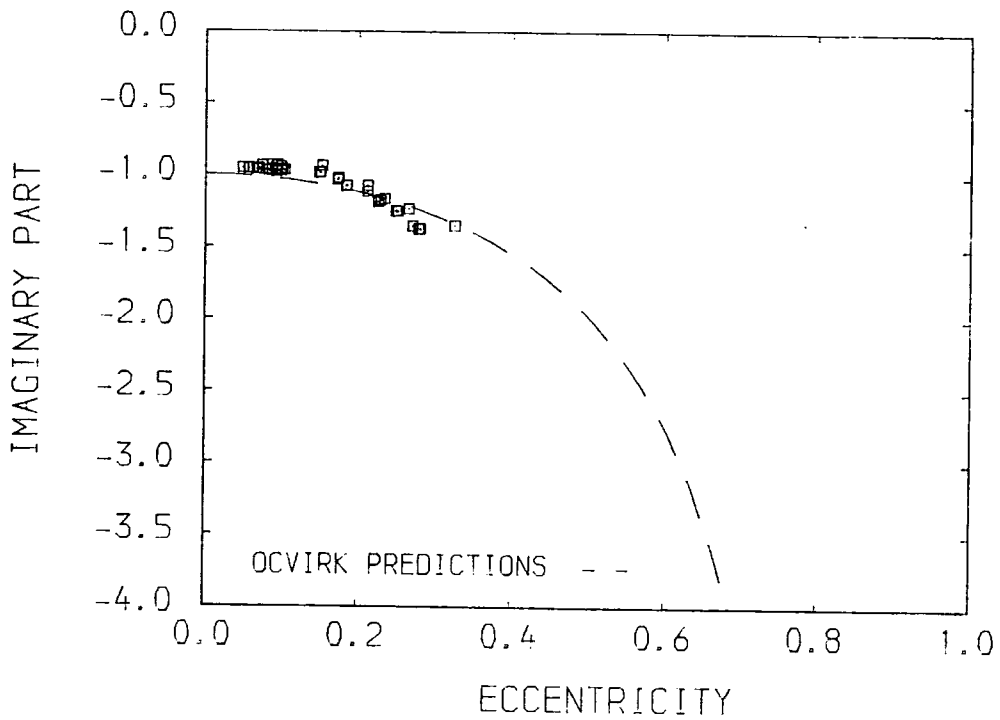FREQUENCY RATIO
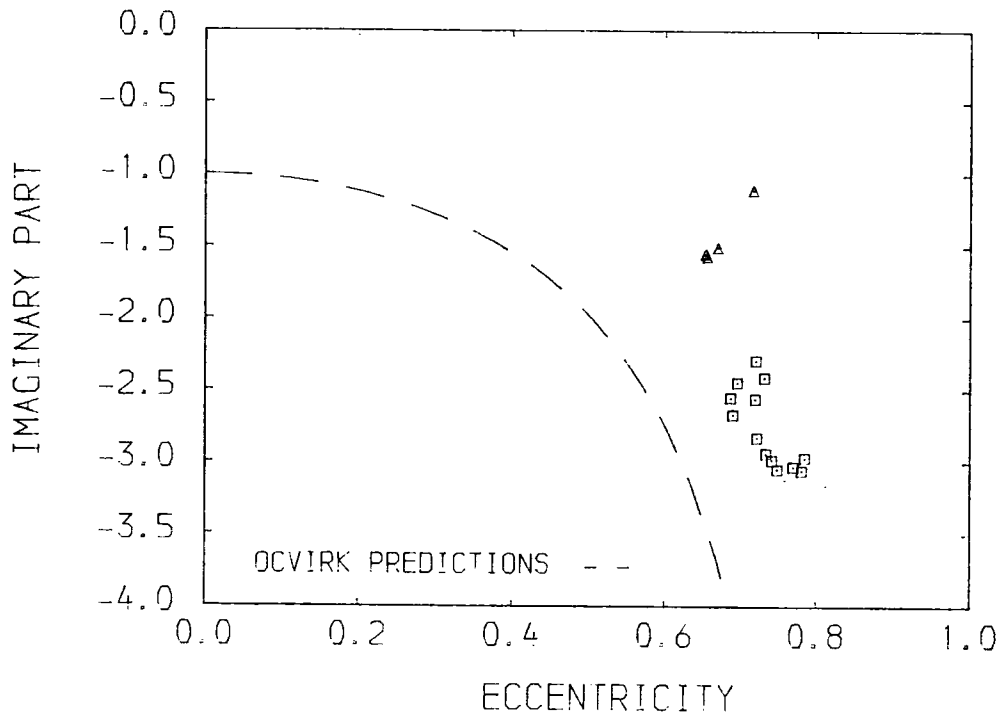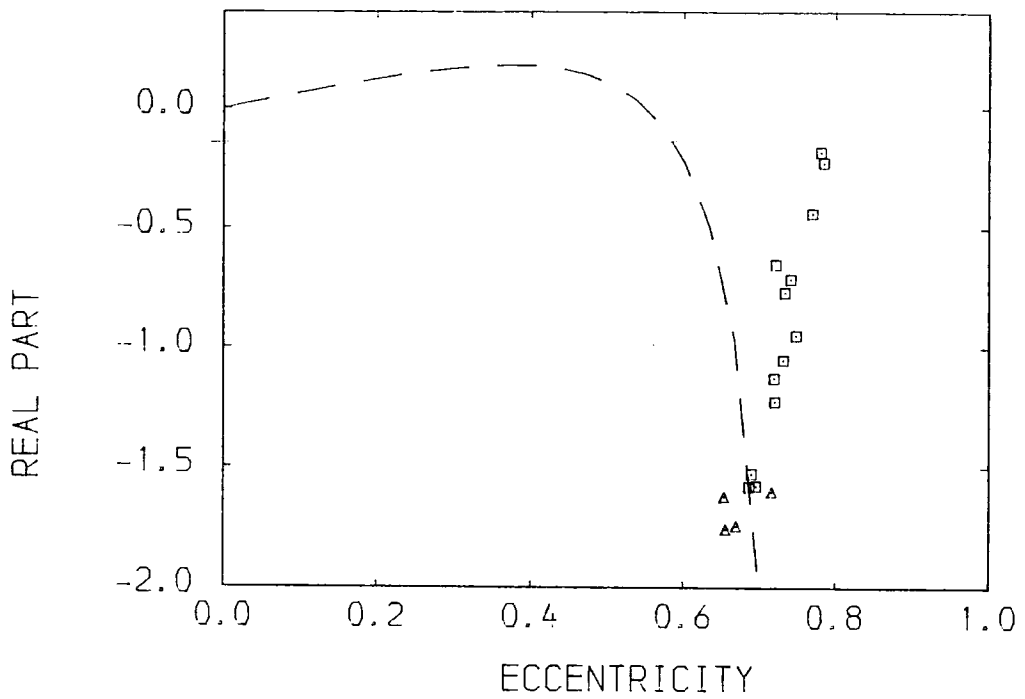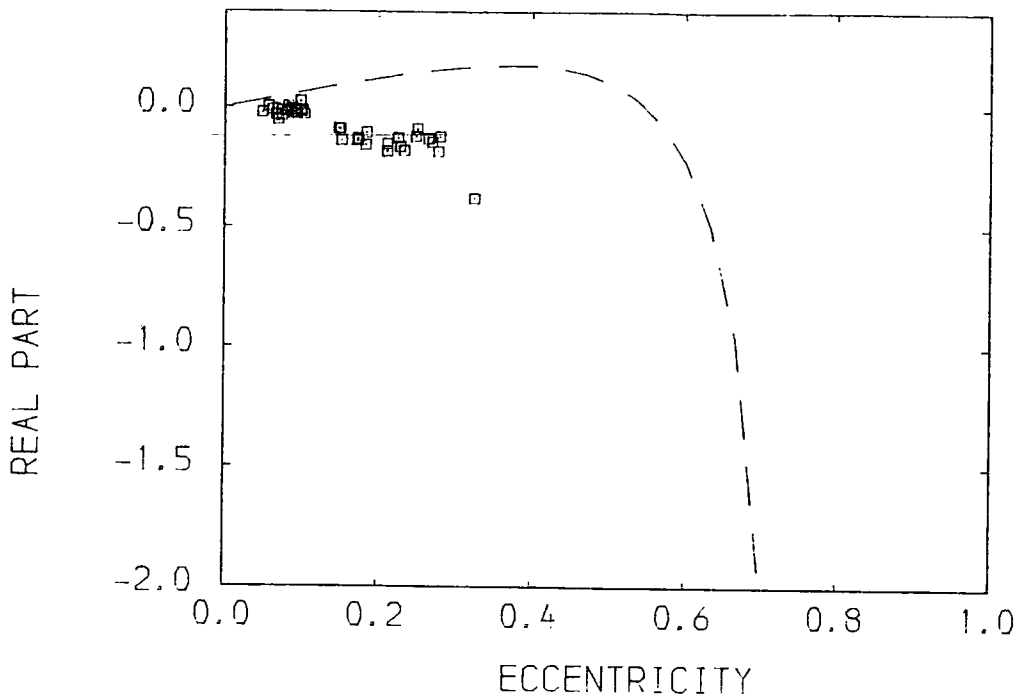
FIGURE 8.41

BEARING LENGTH   0.010 m   FIRST SESSION   □
CLEARANCE RATIO   0.002   SECOND SESSION   △

WHIRL ONSET ORBIT

SHAPE PARAMETER

FIGURE 8.42
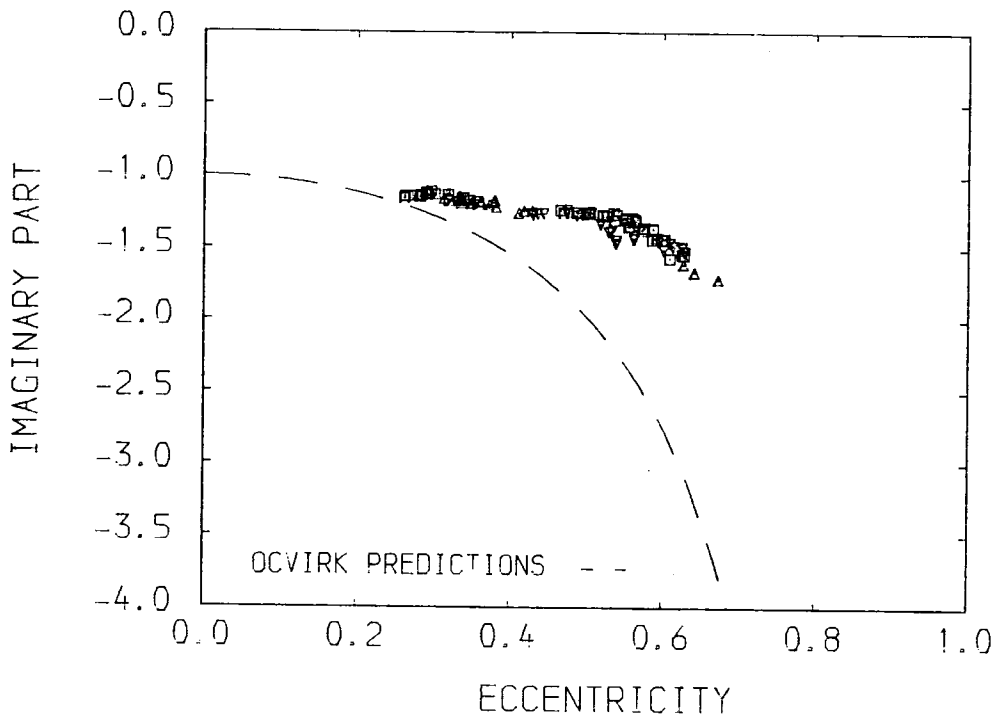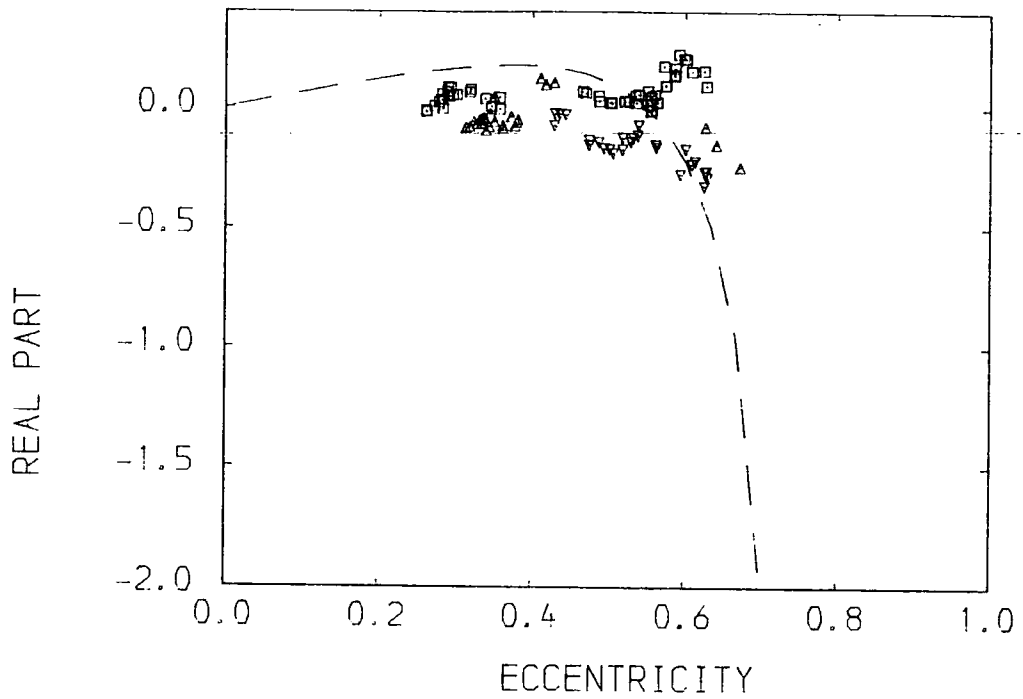
BEARING LENGTH   0.020 m   FIRST SESSION   □
CLEARANCE RATIO   0.002   SECOND SESSION △
                                 THIRD SESSION   ▽

WHIRL ONSET ORBIT

SHAPE PARAMETER

FIGURE 8.43
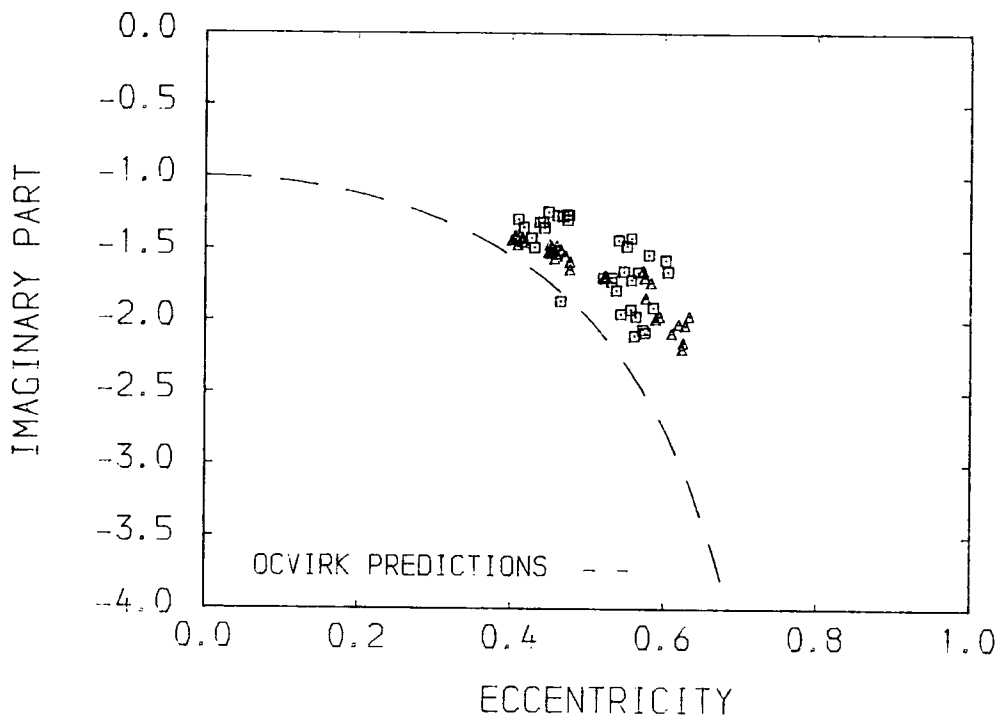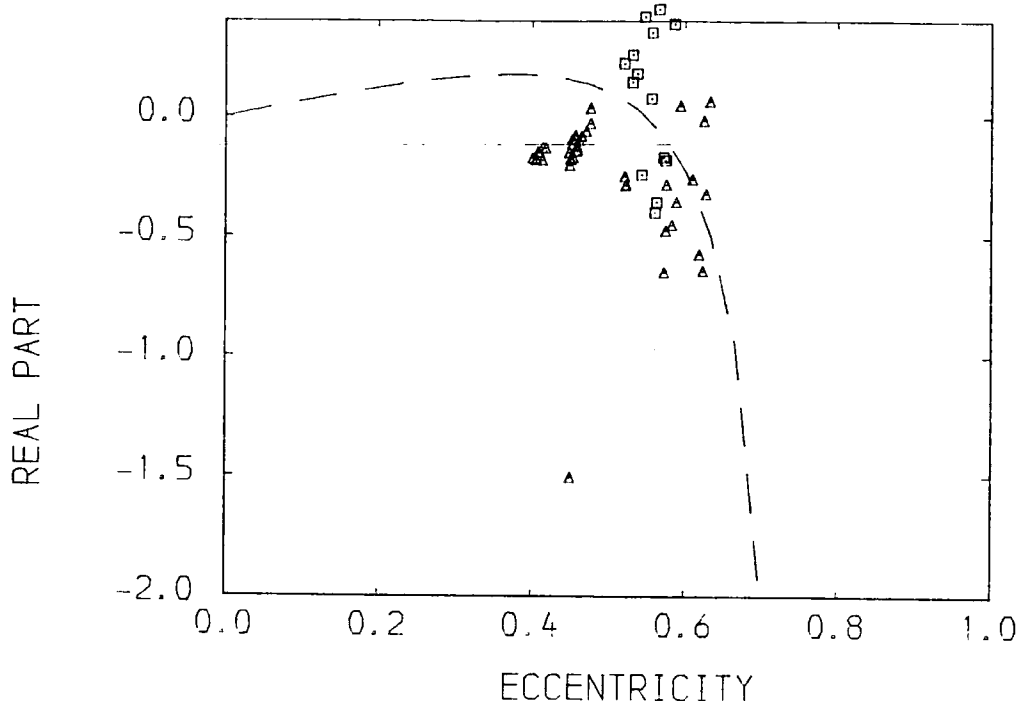
BEARING LENGTH   0.020 m   FIRST SESSION   □
CLEARANCE RATIO 0.003   SECOND SESSION △
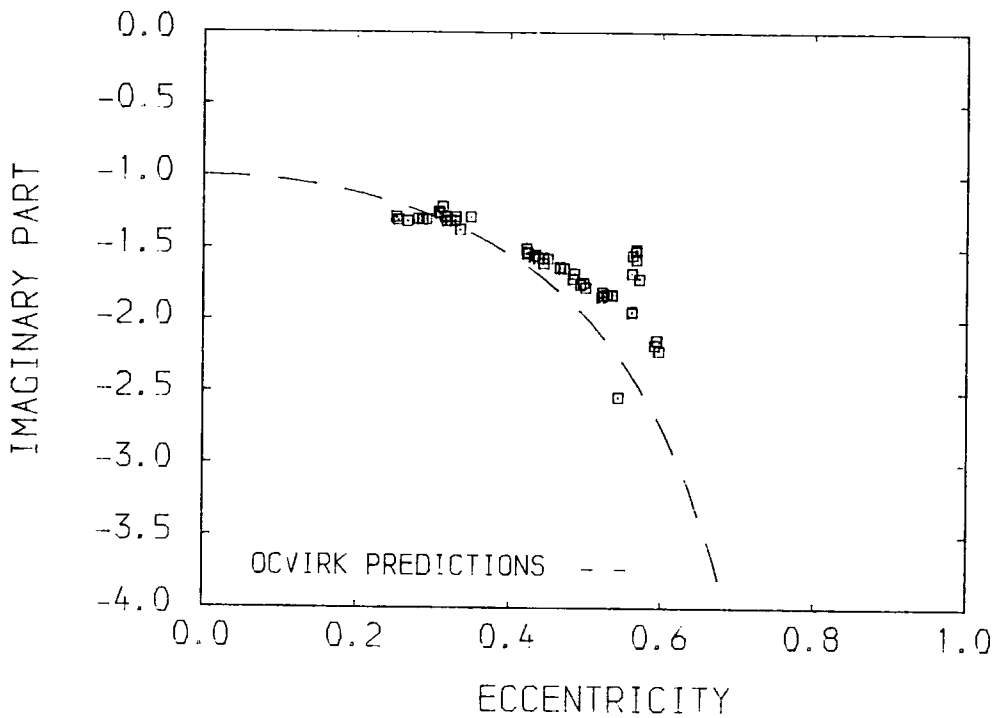
WHIRL ONSET ORBIT

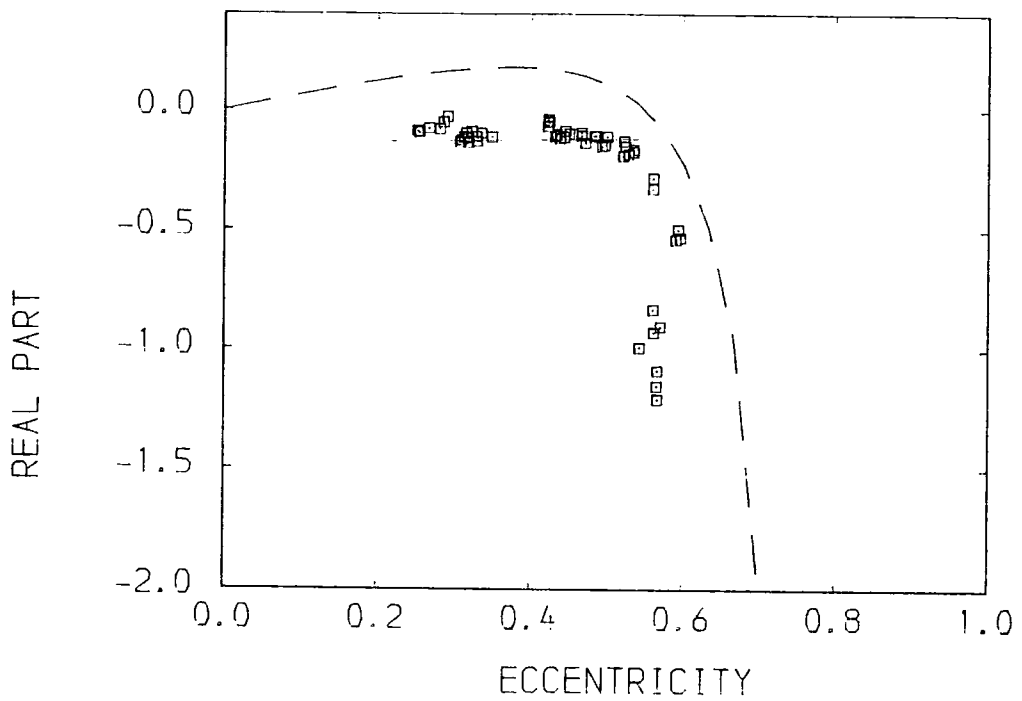SHAPE PARAMETER

FIGURE 8.44
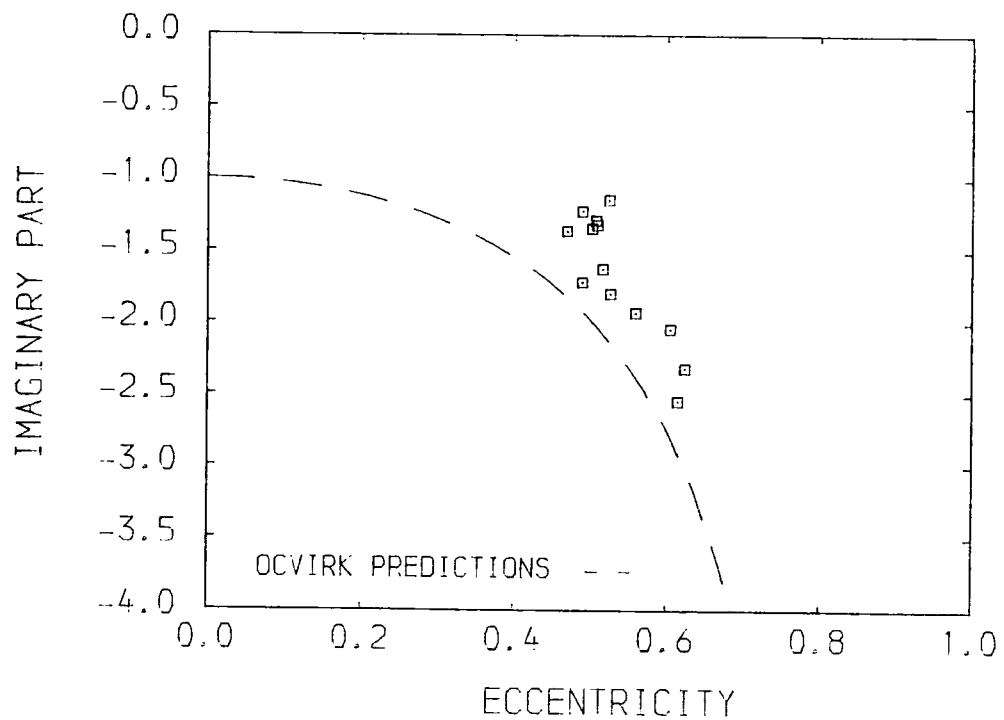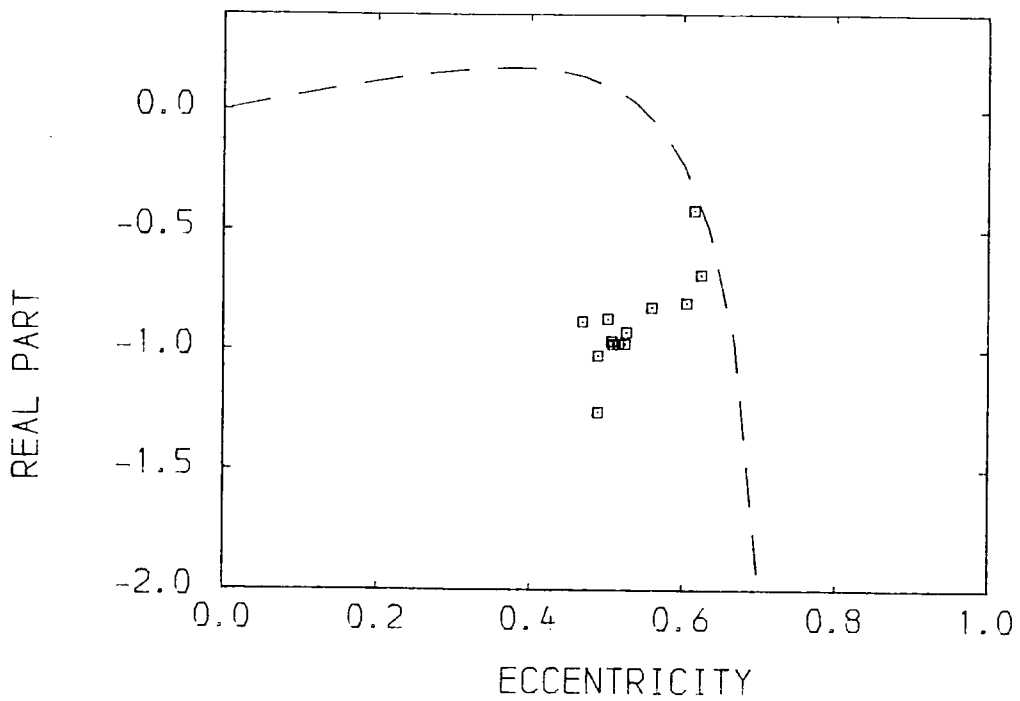
BEARING LENGTH   0.020 m   FIRST SESSION   ▫
CLEARANCE RATIO 0.004

WHIRL ONSET ORBIT

SHAPE PARAMETER

FIGURE 8.45
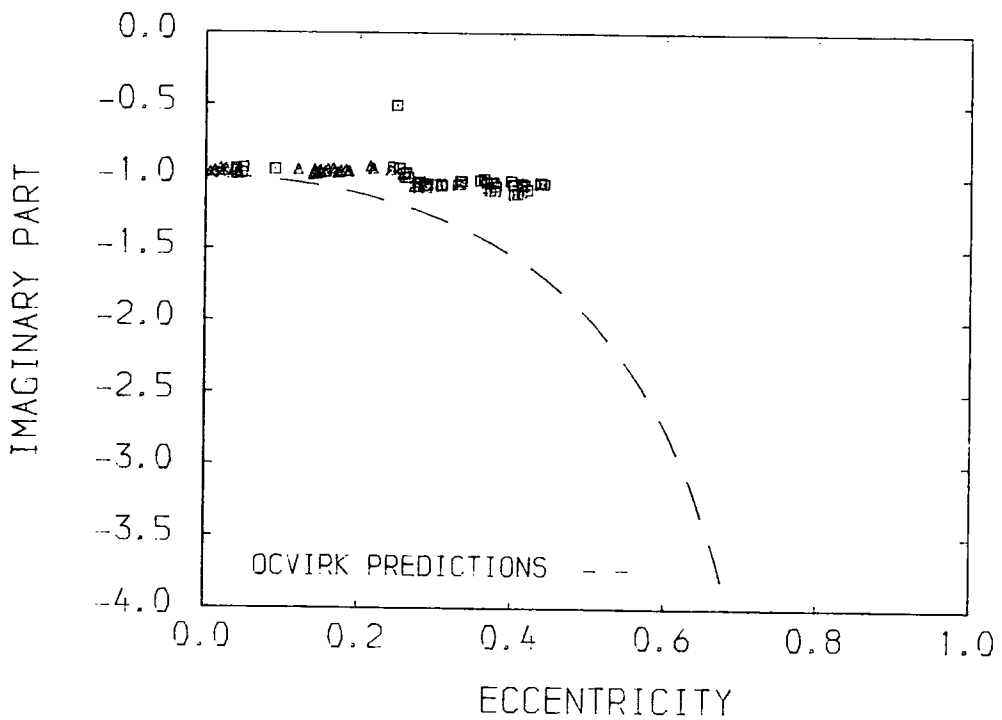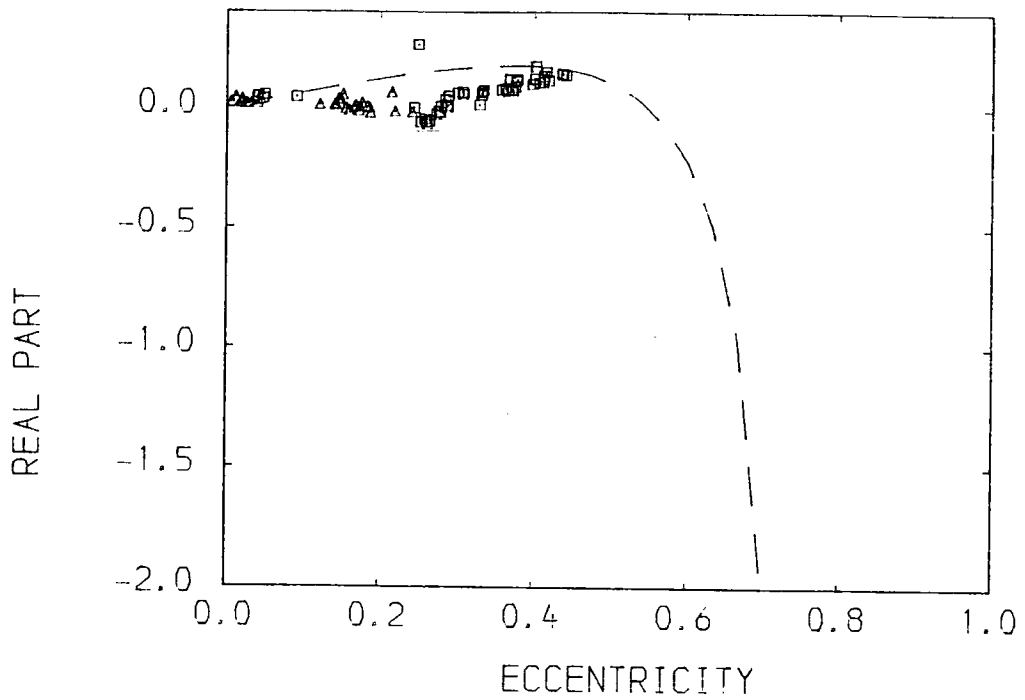
BEARING LENGTH   0.030 m   FIRST SESSION ▢
CLEARANCE RATIO 0.002   SECOND SESSION △

WHIRL ONSET ORBIT

SHAPE PARAMETER

FIGURE 8.46

BEARING LENGTH   0.030 m   FIRST SESSION   ▣
CLEARANCE RATIO 0.003

WHIRL ONSET ORBIT
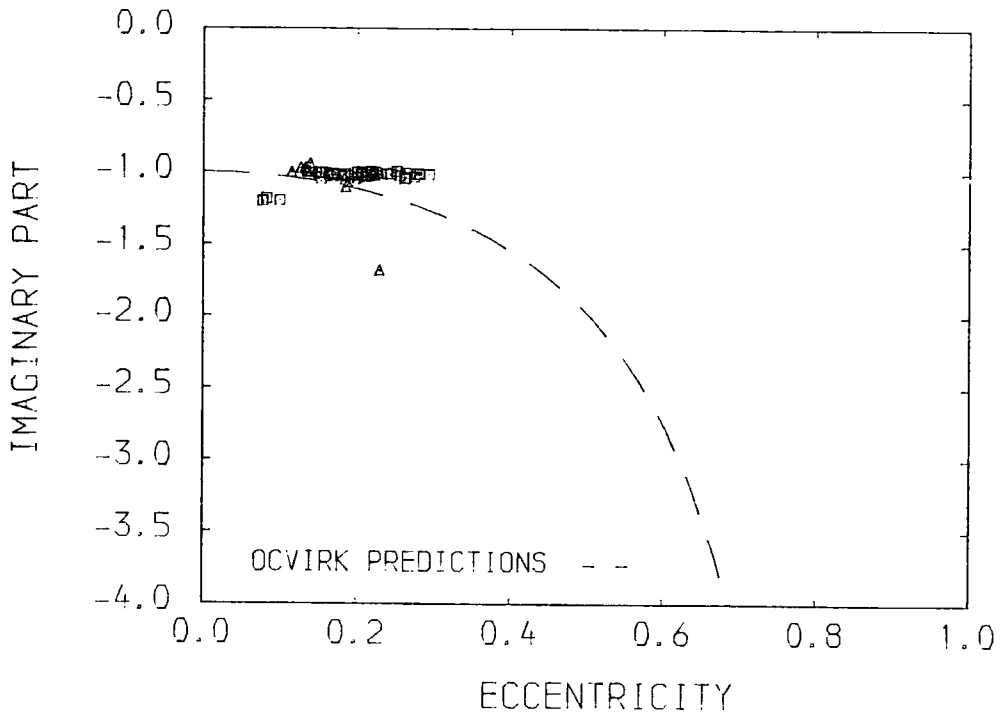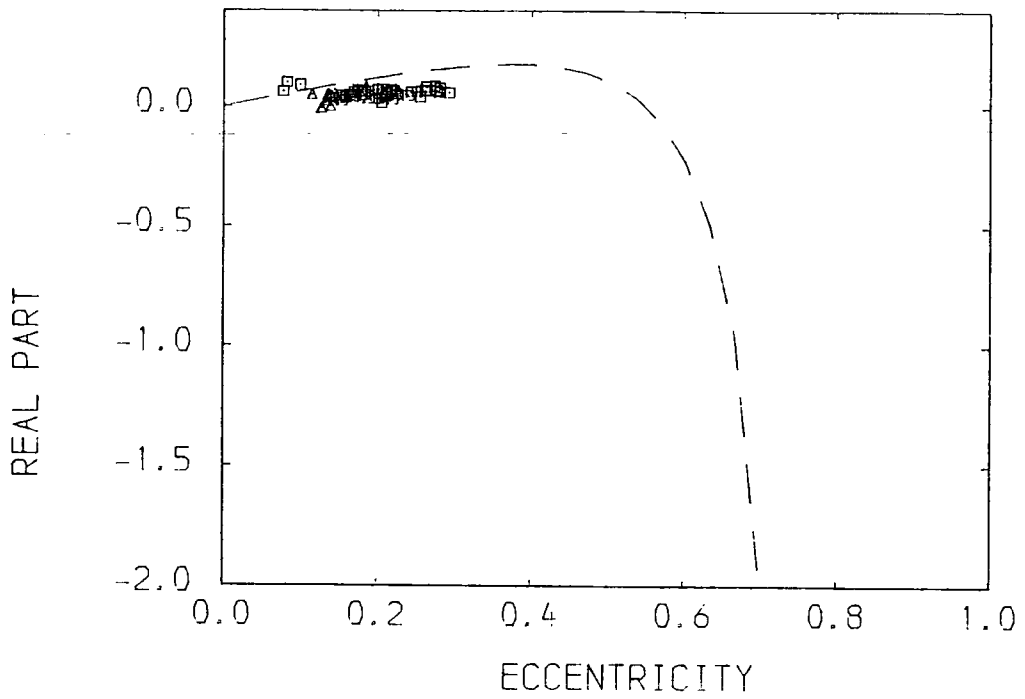
SHAPE PARAMETER

FIGURE 8.47

BEARING LENGTH   0.030 m   FIRST SESSION   □
CLEARANCE RATIO 0.004

WHIRL ONSET ORBIT
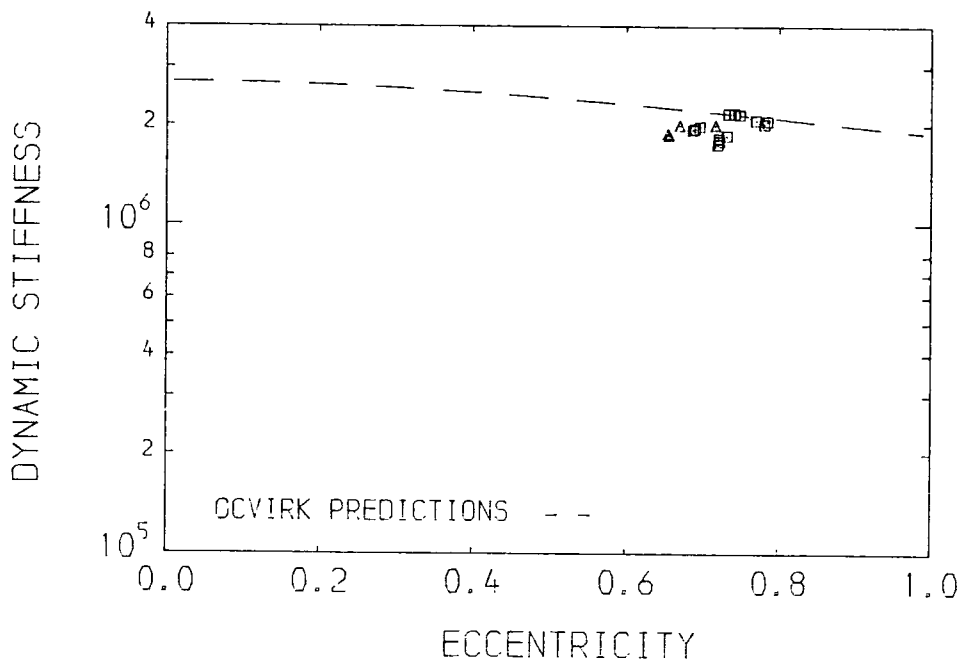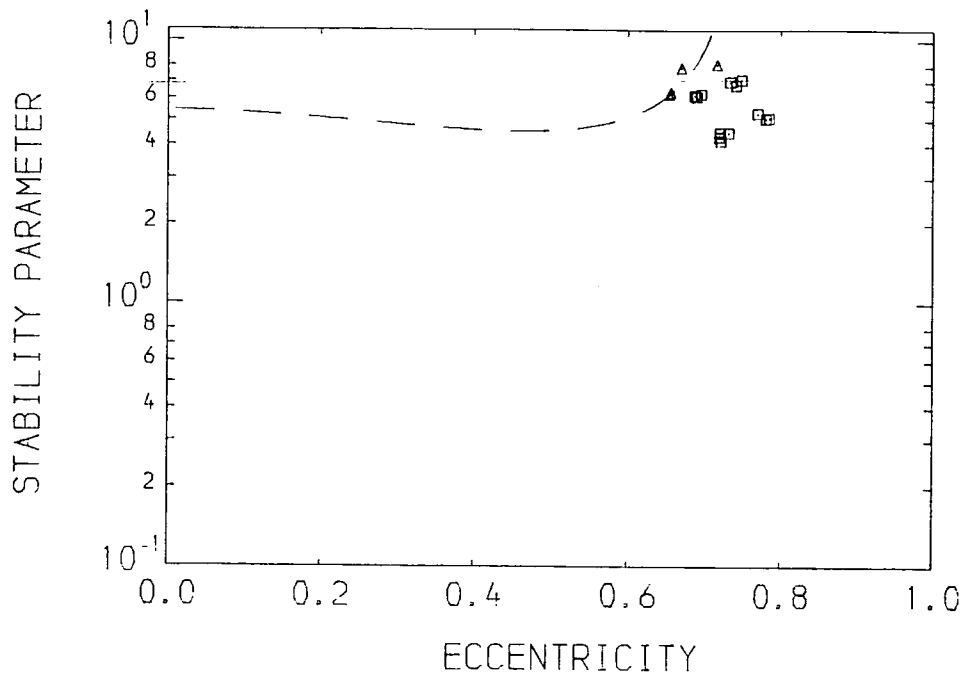
SHAPE PARAMETER

FIGURE 8.48

REAL PART

ECCENTRICITY

IMAGINARY PART

OCVIRK PREDICTIONS - -

ECCENTRICITY

BEARING LENGTH   0.040 m   FIRST SESSION   ▫
CLEARANCE RATIO 0.002   SECOND SESSION   △

WHIRL ONSET ORBIT

SHAPE PARAMETER

FIGURE 8.49

CRITICAL FILM

PERFORMANCE PARAMETERS

FIGURE 8.50

STABILITY PARAMETER vs ECCENTRICITY

DYNAMIC STIFFNESS vs ECCENTRICITY

OCVIRK PREDICTIONS – –

BEARING LENGTH   0.020 m
CLEARANCE RATIO   0.002

FIRST SESSION   ▫
SECOND SESSION   △
THIRD SESSION   ▽

CRITICAL FILM

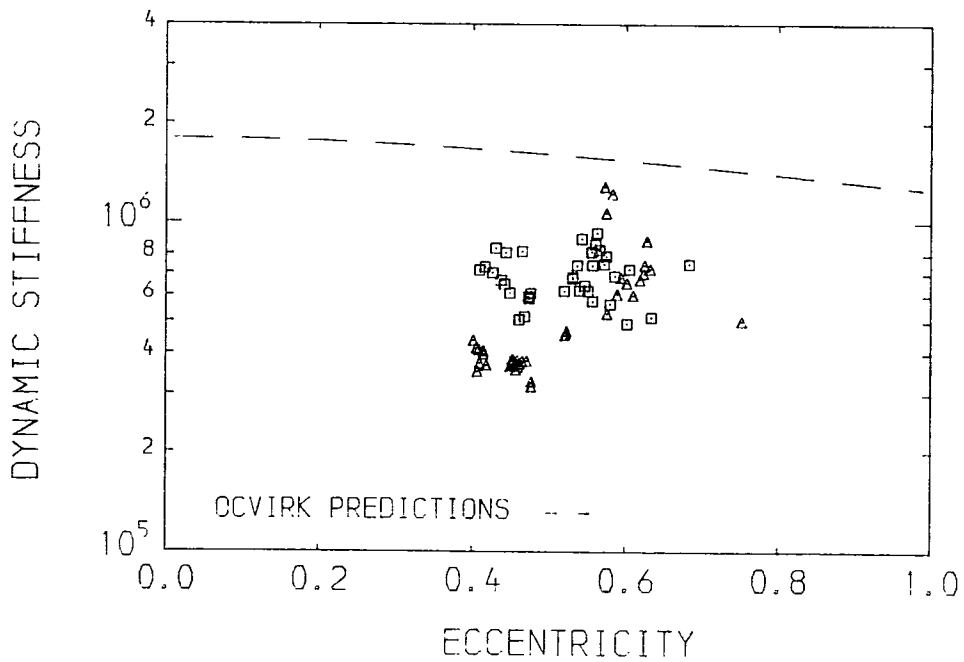PERFORMANCE PARAMETERS

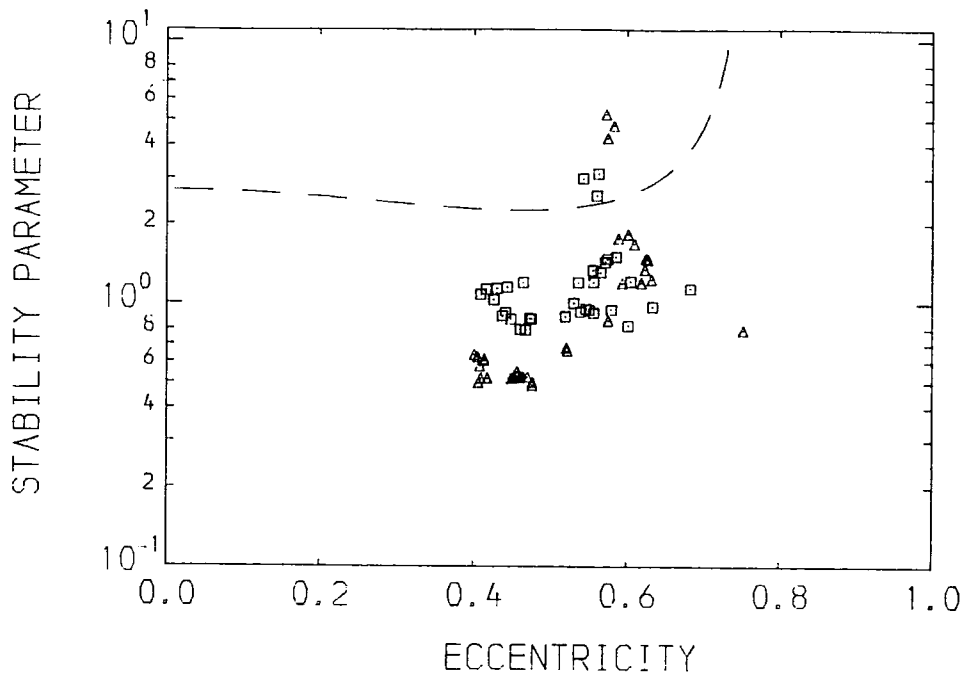FIGURE 8.51

BEARING LENGTH   0.020 m   FIRST SESSION   □
CLEARANCE RATIO   0.003   SECOND SESSION   △

CRITICAL FILM

PERFORMANCE PARAMETERS

FIGURE 8.52

BEARING LENGTH   0.020 m   FIRST SESSION   □
CLEARANCE RATIO 0.004

CRITICAL FILM

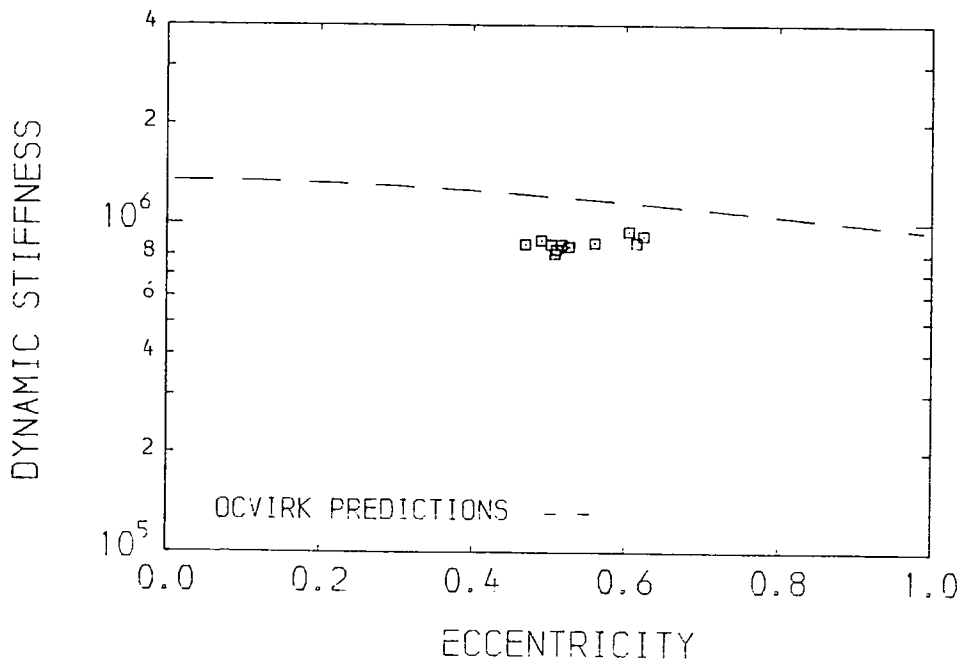## PERFORMANCE PARAMETERS

FIGURE 8.53
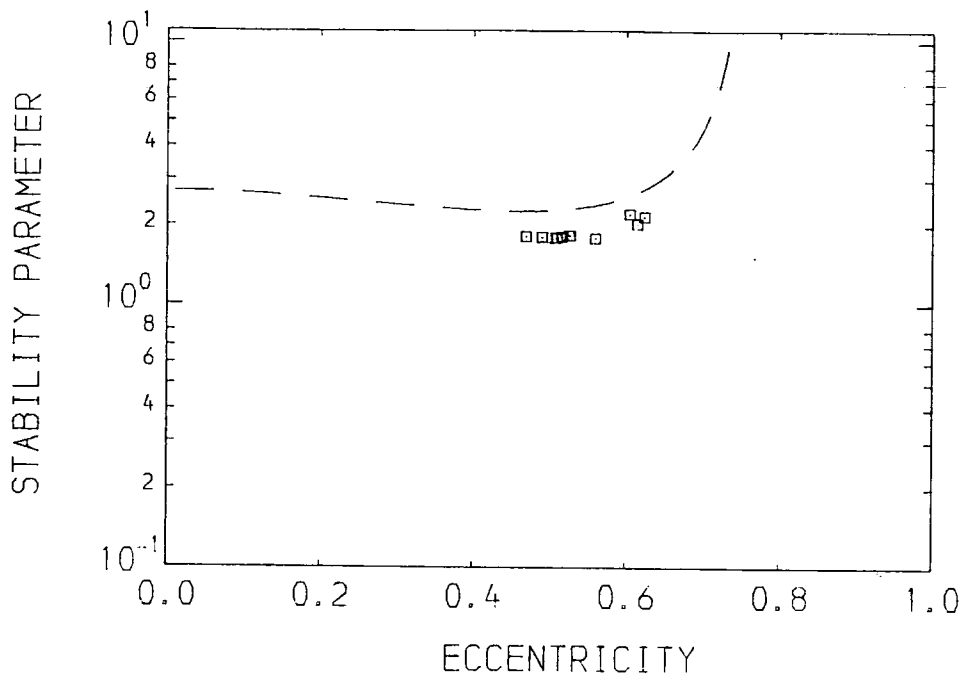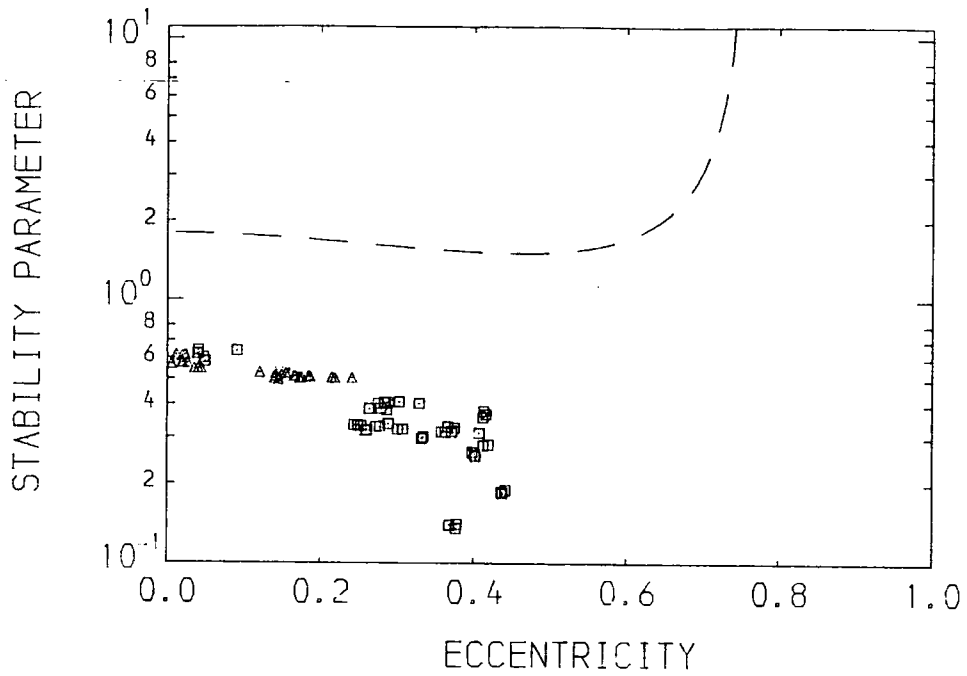
BEARING LENGTH   0.030 m   FIRST SESSION   ▫
CLEARANCE RATIO 0.002   SECOND SESSION   △

CRITICAL FILM

PERFORMANCE PARAMETERS

FIGURE 8.54
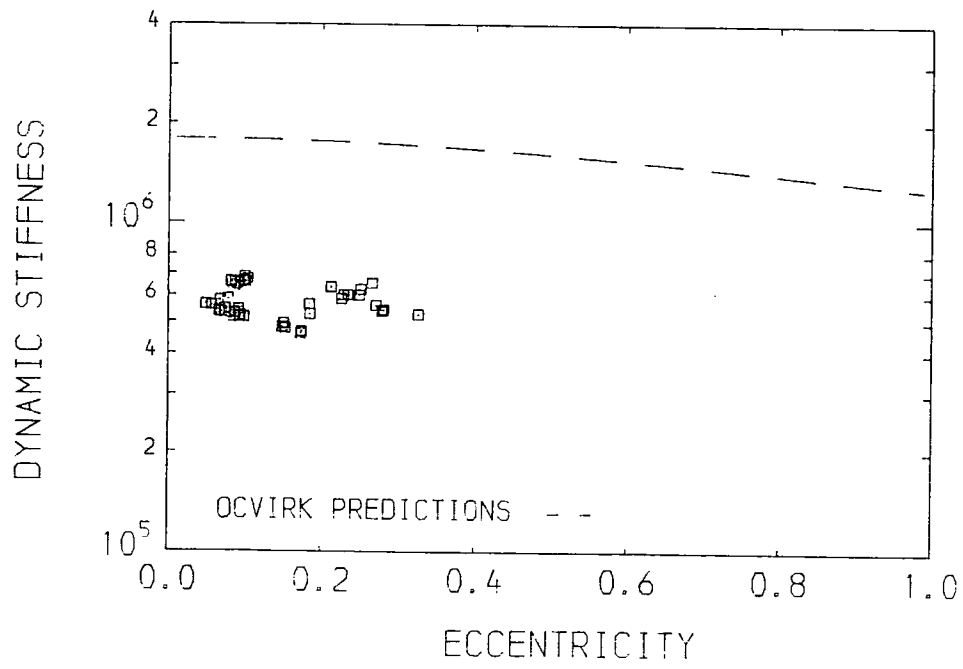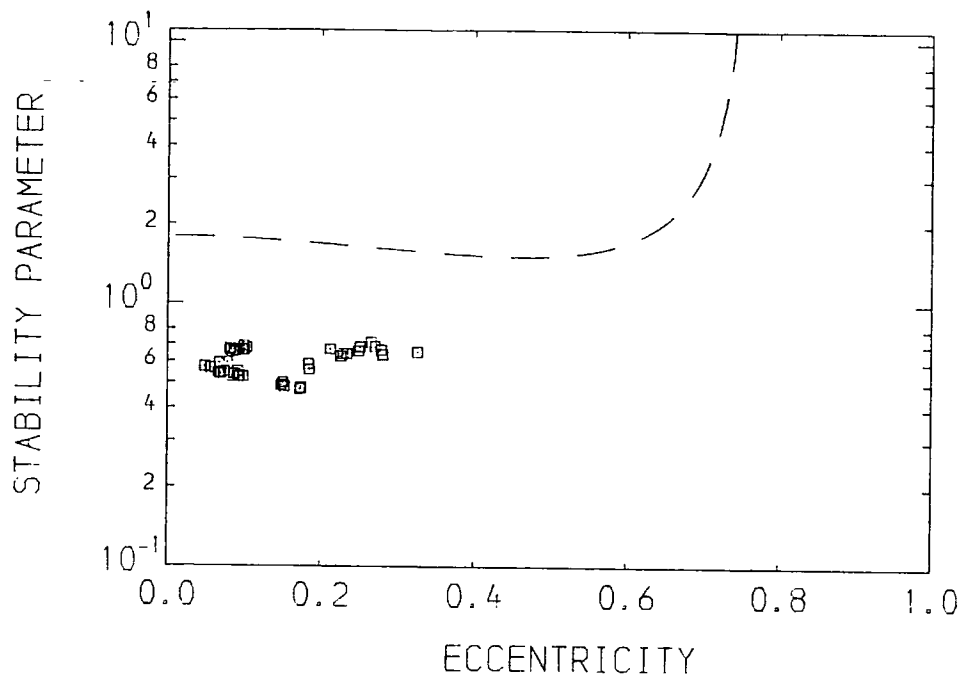
BEARING LENGTH   0.030 m   FIRST SESSION   ▫
CLEARANCE RATIO 0.003

CRITICAL FILM

PERFORMANCE PARAMETERS

FIGURE 8.55
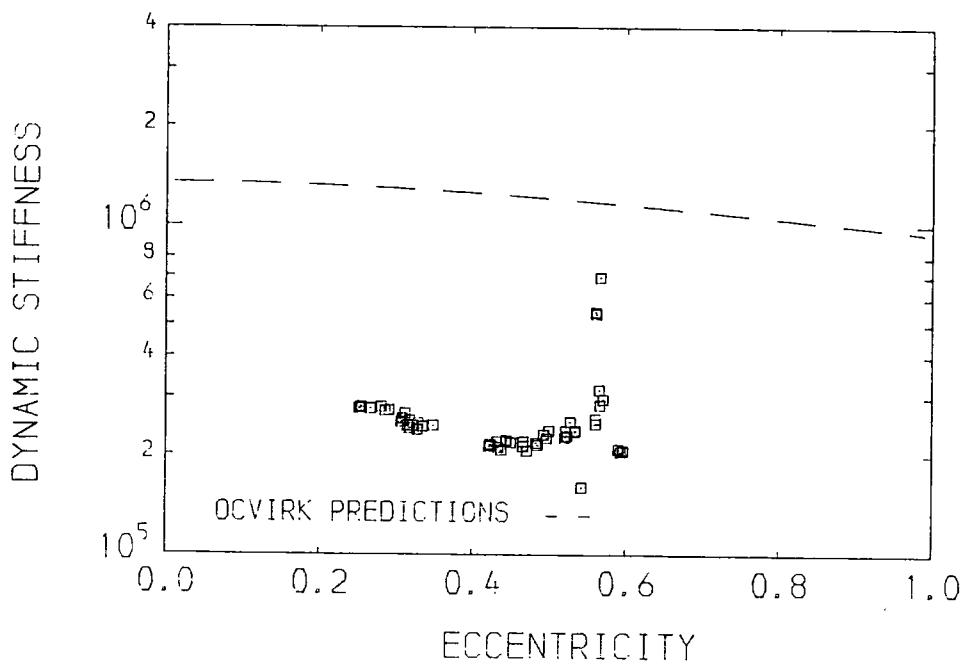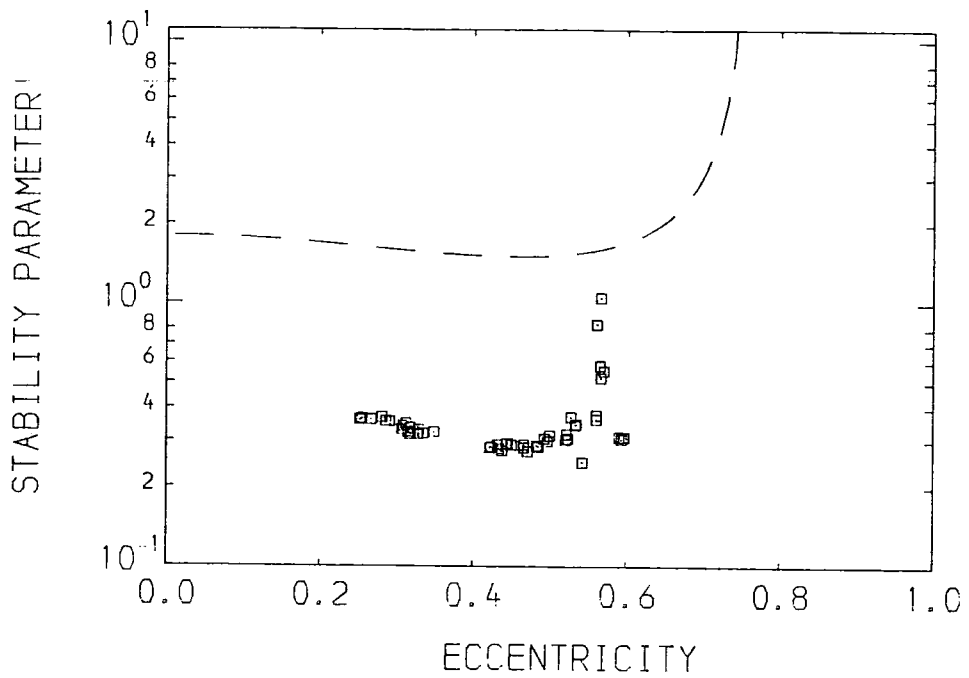
STABILITY PARAMETER

ECCENTRICITY

DYNAMIC STIFFNESS
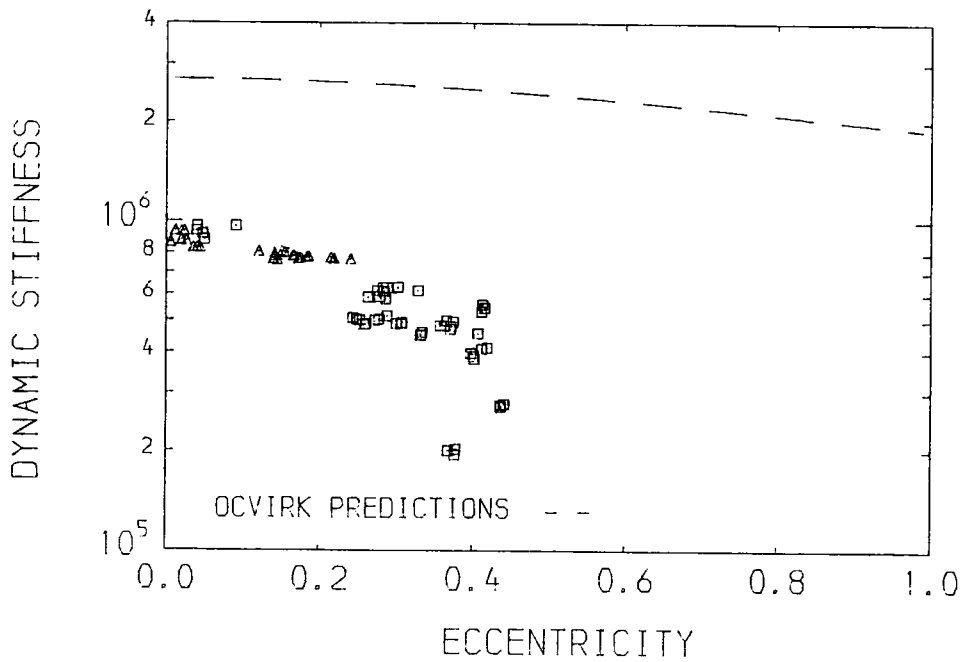
OCVIRK PREDICTIONS   – –

ECCENTRICITY

BEARING LENGTH   0.030 m   FIRST SESSION   □
CLEARANCE RATIO 0.004

CRITICAL FILM

PERFORMANCE PARAMETERS

FIGURE 8.56

STABILITY PARAMETER vs ECCENTRICITY

DYNAMIC STIFFNESS vs ECCENTRICITY

OCVIRK PREDICTIONS – –

BEARING LENGTH   0.040 m   FIRST SESSION   ▫
CLEARANCE RATIO   0.002   SECOND SESSION   △

CRITICAL FILM

PERFORMANCE PARAMETERS

FIGURE 8.57

$$\frac{\gamma_c}{H} \frac{[1 + (L/D)^2]}{(L/D)^2}$$

OCVIRK SOLUTION

—10-2

—20-4

—20-3

—30-3

—20-2

CLEARANCE RATIO × 10⁻³

BEARING WIDTH — mm

30-4

—30-2

—40-2

ECCENTRICITY
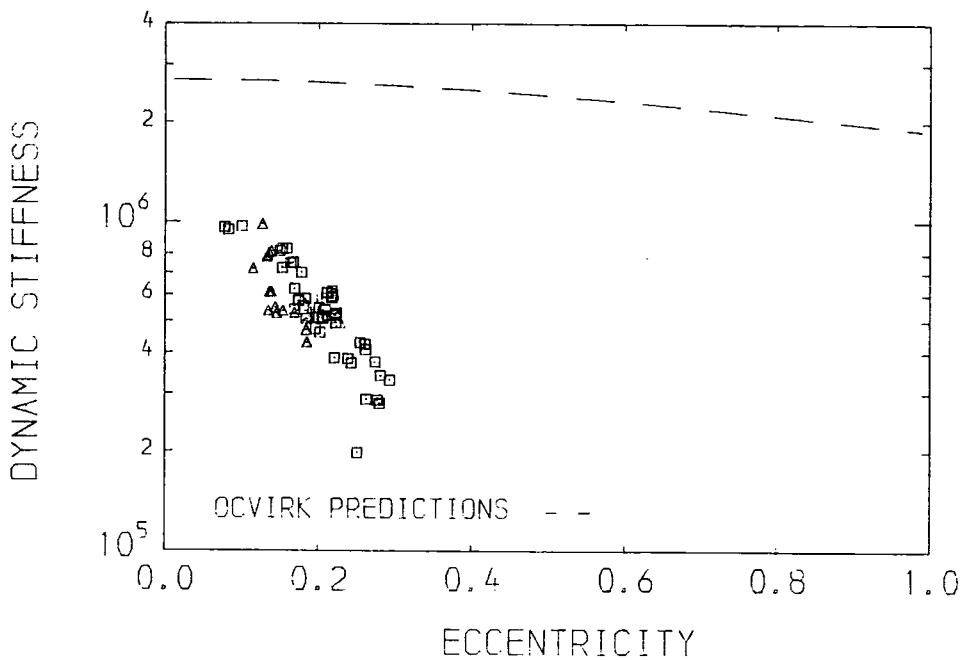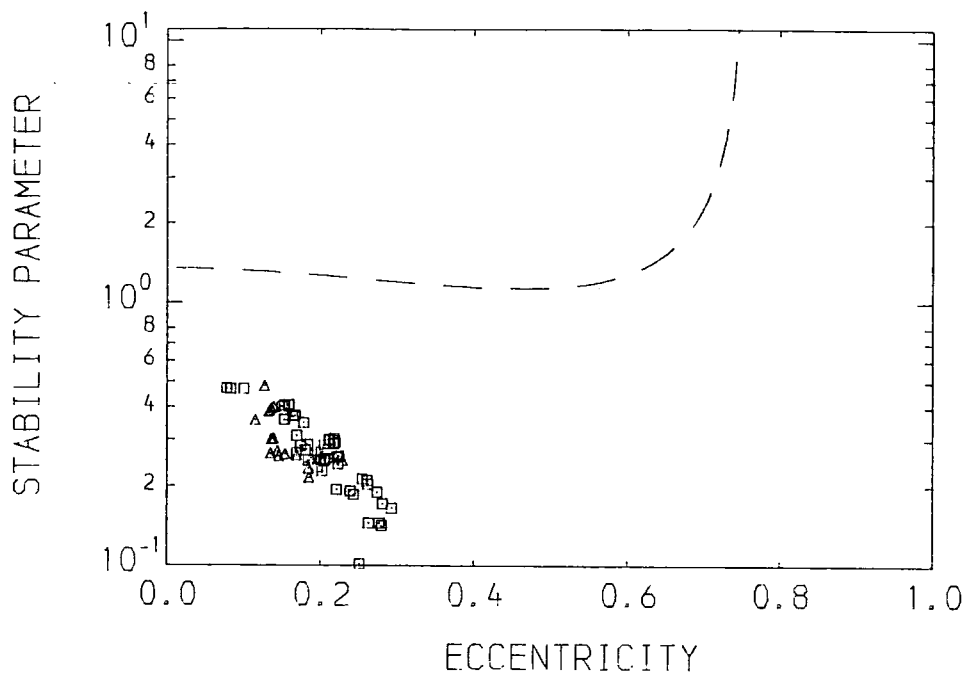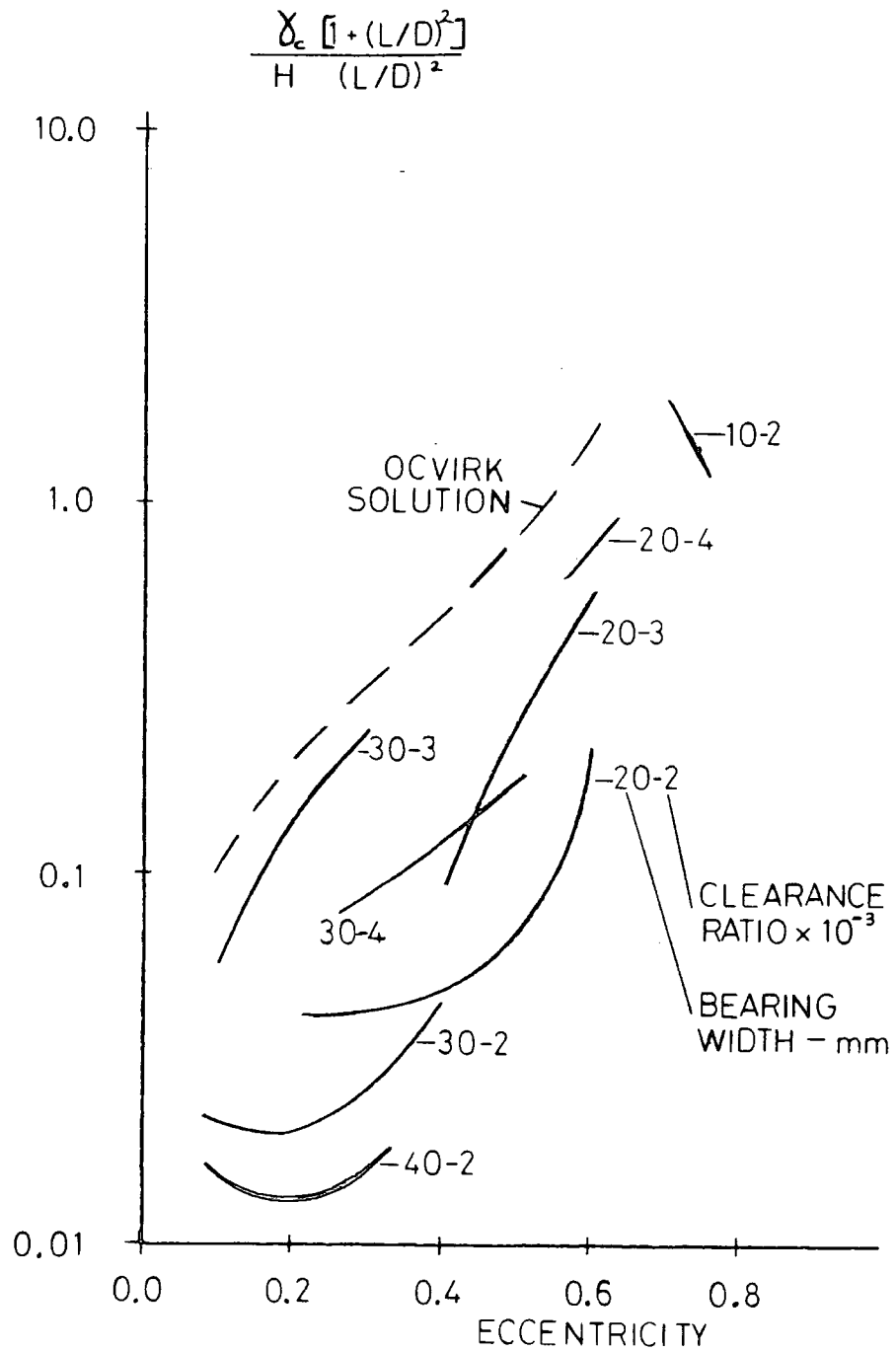
CRITICAL STABILITY PARAMETERS

FIGURE 8.58

$$\text{DYNAMIC STIFFNESS} \times \frac{C}{P_a \, RL} \; \frac{1}{H} \left[\frac{1 + (L/D)^2}{(L/D)^2} \right]$$

10.0

OCVIRK

1.0

10-2

20-4

20-3

20-2

30-3

CLEARANCE RATIO $\times 10^{-3}$

30-4

BEARING WIDTH – mm

0.1

30-2

40-2

0.01

0.0   0.2   0.4   0.6   0.8

ECCENTRICITY
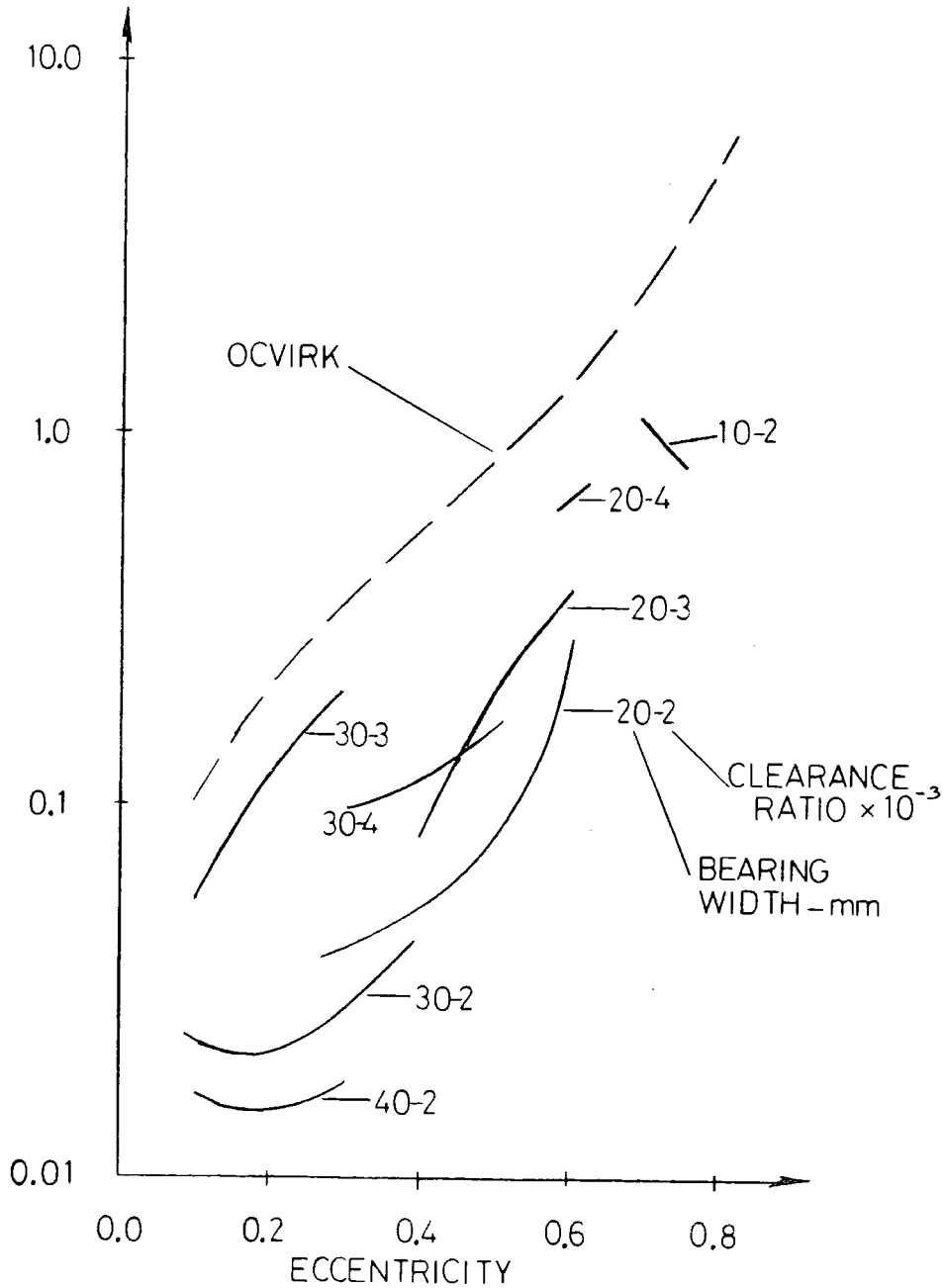
LUBRICATING FILM
DYNAMIC STIFFNESS

FIGURE 8.59

$$\frac{\gamma_c}{H} \frac{[1 + (L/D)^2]}{(L/D)^2}$$

MORI-OKADA-MORI

FEED HOLE   ⊚ — 0°
ANGLE   △ — 45°

OCVIRK

AKKOK-ETTLES
SUPPLY GROOVE
ARC
30°
90°

PRESENT
RESULTS

10.0

1.0

0.1

0.01

0.0   0.2   0.4   0.6   0.8

ECCENTRICITY
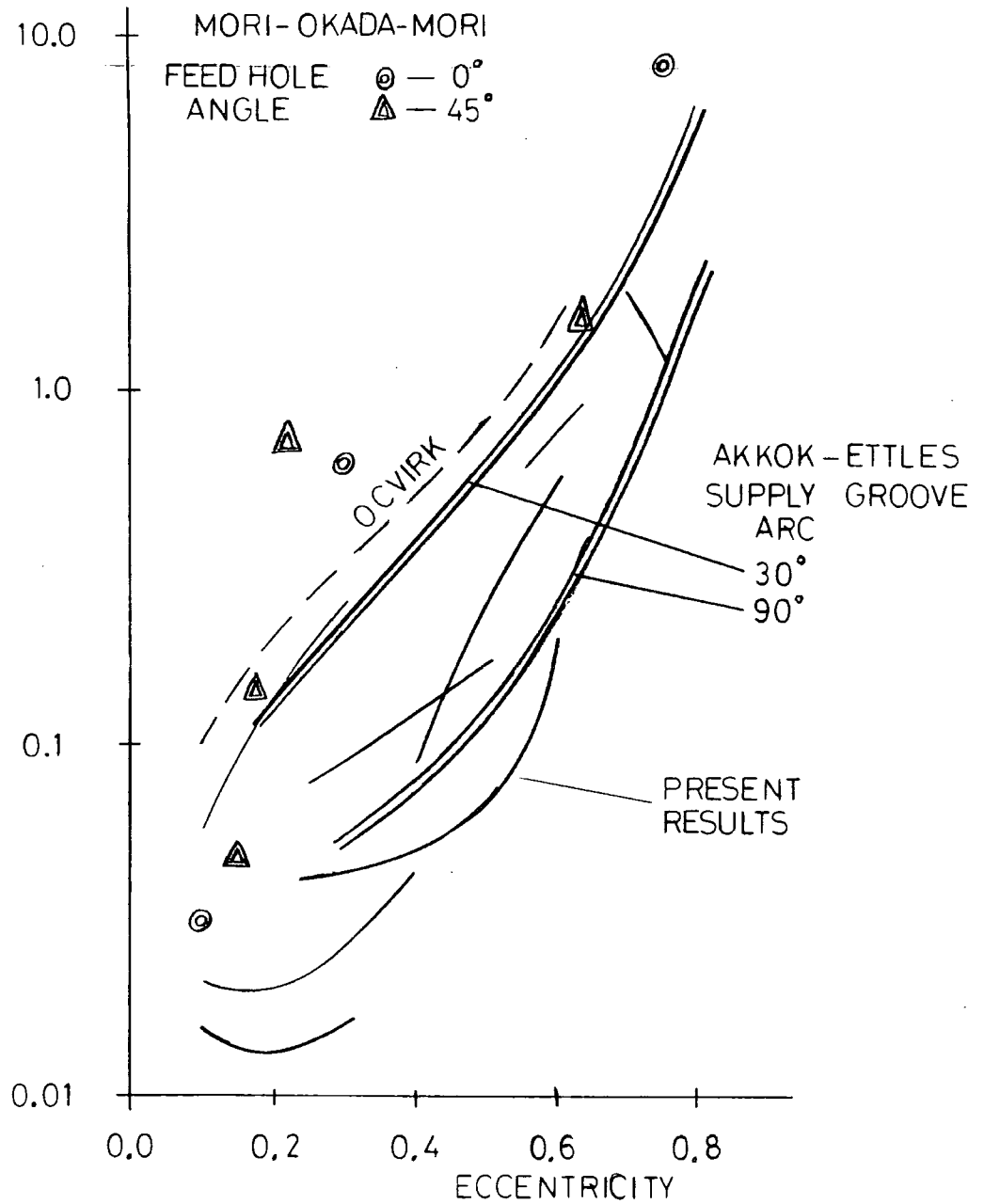
CRITICAL STABILITY
PARAMETERS

FIGURE 8.60

Appendix A

NUMERICAL ALGORITHMS

A-1   SYMBOLS

A   recorded data values

S   signature image values

D   calculated cartesian displacements

E   mapped radial position

Θ mapped attitude angle

C   clearance circle centre

R   clearance circle radius

$\mathcal{E}$ error function

ϵ eccentricity ratio

$\propto$ non-dimensional time constant

ω non-dimensional frequency

τ phase angle

A-1.1 Subscripts

i   coordinate direction   value 1 or 2

j   j'th data pair   value 1 to 510

k   k'th rotor angular position value 1 to 30

r   r'th rotation of rotor   value 1 to 17

0   steady state value

x   parameter describing the dynamic motion

A-1.2 Superscripts

-   current parameter value during iteration

A-2 PURPOSE OF THE ALGORITHMS

The primary duty of the data processing algorithms was to produce parameters describing the dynamics of the observed events from the measurements of the journal position. The electronic data gathering equipment was designed to gather readings from the test apparatus in a short time interval after whirl onset had been deemed to commence. Because of the type of probes used, algorithms had to be developed to eliminate the very strong synchronous components present in the data sets. The synchronous signals also dictated that the probes had to be calibrated whilst

in place and at typical operating conditions. The following algorithms were developed to satisfy these roles.

A-3   SOURCE DATA SET

The set of readings for each test is given the symbol:-

A_{ij}

Each data set comprised 1020 individual readings in 510 pairs. A pair consisted of two readings giving the instantaneous rotor position in mutually perpendicular directions relative to the centrebody. The readings were taken at time intervals equal to one thirtieth of the period of a rotor revolution over a continuous period of 17 complete turns. Hence every thirtieth data pair was taken with the rotor in the same angular position.

In general the dominant signal component in each data set was the synchronous signal arising from the surface properties of the rotor bore. The translational rotor motion generated a lesser component at the orbital frequency. The surface property signal was undesirable since the journal position and motion were required from the signal analysis. Thus the surface signal, or signature, had to be identified and subtracted from the source data as the first part of the signal analysis.

A-4   EVALUATION OF THE SIGNATURE

The signal pattern observed at steady state operating conditions was due to the rotor signature. Hence the numerical image of the signature was derived from data sets captured at steady operating conditions. The data processing consisted of taking the average for all readings at each angular position of the rotor, and then subtracting the mean of the averages to give a signature variation about zero. Thus the following formula defines the sixty values of the signature image.

$$S_{ik} = \frac{1}{17} \sum_{r=0}^{16} A_{i[k+30r]} - \frac{1}{510} \sum_{j=1}^{510} A_{ij} \qquad (A.1)$$

A-5   SIGNATURE SUBTRACTION

In order to subtract the signature from each set of readings, the stored signature image had to be synchronised with the signature component in the data. If a strobing signal had been available from the test bed to indicate when the rotor was in a particular angular position, all the data sets could have been started at the same part of the signature, but no such signal was available. The technique used to synchronise the data and the image was to calculate a sum of change function for each of the thirty possible alignments between the data and the signature.

The function value was calculated using a shortened data set from two rotor revolutions, as shown below.

$$\sum_{r=9}^{10} \sum_{k=1}^{30} \left| \left(A_{i[k+30r]} - S_{ik} \right) - \left(A_{i[k-1+30r]} - S_{i[k-1]} \right) \right| \qquad (A.2)$$

Since the journal signature had very large first difference terms compared to the signal components due to the journal motion, one alignment produced a sum of change function much smaller than any of the others. The correct alignment was assumed to be the one which gave the least value for the change function. This technique worked even for fully developed whirl conditions since some of the first differences in the signature image were always greater than the first differences due to the transverse journal motion. Having found the correct signature alignment, the whole of the initial data sample was converted into the data set $'D_{ij}'$ representing the journal position in cartesian coordinates.

A-6   CLEARANCE CIRCLE IMAGE

The mathematical parameters describing the clearance circle were derived from data recorded whilst the bearing was performing fully developed whirl orbits. Since the signal amplifiers in each data channel were adjusted individually, the image of the journal motion was slightly elliptical. Hence the following general equation for an ellipse was fitted to the data set.

$$1 \quad = \quad \left(\frac{D_{ij} - C_1}{R_1} \right)^2 \quad + \quad \left(\frac{D_{2j} - C_2}{R_2} \right)^2 \qquad (A.3)$$

The parameters $'R_i'$ and $'C_i'$ represent the half lengths of the ellipse axes and the coordinates of the ellipse centre. The values calculated for these parameters define the transformation from cartesian readings $'D_{ij}'$ to polar attitude angle $'\theta_j'$ and eccentricity ratio $'E_j'$.

For ease of solution the non-linear problem was divided into two parts which were solved iteratively. The initial values for the ellipse centre $'C_i'$ and the major dimensions $'R_i'$ were found from the extreme values of each data set. Then the following non-dimensional radius $'X_j'$ was calculated for each of the data coordinate pairs $'D_{ij}'$.

$$X_j^2 \quad = \quad \left(\frac{D_{ij} - C_1}{R_1} \right)^2 \quad + \quad \left(\frac{D_{2j} - C_2}{R_2} \right)^2 \qquad (A.4)$$

Comparing equations (A.3) and (A.4) shows that the value of $'X_j'$ is always approximately equal to one. This non-dimensional radius was then used in the following formula to correct the centre coordinates.

$$C_i \quad - \quad \overline{C}_i \quad = \quad \frac{1}{510} \sum_{j=1}^{510} \left(D_{ij} - \overline{C}_i \right) \left(\frac{X_j - 1}{X_j} \right) \qquad (A.5)$$

The iterative solution for the ellipse dimensions $'R_i'$ was based on minimising an error function $'\varepsilon_j'$ derived from the

non-dimensional radius.

$$\varepsilon_j = \left(X_j - 1 \right) \qquad (A.6)$$

Since each $'X_j'$ is approximately equal to one, the following first order approximation to the error function was used in the analysis.

$$\varepsilon_j = \left(\frac{X_j^2 - 1}{2} \right) \qquad (A.7)$$

Substituting the non-dimensional radius $'X_j'$ into the error function, generates an equation which is suitable for least squares analysis. The resulting matrix equation is:-

$$\begin{bmatrix} \sum_j \left(D_{1j} - \overline{C}_1 \right)^4 & \sum_j \left(D_{1j} - \overline{C}_1 \right)^2 \left(D_{2j} - \overline{C}_2 \right)^2 \\ \sum_j \left(D_{1j} - \overline{C}_1 \right)^2 \left(D_{2j} - \overline{C}_2 \right)^2 & \sum_j \left(D_{2j} - \overline{C}_2 \right)^4 \end{bmatrix} \begin{bmatrix} \left(\frac{1}{R_1^2} \right) \\ \left(\frac{1}{R_2^2} \right) \end{bmatrix}$$

$$= \begin{bmatrix} \sum_j \left(D_{1j} - \overline{C}_1 \right)^2 \\ \sum_j \left(D_{2j} - \overline{C}_2 \right)^2 \end{bmatrix} \qquad (A.8)$$

The two sets of equations defining new values for $'R_i'$ and $'C_i'$, were solved simultaneously during each iteration to avoid calculating the non-dimensional radius more often than necessary. Experience showed that four iterations were sufficient to give reasonable values for all four parameters.

A-7   TRANSFORMATION INTO BEARING COORDINATES

Once the rotor signature and clearance circle images had been generated, all whirl onset data sets $'D_{ij}'$ were converted into eccentricity $'E_j'$ and attitude angle $'\theta_j'$ values using the following transformations.

$$E_j^2 \quad = \quad \left(\frac{D_{1j} - C_1}{R_1}\right)^2 + \left(\frac{D_{2j} - C_2}{R_2}\right)^2 \tag{A.9}$$

$$\text{Tan}(\theta_j) \quad = \quad \left(\frac{R_1}{R_2}\right)\left(\frac{D_{2j} - C_2}{D_{1j} - C_1}\right)$$

A-8   WHIRL ANALYSIS

The object of the whirl onset analysis was not only to find the orbital frequency and the mean rotor position but to take full advantage of the numerical analysis to find the orbit shape and decay constant. As with the clearance circle determination, the orbit analysis is a non-linear problem. The solution technique employed was to fit real counterparts of the general expressions of journal motion (4.1) to the data sets. The following equations demonstrate the method using the series of data values representing the eccentricity ratio $'E_j'$. Exactly the same analysis was performed simultaneously on the attitude angle data to generate the full description of the orbital

motion.

If the following pair of equations are considered as respectively the best fit to the data and the current approximation, a least squares analysis was performed to minimise the error term '$\mathcal{E}_j$' in the second equation.

$$E_j \quad = \quad \epsilon_o + \epsilon_x e^{\alpha j} \text{Cos}(\omega_x j - \tau_\epsilon) \tag{A.10}$$

$$E_j + \mathcal{E}_j \quad = \quad \bar{\epsilon}_o + \bar{\epsilon}_x e^{\bar{\alpha} j} \text{Cos}(\bar{\omega}_x j - \bar{\tau}_\epsilon) $$

From these two equations, a first order expression for the errors '$\mathcal{E}_j$' can be derived in terms of the required corrections to the current values of the parameters describing the orbital motion.

$$\mathcal{E}_j \quad = \quad (\bar{\epsilon}_o - \epsilon_o) \tag{A.11}$$

$$+ \left(\frac{(\bar{\epsilon}_x - \epsilon_x)}{\epsilon_x} + (\bar{\alpha} - \alpha) j \right) \bar{\epsilon}_x e^{\bar{\alpha} j} \text{Cos}(\bar{\omega}_x j - \bar{\tau}_\epsilon)$$

$$+ \left((\tau_\epsilon - \bar{\tau}_\epsilon) + (\bar{\omega}_x - \omega_x) j \right) \bar{\epsilon}_x e^{\bar{\alpha} j} \text{Sin}(\bar{\omega}_x j - \bar{\tau}_\epsilon)$$

If this equation is integrated over a whole number of whirl orbits, the second and third terms on the right hand side will make an insignificant contribution to the integral, provided that the time constant 'α' is not large. Thus finding the simple mean of the data set results in the following correction term for the equilibrium eccentricity value.

$$(\bar{\epsilon}_o - \epsilon_o) \quad = \quad \frac{1}{L} \sum_{j=1}^{L} E_j \tag{A.12}$$

The orbit amplitude and time constant were corrected by

performing a least squares curve fit to a modification of the error function. If the mean value error is assumed to be small, the first term in equation (A.11) can be ignored. Then for all values of 'j' which give a value for the cosine function larger than the sine function, the third term can also be ignored. Rearranging the resulting approximation leaves the following linear relationship between the modified error values and the parameter 'j'.

$$\frac{\mathcal{E}_j}{\bar{\epsilon}_x \, e^{\bar{\alpha}j} \, Cos(\bar{\omega}_x j - \bar{\tau}_\epsilon)} = \frac{(\bar{\epsilon}_x - \epsilon_x)}{\epsilon_x} + (\bar{\alpha} - \alpha) \, j \qquad (A.13)$$

for all j where $Cos(\bar{\omega}_x j - \bar{\tau}_\epsilon) > Sin(\bar{\omega}_x j - \bar{\tau}_\epsilon)$

Performing a least squares curve fit upon this relationship produces the corrections to the orbit amplitude and time constant.

Similarly the following relationship applies for the set of error function values which do not satisfy the condition above.

$$\frac{\mathcal{E}_j}{\bar{\epsilon}_x \, e^{\bar{\alpha}j} \, Sin(\bar{\omega}_x j - \bar{\tau}_\epsilon)} = -(\bar{\tau}_\epsilon - \tau_\epsilon) + (\bar{\omega}_x - \omega_x) \, j \qquad (A.14)$$

for all j where $Cos(\bar{\omega}_x j - \bar{\tau}_\epsilon) < Sin(\bar{\omega}_x j - \bar{\tau}_\epsilon)$

A least squares analysis of this series provides the correction to the phase angle and time period parameters.

The set of attitude angles was also analysed in the same manner. Since the time constant parameters 'α' and 'ω_x' are

common to both the $'E_j'$ and $'\Theta_j'$ data sets, the equations for each coordinate axis were combined and solved simultaneously. The combination was achieved by summing the squared errors from both series, and this sum of squares was minimised.

Initial values for the iterative solution were calculated by searching through the data sets for turning points. The times at which the the turning points occurred were used to find the time period and phase angles by a least squares analysis. The values of the turning points were similarly analysed to give the mean value, initial orbit size and growth constant.

Three iterations proved sufficient to give reasonably accurate interpretation of the data within an acceptable time period. To minimise computing time, integer arithmetic and data storage was used whenever possible. Unnecessary evaluation of trigonometric and exponential functions was also avoided. By these methods the time required for each iteration was reduced by more than half to about twenty seconds. After three iterations the real parameters representing orbit size and phase angle were turned into the complex coefficients of equations (4.1), and a value found for the complex ratio $'\epsilon_2 \Theta_1 / \epsilon_1'$. The full description of the whirl orbit, as used in the theoretical study, was then displayed on the computer screen.